A novel experimental platform for monitoring and imaging bacterial biofilm growth in porous media flows

Christos Papadopoulos

To cite this version:

Christos Papadopoulos. A novel experimental platform for monitoring and imaging bacterial biofilm growth in porous media flows. Fluid Dynamics [physics.flu-dyn]. Institut National Polytechnique de Toulouse - INPT, 2023. English. NNT : 2023INPT0032 . tel-04567789

HAL Id: tel-04567789
https://theses.hal.science/tel-04567789

Submitted on 3 May 2024

THÈSE

En vue de l'obtention du

DOCTORAT DE L'UNIVERSITÉ DE TOULOUSE

Délivré par :

Institut National Polytechnique de Toulouse (Toulouse INP)

Discipline ou spécialité :

Dynamique des Fluides

Présentée et soutenue par :

M. CHRISTOS PAPADOPOULOS

le jeudi 22 juin 2023

Titre :

Une nouvelle plateforme expérimentale pour étudier et imager la croissance de biofilms bactériens sous écoulement dans les milieux poreux

---

École doctorale :

Mécanique, Énergétique, Génie civil, Procédés (MEGeP)

Unité de recherche :

Institut de Mécanique des Fluides de Toulouse (IMFT)

Directeurs de Thèse :

M. YOHAN DAVIT
M. LAURENT MALAQUIN

Rapporteurs :

M. FABRICE GOLFIER, UNIVERSITE LORRAINE
MME NELLY HENRY, UNIVERSITE SORBONNE

Membres du jury :

M. PASCAL SWIDER, TOULOUSE INP, Président
M. RENAUD ESCUDIE, INRAE NARBONNE, Membre

A novel experimental platform for studying and imaging bacterial biofilm growth under flow in porous media

October 30, 2023

Abstract

Biofilms are complex microbial communities that primarily grow on solid surfaces where microorganisms are embedded in extracellular polymeric substances (EPS). This lifestyle is dominant over the planktonic phenotype and is found in various environments such as the suboceanic subsurface and soils. The growth of biofilms in porous media under flow conditions is widespread in natural and man-made systems, and they play a crucial role in Earth's critical zone, driving ecosystem processes and contributing to biogeochemical cycles.

Moreover, biofilms are also used to engineer the properties of porous systems such as hydraulic conductivity, chemical speciation, or physic-chemical properties of multiphase systems. Examples of such systems include biological filters, submerged bed and trickling filters, co-current systems that filter suspended matter, ammonia, phosphorus, and micro-pollutants from wastewater, bio-barriers or bioremediation processes, microbially-enhanced oil recovery, self-healing concrete, and sealing cap rock fractures in CO_2 aquifer storage.

Biofilm formation initiates with the attachment of microorganisms onto surfaces under appropriate flow and nutrient conditions. Porous media with high surface-to-volume ratios provide an ideal environment and substrate for studying biofilm growth. Various natural systems in the environment (such as rocks, soil, sand) and our bodies (such as lungs, bones) can be considered as porous media.

However, understanding the mechanisms that control biofilm development in porous media is challenging due to the structural complexity and the opacity of the 3D porous structure. Several factors control biofilm growth, such as nutrient/oxygen availability, flow rate, communication, and shear stress. Improved quantification of the physical aspects of biofilm growth is essential in unraveling the mechanisms of biofilm formation in porous materials and progressing towards new biotechnologies.

To gain insight into how fluid flow, transport phenomena, and biofilms interact within heterogeneous structures, a versatile, micro-scale, 3D-printed micro-bioreactor has been devised. The bioreactor allows for the precise measurement of several parameters of such systems, enabling controlled and reproducible studies of biofilms in 3D porous systems. The approach to 3D imaging of biofilms in such systems uses X-ray micro-tomography with functionalized gold nanoparticles as a contrast agent. Preliminary results of P. aeruginosa biofilm development in this system suggest that biofilm growth in porous media under flow is a dynamic process resulting from an equilibrium between competing mechanisms such as bacterial growth and detachment due to hydrodynamic stresses.

The experimental setup, with the 3D-printed micro-bioreactor being in the heart of it, provides an adjustable, versatile experimental workbench for the study of the growth and detachment dynamics of biofilms in porous media under controlled conditions over long periods of time. The combination with X-ray tomography imaging provides insight into how physical (flow rate, shear stress) and chemical (oxygen, nutrient availability) parameters of the system affect the biofilm's spatial distribution. Understanding biofilm growth dynamics in the mesoscale could potentially unlock novel biotechnologies. Therefore, the main objective of this work is to develop a methodology to study biofilm growth dynamics in porous systems under flow in a precise and controlled manner, utilizing a 3D-printed micro-bioreactor and X-ray micro-tomography imaging. Furthermore, CFD simulations are used in combination to the obtained X-ray tomography images to have an insight of the biomass distribution within a porous structure. Finally, in this work, the potential of novel contrast agents based on gold nanoparticles will be examined and their suitability as a contrast agent will be assessed.

Résumé

Les biofilms sont des communautés microbiennes complexes qui se développent principalement sur des surfaces solides où les micro-organismes sont intégrés dans des substances polymériques extracellulaires (EPS). Ce mode de vie est dominant par rapport au phénotype planctonique et se retrouve dans divers environnements tels que la subsurface des océans et les sols. La croissance de biofilms dans des milieux poreux dans des conditions d'écoulement est très répandue dans les systèmes naturels et artificiels, et ils jouent un rôle crucial dans la zone critique de la terre, en pilotant les processus écosystémiques et en contribuant aux cycles biogéochimiques.

En outre, les biofilms sont également utilisés pour modifier les propriétés des systèmes poreux, telles que la conductivité hydraulique, la spéciation chimique ou les propriétés physico-chimiques des systèmes multiphasiques. Parmi ces systèmes, on peut citer les filtres biologiques, les filtres à lit immergé et à ruissellement, les systèmes à co-courant qui filtrent les matières en suspension, l'ammoniac, le phosphore et les micropolluants des eaux usées, les barrières biologiques ou les processus de biorestauration, la récupération du pétrole améliorée par les microbes, le béton auto-cicatrisant et le colmatage des fractures de la roche de couverture dans le stockage aquifère du CO_2.

La formation d'un biofilm commence par la fixation de micro-organismes sur des surfaces dans des conditions d'écoulement et de nutriments appropriées. Les milieux poreux présentant un rapport surface-volume élevé constituent un environnement et un substrat idéaux pour l'étude de la croissance des biofilms. Divers systèmes naturels dans l'environnement (tels que les roches, le sol, le sable) et notre corps (tels que les poumons, les os) peuvent être considérés comme des milieux poreux.

Cependant, comprendre les mécanismes qui contrôlent le développement des biofilms dans les milieux poreux est un défi en raison de la complexité structurelle et de l'opacité de la structure poreuse en 3D. Plusieurs facteurs contrôlent la croissance du biofilm, tels que la disponibilité des nutriments et de l'oxygène, l'écoulement, la communication et le cisaillement. Une meilleure quantification des aspects physiques de la croissance des biofilms est essentielle pour élucider les mécanismes de formation des biofilms dans les matériaux poreux et progresser vers de nouvelles biotechnologies.

Pour mieux comprendre comment l'écoulement des fluides, les phénomènes de transport et les biofilms interagissent au sein de structures hétérogènes, un micro-bioréacteur polyvalent, à micro-échelle et imprimé en 3D a été conçu. Le bioréacteur permet de mesurer avec précision plusieurs paramètres de ces systèmes, ce qui permet des études contrôlées et reproductibles des biofilms dans les systèmes poreux en 3D. L'approche de l'imagerie 3D des biofilms dans ces systèmes utilise la micro-tomographie à rayons X avec des nanoparticules d'or fonctionnalisées comme agent de contraste. Les résultats préliminaires du développement du biofilm de P. aeruginosa dans ce système suggèrent que la croissance du biofilm dans les milieux poreux soumis à un écoulement est un processus dynamique résultant d'un équilibre entre des mécanismes concurrents tels que la croissance bactérienne et le détachement dû aux contraintes hydrodynamiques.

Le dispositif expérimental, au cœur duquel se trouve le micro-bioréacteur imprimé en 3D, constitue un banc d'essai réglable et polyvalent pour l'étude de la dynamique de croissance et de détachement des biofilms dans les milieux poreux, dans des conditions contrôlées et sur de longues périodes de temps. La combinaison avec l'imagerie par tomographie à rayons X permet de comprendre comment les paramètres physiques (débit, contrainte de cisaillement) et chimiques (oxygène, disponibilité des nutriments) du système affectent la distribution spatiale du biofilm. La compréhension de la dynamique de croissance des biofilms à l'échelle méso pourrait potentiellement débloquer de nouvelles biotechnologies. Par conséquent, l'objectif principal de ce travail est de développer une méthodologie pour étudier la dynamique de croissance des biofilms dans les systèmes poreux sous écoulement de manière précise et contrôlée, en utilisant un micro-bioréacteur imprimé en 3D et l'imagerie par micro-tomographie à rayons X. En outre, les simulations CFD sont utilisées en combinaison avec les images de tomographie à rayons X obtenues pour avoir un aperçu de la distribution de la biomasse au sein d'une structure poreuse. Enfin, dans ce travail, le potentiel de nouveaux agents de contraste basés sur des nanoparticules d'or sera examiné et leur pertinence en tant qu'agent de contraste sera évaluée.

Acknowledgements

I extend my deepest gratitude to those whose support and guidance were instrumental in the completion of this thesis.

First and foremost, I express my sincere appreciation to Yohan Davit, my main supervisor, and Laurent Malaquin, my co-supervisor, for their unwavering support, invaluable insights, and encouragement throughout this academic journey.

I am indebted to the guidance and suggestions provided by the esteemed researchers Pascal Swider, Christophe Coudret, and Diana Ciuculescu-Pradines, whose expertise significantly enriched the content and direction of this work.

I owe a debt of gratitude to the dedicated lab technicians—Julien Lefort, Emmanuel Libert, Yara Abidine (IMFT), and Julie Foncy (LAAS)—for their tireless technical assistance and ideas, which was fundamental to the execution of this research.

I am immensely grateful to my labmates, Gabriel, Massi, Perrine, Deppy and especially Clara, whose companionship and shared experiences, were an invaluable source of support during the long hours and challenges faced in the lab.

To my family—Chrysoula, Evangelos, Melpomeni, Cédric, and Néféli—your unwavering encouragement and support have been the pillar of my strength throughout my academic pursuits.

Special thanks to my close friend Yorgos for providing invaluable stress relief and nice moments during those years and to his brother Rigas, who provided valuable assistance on graphic design, which contributed to the creation of some stunning 3D images in this work.

I am deeply appreciative of Katerina for sharing meaningful moments during challenging periods. However, I reserve the utmost gratitude for Nathanaëlle. Her enduring patience and unwavering assistance were indispensable, without which this thesis would not have come to fruition. Her presence and contribution, in her own way, have been an integral part of this journey, and for that, I am immensely grateful.

To each and every individual mentioned and to those not named but who played a part in this academic endeavor, I extend my heartfelt gratitude. Your support, encouragement, and contributions have been invaluable and deeply appreciated.

Thank you all.

Contents

List of Figures

Part I

Biofilms in porous media

1 Biofilm basics

1.1 Biofilms are everywhere

Microorganisms are tiny living organisms that can only be seen through a microscope. They include bacteria, viruses, fungi, protozoa, and algae, and play important roles in various ecosystems. For most of the history of microbiology, microorganisms have been thought of as free-floating, suspended cells, characterized as planktonic and described in regard to their growth characteristics in nutritionally rich culture media. The phenomenon where microorganisms attach and grow on exposed surfaces was first described by van Leeuwenhoek in the 17th century [178] but the extensive study of surface associated microorganisms started at the end of the twentieth century when Characklis and Costerton [88] demonstrated the importance of this mode of life, namely biofilms. It is generally agreed upon that a biofilm is an aggregate of microorganisms, for example bacteria, algae, fungi or protozoa, attached onto a surface and embedded in a self-produced matrix of extracellular polymeric substances (EPS) [130]. EPS is a fundamental part of biofilms and its role is, among others, to provide biofilms with structural support, protect the colony from predators and harmful chemicals, facilitate communication/chemical signaling between cells and entrap nutrients (figure 1.1 top) [129].

Biofilms are, by far, the predominant form of life compared to their free-floating counterparts [128] and can be found in various natural, industrial and medical environments. Approximately 80 % of the $1.2{\cdot}10^{30}$ bacteria and archaea cells on Earth can be found in biofilms in five key habitats: the deep oceanic subsurface ($4{\cdot}10^{29}$ cells), upper oceanic sediment ($5{\cdot}10^{28}$ cells), deep continental subsurface ($3{\cdot}10^{29}$ cells), soil ($3{\cdot}10^{29}$ cells), and oceans ($1{\cdot}10^{29}$ cells) (figure 1.1 bottom) [128] . In comparison, other habitats such as groundwater, the atmosphere, the ocean surface microlayer, humans, animals, and the phyllosphere house fewer cells by orders of magnitude. Biofilms are prevalent on all surfaces except the oceans and make up 80% of bacterial and archaeal cells. Overall it is estimated that 40-80% of all cells on Earth are found in biofilms [128].

Our work focuses more specifically on biofilms produced by bacteria. Bacterial biofilms can be found in almost every environment, from freshwater and marine ecosystems [128], to industrial equipment [446] and medical devices [140], to the human body. These communities of microorganisms are able to colonize a wide range of surfaces and can persist in environments that would otherwise be inhospitable to individual bacteria. Bacterial biofilms play important roles in a variety of ecosystems, from breaking down organic matter in soil and water [350], to aiding in nutrient cycling [419]. However, biofilms can also cause problems such as infections, fouling of industrial equipment [244], and bio-corrosion [26]. Despite the potential challenges posed by biofilms, they are a ubiquitous presence in the natural world, and understanding the formation and behavior of these structures is crucial for a variety of fields, including medicine, environmental science, and biotechnology.

Bacterial biofilms are an important area of study for several reasons:

- Medical significance: Bacterial biofilms can develop on implants [443], catheters [411] and in blood vessels [370]. They can cause persistent infections [352] and are associated with increased antibiotic resistance[179], making it difficult to treat biofilm-associated diseases [392].
- Environmental impact: Bacterial biofilms are a key part of most biogeochemical processes. They can play a role in biodegradation [1] and bioremediation [395].
- Engineering: Bacterial biofilms can develop in a variety of industrial systems, such as cooling towers [108], disrupting normal functioning conditions [201]. They can also cause problems such as biofouling of industrial equipment [277] and biocorrosion [26].
- Biotechnology applications: Bacterial biofilms can be used in bioreactors to produce chemicals [105], degrade pollutants [285], and treat wastewater [295].
- Basic science: Understanding the formation and behavior of bacterial biofilms can provide insights into microbial ecology [121], evolution, and cell-cell communication [162].

Therefore, studying bacterial biofilms has important implications for a variety of fields, including medicine, engineering, environmental sciences, biotechnology, and basic biology, and can lead to the development of new treatments and biotechnologies.

P. aeruginosa Our work is focused on *Pseudomonas aeruginosa* biofilms. *Pseudomonas aeruginosa* is a versatile opportunistic pathogenic bacterium that is able to adapt to different environments and is able to form biofilms on various surfaces, including medical devices [140], wound sites, plant tissues and food industry equipment [89]. In addition, *P. aeruginosa* is associated with a wide range of infections in humans and animals, including burn and wound infections, urinary tract infections, pneumonia, and ear infections [115]. This pathogenic potential combined with its ability to form persistent and antibiotic-resistant biofilms makes it a significant public health concern, and a focus of biofilm research. These infections are often persistent and difficult to treat, even with strong antimicrobial therapy and a strong immune response. This resilience is mainly attributed to the fact that *P. aeruginosa* is a notorious biofilm producer. One of the most well-known examples of this type of persistent infections caused by *P. aeruginosa* is in patients with cystic fibrosis [300].

P. aeruginosa is considered a model organism for the study of biofilms in laboratory experiments [242] and it has been extensively used in research related to environmental sciences [93], in the medical field [347] and even in material science [293]. It is often used in experiments to study biofilms because of its ability to form well-defined and reproducible biofilms, making it a suitable model organism for such studies [54]. Additionally, *P. aeruginosa* is a well-studied bacterium with a wealth of genetic and metabolic information available [459], making it easier for researchers to manipulate and study in a controlled microfluidic environment [220]. Furthermore, *P. aeruginosa* is capable of forming biofilms that are both persistent and antibiotic-resistant, making it a good model to study the mechanisms underlying these properties [276]. Understanding these mechanisms is important for the development of new treatments for biofilm-associated infections. Overall all the above mentioned properties make it a popular choice for microfluidic experiments to study biofilms.

1.2 Bacterial biofilm life cycle

Bacteria use specific mechanisms for initial attachment on surfaces, development of a community and detachment [110] in a cyclic process that occurs in a stage-specific and progressive manner. Biofilm formation process can be typically divided into five stages through its life cycle [412]: (i) the initial attachment of cells to a surface or a substrate, (ii) the production of EPS and irreversible attachment, (iii) the development of the biofilm architecture (maturation I), (iv) maturation of the structure and composition of the biofilm (maturation II) and (v) dispersal of individual cells from the biofilm that revert to the planktonic phenotype to colonize another surface (figure 1.2 top). During the first stage of attachment, bacteria attach to the surface through their cell poles or flagella. This is followed by a transition to irreversible attachment, which is marked by a decrease in flagellar movement and gene expression, and the production of substances that make up the biofilm matrix. At this stage, the attached cells also become resistant to drugs. The later stages of biofilm maturation involve the formation of clusters of cells that are several cells thick, and are surrounded by the biofilm matrix. Eventually, these clusters mature into microcolonies. The process of biofilm formation ends with the dispersal of the cells, which is marked by the breakdown of the matrix and a decrease in drug resistance.

In a recent publication, Sauer et al. argued that the typical 5-stage life cycle model fails to capture satisfactorily what is commonly observed in various clinical, industrial and environmental settings [368] (figure 1.2 bottom). The main point of the article is that biofilms are not strictly surface associated communities and that they can also develop as non-surface-attached aggregates. They presented an adapted biofilm growth model, separating the life of a biofilm in three main events (1.aggregation/attachment, 2. Growth/accumulation, 3. Disaggregation and detachment) and in addition they tried to list the mechanisms of microbial aggregate formation independently of a solid substrate/surface. This approach is going beyond the scope of this thesis and therefore in this section, the life cycle of biofilms will be detailed in the typical 5 stage manner.

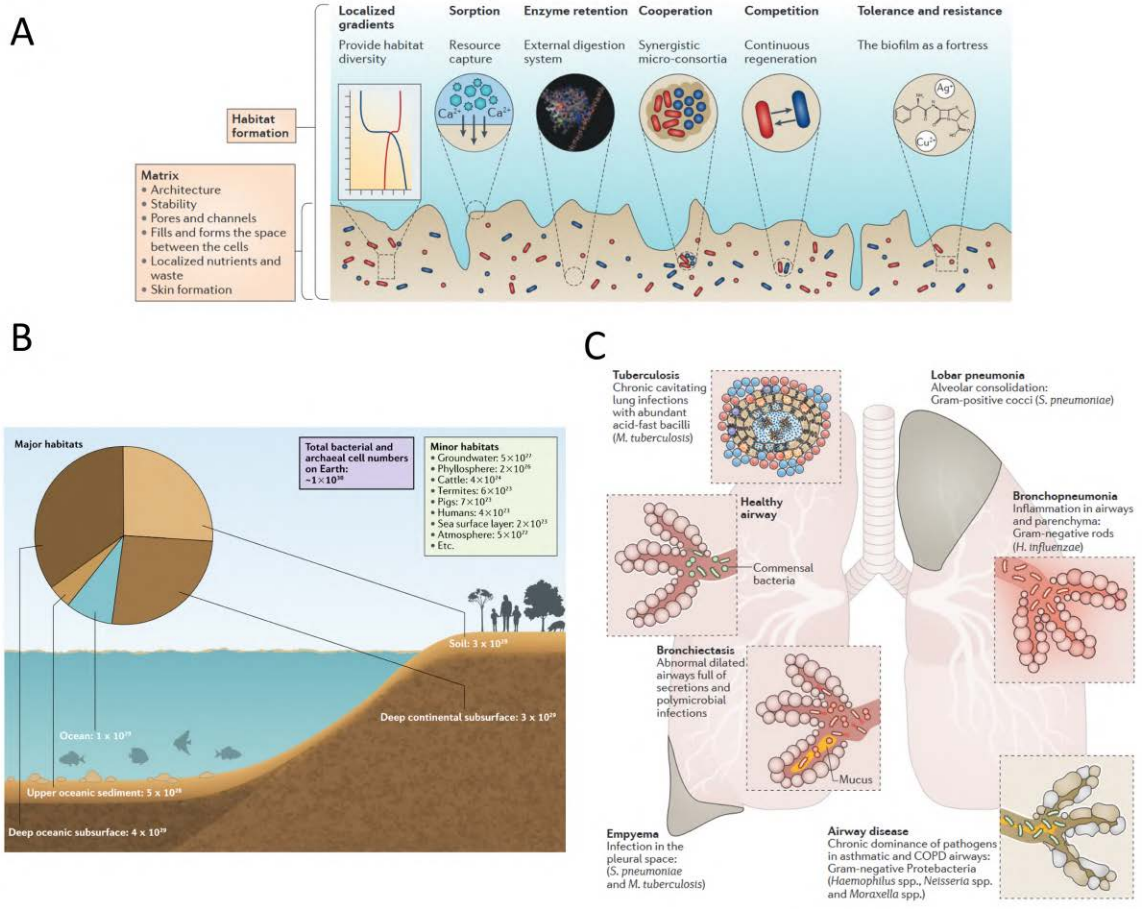

Figure 1.1: (A) Properties of biofilm formation. Biofilms exhibit several emergent properties, properties that are not predictable from the study of free-living bacterial cells . Some of these emergent properties include creating diverse habitats through localized gradients, absorbing resources through sorption, retaining enzymes for digestion, facilitating social interactions, and exhibiting the ability to tolerate or resist exposure to antibiotics. Image taken from [127] (B) Biofilms are a predominant form of bacterial life: The total number of bacterial and archaeal cells on Earth has been estimated to be approximately $1.2{\cdot}10^{30}$. Among the known habitats, the most significant ones for bacterial and archaeal populations are the ocean, upper oceanic sediment, deep oceanic subsurface, soil, and deep continental subsurface. These habitats contain the vast majority of microbial cells on the planet. Image taken from [128]. (C) Pulmonary infections associated with bacterial pathogens that develop in biological porous media [301].

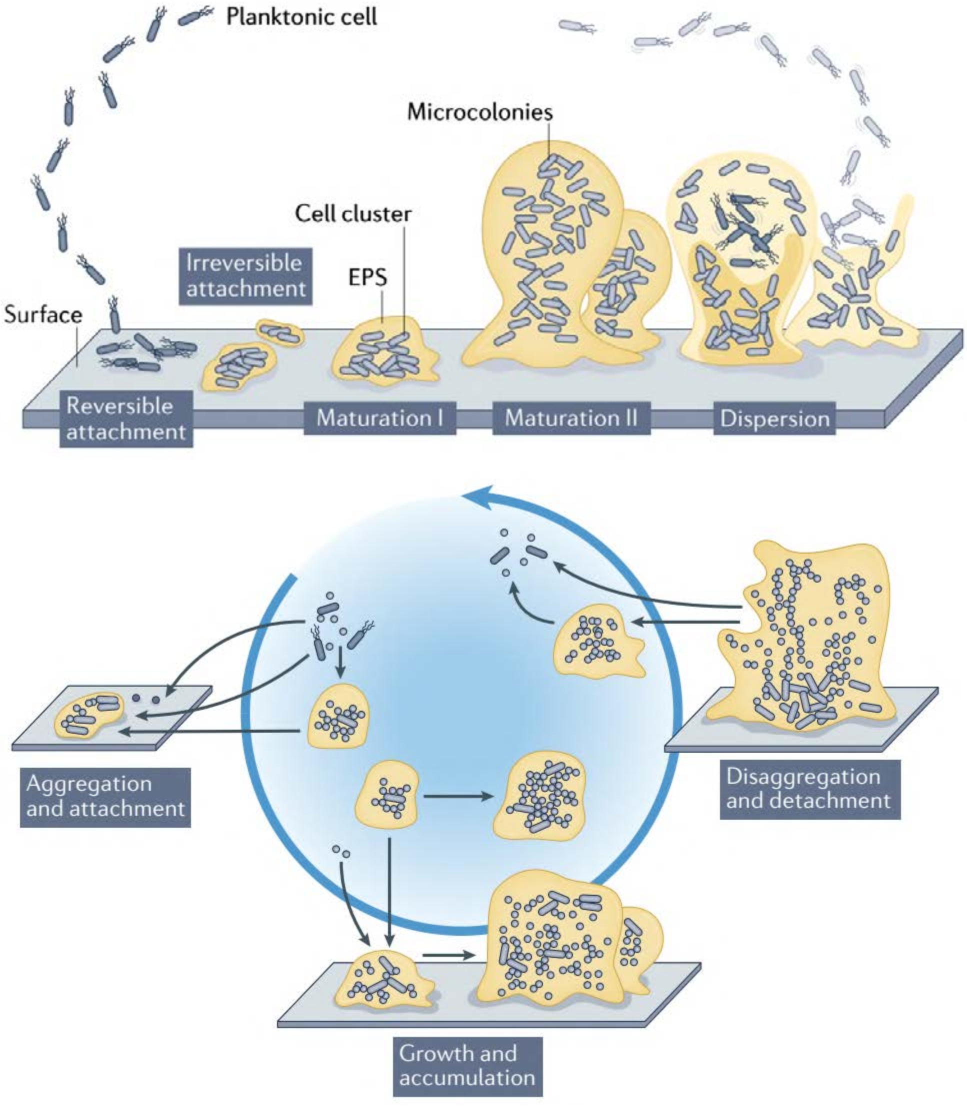

Figure 1.2: The typical five-step model of biofilm development and an adapted model to include non-surface-associated biofilm growth. Image taken from Sauer et al. [368].

1.2.1 Stage I & II: Reversible and irreversible surface attachment

In the first step, the formation of these multicellular communities starts with the adhesion of a few planktonic cells to a surface. The transition from a planktonic lifestyle to a sessile, attached state is a multi-factorial process that is determined by biological, chemical and physical properties of the environment, the surface and the bacterial cell. Examples factors include the presence of surface proteins, flagella, pili and adhesins [52, 66, 116, 229] on the bacteria, physical factors such as surface hydrophobicity [131, 397, 426], temperature [125] and flow velocity [67], and chemical factors like chemotaxis, surface charges McNamee, Pyo, and Higashitani [281] and Terada et al. [424], ionic strength and pH [384].

Biofilm formation process is initiated with a small number of planktonic cells attaching onto a surface. This process occurs in two stages: reversible and irreversible attachment. During the reversible stage, the attachment is weak and unstable, mainly mediated by electrostatic and hydrophobic interactions. The cells can easily detach from the surface during this stage and return to the liquid phase. Surface contact by rod-shaped flagellated cells is primarily mediated via the flagellum during this stage. Other mediators of attachment include pili such as type I and type IV pili, curli fibers and antigen [230]. Non-motile Gram-positive bacteria also attach to surfaces using pili and adhesins, for example SagA and Acm of *Enterococcus faecium*, and Ace, Esp, and enterococcal biofilm pili (Ebp) of *Enterococcus faecalis* [230]. Once the cells are irreversibly attached, they stop moving and start producing matrix, likely to secure themselves to the surface or to each other which is commonly observed through microscopic observations. This highlights the fact that regardless of the species, biofilm formation follows distinct stages and patterns.

Bacterial cells are known to be able to attach on a wide variety of solid surfaces such as sand [193], metal oxides [256], plastics [74] and biological tissues [273]. According to a proteomic study using wild-type PAO1, the responses and biofilm formation of *P. aeruginosa* are specific to the material they are encountering. This can be seen through the presence and changes in certain bacterial proteins in response to different surfaces [154]. These surfaces exhibit several characteristics that play an important role in the attachment process. For example, Characklis et al. [68] noted that bacterial colonization appears to increase as the surface roughness increases because shear forces are diminished and surface area is higher on rougher surfaces. In addition, the physicochemical properties of a surface strongly influence the rate and the extent of the attachment. There are several studies suggesting that microorganisms have higher affinity for hydrophobic, non-polar surfaces like plastics than for hydrophilic materials such as glass or metals [131, 397, 426]. In addition, studies have been made using various topographic patterns to study bacterial surface attachment with varying results [182, 262, 316]. Regarding surface charge, it is generally observed that there are stronger adhesion forces with positively charged surfaces [281, 424] but no statistically significant deduction can be made. In another approach, it is observed that initial bacterial adhesion is favored on surfaces with high free energy [481]. In a recent study, it was found that characteristics of the biofilm form (e.g. wrinkles) grown in flow cells, can be affected by the degree of adhesion of the film to the substrate [137]. More specifically, by increasing the affinity of the surface to the biofilm, it develops a wrinkly surface that, in turn, affects the hydrodynamical environment by providing micro-scale flow paths.

P. aeruginosa The transport of *P. aeruginosa* bacteria to a surface before attachment is believed to involve a combination of diffusive, convective, and active flagellum-driven motility [438]. The initial attachment starts with the reversible adhesion of the bacteria to the surface through the use of appendages such as flagella and type IV pili [225, 298] — although attachment in laboratory conditions using flow chambers can still occur without these [225]. Once bacteria have attached to a surface, they can either detach, stay attached, or move along the surface through the use of type IV pili or flagella [224, 386, 394]. The different bacterial classes of surface motility include swarming motility, twitching motility, gliding motility and sliding motility [166]. Studies have also identified a gene called sadB, which controls the rate at which *P. aeruginosa* attaches and detaches from surfaces [58]. The synthesis of the attachment regulator SadB is regulated by the amount of a second messenger molecule within the cell, namely, cyclic diguanosine-50-monophosphate (c-di-GMP) [283]. In addition, several other components such extracellular DNA [458] and Psl polysaccharide [267] production have been found to play a role in the initial attachment process to surfaces in laboratory experiments using microtiter plates and flow chambers.

The transition between mobile and stationary surface behavior in *P. aeruginosa* is regulated by proteins that control the levels of the second messenger molecule c-di-GMP through diguanylate cyclase or phosphodiesterase activities [176, 237, 283]. When the levels of c-di-GMP are low within the cells, it promotes motility, while high levels of c-di-GMP within the cells lead to the formation of cell-to-cell interconnecting matrix components and the formation of microcolonies. Limited movement of the flagella has also been linked to the process of twitching motility and the synthesis of additional exopolysaccharides necessary for attaching to surfaces [176]. At a molecular level, these changes include the activation of genes related to the biosynthesis of lipopolysaccharide core and exopolysaccharide alginate [98, 99], genes involved in the biosynthesis of the Psl matrix polymer [85], as well as genes for antibiotic resistance, like those for beta-lactamase [19], phenazine [465], SagS and BrlR [155].

1.2.2 Stages III & IV: Biofilm development and maturation

Once bacteria attach, they will begin to form a more complex multicellular structure, sometimes characterized by mushroom or pillar-like shapes, called microcolonies, with channels filled with fluid [466]. This structuring is dependent on small messenger molecules (e.g. acylated homoserine lactones, AHLs) for bacterial communication, as well as regulatory proteins [236] and lipids [252]. However, even in the absence of these signaling molecules, some bacterial species, including *P. aeruginosa*, are able to form these structures, suggesting that the environment also plays a role [331]. As the biofilm develops, the bacteria at the base becomes increasingly isolated from the liquid interface and therefore from resources, leading to stratification within the biofilm and the creation of sub-populations with different exposure to resources, oxygen and waste products [379, 408, 462]. This is supported by the observation that resident biofilm cells express genes associated with stress, nutrient deprivation, and slow growth [170, 408].

The extracellular polymeric substances (EPS) are biopolymers of microbial origin in which biofilm microorganisms are embedded [126]. Apart from bacteria, fungi and archaea and other microorganisms are known to produce biopolymers. The exact chemical composition of the EPS can vary depending on the species of bacteria and the environment in which the biofilm forms but it generally consists of a wide variety of polysaccharides, proteins, lipids and in some cases, some amounts of extracellular DNA (eDNA) [368]. In environmental biofilms, polysaccharides can only be a minor component [134]. It is well established that EPS biopolymers are highly hydrated and form a matrix, which keeps the biofilm cells together and retains water [126]. This matrix interacts with the environment, for example it is the main factor by which biofilms attach to surfaces. In addition, the ability of a biofilm to absorb various substances from its environment also provides nutrients for the organisms within the biofilm [126]. The EPS influence predator-prey interactions, as demonstrated in experiments [278] where *Vibrio cholerae* strain which produced EPS appeared to be able to survive protozoan grazing compared to their planktonic counterparts. Besides offering structural stability, protection against grazing and nutrient availability, EPS also enhance biofilm tolerance to antimicrobials and immune cells [113, 228]. Bacteria within a biofilm can escape host immune responses and resist antimicrobial treatments up to 1000 times more than their planktonic counterparts [255].

P. aeruginosa The biofilm matrix produced by *P. aeruginosa* is composed largely of polysaccharides, extracellular DNA, proteins, and lipids [140, 418]. This matrix, which makes up over 90% of the biofilm's biomass, acts as a support for attaching to surfaces and provides protection for the encased bacteria from harsh conditions such as antibiotics and immune responses [40]. It also supplies essential nutrients and enzymes to the biofilm community and facilitates communication between cells [192, 359]. More specifically, three exopolysaccharides, Psl, Pel, and alginate, play significant roles in the attachment, formation, and stability of the biofilm's structure [140].

Psl is a neutral pentasaccharide composed of d-glucose, d-mannose, and l-rhamnose [55, 267]. It is necessary for the adhesion of sessile cells and cell-to-cell interactions during biofilm formation in both non-mucoid and mucoid strains [203, 268]. Psl has several notable characteristics: 1) it is beneficial for biofilm communities, but not for unattached populations. 2) It has been observed that non-Psl producing cells have better growth in mixed biofilms with Psl producing cells [40, 189]. 3) Psl positive populations dominate Psl negative populations in biofilm growth and 4) strains which do not produce Psl are unable to successfully exploit cells which produce Psl [189]. In a mature biofilm, Psl is found in the peripheries of the mushroom-like structure where it helps maintain structural stability [267]. Increased Psl expression is linked to the induction of cell aggregates in liquid culture, a phenotype observed in the sputum (mucus coughed up from the lower airways) of cystic fibrosis patients [406]. Psl also acts as a signaling molecule to increase the production of c-di-GMP (bis-(3´-5´)-cyclic dimeric guanosine monophosphate), which leads to thicker and more robust biofilms [188]. Furthermore, Psl protects biofilm bacteria from antibiotics [40] and neutrophil phagocytosis [284], contributing to persistent infections.

Pel is a cationic polysaccharide made up of partially deacetylated N-acetyl-d-glucosamine and N-acetyl-d-galactosamine. It is an essential component of biofilm matrix in nonmucoid strains and is involved in the initial attachment to surfaces and the maintenance of biofilm integrity [84, 198]. The synthesis of Pel and Psl is strain-specific and can be altered in response to environmental conditions [85]. In addition, Pel is known to enhance the tolerance of biofilm-embedded bacteria to aminoglycoside antibiotics [475]. Biofilms containing Pel are also more resistant to the antibiotic colistin and less susceptible be killed by neutrophils derived from human HL-60 cell lines [20].

Alginate is a negatively charged acetylated polymer made up of mannuronic acid and guluronic acid residues [124]. It is primarily produced in the biofilms of mucoid Pseudomonas strains, which are often found in cystic fibrosis patients and are associated with the transition from acute to chronic infections [82]. Alginate has a number of important functions in biofilms, including promoting biofilm maturation, protecting against phagocytosis and opsonization, and decreasing the diffusion of antibiotics through the biofilm [168, 169, 418, 433]. Finally, the ratio of mannuronic acid to guluronic acid in alginate influences the viscoelastic properties of biofilms which consequently has an effect on the cough clearance in the lungs of cystic fibrosis patients infected with P. aeruginosa [142, 463].

1.2.3 Stage V: Dispersal of biofilm

Biofilms are dynamic structures where cells within a biofilm can detach and return to a planktonic mode of growth through a process known as dispersion [356]. Dispersion is an active event in which cells that were previously embedded in the matrix of the biofilm actively escape and detach from the biofilm. This process can lead to the erosion of the biofilm and the formation of central voids in the biofilm [324]. This is not just a passive process but an active event that enables the biofilm to disseminate and colonize new locations so that a new life cycle of a bacterial colony commences [338]. Dispersion is often referred to as seeding dispersal, as it is believed to lead to the translocation of bacteria to new sites for colonization. [332]. This process allows the biofilm to spread and colonize new surfaces and environments. This active and regulated process should not be confused with passive processes of desorption and detachment. Dispersion of biofilm cells to the bulk of the liquid is a potential response to these stimuli through mechanisms like quorum sensing [400], mechanosensing [164] and chemotaxis [290]. It has been demonstrated that this process can be facilitated by the enzyme EndA, which degrades eDNA to allow for the dispersion of existing biofilms [78].

1.3 Effect of flow and transport phenomena on bacteria and biofilm

While microbiology studies have traditionally focused on the influence of the chemical environment on bacterial behavior in static systems such as well-mixed batch cultures and agar plates [90, 384], more recent studies stress out the importance of the effect of the hydrodynamic environment of the bacteria. Liquid flow and biofilm interactions is one of the most important environmental factors driving biofilm dynamics and structure [67, 234, 341]. Liquid flow is generally considered the major agent of physical forcing on the biofilm [39]. Indeed, flow has a direct impact through mechanical stress but it also has an indirect effect on biofilm growth through mass transport phenomena such as diffusion of molecular species at the interface and quorum sensing.

During the initial steps of biofilm growth, the transition of one microbe from the planktonic to the biofilm lifestyle, and vice-versa, depends on a range of environmental conditions among which the local hydrodynamics are of high importance [358]. Hydrodynamic parameters such as fluid velocity, flow direction, and turbulence can influence the initial attachment of bacteria on surfaces by affecting the transport of bacteria towards the surface, by altering the orientation of bacteria as they approach the surface or by changing the likelihood of bacteria encountering and sticking to favorable sites on the surface (figure 1.3) [321]. In addition, during the maturation stages of biofilm growth, high levels of shear stress can promote the detachment of biofilm aggregates, reducing biofilm thickness [118]. In addition fluid flow can indirectly affect bacterial growth through the transport of chemical species. Examples include:

- Nutrient transport where fluid flow can bring fresh nutrients to the surface, promoting growth and expansion.
- Quorum sensing, a process by which bacteria communicate and coordinate their behavior based on population density. Fluid flow can affect the distribution of bacteria within a biofilm, altering the concentration of signaling molecules and impacting the coordination of bacterial behavior.
- Oxygen availability. For example in environments with fluctuating flow, oxygen availability is also fluctuating which in turn impacts bacterial growth.
- Removal of waste products where fluid flow can transport waste products away from bacteria and promote growth by maintaining a clean and nutritious environment.

1.3.1 Mechanical effects of flow

The mechanical aspects of fluid flow play a critical role in the initial attachment and growth of biofilms. Shear stress, fluid velocity, turbulence, and flow direction can all impact the likelihood of bacterial attachment and the formation of a stable biofilm. Most of the time, these studies focus on one particular aspect of the hydrodynamic environment, namely shear stress, or the force applied by fluid flow on the surface. The effect of shear stress on bacterial attachment is complex and depends on the specific type of bacteria and surface [48, 248] but in general shear stress affects initial bacterial attachment by physically removing unattached bacteria from the surface or altering the orientation and shape of bacteria [320, 358], affecting their ability to adhere to the surface. If the hydrodynamic force is too strong or the hydraulic retention time is shorter than the doubling-time of the cells, the microbes will detach from the surface. Those that manage to stick to the surface and stay, are the ones that grow and form a biofilms [138]. In another study, the influence of the wall shear stress on the early-stage adhesion of *P. aeruginosa* PA14 on glass and polydimethylsiloxane surfaces was studied [248]. Results show that the characteristic residence time of bacteria increases linearly with shear stress, and that bacterial surface features (type I pili, type IV pili, flagellum, or extracellular matrix production) do not play a role in the trend in shear-enhanced adhesion time, highlighting the importance of the hydrodynamic environment to the initial cell attachment. While the results of this study might seem counter intuitive and contradictory to the overall view that shear stress promotes bacterial detachment in the initial stage, it should be noted that the study focuses on the retention time of individual bacteria rather than the their number implying that even though the majority of bacteria are dispersed due to the flow, those that manage to attach, tend to adhere for longer times in higher shear stress conditions.

The velocity [399] and turbulence [314] of fluid flow can affect the transport of bacteria towards a surface and alter their orientation, influencing the likelihood of initial attachment but also affect

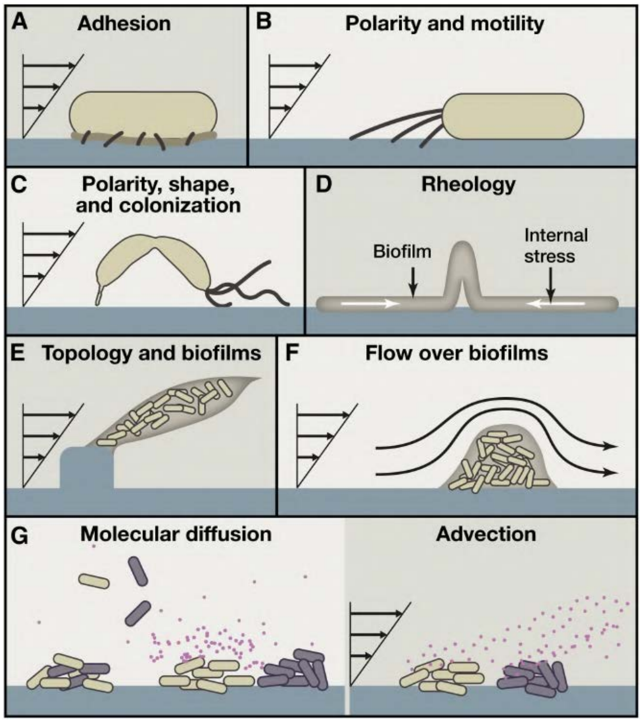

Figure 1.3: Bacteria use various mechanisms to attach to surfaces and move in the presence of flow. (A) They use appendages called fimbriae and other adhesive structures or substances to remain strongly attached, and (B) motorized pili located at their poles to move against the flow. (C) Additionally, they exploit their shapes to orient in flow, which enhances their ability to colonize surfaces. At the scale of multicellular communities, (D) bacteria can alter the viscosity of their extracellular polymeric substances to optimize growth. (E and F) Flow also affects the structure of bacterial biofilms by forming filamentous structures called streamers, which can obstruct flow but also capture cells and metabolites suspended in the surrounding fluid. (G) Nutrient and solute transport by diffusion and advection drives the growth and interactions of surface-associated bacteria. Image taken from[321].

the architectural aspects of a mature biofilm. In one study it was found that *P. aeruginosa* biofilm architecture changes depending on the flow regime. Under laminar flow the total number of cells was higher than in biofilms formed under turbulent flow, but the latter had a higher number of cells per unit volume [315]. Another study found that the different flow regimes resulted in structurally different *P. aeruginosa* biofilms [391]. Biofilm cells grown under turbulent flow were smaller, had lower metabolic activity, and a lower composition of proteins and polysaccharides compared to those grown under laminar flow. However, turbulent flow generated biofilms were more active, had more mass and protein content, and higher cellular density. Laminar flow-generated biofilms had higher polysaccharide content. The direction of fluid flow can also impact the distribution of bacteria within a biofilm, affecting their exposure to environmental stresses and promoting or hindering growth. It has even been shown that bacteria can disperse against the flow in microfluidic channels, by using mechanisms such as twitching, which provides them with a selective growth advantage [383, 396]. In another study it was suggested that biofilms arrange their internal structure based on the flow velocity at which they are grown, which affects their internal mass transfer rate and microbial activity. The study suggests that biofilms attempt to increase their mechanical strength to resist the shear stress of the water flowing past them, but at the expense of the nutrient transfer rate to deeper layers. Biofilms grown at higher flow velocities are denser and can resist higher shear stress but have a lower effective diffusivity [35].

1.3.2 Effects of flow on the chemical landscape

The movement of fluid in a habitat can also impact microorganisms by affecting the availability of essential nutrients and signaling cues. The acquisition of nutrients, respiration, perception of predators and prey, and communication rely on the transport of dissolved substances [456]. When there is no fluid flow, these molecules move only through molecular diffusion. But when fluid is present, they are mainly transported through advection, which can be much faster than diffusion. The scale of the environment, the speed at which molecules diffuse, and the speed of fluid flow determine which process prevails, greatly impacting the lives of bacteria in small habitats. In addition, flow patterns can greatly affect the spatial distribution of chemical species which in turn affect biofilm growth (examples in figure 1.4).

Planktonic bacteria can detect changes in chemicals and adjust their movement accordingly through a process called chemotaxis. However, fluid flow can interfere with this process, causing the bacteria to swim in the wrong direction or preventing them from turning towards the source of beneficial chemicals. For example, in a study it was shown that shear trapping prevents bacteria from turning effectively in the direction of the gradient [358]. In another work, it was demonstrated how flow can trick bacteria to move in incorrect direction [263]. This can occur when the rate at which the bacteria sense chemicals is similar to the speed at which they are reoriented by the flow. This can result in negative chemotaxis, where the bacteria move away from the source of beneficial chemicals. In the case of bacterial biofilms, mass transport phenomena and more particularly nutrient and oxygen transport, play a critical role in biofilm growth and shape. Adequate availability of nutrients such as carbon, nitrogen, and phosphorus is essential for biofilm growth and metabolism which in turn has an effect on its structure [415]. In a study aimed to decipher the influence of hydrodynamics on bacterial biofilms in moving fluids, it was found no direct impact of mechanical forces on biofilm growth rate, but rather that hydrodynamic molecular transport, specifically oxygen availability, was crucial for biofilm growth [427].

Bacterial populations coordinate their collective actions through quorum sensing, a communication process that utilizes diffusible chemical signals known as autoinducers. When the concentration of these autoinducers reaches a critical point, it triggers a variety of behaviors in bacteria, including light production in marine *Vibrio cholerae* in squid light organs [22] and production of extracellular matrix and expression of virulence factors in human pathogens like *S. aureus, V. cholerae*, and *P. aeruginosa* [296]. Fluid flow can impact quorum sensing by altering the transport and concentration of autoinducer molecules. For instance, *S. aureus* and *V. cholerae* cells grown in biofilms under flow display non-uniform quorum sensing across the biofilm [219, 417]. Only cells at the base of the

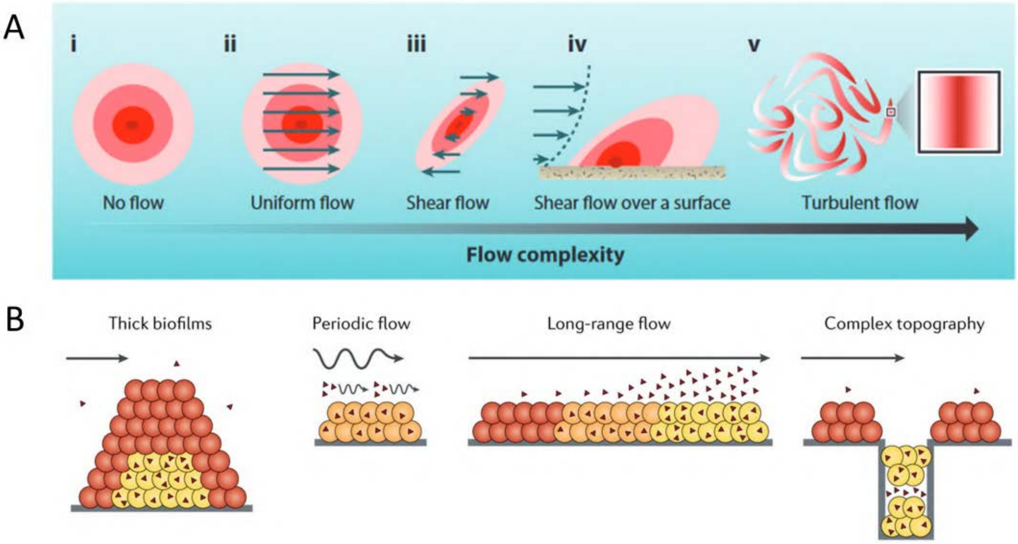

Figure 1.4: Effect of flow on the propagation of a chemical signal in fluid environments of increasing complexity is shown in A. Dark red represents high chemical concentrations and light red represents low concentrations. In no-flow conditions, molecules diffuse symmetrically from a point source, with the highest concentration at the source and decreasing with distance. A uniform flow does not change the shape of the chemical cloud, as all molecules are transported with the same flow velocity. In a shear flow, the chemical cloud is stretched into a diagonal plume by different flow velocities. In a shear flow over a surface, the plume is stretched away from the surface. In turbulent flow, a plume is stretched and deformed into filaments with higher chemical concentrations near their centers that diffuse away to the edges. Image taken from [456]. (B) Bacteria populations can have varying levels of quorum sensing activation depending on the flow and structure of their environment. Some cells may not have quorum sensing activated at all (shown in red), while others may have partial activation (orange) or full activation (yellow). The flow of the environment, whether it is continuous or periodic, can affect the ability of the bacteria to sense each other by washing away the chemicals they use to communicate, unless they are protected in a thick layer of biofilm or in specific areas called crypt-like niches. Image adapted from [219].

biofilm exhibit quorum sensing while stopping the flow activates quorum sensing in the upper layers too according to what has been observed in microfluidic studies [219]. In addition, they showed that flow can wash away autoinducer molecules in biofilms grown on flat surfaces but bacteria in narrow, sheltered environments such as cracks and dental cavities can still perform quorum sensing despite strong ambient flow [219]. In *P. aeruginosa* biofilms, a thick extracellular matrix reduces washout of autoinducers and enables quorum sensing in the presence of moderate flows [123, 222]. Fluid flow is generally unable to reach into the interior of the biofilm matrix, where molecules are transported primarily by diffusion [407] (figure 1.4). This concept also applies to the delivery of nutrients and oxygen, where cells within the biofilm receive only those that can diffuse through the matrix, while cells on the outer layers receive a much higher supply rate due to flow [414, 427].

2 Biofilms in porous media

There are several reasons why studying biofilms in porous media is important. Firstly, porous media are ubiquitous in natural systems, such as soils [56], sediments [467], and aquifers [454], and are also commonly used in engineering applications, including water treatment [247, 275] and oil recovery [210]. Biofilms are known to form readily in these environments and can have a significant impact on biogeochemical cycling [305], water quality [286], and the performance of engineered systems [12]. Therefore, understanding the behavior and structure of biofilms in porous media is essential for managing and controlling their effects on these systems.

Secondly, porous media provide an ideal environment for biofilm growth, as they offer a large surface area for attachment and colonization by microorganisms [344] and provide protection from predation [278] and environmental stress [87]. The complex and heterogeneous structure of porous media also creates a range of micro-habitats, which can result in diverse and spatially structured microbial communities. By studying biofilms in porous media, we can gain insights into the factors that control their growth and distribution, including physical and chemical properties of the matrix and microbial interactions.

Thirdly, biofilms in porous media can have both beneficial and detrimental effects [366]. For example, biofilms in soils and sediments can play a key role in nutrient cycling and the degradation of organic matter [95, 305], while biofilms in water treatment systems can clog filters and reduce system performance [114]. By understanding the mechanisms underlying these effects, we can develop strategies to harness the beneficial effects of biofilms and mitigate their negative impacts.

Overall, studying biofilms in porous media is important for advancing our understanding of microbial ecology and biogeochemical cycling in natural systems, developing more effective and efficient engineered systems, and addressing environmental and health challenges associated with biofilm growth. In the following section, the influence of biofilm growth on porous media hydrodynamics will be discussed with a focus on the effect on transport phenomena such as nutrient transport and quorum sensing. Throughout this section, it should be noted that biofilm growth influences the hydrodynamics of porous media but also the hydrodynamics conditions have an influence on biofilm growth characteristics. It is generally observed that biofilm structure responds to the change of these conditions and adapts in order to optimize mass transport (e.g. absorption of nutrients) and/or its stability (e.g. minimization of interface shear stress).

2.1 Biofilms in natural and industrial porous media

2.1.1 Biofilms in soils, aquifers and streams

Biofilms can form in a variety of environments, including soil, aquifers and riverbeds, which are all characterized by their porous nature. In all of these systems, biofilms play an important role on the ecosystem by driving biochemical processes such as carbon and nitrogen cycles [23].Streams and rivers form intricate networks and shape the Earth's surface, offering vast amounts of sediment space for microbial growth. Biofilms play a dominant role in microbial life in streams and rivers, facilitate vital ecosystem processes, and have a significant impact on global biogeochemical exchanges [128], for example they participate in various biochemical cycles of their ecosystem (e.g. Carbon [485], nitrogen [77] etc.).

On the other hand, water flow and the supply of nutrients and organic matter to biofilms significantly impact microbial life. The global surface area of streams and rivers is estimated at 662.041 km^2[112] and with rough calculations this is translated into $6{\cdot}10^8$ km^2 of surface area available for microbial colonization on stream beds. On these porous regions, a somewhat $5{\cdot}10^{11}$ to $5{\cdot}10^{13}$ cells are expected to be found. These numbers highlight the importance of microbial cells on such natural environments. The vast microbial surfaces found in streams are considered as a significant aspect of the overall "microbial skin" that covers the entire catchment area, including the microbiomes in the phyllosphere [449] and soils [21]. Proteobacteria and Bacteroidetes often dominate the communities of stream biofilms [34].

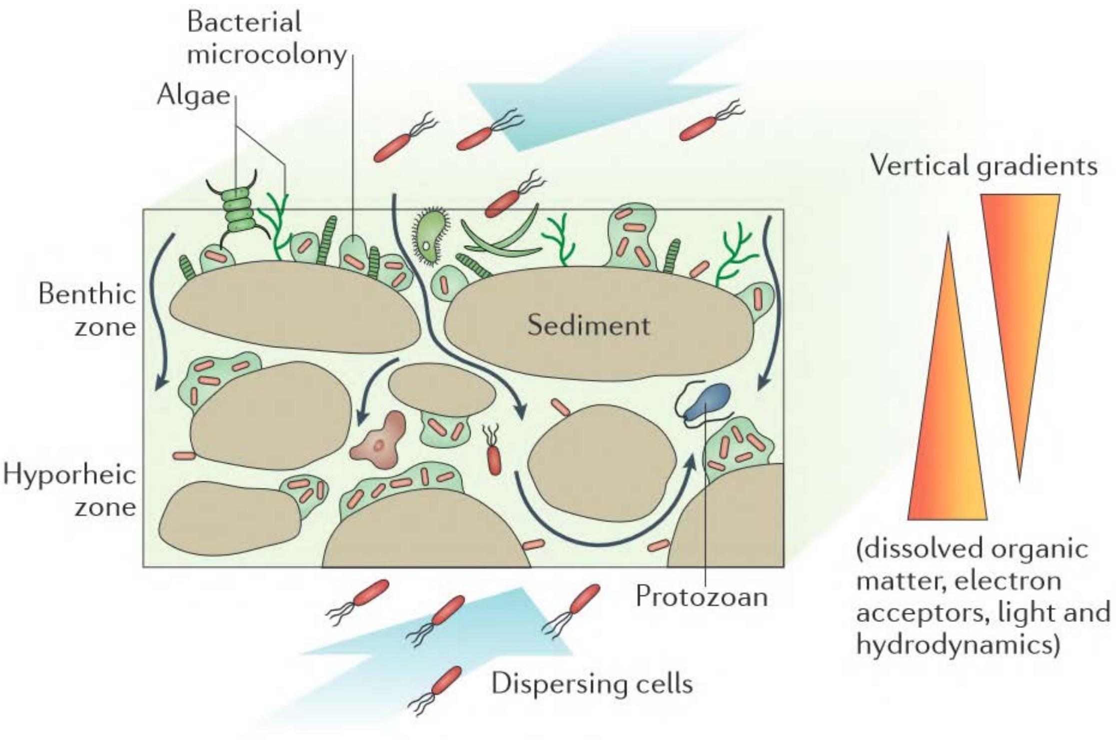

Figure 2.1: Microbial ecology in the stream bed [23].

Aquifers are underground layers of rock, gravel, sand, or soil that hold and transmit groundwater. They are an important source of fresh water for human consumption, irrigation, and industrial purposes [194]. Biofilms in aquifers can have both positive and negative effects. On the positive side, they can help to filter contaminants from groundwater [11] and promote the growth of other organisms. They can also act as a source of nutrients for other organisms, such as bacteria and fungi, that live in the aquifer [447].On the negative side, biofilms can also clog the pores in aquifers, reducing the flow of groundwater and causing problems for wells and other water extraction systems. In addition, some biofilms can contain pathogenic microorganisms or be contaminated with antibiotics that can pose a risk to human health if they contaminate drinking water sources [388]. Understanding the interactions between aquifers and biofilms is important for managing and protecting groundwater resources. By studying the ecology and biogeochemistry of aquifer biofilms, researchers can gain insight into the processes that affect water quality and availability in these important ecosystems.

2.1.2 Engineering biofilms in porous media

In bioengineering applications, bacterial biofilms can be used to perform specific tasks, for example in engineering the properties of porous media [302, 344] such as hydraulic conductivity and chemical speciation. Examples include reactive bio-barriers [480], bioremediation [226] or microbially-enhanced oil recovery [310] — a tertiary oil extraction technology increasing sweep efficiency via the production of bio-surfactants and selective clogging of pores. Emerging biotechnologies also include self-healing concrete [204] or sealing cap rock fractures in CO_2 aquifer storage [107, 325]. An area of particular importance in biofilm engineering is the design of bioreactor technologies [329]. Examples in wastewater treatment — e.g. for the removal of organic matter, nitrates, phosphorus or micro-pollutants [480] — include fixed or fluidized beds, trickling filters, and membrane-based reactors [72]. Biofilm-based reactors can also be used to produce a variety of added-value products such as fuel ethanol [233] or organic acids [75]. In many of these systems, the biofilm is submitted to flow to increase efficiency and the substrate is some kind of porous medium that provides a large surface to volume ratio and increases the amount of biomass per unit volume. This idea of using flow and porous scaffolds goes well beyond biofilm engineering and is found, in particular, in bioreactors for ex vivo engineering of living tissues [274].

2.2 Biofilm growth and hydrodynamics in porous media

Flow in porous media is a distinct field of study due to its complex nature. It is a special type of flow because it involves the interaction of fluid and solid phases, and the fluid is influenced by the structure and properties of the porous material. This makes porous media flow unique and challenging to model, as it is influenced by factors such as permeability, porosity, and fluid viscosity, among others. Porous media flow in the presence of biofilm is special because it adds an additional layer of complexity to the already challenging problem of porous media flow. In the presence of biofilm, the porous media flow becomes a multi-phase system, with both fluid and solid phases, as well as a biological phase represented by the biofilm. This makes it difficult to model, as the behavior of the system is influenced by multiple factors, including the structure of the biofilm, the flow rate of the fluid, and the chemical and biological interactions between the biofilm and the fluid.

2.2.1 Interplay between biofilm and hydrodynamic conditions in porous media

Effect of flow on biofilm growth Biofilm growth in porous media has been studied in many contexts. Until now, there has been a lack of clarity surrounding the impact of flow on the growth of biofilms, likely due to the fact that fluid flow influences multiple driving forces that are inherently different in nature, but challenging to distinguish from one another technically. These driving forces include mechanical stress and solute transport [427]. There is significant experimental evidence that biofilm accumulation throughout porous media is not homogeneous both temporally and spatially. More specifically, regarding the initial stage of biofilm growth, it has been observed that biofilm initial cluster distribution is heavily influenced by the availability of nutrients, the effective porous media particle size, and local hydrodynamics [344, 377, 427, 428]. Porous media exhibit inherently a wide range of shear stresses. At the pore scale, biofilms tend to grow initially in low shear-stress regions with an eventual growth towards the rest of the pore space [413]. This can be attributed to the fact that high shear zones and pore throats provide an unfavorable environment for the attachment and initial development stage of the biofilm. In the work of Thomen et al. [427] in order to isolate the effect shear stress in initial biofilm growth, they fabricated millifluidic channels of variable height to apply a range of shear stresses under the same flow rate. They concluded that above a threshold shear stress value of 10mPa, no direct initiation of the biofilm on the surface could occur. However, as previously discussed, high shear zones appear to result in higher initial retention times of planktonic bacteria on surfaces, and sturdier biofilms later on [248]. In general, high shear stress environments result in thinner and smoother biofilms while low shear stress regions produce thicker and rougher biofilms [291]. Furthermore, Stoodley et al. studied biofilm growth in laminar and turbulent growth conditions in parallel and concluded that with an increase of the Reynolds number, biofilm grown in laminar conditions detached while biofilm grown in turbulent conditions increased its hydraulic resistance by 1.6 times. Indeed, this finding is coherent with the general perception that biofilms grown at higher shear stress environments tend to be generally stronger and more resistant to high flow rates [413].

Effect of biofilm on the hydrodynamic environment The presence of a biofilm can, in turn, affect the hydrodynamic parameters of porous media, such as permeability and porosity. More precisely, the biofilm can clog the pores of the medium and reduce the flow of fluid through the medium, which can lead to an increase in the resistance to flow and a decrease in the permeability. In addition, biofilm occupies some of the volume of the pores and therefore the porosity of the medium is reduced. The extent to which the biofilm affects the hydrodynamic parameters of the medium will depend on the thickness and density of the biofilm and the size and shape of the pores in the medium [10]. Furthermore, biofilm plays a major role in shaping the hydrodynamic environment of a porous medium by enhancing anomalous characteristics, such as intermittent behavior in Lagrangian velocities, solute spreading in breakthrough curves, and solute retention [317]. However, the hydrodynamic environment of biofilm inoculated porous media is not always changing due to the direct effect of the EPS production but can be affected by the deposition of minerals produced by the bacteria. In one case where the effect of biofilm growth in porous media was studied, the main clogging material was identified as calcium carbonate [353]. In a more recent study, the microbial induced calcium carbonate precipitation was studied and visualized within a meter-long microfluidic porous medium with a simultaneous calculation of the permeability evolution, indicating the important effect of the minerals on the hydrodynamics of the medium [122].

In another study, focused on the effect of flow on the bacterial ecology aspect of such systems, investigated the effect of flow on the interaction between *Pseudomonas aeruginosa* and *Candida albicans* in biofilm environments and it was found that the expected antagonistic interaction between the two pathogens can be reversed under flow, resulting in increased biovolume accumulation for both species in dual-species biofilms compared to single-species biofilms [209]. The study highlights the importance of cellular-scale spatial structure in biofilms for understanding multispecies population dynamics, particularly in the presence of flow. On the same aspect of bacterial ecology, another group investigated how two bacterial biofilm mutant strains evolve and compete in porous environments under flow [92]. The authors found that cells that rapidly form biofilms tend to block their access to fluid flow and redirect resources to competitors. To understand how these dynamics influence bacterial growth rates, the authors coupled a model of flow-biofilm interaction with a game theory analysis. This investigation revealed that hydrodynamic interactions give rise to an evolutionarily stable growth rate where cells within a biofilm can outcompete other genotypes by growing more slowly. The results suggest that hydrodynamics can profoundly affect how bacteria compete and evolve in porous environments,

On permeability/differential pressure As biomass accumulates, be it individual bacterial cells or EPS matrix, the hydrodynamic environment is affected and as a result, differential pressure is developing across a porous medium. First steps towards the study of these pressure variations in porous media have been made since they can provide valuable real-time information regarding the biomass distribution and the evolution of permeability of the porous medium [120, 217, 423, 441]. These variations are naturally attributed to biofilm pore clogging and detachment [239, 428], biomass redistribution within the pore space and the creation of preferential flow paths [49, 103]. It is believed that this oscillatory behavior is more pronounced under constant flow conditions, commonly used in laboratory environments, rather than constant head conditions, most commonly observed in natural systems (e.g. subsurface) [436]. These pressure variations are reported in a plethora of publications but a precise description of the clogging/detachment mechanism is hard to identify. In an effort to better understand biofilm detachment/clogging in porous media, Kurz et al. showed that the mechanism driving the preferential flow path intermittency is the competition between microbial growth and shear stresses at the liquid/biofilm interface [239]. Stewart et al., in an effort to decipher the pressure fluctuations observed in 2D and 3D porous media, described a cyclic process in which pressure increases due to biofilm formation at the region close to the inlet due to the fact that nutrients (in this case sucrose) are readily available [409]. A gradient of nutrients is formed and therefore biofilm formation is concentrated towards the inlet until the pore network is locally completely clogged. Eventually a sharp pressure drop occurs due to the creation of a flow path that also allows for the transfer of fresh nutrients. Then the region next to the first one is progressively filled with biofilm due to the newly available nutrients until the space is in turn completely clogged and the same process continues in cycles producing oscillatory pressure behavior. It should be noted that in this study, the bacterial strain used produced a biofilm comprising mainly of dextran, a water-insoluble exopolymer, a distinct difference from the exopolymer composition produced by the strain used in this study.

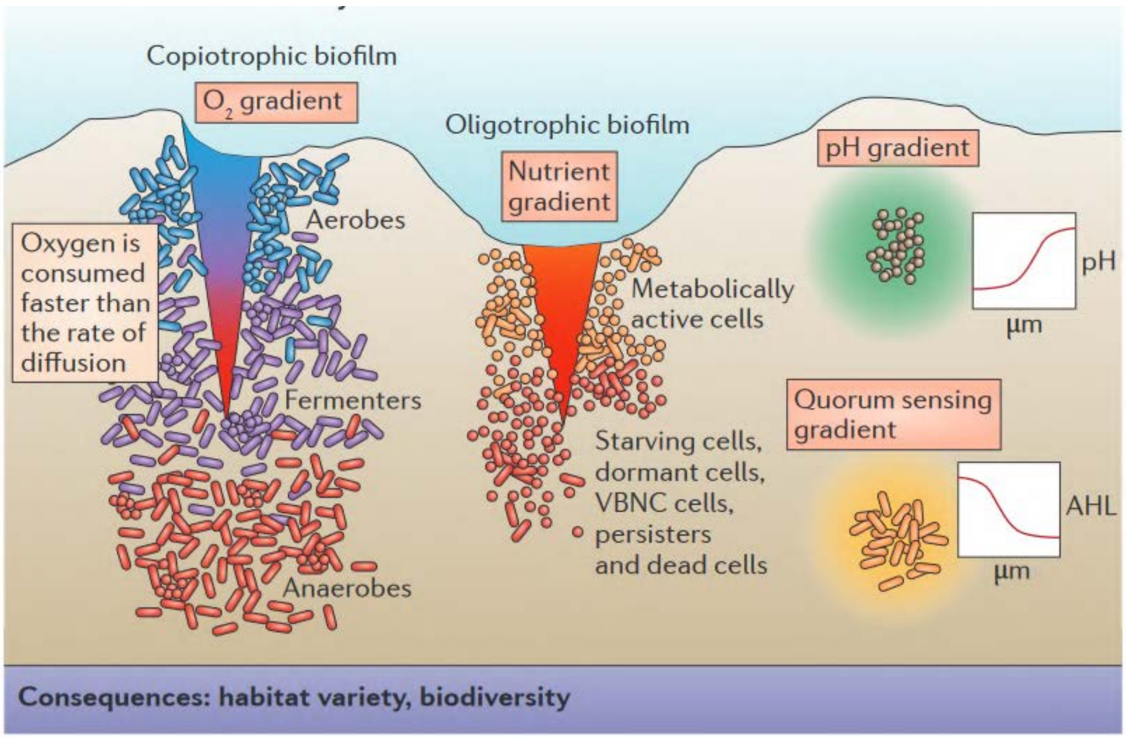

Figure 2.2: The biofilm micro-environment can be highly heterogeneous in terms of chemical species. The formation of the extracellular polymeric substance (EPS) matrix leads to the establishment of stable gradients that provide different localized habitats at a small scale. Image taken from [127].

2.2.2 Mass transport phenomena in heterogeneous media

Mass transport in porous media refers to the movement of fluids and solutes within porous materials such as soils, rocks, and biological tissues. This movement is influenced by various factors such as fluid pressure, concentration gradients, pore geometry, and fluid properties. When biofilm growth takes place in porous media, the change in the hydrodynamic landscape can directly affect the transport phenomena of chemical species (e.g. nutrients, carbon sources, metabolism byproducts, QS, biocides) that take place within the pore space. As discussed in the previous chapter, a direct effect of mass transport of chemical species in respect to bacterial behavior is chemotaxis. Bacterial chemotaxis is the process by which bacteria move towards or away from a chemical stimulus in their environment. This movement is mediated by a system of receptors and signaling pathways that allow the bacteria to sense and respond to changes in the concentration of specific chemicals. The ability to sense and respond to different chemical signals enables bacteria to locate and move towards favorable environments, such as sources of food, and to avoid harmful or toxic environments. Although bacterial chemotaxis has been observed in a wide range of environmental settings, insights into the phenomenon are mostly based on laboratory studies of model organisms and therefore lack the complexity of natural systems. These systems provide a heterogeneity in terms of geometrical features which therefore affect the hydrodynamic environment in which bacterial biofilms develop [132].

Heterogeneities in terms of concentration of chemical species throughout a porous medium frequently occur due in biofilm inoculated porous media. Biofilm growth can significantly impact solute transport in porous media as demonstrated by Kone et al. [227] (fig. 2.3E). The study used tracer experiments with Blue Dextran to monitor and estimate biofilm volume fraction and thickness, and found that biofilm growth resulted in up to 50% of the void space volume being plugged within 29 days. The effective porosity, representing the non-biocolonized porosity, was correlated with biofilm-affected dispersivity, indicating that biofilm growth has an impact on the transport properties of the porous medium. The findings highlight the need to consider biofilm-induced heterogeneities when studying solute transport in subsurface systems, and provide insights into the relationship between biofilm growth, porosity, and dispersivity.

Furthermore it can be observed most of the time at the influent regions of such systems where important nutrients are most available. The decreasing availability of nutrients (e.g. carbon, phosphorous, nitrogen, dissolved oxygen etc) can be as responsible for the decrease of biofilm formation and detachment [184, 367], as the presence of inhibitory compounds (e.g. metabolism byproducts, QS molecules) [50, 307]. However, there are also studies reporting that biofilm growth takes place at the effluent side of the porous medium where carbon availability might be limited [457]. This can be attributed to other limiting factors such as oxygen depletion at the inlet and oxygen-rich environment at the outlet due to the gas-permeable material of the bioreactor. The shape and the size of biofilm patches developed within the porous medium is, by itself, known to create heterogeneities in terms of oxygen availability. Biofilm dense regions form anoxic micro-environments that eventually hinder biofilm growth [64]. Additionally, it has been reported that carbon source depletion can negatively influence the biofilm formation in porous media [160].

Several studies have been conducted to shed light on the interplay between chemotaxis and hydrodynamics of biofilm growth, more specifically in porous media. In one study, de Anna et al. used a chemoattractant (chemical signal molecule that promotes biofilm growth) and a chemorepellent (molecule that inhibits biofilm growth) in a heterogeneous microfluidic porous medium where they concluded that the morphology of the porous medium affects the residence times of chemical species, be it chemoattractants or chemorepellents, that, in turn, mediates the biomass accumulation accordingly [102] (fig. 2.3).

In the work of Bearon and Hazel [24] it has been shown that bacteria swimming in channel flow become trapped in regions of high shear, leading to reduced concentrations near the channel's centerline. The commonly used advection-diffusion equation fails to predict the concentration of bacteria in the channel, but the Smoluchowski equation can successfully describe the probability distribution of the bacteria in both macroscopic and microscopic space variables. Using a simple analytic approximation to model the distribution of the bacteria indicates that flow-induced modification of the bacteria's swimming direction has a dominant effect on equilibrium behavior. The research tires to explain how the equilibrium distribution of chemotactic bacteria is altered in the presence of spatially varying shear flow. Finally, the study demonstrates that while advection is an appropriate description of transport due to the mean swimming velocity, the random reorientation mechanism of the bacteria cannot be simply modeled as diffusion in space.

Quorum sensing Our understanding of quorum sensing mechanisms comes mainly from studying pure strains of bacteria in controlled laboratory conditions. These studies have given us a fundamental knowledge of how quorum sensing works in different types of bacteria. However, bacteria often exist in a mixture of species and under non-ideal conditions where hydrodynamic fluctuations and chemical/physical gradients occur. As previously discussed, the presence of biofilm can further affect the hydrodynamic parameters of the bacterial environment. Unlike bacteria cultures that are well-mixed in liquid, biofilms are not uniform and can change over time, therefore understanding how quorum sensing operates within the structural limitations of biofilms is a crucial question. Recent research has focused on understanding how quorum sensing operates in more realistic bacterial habitats such as heterogeneous structures, in the presence of fluid flow and within eukaryotic hosts where pathogens encounter the host microbiota [357].

Bacteria have different behaviors when it comes to forming biofilms in relation to their quorum-sensing states. An important observation is that the amount of bacterial biomass required to initiate quorum sensing in a particular bacterial population increases with increasing fluid flow rate. Specifically, fluid flow removes autoinducers by advection and so a higher cell density is required to achieve a quorum under flow than in well-mixed liquid cultures. One unexpected result from new studies in this area is that in bacterial species such as *V. cholerae* and *S. aureus*, in which quorum sensing represses biofilm formation, increased biofilm formation occurs under flow compared with no flow conditions [219] (fig. 2.3D). Autoinducer removal by flow relieves repression, promoting increased biofilm formation relative to biofilms formed on surfaces without flow (fig. 1.4). Nonetheless, once thick biofilms are established, quorum sensing is activated in the cells residing at the base and interior of the biofilms, presumably because those cells are shielded from autoinducer advection by the neighboring cells and the deposited extracellular matrix. Because externally residing cells experience a different flow regime from internally residing cells, cells in different regions of the biofilm enact discrete quorum-sensing-controlled gene expression programs. Thus, the flow environment drives spatial fate decisions, enabling genetically identical bacteria that exist in close proximity to nonetheless undertake distinct biological functions. Intermittent flow, which involves switching between flow and no-flow, or reduced-flow, is common in various living systems, such as during rain, digestion, and urination. Under these conditions, bacteria in biofilms can alternate between two modes: quorum-sensing-on when flow stops and quorum-sensing-off when flow resumes, which is linked to changes in autoinducer accumulation and advection respectively [219]. This has been demonstrated through the analysis of GFP output from the quorum-sensing-activated P3 promoter of *S. aureus*. This reporter showed step-like increases in expression during periodic flow, and a linear increase without flow, with total repression under steady flow. This suggests that intermittent flow can lead to non-uniform quorum-sensing gene expression over time.

Surface topography, in addition to fluid flow, also affects quorum-sensing dynamics and the two are often connected. Examples include: in confined spaces such as industrial pipes or plant phloem, the length of the confined area determines the spatial activation of quorum sensing. In long microfluidic channels, quorum sensing is repressed near the inlet due to flow-mediated advection of autoinducers, but highly activated near the outlet where autoinducers have accumulated [219]. In another example, in a long channel, *P. aeruginosa* exhibit different behaviors such as motility upstream and quorum-sensing-regulated group behaviors downstream [396]. Another study found that the topography of the growth substrate dictates the spatial range of successful quorum-sensing signaling in a viscous environment where autoinducers are diffusion limited [96]. This study suggested that in viscous environments where autoinducers are diffusion limited, a higher concentration of autoinducer is needed

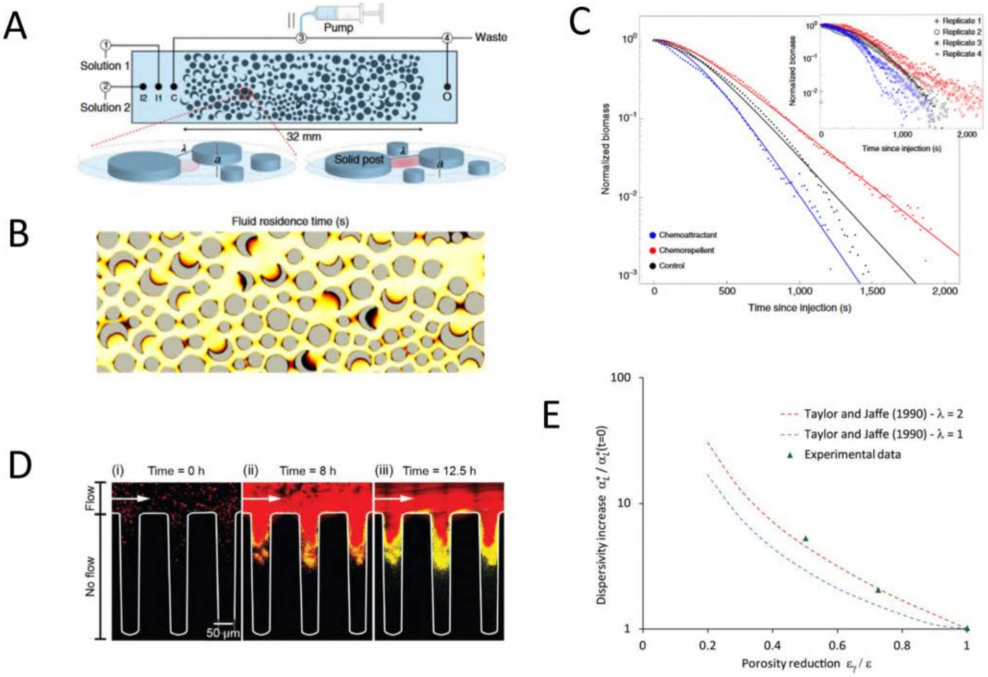

Figure 2.3: Mass transport phenomena in heterogeneous media. (A) Schematic of a microfluidic that consists of a disordered arrangement of disks and crescent-shaped obstacles, serving as an analogue for porous media. Enlargement of a portion of the microfluidics device, showing the definition of the pore width λ and channel depth a. (B) Map of fluid local residence time (in seconds), representing the time required for a small fluid volume to be displaced by 1 pixel (1.1 μm). (C) Shown is the temporal evolution of the total biomass Mb in a 16-mm-long region of the porous medium, rescaled by the initial biomass, averaged over four replicates, following injection of a chemorepellent (red symbols), a chemoattractant (blue symbols) and the bacterial supernatant (control; black symbols). In the inset, different symbols indicate the four replicates of each experiment. In all cases, the bacterial population decreases as the invading fluid displaces the initial fluid [102]. (D) Merged images of S. aureus in a complex topography. Red shows QS-off cells, and yellow shows QS-on cells. The images are based on n = 6 independent replicates [219]. (E) Comparison of dispersivity increase as a function of porosity reduction between experiment and theory [423]. Image taken from [227].

for inter-community communication in *P. aeruginosa* biofilms.

A further example of how flow and topography affect bacterial behavior is seen in *S. aureus* biofilms grown in microfluidic chambers with crevices that resemble intestinal crypts. On the main flow channel, outside of the crevices, the bacteria experience the flow and autoinducers are washed away, resulting in the suppression of quorum sensing. However, bacteria that have colonized the spaces inside the crevices experience little to no flow and therefore transition into the QS-on mode due to autoinducer accumulation [219]. This localized activation of quorum-sensing signaling, facilitated by the combination of topography and flow, can increase bacterial colonization of certain niches. For example, *S. aureus* activates the quorum-sensing-dependent production of enterotoxin B only inside of intestinal crypts, which increases the crypt depth [29]. Similarly, *V. cholerae* activates quorum sensing only inside of crevices and not outside of them [219]. This suggests that bacteria use flow conditions to allow isogenic cells in different environments to execute unique quorum-sensing-directed programs that provide fitness advantages in different locations and/or at different times during host infections.

2.2.3 Effect of flow on bacterial ecology

Bacterial ecology refers to the study of the interactions of bacteria with other living organisms as well as between bacteria, their physical environment and chemical surroundings. This includes the interactions between bacteria and other microorganisms, as well as between bacteria and their physical and chemical surroundings. The field of bacterial ecology is concerned with understanding how bacteria respond to environmental changes, how they interact with one another, and it also examines how bacteria adapt to different environments, such as the highly-hydrodynamically-heterogeneous porous media. Flow in porous media can have a significant impact on bacterial ecology. In porous environments, such as soil or rock, fluid flow can play a key role in determining the distribution and behavior of bacteria. As previously discussed, fluid flow can change the physical and chemical conditions within a porous environment, which can in turn alter the interactions between bacteria and their surroundings. This can influence the competitiveness of different bacterial strains and drive changes in bacterial community structure and function [425].

One major example would be a study by Coyte et al. [92] that combined microfluidic experiments, models, and game theory to explore how porous media hydrodynamics can impact competition between bacterial genotypes. The results showed that cells that form biofilms quickly face a problem as they restrict fluid flow and divert resources to competitors. A model and game theory analysis was used to understand the impact of these dynamics on bacterial growth rates and it was found that hydrodynamic interactions result in a growth rate that is different from what is observed in lab experiments, where cells within a biofilm can outcompete other genotypes by growing slower. This research highlights that hydrodynamics can have a significant impact on bacterial competition and evolution in porous environments.

Another study[209] compared the kinetics of biofilm formation between *P. aeruginosa* and *C. albicans*, two microorganisms commonly found together in various clinical sites such as urinary catheters and the lungs of people with cystic fibrosis. In that study, S. Kasetty et al. engineered fluorescent protein constructs for each species to enable single-cell resolution imaging, and they found that both *P. aeruginosa* and *C. albicans* displayed increased growth in dual-species biofilms compared to single-species biofilms. This result was specific to the biofilm environment and was not observed in planktonic cocultures. *C. albicans* was found to be stimulated by *P. aeruginosa* regardless of when it was added during the biofilm development process.

In a final example [288], a simplified four-species model of multi-species biofilm was established in a non-invasive laboratory setup for real-time monitoring of community development. The researchers observed that the community reaches its equilibrium after about 30 hours of growth, with an increase in spatial heterogeneity and non-monotonic developmental kinetics. They also found that interspecies interactions involving competition for resources, particularly oxygen, and both direct and indirect physical interactions contribute to the emergence of complexity in the community.

3 Experimental systems for biofilms in porous media

3.1 Controlled environments for biofilm studies

Studying biofilms can be challenging due to the many environmental factors that can influence their growth and behavior, such as temperature [42], nutrient availability [440], pH [384], and flow conditions [360, 414]. As a result, it is crucial to experimentally control these environmental parameters when studying biofilms. By doing so, researchers can systematically investigate the impact of individual factors on biofilm formation and behavior, develop effective strategies for controlling or preventing biofilm growth, and generate reproducible results that can be compared across different studies.

In the following paragraphs we aim to provide an overview of different experimental setups utilized for controlled biofilm studies. The discussion begins with large-scale experimental systems and mesocosms and then moves towards smaller laboratory scale setups, such as column and bioreactor models. The section concludes with an examination of miniaturized models such as microfluidics and micromodels.

3.1.1 Large-scale experimental systems and mesocosms

In the context of biofilm studies, mesocosms are experimental systems that allow for the controlled study of biofilms in a natural or semi-natural environment [241]. Mesocosms can be used to investigate the influence of complex environmental factors on biofilm growth and function. Mesocosms can also help bridge the gap between laboratory experiments and real-world environments, providing a more realistic and ecologically relevant context for studying biofilms.

Experimental systems at that scale have been utilized in various studies to investigate the dynamics of biofilms in different environments. For instance, in a study investigating the impact of nutrient enrichment on stream biofilms, mesocosms were set up using large channels with a length of 10 meters, a width of 1.2 meters, and a depth of 0.2 meters (fig. 3.1A) [147]. The large size of the mesocosms allowed for the establishment of complex and diverse biofilm communities resembling natural stream conditions. The study revealed the effects of nutrient enrichment on biofilm composition, biomass, and metabolism, providing insights into the response of stream biofilms to anthropogenic nutrient inputs.

In another study, the publication presents a study that utilized a large-scale experimental setup, specifically an oscillating grid mesocosm (fig. 3.1B), to investigate the dynamics of turbulence and oxygen penetration in sediment cores in shallow environments [264]. The mesocosm was able to produce homogeneous turbulence at the sediment-water interface of multiple sediment cores, allowing for controlled experiments with low variability between cores. The setup allowed for easy control of turbulence intensity, enabling the simulation of diffusive boundary layer thickness dynamics on different timescales. The mesocosm device provided a valuable tool for studying microbial dynamics under transient oxygen dynamics.

Another publication reports on a study conducted in an experimental mesocosm site (PISCO2, Spain) (fig. 3.1C) to investigate the effects of carbon capture and storage (CCS) leakages on soil bacterial communities [362]. The controlled environment of the mesocosm allowed for precise manipulation of CO_2 fluxes and short-term emissions. High-throughput sequencing of 16S RNA genes was used to analyze bacterial community composition and structure in two soils. The study highlights the importance of considering mesocosm experiments to evaluate the impacts of CCS leakages on soil microbial communities in a controlled and replicated experimental setup.

Overall, these publications demonstrate the use of large-scale experimental systems or mesocosms in studying the dynamics of biofilms in different environments, providing valuable insights into the complex interactions between biofilms and their surrounding ecosystems.

3.1.2 Column experiments and biofilm reactors

A bioreactor in the context of biofilm studies is a laboratory device used to grow biofilms under controlled conditions [171] usually to synthesize useful substances [233] or break down harmful ones

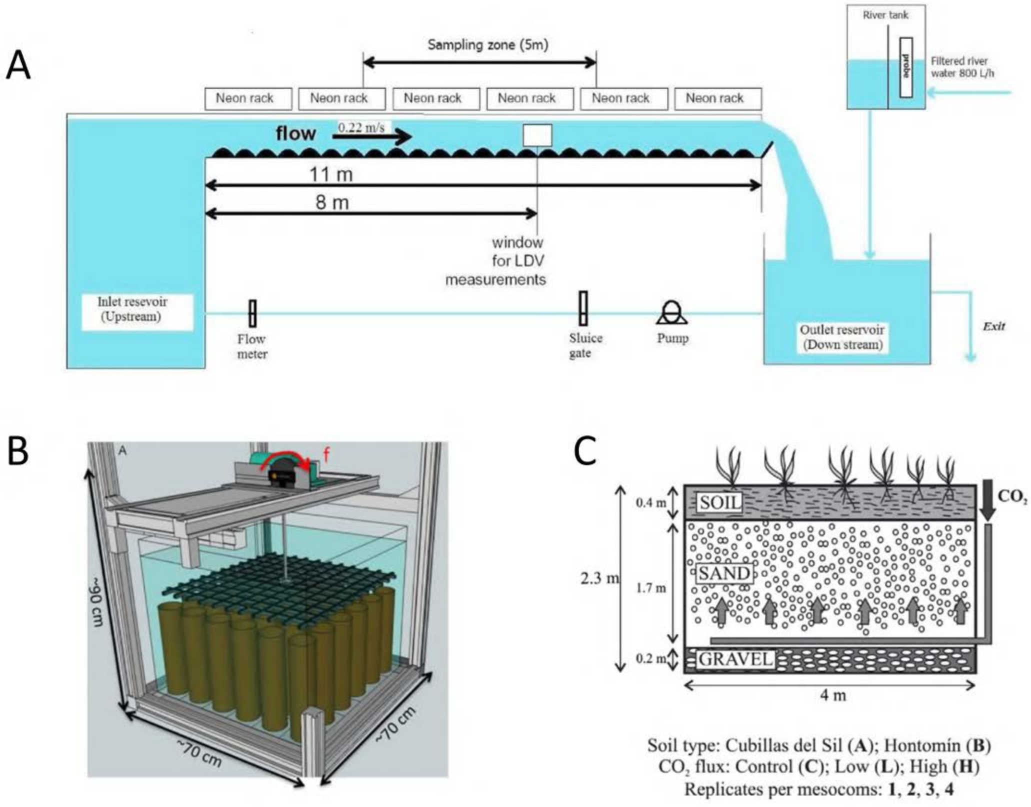

Figure 3.1: Various types of mesocosms. (A) Experimental setup from [147] showing the indoor flume (11 m x 50 cm x 20 cm) with Plexiglas sides at the Institute of Fluid Mechanics, Toulouse, France. The flume was modified for partial recirculation using river water with controlled hydrodynamic conditions. Water was supplied from the river to an outlet reservoir (3300 l) using an initial pump (800 l/h) and to an inlet reservoir (1500 l) using a submerged pump. (B) Experimental setup with oscillating grid above sediment cores from [264]. (C) Layout of experimental unit profile from [362].

[146]. A bioreactor typically provides a controlled environment for the growth of biofilms, allowing for the manipulation of various parameters such as temperature [421], pH [381], nutrient availability [156], shear stress [63], and other factors to mimic specific environmental conditions.

Regarding biofilm studies some examples include the design of bench- and pilot-scale porous media biofilm reactors for the study of the effects of biofilm growth and biomass accumulation in porous media [208], as well as the impact of biofilms on the hydrodynamic properties and mass transport in three-dimensional porous media [337]. In the field of biofilm studies, macro-scale biofilm reactors have gained a reputation as the standard for growth and evaluation of biofilms [439].

On the other hand, column reactors have been traditionally used for the study of physical aspects of porous biofilm systems. These measure from a few millimeters to several meters in length and from several millimeters to approximately 1 meter in diameter. The term is most commonly among the geosciences and hydrology community.

Biofilm reactors differ from standard column setups in terms of the level of control and reproducibility they offer but also in terms of applications. In a standard column experiment, biofilms may grow naturally on surfaces inside a column or container offering a more realistic porous media conditions. A typical example where column systems are used to study biofilm growth is to simulate a natural porous environment for the biofilm to grow in. For example in many studies, gravel was used in a packed column as a substrate for biofilm growth [348]. More recent studies have used polystyrene [100], PMMA [61] or glass beads to better define the porous geometry and therefore perform more consistent studies. Such systems typically imaged with techniques such as MRI and µCT due to the opacity of the porous media that does not allow for direct optical interrogation, however, in more recent studies, column experiments with transparent porous media have been developed [62].

3.1.3 Quasi-2D meso- and micro-models

Most natural porous media, but also materials used to fabricate model porous media (e.g. column bioreactors), are opaque and therefore do not allow for the direct observation of the biofilm processes that take place within the porous structure. Therefore, many setups are designed either as high-optical quality/transparent flow cells [175], or as flat-plate reactors [206]. These systems are designed to represent natural porous systems and fractured media, at a certain degree in order to study fundamental processes of biofilms in porous media [173]. These bioreactors contain either thin layers of porous media such as sand or glass beads [206, 413] or contain porous media with different types of material, organized in 3D space with a certain pattern, (e.g. hydrogel, glass, clay, PTFE [36, 62, 100, 349]). Depending on the optical properties of the bioreactor material, each application can be used in combination with a different imaging method (e.g. µCT [245], index matching [250]), that would allow for direct (e.g. fluorescence microscopy [209]) or indirect observations (e.g. PTV [60]) of biofilm formation and mass transport.

Quasi-2D meso and micro models have been developed to study the phenomenon of bioclogging in porous media [217, 410]. Particularly, in one study the influence of biofilm-induced heterogeneities on solute transport was investigated in a quasi-2D porous medium using a flow cell system which was packed with silica sand [227].

3.1.4 Microfluidics and miniaturized reactors

Microfluidic techniques present a variety of advantages over traditional approaches. These devices offer precise control over the geometry of the porous structure and over the physicochemical conditions of growth [18]. Fluid flows in these devices are very stable due to low Reynolds number, which can be used to generate gradients of chemical attractants/repellents to study bacterial chemotaxis [102]. Microfluidic approaches can also be combined with on-chip measurement of biological processes [387]. Chips are easily fabricated out of relatively low cost materials in large quantities with high reproducibility, for instance using soft-lithography with PDMS, which allows for multiple parallel

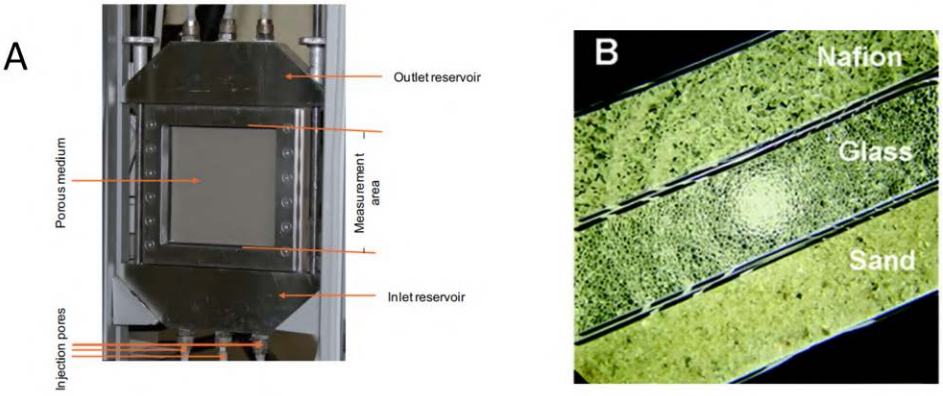

Figure 3.2: (A) The features of the quasi 2D flow cell developed in [227] are shown. The system is packed with silica sand and it measures 10×10×0.6 cm. (B) Various types of dry porous media in a micro-model system [250].

experiments running at the same time. Therefore microfluidic approaches are well suited to studying fundamental aspects of biofilm development [205, 477].

Capillary flowcells are sometimes used to represent single pores and therefore study the effects of biofilm growth in porous media in a more fundamental level [331, 416]. More complex examples of porous media include simple homogeneous pillars for the study of biofilm formations called streamers [373], randomly placed and sized pillars for studying the effect of hydrodynamic factors on the phenotype of bacteria [372] and finally more complex, granular geometries for studying the effect of hydrodynamics on the spatial evolution of bacterial biofilm [17]. Microfluidic platforms can also be used to study the effect of parameters such as pH, flow rate, and temperature on biofilm formation with high reproducibility and throughput [136, 328]. While these systems can sometimes be used as standalone devices, they often need to be integrated with standard biofilm characterization platforms involving confocal microscopy, colony forming units (CFUs), or crystal violet staining assays. However, due to the need for sample treatment, labeling agents, optical corrections, and invasive procedures, only a few microfluidic platforms have been adopted for real-time, non-disruptive analysis [420]. For instance, microscopy-based techniques require continuous correction of the lens focus to accurately capture variations in biofilm thickness.

Appart from the greater control and precision offered by these miniaturized systems, it is also possible to integrate small sensors or micropatterned growth substrates [202, 328, 340]. For example, a millimeter scale flow-through system developed by Tolker-Nielsen et al. for studying biofilm growth using microscopy overcomes some challenges associated with macroscale approaches, which allows for continuous, non-destructive analysis of the biofilms [430]. However, this system still requires relatively larger sample and reagent volumes compared to other microscale systems. In contrast, microfluidic systems can be designed to work with smaller sample and reagent volumes, often in the nanoliter range. This is especially useful when larger amounts of reagents, antibiotics, or experimental drugs are difficult to obtain or when only small amounts are available. Miniaturized versions of standard macroscale methods, such as electrophoresis and PCR, have also been developed for use in microscale systems [199].

The advent of microfluidics and miniaturized bioreactors is also providing a new way of approaching the problem of biofilm engineering in porous media [139, 223, 231, 329]. These technologies offer a relatively cheap and reproducible way of parallelizing, testing new ideas and optimizing processes in limited volumes and highly controlled conditions [251], before scaling up for applications [272, 308].

Such systems have also been used to assess the efficacy of newly constructed organisms or develop portable biomanufacturing platforms [318] or in selecting screening microbial strains for fermentation processes [171, 371].

3.1.5 Additive manufacturing

Additive manufacturing, also known as 3D printing, is a process of creating three-dimensional objects by building up layers of material, rather than subtracting material through machining or other traditional manufacturing techniques [235]. The basic process of additive manufacturing involves creating a 3D digital model of the object to be created, and then using specialized software to slice the model into thin layers. The 3D printer then uses various techniques to add material layer by layer, such as extruding molten plastic (Fused Deposition Modeling or FDM) [215], sintering powdered metal or plastic (e.g. Selective Laser Sintering or SLS) [117], or using photo-polymerization to cure liquid resin (e.g. Stereolithography or SLA) [471]. Additive manufacturing, has revolutionized the field of manufacturing and engineering, enabling the creation of complex, customized structures and devices with a high degree of precision and accuracy in a wide range of industries, including aerospace [422], medical [474], and consumer goods [44]. In the field of biotechnology, additive manufacturing is increasingly being used to produce microfluidic devices [9, 16, 346] and micro-scale bioreactors [319, 329, 471]. Examples include devices for drug discovery [259, 483], environmental monitoring [482] and fluid flow study [53], as well as micro-scale bioreactors to provide a controlled environment for the growth and study of cells [260] and microorganisms [94], with potential applications in tissue engineering [339] and pharmaceutical development [81].

Advantages One advantage of using 3D printing for the production of microfluidic devices and micro-scale bioreactors is the ability to create complex geometries [261] that cannot be easily achieved with traditional manufacturing methods such as milling or injection molding. The use of 3D modeling software allows designers to create intricate designs and shapes, including channels, chambers, and other features, with a high degree of precision and accuracy . Furthermore, complex geometries can also be used to create 3D scaffolds for tissue engineering applications, enabling the fabrication of structures that mimic the complexity of native tissues and organs.

Additive manufacturing techniques offer several advantages for achieving high precision in the fabrication of microfluidic devices and micro bioreactors. One of the key advantages is the ability to create features with sub-millimeter accuracy. For example, 3D printing techniques such as stereolithography and digital light processing (DLP) can achieve feature sizes down to 10-50 microns, which is essential for precise control of fluid flow and mixing in microchannels [393]. This can improve the functionality and efficiency of microfluidic devices and bioreactors by enabling more precise control of fluid flow and better mimicry of physiological conditions [174]. In addition, precise control of fluid flow and mixing can minimize sample and reagent usage, reduce reaction times [28], and improve the reliability and reproducibility of experimental results. The high precision/resolution of the technique provides the possibility to create molds and templates for replica molding [16, 101, 444]. With this technique, a master mold can be 3D printed with high precision, and then replicated many times using soft lithography or injection molding . This allows for high-throughput fabrication of microfluidic devices with precise features and dimensions.

Reproducibility is another advantage of using 3D printing for the production of microfluidic devices [47, 363] and micro-scale bioreactors [374]. With 3D printing, the same design can be easily replicated multiple times with a high degree of precision and accuracy, ensuring consistency across devices. This is particularly important for biological applications where consistent microenvironments are required for reliable results. Reproducibility also allows for the optimization of device design through rapid and inexpensive prototyping [297, 429]. Furthermore, 3D printing enables the automation of the manufacturing process, reducing the potential for human error and variability in device fabrication. Reproducibility is therefore a key advantage of 3D printing for microfluidic devices and micro-scale bioreactors, offering potential benefits in terms of reliability, efficiency, and ease of use.

Another advantage of 3D printing for microfluidic devices and micro-scale bioreactors is the ability to rapidly and inexpensively prototype designs [297]. With traditional manufacturing methods, producing a prototype can be time-consuming and expensive, as it may require specialized tooling and equipment. In contrast, 3D printing allows for the rapid and cost-effective production of prototypes, enabling designers and researchers to quickly test and refine their ideas. This can be particularly important for early-stage research or development, where multiple iterations of a design may be required before reaching an optimal solution. Additionally, 3D printing allows for the integration of multiple functionalities and components into a single device, reducing the need for separate components and increasing overall functionality and ease of use. The ability to create complex geometries also enables customization and tailoring of devices to specific applications and research needs, allowing for greater flexibility and versatility. Overall, the ability to create complex geometries is a significant advantage of 3D printing for microfluidic devices and micro-scale bioreactors, offering potential benefits in terms of functionality, efficiency, and innovation.

Limitations While many 3D printers claim to have a resolution as low as a few tens of microns, the smallest open channel that has been successfully printed using 3D printing technology is still approximately 200 micrometers wide [16]. As a result, most of the microfluidic devices that have been reported using 3D printing have channel sizes ranging from hundreds of microns to a few millimeters in size [71]. The limited resolution of current 3D printers can result in rough surface profiles in microchannels that are 3D printed. In one study [151], a microfluidic device was fabricated using a high-resolution 3D printer, however, after the supporting material was removed, the inner wall of the channel showed large rough ridges, which could lead to issues such as dead volumes and inconsistent surface modifications. Additionally, the 3D printing materials, which are often based on acrylate and acrylonitrile butadiene styrene (ABS) polymers, have a tendency to absorb molecules such as proteins and lipids. This can result in a reduction of the concentration of analytes of interest, ultimately altering a measurement [469]. Furthermore, the rough surface of the channels may increase adsorption, posing biotoxicity concerns for 3D-printed devices. To address these issues, some coating protocols can be applied, such as a layer of PDMS on the inside of a 3D-printed channel [151]. The integration of cells into microfluidic devices is popular, but there are concerns about the biocompatibility of most 3D-printing resins and plastics, as they are complex mixtures containing components that may be harmful to cells [232]. While biocompatible 3D-printing materials are being developed [157], their transparency pose additional challenges [335]. Clear materials are available for 3D-printing [435], but they are typically translucent or semi-transparent and require labor-intensive polishing to achieve transparency [351]. Finally, most 3D-printing materials are not gas permeable, which limits their application in long-term cell culture without additional gas exchange modules [282].

3.2 Characterization of biofilms in porous media

3.2.1 Basics

Biofilms on 2D (flat) and 3D substrates have been studied and characterized using various destructive and non-destructive techniques to assess their presence [294], structure [180], physicochemical properties [148, 311] and distribution in porous media [100]. The purpose of this section is to discuss recent advances in microsystems for studying and sensing bacterial biofilms as well as presenting various imaging techniques used in the biofilm field. Traditional methods for studying biofilms are invasive and do not allow for repeated experiments, making it difficult to accurately compare and understand the temporal characteristics of these organisms. Non-invasive microsystems, including optical [106], electrochemical [12], and mechanical systems [97], have been developed to address these challenges and provide a better understanding of the physiology and function of bacterial biofilms. In addition, several imaging techniques, including optical/microscopy methods (fluorescence microscopy, CLSM, TPLSM etc) [245, 292], scanning or transmission electron microscopy (SEM or TEM) [4, 364], atomic force microscopy (AFM) [27] as well as more recent methods such as ultrasound-based imaging techniques [382], nuclear magnetic resonance (NMR) spectroscopy [376], optical coherence [180] and X-ray tomography [303] (OCT and µCT) are established for the study of biofilms. The following section will be focused on presenting the state of the art of microsystems used for the biophysical and chemical characterization of biofilms as well as list the aforementioned imaging techniques. The capabilities and the limitations of each technique will be discussed. Special attention will be give to X-ray micro tomography at the end, since this is one of the methods used in this work.

3.2.2 Sensors to investigate biofilm processes

There are several challenges in understanding the temporal and spatial dynamics (e.g. distribution of metabolites [361]) in microbial biofilms, including the high heterogeneity and variability within the biofilm structure and the difficulty in measuring properties of the bacteria and extracellular polymeric substances (EPS) without disrupting the biofilm. Sensing techniques have been developed to address these challenges, but they are not without their own limitations. For example, micro-electrode probes have been used to measure properties within the biofilm, but they can compromise the physical structure of the biofilm by perforating it, which can alter cell permeability [279, 323]. Similarly, the use of dyes to stain the biofilm can alter the biochemical and biophysical properties of the bacterial cells. These issues have motivated researchers to search for less invasive approaches to monitor indicators such as pH and oxygen levels within the biofilm.

Electrical sensors Micro-electrodes and electrical sensors have been used to measure various properties within biofilms, including oxygen levels [342, 479], pH [181, 249], ion concentrations (e.g. ammonium, nitrile, nitrate [375], calcium [42, 165] etc), glucose levels, and temperature variations [460]. These sensors are generally robust and flexible, but they do have some limitations. For example, they can sometimes be affected by cross-sensitivity or interference, and they may require physical contact with or penetration of the biofilm in order to make measurements [455]. While this can affect the accuracy and reproducibility of the measurements to some extent, these sensors are still widely used due to their convenience and versatility.

Optical sensors Optical systems are frequently implemented to detect changes in oxygen and pH levels within biofilms. These systems often involve the use of a light source that directs the light towards planar optodes [464], which are thin, 2D films made of polymers that contain luminescent probes that are sensitive to oxygen or pH levels. While planar optodes can be used to study biofilms on their surface, they cannot provide information about what is happening inside the biofilm [143, 216, 238, 405]. To gather information about the interior of a biofilm, researchers may use micro- and nanoparticles that have been labeled with fluorescent or luminescent dyes that are sensitive to pH or oxygen levels coupled with optical imaging techniques such as confocal and fluorescence microscopy. These particles can be dispersed within the biofilm, providing a 3D map of oxygen concentration and pH within the biofilm. In addition, these methods are non-destructive, meaning they do not damage the biofilm during the course of the study [5, 200, 402]. Fluorescent probes have also been used to detect the presence of heavy metals such as Fe3+, Cu2+, Zn2+, and Hg2+ in biofilms that are relevant to bioremediation applications [163].

Mechanical sensors Another group of sensing devices used to study biofilm growth and formation involves mechanical systems such as quartz crystal microbalances (QCM) [369, 404], quartz tuning fork oscillators [452], surface acoustic wave (SAW) sensors [32], differential pressure sensors [212, 265], and interfacial rheometry and tensiometry [354, 355, 468]. These devices often include piezoelectric components that produce an electrical response when pressure is applied. In the case of microbalances and quartz tuning fork oscillators, this can be the result of inorganic or organic substances, including cells, that are deposited or adsorbed onto the surface of the device. In the case of differential pressure sensors, the piezoelectric element consists of a membrane that is in contact with the fluidic circuit on both sides so the differential pressure developed on both sides is due to the biofilm growth that

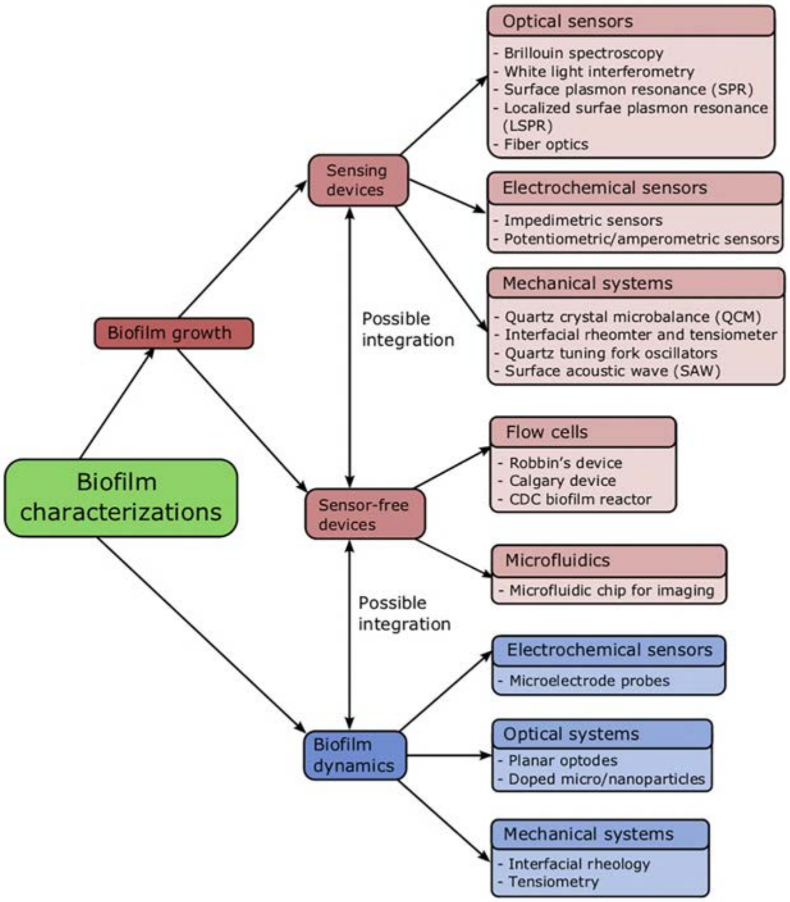

Figure 3.3: Different detection approaches to study bacterial biofilm formation and dynamics [135].

is changing the permeability of the measured system. These systems can be used to monitor biofilm formation in real-time with high temporal resolution at relatively low cost. Some quartz crystal microbalance systems even allow for the measurement of dissipation, providing additional information about the mechanical properties of the adhering biofilm [343]. By measuring the mechanical response of bacteria or biofilm on a surface (e.g. interfacial elasticity and interfacial tension) using interfacial rheometry and tensiometry, researchers can determine bacteria adsorption kinetics and their ability to adhere to a specific surface. This information can be useful for optimizing eradication procedures or designing surfaces that are resistant to bacterial attachment.

4 Imaging of biofilms in porous media

4.1 State of the art of imaging techniques on 2D flat substrates

Electron microscopy techniques such as SEM and TEM have been used on biofilms grown on flat surfaces, to map their structure [185, 470] and study their formation stages [4]. The principle of these techniques is based on ejecting a focused beam of electrons onto the sample. In the case of TEM, the beam penetrates the sample while in SEM the beam is reflected. In the first case the denser the specimen, the more the electrons are scattered forming a darker image because fewer electron reaches the screen for visualization while thinner, more transparent specimens appear brighter. In the second case (SEM), when high energy electrons reach the sample, several signals are generated. These include back-scattered electrons (BSE), secondary electrons (SE) and X-rays and each one of them provide information about the sample's chemical composition and surface topography. Even though these techniques have widely been used to characterize biofilms on flat surfaces, their use on porous media is limited due to destructive nature of these techniques. Usually the samples are prepared by being freeze-dried or covered with a layer of a conductive material and the measurement takes place in vacuum. Environmental scanning electron microscopy (ESEM) [4] is used to overpass this limitation by enabling the scanning of fully hydrated samples and therefore eliminating artifacts introduced due to sample preparation.

Atomic force microscopy is mainly used to study the interactions of biofilm with its substrate [27, 299], determine its thickness [69], and its mechanical properties [195, 257]. AFM is a technique where information is obtained by scanning a surface with a mechanical probe, a cantilever, with a tip of a size of several nanometers. The tip is either brought in contact or at the proximity of the surface so that forces between the two lead to deflection of the cantilever that is captured usually by laser deflection on the back of the cantilever or by piezoelectric elements, interferometry etc. The deflection of the probe reveals the topography of the scanned sample. Both AFM and electron microscopy can produce images of very high resolution, on the order of nanometers.

A typical method for observing biofilms in 2D substrates is optical microscopy where a light source, be it ultraviolet or visible light, is used to illuminate the sample and a system of lenses collects the reflected light, generating a magnified image of small objects. Usually the limitation of these techniques lies in the light source wavelength and the numerical aperture of the objective lens. These two parameters define the diffraction limit of an optical microscope. In addition, optical techniques have a limited applicability on observing biofilms in natural porous media due to the complex nature of the media (e.g. sand grains, glass beads). Porous media are rather irregularly shaped, resulting in increased background signal and image blurriness. Optical microscopy is commonly used in combination with fluorescent labeling techniques to increase the spatial resolution and decrease the signal-to-noise ratio. Fluorescence can naturally occur on a specimen (auto-fluorescence) [287] but also fluorescence can be introduced on the specimen according to the needs. Regarding biological specimens like microorganisms and more particularly bacteria, a fluorophore that would bind on a specific component of the sample can be directly introduced or the genome of a microorganism can be modified, (e.g. introduction of a plasmid) so that it express a certain fluorophore. Also arguably, this can be considered both as an imaging technique and a sensor. For example, bacteria become fluorescent when they come in contact with a specific level of oxygen [161]. On the other hand there are reports that evaluate the limitations of using classical fluorescent genetic reporters, especially those of the GFP (green fluorescent protein) family for quantitative measurements in living biofilms. In one it has been found that the fluorescence signal of GFP saturated quickly due to a reduction in oxygen concentration induced by bacterial consumption, which limits its use. To overcome this limitation, the paper proposes the use of a recently introduced fluorescent protein tag, FAST, which is less sensitive to oxygen concentration [289].

A widely used technique for observing biofilms is confocal scanning laser microscopy (CSLM) and more recently two-photon laser scanning microscopy (TPLSM). In optical microscopy, the depth of field (DOF) is the distance between the nearest and the furthest objects that are in acceptably sharp focus in an image captured with a camera. In traditional optical methods, the whole sample is illuminated at once and the image obtained contains a certain amount of background noise due to out-of-focus planes giving off light signal. On the other hand, a confocal microscope uses fluorescence optics and a laser light is focused onto a defined spot at a specific depth within the sample. This leads to the emission of fluorescent light at exactly this point. A pinhole inside the optical pathway cuts off signals that are out of focus, thus allowing only the fluorescence signals from the illuminated spot to enter the light detector. The sample is thus scanned layer by layer and the whole volume of the sample is obtained. Even though the technique has the advantage of eliminating background noise, providing spatially resolved details of biofilm structures in 3D [6], the penetration depth is limited to several micrometers. Confocal microscopy combined with fluorescence tagging, has been extensively used to

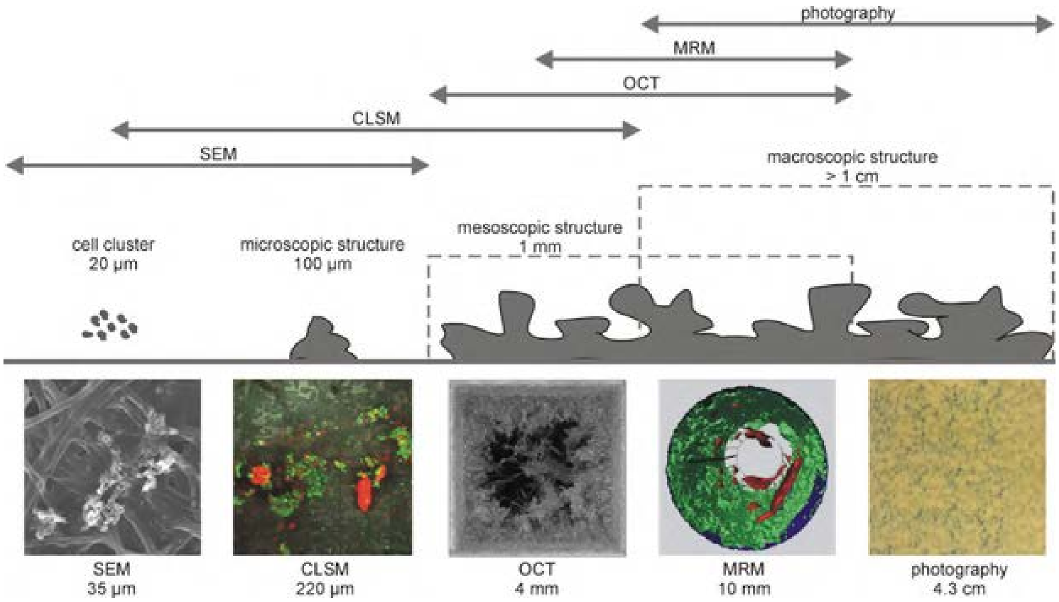

Figure 4.1: Scheme illustrating the definition of scales at which biofilm structure might be investigated. The definition of scales is not based on the resolution of the imaging techniques. Moreover, recent developments extended the capabilities of the methods shown here. Thus, methods might overlap in some cases. Image taken from [451].

explore biofilm structural and metabolic information such as measuring its thickness [266], determining the pH gradients within biofilms [450], quantifying the penetration rate of antibiotics into the biofilm matrix [197] and diffusion coefficients [104].

Optical coherence tomography (OCT) is an interferometric optical method that non-destructively visualizes biofilm samples on 2D surfaces in the mesoscale with high axial and spatial resolutions (< 20 µm). It has been used to study the structure as well as the dynamic behavior of biofilms [451]. The method does not require the use of a contrast agent [326] and can provide information regarding the spatiotemporal evolution of biofilms [106]. The light source used with this technique provides low-coherence near-infrared light (coherence length of several µm) with relatively good penetration characteristics in biological samples such as biofilms (penetration depth of several millimeters). A small percentage of the light emitted by the light source, is reflected by the first several millimeters of the sample. An interferometry technique is used to selectively filter the photons that were scattered from the surface of the sample. The limiting penetration depth, restrains the application of OCT for monitoring biofilm formation in 3D porous media [62], therefore the technique is sometimes referred to as a 2.5D technique.

4.2 State of the art of imaging techniques in 3D substrates

Direct observation of biofilm in 3D porous structures at a milli- to micro- scale is a challenging task up to this day either due to the opacity of the porous medium or the lack of penetration depth of the optical methods used when the porous medium is transparent.

One approach to this problem is the use of transparent porous structures where the optical index of the fluid and the solid are tuned to match so that direct optical observation of the biofilm can be achieved. The method typically uses a laser source and a camera, with a combination of a fluorophore. This technique provides the advantage of allowing for the study of complex flows in 3D porous media [175] as well as the in situ, spatiotemporal observation of biofilm growth in such structures [37]. This approach has also been used to study sediment [250] and soil analogs [111], as well as generic 3D porous media containing biofilm [62]. However, the use of this technique is quite limited due to the narrow choice of porous media materials that can be used when aqueous solutions are to be used to grow biofilms.

Magnetic resonance imaging/microscopy (MRI/MRM) was the preferred technique to visualize biofilms in the mesoscale in 3D. The idea is that MRI makes use of the high water content of biofilms [59]. Water contains protons 1H that interact with the magnetic fields produced by MRI. The relaxation behavior of 1H2O after excitation, that depends on the interaction with the surrounding matter (e.g. EPS), is captured which allows for the 3D mapping of "free" and "bound" water present inside the biofilm. This technique can be used to image large sample volumes of up to several mm^3 for example in fuel cell electrodes [158], tube bioreactors [271], and complex porous media [380] and can also provide spatial and temporal-resolved images of flow fields around biofilm [271]. However, the resolution of clinical machines is usually in the range of 1 to 3 millimeters, which is limiting for delineating the biofilm architecture, and chemical compounds of the porous structure. In addition, the use of the technique is limited when it comes to measuring systems that contain heavy metals that would interfere with the imaging, in particular, iron found in soils [431].

X-ray tomography, also known as X-ray computed tomography (CT), is an emerging technique, often used to image opaque, complex structures [461]. X-ray tomography has been widely been used in the medical field, as a common tool to non-invasively image the human body due the fact that X-rays can penetrate most of matter, especially soft tissues. It has been more than a decade that X-ray micro tomography has been used to image biofilms in 3D opaque porous media in the mesoscale for research purposes. This technique offers voxel resolutions typically in the order of several microns [303] and is compatible with most porous media. The technique is based on the difference in X-ray absorptivity of materials. An source emits X-rays that then go through the sample and the attenuated signal is captured by a detector. The sample is rotated 360° and a 3D volume is thus reconstructed from the 2D projections. This imaging technique is mainly used in this work and will be further detailed in the following section.

4.3 X-ray computed microtomography

4.3.1 Working principle

X-rays are a form of high-energy electromagnetic radiation. The wavelength of X-rays range from 10 picometers to 10 nanometers corresponding to energies in the range 145 eV to 124 keV. In a common laboratory scale micro-computed tomography (µCT) or clinical X-ray tomography, X-rays are typically produced in X-ray tubes that (roughly) consist of a vacuum chamber, a filament that serves as the cathode and a metal target that serves as the anode (fig. 4.2). The filament, typically made out of tungsten, is heated by an electric current and electrons are produced by thermionic effect. The voltage potential between the anode and the cathode is then accelerating the free electrons towards the anode. These fast moving electrons travel unobstructed in vacuum and hit the metal target (anode) at velocities approximately half of the speed of light. When the beam of electrons hits the metallic target, the electrons penetrate the surface for several micrometers and through complex interactions at a subatomic level, nuclei, ions and other electrons from within the anode material are in turn accelerated. About 99 % of the energy generated from these processes has the form of thermal energy while the rest 1 % has the form of X-rays, usually emitted perpendicular to the path of the electron beam.

There are mainly two types of interactions of these accelerated electrons with the atoms of the metallic target: an interaction that produces the characteristic peaks of the emission spectrum of the source and the Bremsstrahlung X-ray radiation. The first one occurs when a high energy electron collides with an inner shell electron and both are ejected from the tungsten atom leaving a 'hole' in the inner layer. This hole is filled by an outer shell electron with a loss of energy emitted as an X-ray photon. The latter one occurs when an electron passes near the nucleus, it is slowed and its path is deflected. Energy lost is emitted as a bremsstrahlung (braking) X-ray photon. Approximately 80 %

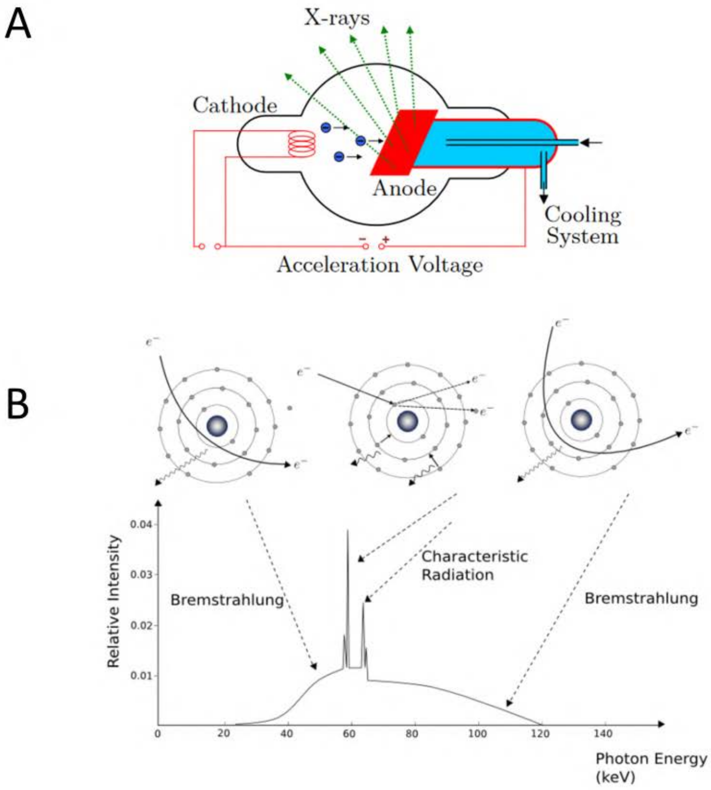

Figure 4.2: (A) A schematic of a typical laboratory-scale X-ray generating tube. (B) X-ray spectrum of a tungsten tube. The peaks correspond to the characteristic radiation while the continuous part of the spectrum represents the Bremsstrahlung radiation. Images taken from [31].

of the X-rays in the X-ray beam consists of X-rays generated in this way.

The voltage developed between the anode and the cathode is referred to as the tube potential (in kV) and the higher the potential, the faster the electrons accelerate towards the target and therefore the X-rays produced have a higher energy. For denser materials, a higher tube voltage is preferred as the higher energy X-ray photons can more easily transverse the sample. In addition The current running through the filament, referred to as the tube current (in mA), affects the temperature of the filament and therefore the amount of electrons liberated and shot towards the target. Therefore, the tube current affects the flux of X-ray photons generated from the source and therefore the luminosity of the generated images. The resulting spectrum of the source can be manipulated by changing the X-ray tube current or voltage settings, or by adding filters to filter out low energy X-rays. In that way, the X-ray spectrum can be modified according to the application.

Another type of X-ray source, used mostly for research purposes, is a synchrotron light source. A synchrotron is a circular loop particle accelerator where electromagnetic radiation is generated when relativistic charged particles are forced by some external force to bend their trajectories [190]. Initially an electron beam is generated using an electron gun and the beam is accelerated with a series of undulators. The path of the electron beam is controlled and the particles' trajectory is deflected through the use of magnetic fields. This synchrotron emitted radiation covers a large spectrum of electromagnetic waves, from infrared to hard X-rays and its characteristic is its high-brilliance, coherent (parallel/low divergence) beam [473]. To do so, synchrotron facilities typically cover an area of several square kilometers and have a high operating cost. On the other hand, compared to laboratory-scale X-ray imaging, the high flux and partially coherent parallel beam produced in synchrotrons can generate higher quality images in a much shorter time, at an energy that can be easily tailored to the sample's nature and experimental needs. Monochromatization of the beam eliminates beam-hardening artifacts, a phenomenon linked to the selective attenuation of lower energy photons in a polychromatic beam. The partially coherent beam provides phase contrast, allowing very subtle structural changes in the sample to be detected [153]. Examples of this technique include imaging of live mice tissue at a voxel size of 1 micron [45].

Interaction of X-rays with matter X-rays interact with matter primarily in three modes: photoelectric, Compton and Rayleigh (fig. 4.3). The photoelectric effect refers to the phenomenon where an incident photon interacts with an electron of the inner shell of an atom. The photon disappears and the electron is ejected from its orbit. The electron absorbs all of the energy of the incident photon, minus the binding energy of the electron to the atom. Consequently there are two possibilities: i) A higher-orbit electron fills the hole with a simultaneous emission of a photon of energy corresponding to the energy difference of the two orbits. ii) A higher-orbit electron moves to the lower orbit and the energy liberated is absorbed by another higher-orbit electron [65].

In a Compton scattering (also known as incoherent), a photon collides with an electron. It then loses some of its energy and is deflected from its original direction. Finally a Rayleigh (known as either coherent or elastic) scattering, is a process where photons are scattered by bound atomic electrons and in which the atom is neither ionized nor exited. This process occurs mostly at low energies and for high atomic number materials in the same region where electron binding effects influence the Compton effect [65].

The relative contribution of the three effects varies depending on the energy of the incident photon. Below 100 keV, for elements other than water and aluminum, the photoelectric effect largely prevails being more than 80 % of the whole range of energies for elements with an atomic number larger than 40. The Rayleigh scattering is relatively constant with respect to energy and atomic number, accounting for 5 to 10 % of the total energy. Finally the Compton effect is important, especially at high energies and low atomic number elements [65].

These three interactions, when combined, they all contribute to the attenuation of X-rays of a material. This quantity is described by the X-ray attenuation coefficient and it is noted μ. The attenuation of X-rays follows the Beer-Lambert law and it can be derived by the following way: The number of absorbed and scattered photos of a beam dI in a thin slice of matter, ds, is proportional to

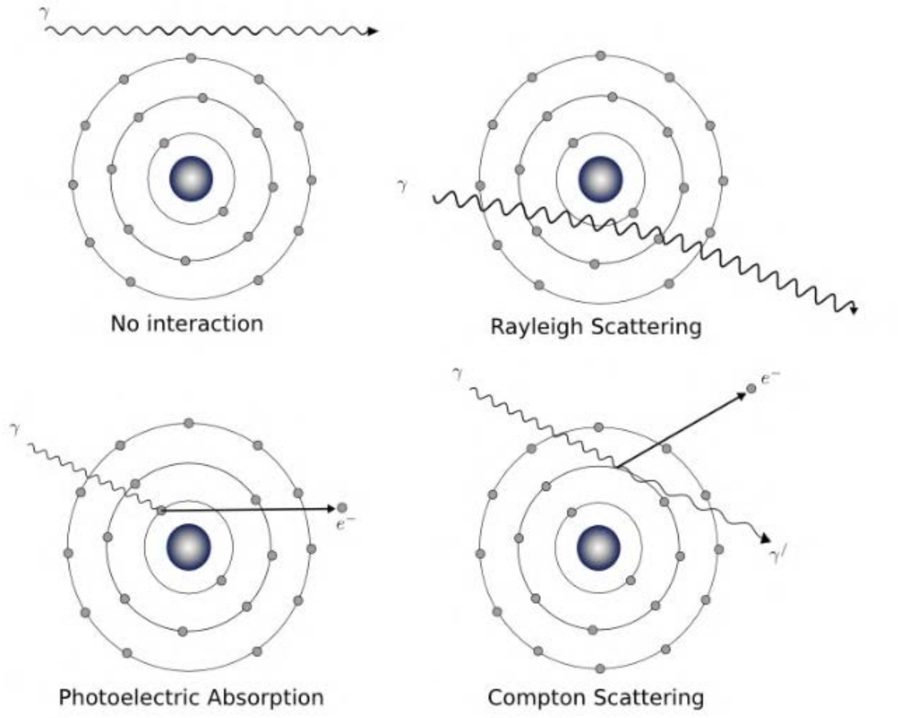

Figure 4.3: Main principles of X-ray/matter interaction. Image taken from [31].

the intensity I_s of the beam in this particular slice [41]. Mathematically, this reads as:

$$\frac{dI}{ds} = -\mu I_s \tag{4.1}$$

The solution to the differential equation is

$$I_s = I_0 \cdot e^{-\mu s} \tag{4.2}$$

where I_0 is the initial number of photons and s is the thickness of the material. The principle of X-ray imaging is based on the difference of X-ray attenuation of the different materials that comprise the sample. The degree of attenuation depends on the atomic number of the material, the density, the photon energy and the material thickness Birkfellner [41]. According to equation 4.2, this effect is not linear but exponential.

4.3.2 3D image reconstruction

In a typical, laboratory-scale X-ray tomography, 2D projections, also known as radiographs (fig. 4.4), are obtained when a cone-beam source emits X-rays that transverse the sample and the attenuated signal is captured by a detector (see fig. 4.4). The sample is then rotated by a small, fixed angle and the procedure is repeated until a full 360° rotation is achieved. In this way, projections from many different directions are recorded and a two-dimensional integral of attenuation is obtained.

Several algorithms have been developed over the years to reconstruct 3D volumes from two-dimensional projections, the first one proposed by Johann Radon in 1917. Johann's approach is an analytic method that is used until today and it is known as filtered backprojection (FBP) method. In the end of 1970s, the interest of the scientific community turned towards the study of incomplete data problems (e.g. limited-angle data) which gave birth to a family of methods, namely Fanbeam reconstruction methods. This approach had an iterative algorithm that resulted in accurate but computationally expensive solutions [83]. Recently, with the advances of artificial intelligence and machine learning, a novel approach has been developed where deep learning techniques, known as deep learning reconstruction (DLR) have been implemented to perform the 3D volume reconstructions of medical-related datasets [280]. The main strong-points of this technique are its high image quality, low radiation dose used to produce the 2D images and its fast reconstruction speed.

After 3D volume reconstruction, occasionally artifacts can be observed. These can be the result of physical aspects of the sample, malfunctions/limitations of the equipment, inconsistencies during the acquisition process or simply the nature of the X-ray beam. A brief list of the most common artifacts is given below [41]:

- **Partial volume effects** occurs when objects of very different attenuation coefficients are encompassed on the same CT voxel producing a voxel value that is proportional to the average value of these objects. This artifact usually appears as blurring of sharp edges.
- **Ring artifacts** are a consequence of local irregularities in detector sensitivity. This artifact is quite common and can be easily corrected.
- **Noise artifacts** are caused due to the low signal-to-noise ratio and result into grainy images. This can be fixed by adjusting the X-ray source tube voltage and current or by using a more powerful X-ray source.
- **Motion artifacts** are a result of a sample having moved during the acquisition process. This appears as a local blur or a streak on the reconstructed image. There are sophisticated algorithms that can partially correct this effect in a post processing step.
- **Beam hardening** refers to the phenomenon where a polychromatic X-ray beam passes through an object, resulting in selective attenuation of lower energy photons. In that sense, only the higher energy photons continue through the object and thus the mean beam energy is increased ("hardened"). This artifact is depicted as dark streaks in the image, originating from a high attenuating material. Since a polychromatic X-ray beam is a prerequisite for this artifact to occur, a synchrotron X-ray source can eliminate this effect.

4.3.3 X-ray imaging of biofilms in porous media

X-ray microtomography is a powerful tool that has gained attention over the past decade on the matter of imaging biofilms in 3D porous media. This technique enables the imaging of the biofilm structure and its spatial distribution within opaque 3D substrates in the mesoscale with a resolution of several micrometers. The main challenge stems from the fact that biofilms are primarily composed of water (estimated to be more than 80 % water [484]) and develop in aqueous conditions. X-ray imaging is based on the principle that different phases of a sample attenuate X-rays in a different way. Thus, the delineation of the biofilm phase and the liquid phase in between is a difficult task, given that both phases consist primarily of water. To surpass this limitation, the predominant approach is the use of a contrast agent to stain either the liquid or the biofilm phase to be able to differentiate one from the other.

Up to date several contrast agents have been proposed, such as barium sulfate, silver-coated microparticles, 1-chloronaphtalene or iron sulfate to enhance the contrast of the liquid phase, the biofilm or the interface between both. Even through each of these contrast agents has been used successfully, they all have a limited scope due to inherent limitations such as incomplete staining of the liquid phase, toxicity [191, 348], flocculation of the agent [61], biofilm detachment during agent ingection [100] and limitations related to the segmentation of the obtained x-ray images [186]. A more detailed review of each approach is given in part IV.

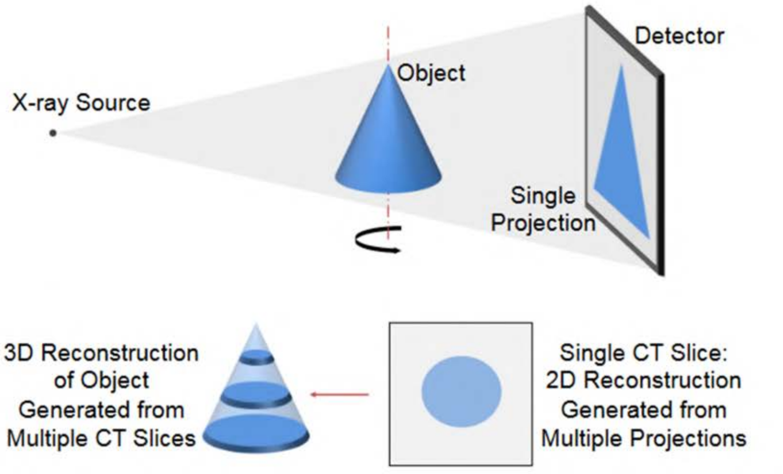

Figure 4.4: Basic principle of X-ray tomography [442].

Promising novel approaches A novel idea as a contrast agent, that has already been used in the medical field [57, 403] are ligand-coated gold nanoparticles (AuNP). Gold is known to have high X-ray attenuation coefficient [159] and through the functionalization of its surface [207, 211], it can be an ideal contrast agent for imaging biological tissues [207, 218], fluids [57] and potentially bacteria [145]. In order to selectively attach gold nanoparticles on the surface of bacteria, a careful selection of ligands should be considered. The cell-binding properties of Concanavalin-A (conA) are well known and studied [15] in the field of biology and when it is conjugated to a fluorophore such as rhodamine, it is used to stain bacteria. These cell penetrating properties of another protein, Trastzumab, are exploited in the work of N. Chattopadhyay et al. in order to selectively inject AuNPs in cells [70] and to induce their destruction through enhanced absorption of X-ray radiation. The protein was PEGylated using the bi-functional cross-linker OPSS-PEG-SVA resulting in a trastzumab-PEG-AuNP conjugate that was able to penetrate the membrane of the cells by specifically attaching to the HER-2 receptors and forming endosoms. Another protein that was used in the same manner is crotamin in the work of R. Karpel et al [207] where a similar conjugate of Crotamin-PEG-AuNP was synthesized using the same cross-linker OPSS-PEG-SVA so as to specifically target actively proliferating cells, such as tumor cells. A good example of functionalized AuNPs that are used in vivo to enhance the contrast in CT images is described in the work of P. Kee et al. [211] where gold nanoparticles were functionalized with the collagen-binding adhesion protein 35 (CNA35) rendering it a good contrast enhancer for vascular imaging of the coronary arteries by specifically targeting collagen within the myocardial scar.

4.3.4 Is there a need for a novel 3D biofilm imaging approach?

All the above mentioned contrast agent approaches appear to be designed for specific applications under well-predefined conditions and therefore they are adapted for their respective experimental setup. In addition, each contrast agent proposed, has its limitations, therefore there is no universal, one-size-fits-all solution. Considering the variability of biofilm types and that of porous media, there is a need of a wide range of application-specific contrast agents.

The choice of an appropriate contrast agent is a complex problem where several parameters need to be considered. The ideal contrast agent should fulfill several criteria. Firstly, the contrast agent should be specific to the phase that it is staining. In other words, the contrast agent should target only one phase of the system to be imaged and should be homogeneously distributed in that phase. In addition, a contrast agent should be chemically inert and biocompatible so as to not interfere with the biomass distribution within the porous medium during the image acquisition process, or alter the interface of the selected phase in any way. Furthermore, a contrast agent should provide adequate contrast. This can be translated as either having a high X-ray attenuation coefficient that greatly surpasses the absorption coefficients of the rest of the phases, or having a finely tuned attenuation coefficient that would allow for the differentiation of neighboring phases when the sample is imaged with a synchrotron source.

If a contrast agent can be designed in such way with the above mentioned parameters in mind, this would unlock novel biotechnological applications in 3D biofilm imaging. For example by selectively staining different parts of the biofilm matrix using contrast agents with varying attenuation coefficients, we could visualize different elements present in the EPS matrix in 3D, given that a monochromatic X-ray source (synchrotron) is used.

In this work we will evaluate the potential of a novel approach to the contrast agent problem by comparing well established techniques to newly designed contrast agents based on gold nanoparticles and further discuss its potential as a basis for the creation of "contrast agent libraries", tailored to the needs of specific applications.

5 Structure of the thesis

The main objective of this thesis was to develop and employ innovative experimental and imaging techniques to gain a deeper understanding of biofilm growth dynamics in porous media. Apart from the introduction (Part I) and the general conclusion (Part V), the thesis is divided into three main parts, each focusing on a different aspect of the research.

The following part (Part II) describes the development of a modular experimental setup for the study of biofilm growth dynamics in porous media. This setup includes an innovative 3D-printed bioreactor and a fluidic circuit with various measuring and parameter controlling units to monitor the biofilm growth dynamics. The setup allows for the real-time tracking of the evolution of differential pressure, permeability, O_2 consumption, and biofilm detachment events under controlled hydrodynamical environment using spectrophotometry and direct observation of the effluent stream using a camera. Measurements of a typical experiment are shown as a demonstration of a proof of concept for each element of the setup.

Part III focuses on the interplay of hydrodynamics and biofilm growth in porous media. Here, a deeper analysis of the previously obtained data is performed followed by an attempt to interpret the data and deduct conclusions regarding the dynamics of biofilm growth in porous media. X-ray micro tomography (µCT) and computational fluid dynamics simulations were used to gain a better understanding of the hydrodynamic environment within the porous substrate. X-ray tomography was performed with a well-established contrast agent protocol for 3D biofilm imaging to determine the spatial distribution of biomass within the pore space. Furthermore, CFD simulations were performed on a mesh extracted from these X-ray tomography datasets and on a mesh corresponding to an empty bioreactor, providing a better view of the fluid velocity and shear stress within the porous structure. Through further analysis, a correlation between these parameters and biomass distribution is suggested, indicating that biomass tends to develop in high shear areas.

Part IV investigates the potential of gold nanoparticles (AuNPs) as X-ray tomography contrast agents. Non-functionalized and functionalized commercial AuNPs were tested for their ability to stain biofilms and provide enhanced contrast in X-ray tomography. Initially, calibration tests were performed using non-functionalized AuNPs to determine and quantify the contrast given in X-ray tomographs and preliminary experiments were performed to asses their interaction with bacterial biofilms, suggesting that the size of the nanoparticles plays a major role in terms of diffusion within the biofilm matrix. Subsequently, the biofilm matrix's potential for selective and specific attachment was assessed by testing functionalized AuNPs through a sophisticated surface functionalization mechanism. The hypothesis was that these AuNPs would bind onto the biofilm matrix in a more targeted manner. The developed staining protocol included two steps. First, biotinylization of specific polysaccharides present on the matrix and then injection/interaction of the Streptavidin-functionalized AuNPs with these biotinylated sites. X-ray imaging revealed that these nanoparticles accumulate onto the biofilm matrix, providing an enhanced contrast relative to the one provided by the initially injected AuNP solution. Although this approach was successful in producing sufficient contrast to differentiate between the biofilm and liquid phases, the resulting biomass visualization indicated that the staining was not uniform throughout the entirety of the porous medium. Overall, the preliminary tests carried out in this study on the use of AuNPs as a contrast agent for X-ray imaging of biofilms have shown promising results. However, further and more extensive studies are required to fully understand the potential of AuNPs as a contrast agent for biofilm imaging in porous media.

Finally, the conclusion (Part V) of the thesis provides a global summary of the findings related to the biophysics of biofilm growth in porous media as observed through the presented experimental setup. It highlights the key factors influencing biofilm formation, discusses their implications for various applications, and suggests future research directions.

Part II

A novel experimental approach to study biofilm growth dynamics in porous media

6 Introduction

As discussed in chapter 2, developing biofilms within porous media is a crucial process in various natural phenomena, engineering, and medical applications. Biofilms can impact the properties of porous media by reducing pore size, inducing clogging and modifying local/global transport properties. Even though the impact of biofilm growth is well-observed, the underlying mechanisms, particularly with regards to the retroactive effect of fluid flow and biomass accumulation, are poorly understood. Research in these areas is limited by imaging in opaque 3D porous structures (as described in chapter 4) as well as by the complexity of these phenomena, which are difficult to experimentally reproduce and monitor.

Micromodel technologies have long been used in biofilm process engineering [205, 272, 478]. The advent of miniaturized systems offers new opportunities for rapidly testing new concepts in the field and creating tools to explore fundamental mechanisms [357]. Through such technologies, researchers have been attempting to replicate the complex nature of biological systems, either partially or wholly, in laboratory settings. This has been achieved through a reductionistic approach that is commonly used in research, as well as through more recent attempts to create models that approximate the most realistic behavior [171, 308]. These endeavors have resulted in a diverse array of bioreactor systems that are currently accessible [94, 139, 171].

In this section of the thesis, we present a novel porous micromodel technology for bacterial biofilms under flow, which can be used to explore a broad range of three-dimensional geometries and topologies of pore networks. Our approach relies on a "lego-like" design and a range of 3D printed modules that can be conveniently assembled as needed for a specific experiment. The central module is a micromodel containing a 3D printed porous medium for biofilm growth. High resolution 3D printing allows us to create arbitrary porous media with controlled architectures including flow channels with a diameter down to several hundreds of micrometers. The micromodel is instrumented to measure the differential pressure across the porous medium, oxygen consumption, optical density at the effluent stream and images of biofilm detachment through monitoring of the effluent using a camera. We show how this system can be used to study the dynamics of growth and detachment of a biofilm of *Pseudomonas aeruginosa*.

We will begin by addressing fundamental questions, such as whether a new experimental setup is necessary (6.1) and discussing its characteristics (6.2-6.4). Next, we will present each instrumentation module of the setup individually (7.1) before shifting our focus to the technical characteristics of the bioreactor itself (7.2). In chapter 8, we will introduce the various data analysis methods that were used on the data obtained from the experimental setup, including differential pressure, oxygen, spectrophotometric, and camera measurements. In chapter 9, we will delve into the advantages of the setup, as well as the difficulties and limitations encountered during experimentation. Finally, chapter 10 will conclude with a brief summary and discuss potential future directions for the research.

6.1 Why do we need a new experimental system?

Hydrodynamics have a significant impact on the distribution and morphology of biofilms within porous media, as discussed in the previous chapter. The presence of biofilms also affects the flow paths and transport of mass and momentum through the porous structure [49, 239]. However, the underlying mechanisms governing this process are not well understood, primarily due to experimental challenges [420].

To study the influence of hydrodynamics on biofilm development in porous media using experimental setups, it is necessary to consider multiple parameters that combine biological features such as nutrient availability, substrate properties, and bacterial strain type with mechanical aspects like flow rate, pore size, and shear stress. Controlling this wide variety of parameters at once has proven to be challenging [420, 472]. Most of the time, the difficulties stem from the fact that biofilm growth is quite sensitive to small environmental changes [144, 303] and therefore, in order to properly study biofilms, precise control of the growth parameters is vital. Examples include the tendency of bacteria to move towards the nutrient source (chemotaxis) [102], which has potential consequences such as sensor fouling, perturbating the performed measurements and/or changing the nutrient profile that reaches the designated growth region of the system. Therefore, a new experimental system could provide more precise control over these parameters and enable a more thorough investigation of the effects of hydrodynamics on biofilm development.

6.2 Why miniaturized system?

Miniaturized fluidic systems have several advantages for studying bacterial biofilms. One key advantage is that they offer a high level of control over microenvironments, which can be varied in space and time to mimic a variety of conditions, enabling more accurate and reproducible results [205, 357, 477], making it easier to compare results across studies and experiments. These systems can also be combined with molecular biology and optical microscopy to visualize processes from the cellular to the biofilm scale [119]. Moreover, miniaturized fluidic systems offer a relatively cheap and reproducible way of parallelizing, testing new concepts, and optimizing processes before scaling up for applications in biofilm engineering [272, 308]. For example, microfluidic reactors have been used to assess the efficacy of newly constructed organisms [43], to develop portable biomanufacturing platforms [318], to screen microbial strains for fermentation processes [171, 371], and to test antibiotic susceptibility and toxicity [334]. Some miniaturized fluidic systems can also enable high-throughput screening of biofilm formation under various conditions, identifying factors that promote or inhibit biofilm formation [389]. These systems can be coupled with microscopy or other imaging techniques, enabling real-time monitoring of biofilm growth and development, providing valuable insights into the dynamics of biofilm formation [8]. Finally, miniaturized fluidic systems require smaller volumes of fluid to culture biofilms, reducing the amount of sample needed and the potential for contamination. This can be particularly useful when studying either rare or difficult-to-culture bacteria, as well as when performing experiments over long periods of time.

6.3 Why 3D?

Even though standard microfluidic approaches, in particular PDMS micro-patterning, have proven a powerful tool in studying biological objects such as biofilms, they also have limitations. One important limitation is the geometrical constraint and the level of confinement placed upon the microorganisms. Most systems use quasi-2D geometries with a strong confinement in the Z-direction, with a depth that rarely goes beyond 100 micrometers. This limitation is partially the consequence of the fabrication processes used in microfluidics that use planar micro-fabrication technologies which has important consequences. The geometry and topology of a structure constrained into a plane is very different from that of a 3D porous medium, which leads to fundamental changes in flow and transport properties [25, 33, 177, 385]. For example, dimensionless numbers such as Reynolds and Damköhler numbers, which characterize the nature of the flow and transport phenomena, depend upon a characteristic length scale. The confinement in Z is thus associated with strong constraints upon the regimes accessible through microfluidics, for example simple flows at low Reynolds number in PDMS chips only generate a narrow range of shear and pressure stresses that is not representative of the heterogeneity found in many porous media. Furthermore, the nature of mixing, even at low Reynolds numbers, is intrinsically different from 3D systems, especially those with random geometries, due to the topological complexity [448]. This complexity affects the flow and transport dynamics. It has been established that this complexity generates chaotic advection due to a 3D fluid mechanical analogue of the baker's map. Simply put, advection in 3D porous media promote rapid scalar mixing in the presence of molecular diffusion [253]. Therefore, pore-scale mixing is governed by 1) chaotic advection 2) molecular diffusion and 3) a broad distribution of fluid velocities that arise from the non-slip boundary condition at pore walls. Recent experimental studies have evidenced that creeping flow in 3D porous media generates chaotic mixing, while 2D geometries such as those used in standard microfluidics do not [254]. In addition, it has been generally observed that the increased complexity of two- or pseudo-three-dimensional systems can result in lesser permeability reductions, presumably due to the possibility of flow around biofilm-clogged areas [428]. Through direct observations and simulations, it has been indeed observed that flow is diverted around biofilm clogged areas [378].

6.4 Why 3D printed?

As detailed in the previous chapter, 3D printing offers several advantages over traditional manufacturing methods of bioreactor fabrication. One significant advantage is the ability to create complex geometries using 3D modeling software with high precision and accuracy, including channels, chambers, and other features [9, 297]. This feature enables the creation of 3D scaffolds adapted for our application, notably the study of bacterial biofilms in porous media, approaching and mimicking the complexity of natural systems where biofilms develop. Additive manufacturing techniques such as 3D printing can achieve sub-millimeter accuracy in creating features, down to 10-50 microns, enabling precise control of fluid flow and mixing in microchannels [346]. This leads to improved functionality and efficiency the device, reduces sample and reagent usage, and improves the reliability and reproducibility of experimental results. In addition it allows for direct integration of connectors which is a common bottleneck in microfluidics [437]. Furthermore, reproducibility enables the optimization of device design through rapid and inexpensive prototyping, reducing the potential for human error and variability in device fabrication [141]. Finally, 3D printing facilitates the integration of multiple functionalities and components into a single device, increasing overall functionality and ease of use [80].

7 Description of the experimental setup

Every component of the proposed experimental setup has been meticulously chosen and developed to address the scientific questions being investigated. It should be noted that the arrangement of the modules that comprise the presented experimental setup can take many forms according to the needs, here we will focus on one configuration, adapted for the study of biofilm formation in porous media. In order to properly present the system, we will begin by outlining the fluidic circuit in its entirety, with an explanation of the role of each component and we will continue with the details of the central part of the setup, that being the 3D-printed micro-bioreactor.

7.1 The fluidic circuit

7.1.1 General description

Figure 7.1 shows a schematic of the experimental setup. Multiple bioreactors can be run in parallel, although one example of the circuit is displayed in the figure for clarity. The setup includes a UV-C illuminated and constantly oxygenated water tank that continuously supplies deionised water to the bioreactor through the use of a micro- annular gear pump that provides a constant flow throughout the experiment. A second gear pump delivers the necessary nutrients from a sterilized glass bottle to the bioreactor. The 3D-printed micro-bioreactor that contains the porous medium has been designed to accommodate the water, nutrient and biocide inlets as well as bubble traps and differential pressure sensors. The system is equipped with sensors that monitor the dissolved oxygen at the inlet and at the outlet of the bioreactor. A spectrophotometric flow cell is placed at the end of the effluent tube in order to perform absorption measurements. A transparent flow cell, thereafter called 'camera cell', is installed at the effluent stream to directly observe biofilm patches that are flowing out of the system. A third gear pump is constantly supplying a biocide solution at the outlet of the bioreactor in order to protect the oxygen sensor, the spectrophotometric and the camera cells from biofouling due to their positions in the circuit. To ensure that biofilm growth remains limited to the porous medium, two quartz windows were installed at the inlet and outlet of the micromodel. These windows are constantly illuminated with bactericidal UV-C light, which is provided by either a UV-C lamp or UV-C LEDs.

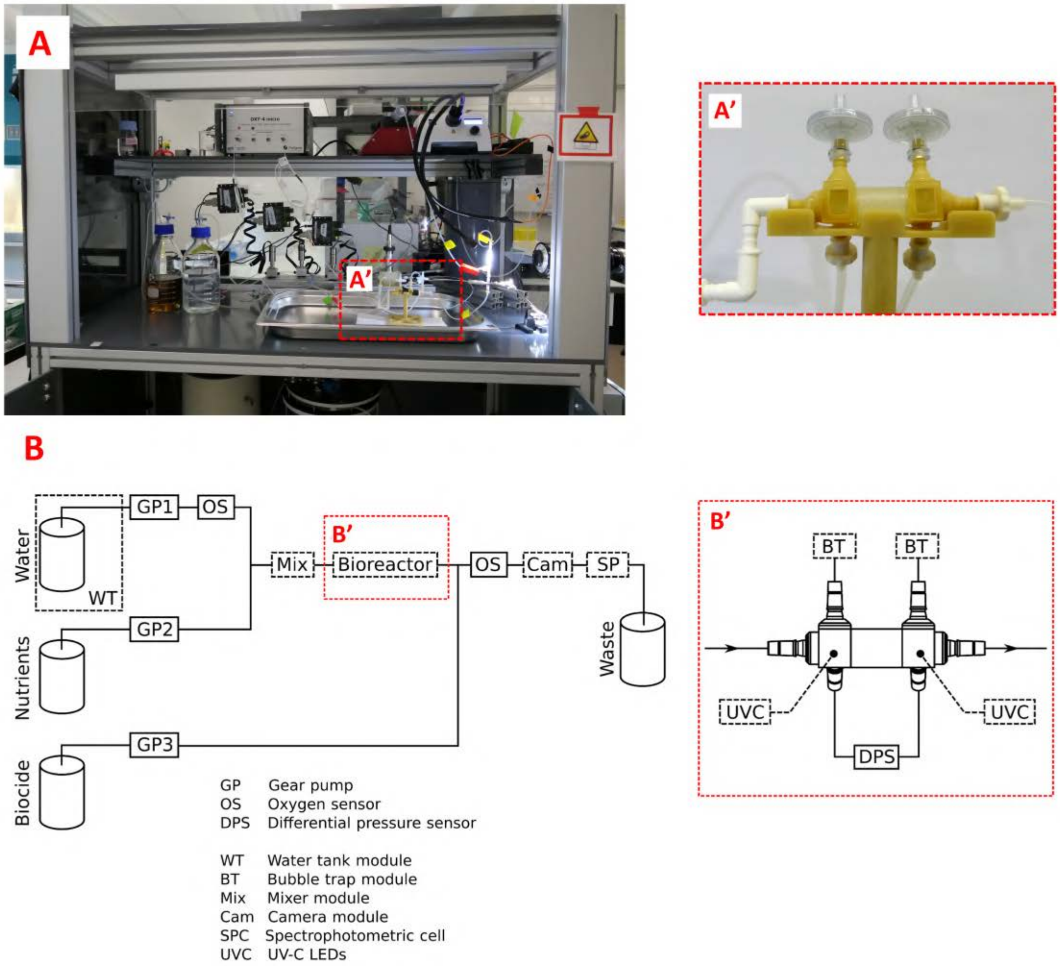

Figure 7.1: Fluidic circuit of the experimental setup. Figure (A) depicts the overview of the experimental setup within the three-storey homemade workbench. The inset (A') is a zoomed in view of the bioreactor mounted on a 3D-printed support showing a potential configuration. The schematic of the fluidic circuit is shown in figure (B). Flow is induced by three gear pumps that are constantly supplying the system with water and nutrients at the inlet of the bioreactor and a biocide solution at the outlet of the bioreactor. The additional boxes indicate the positioning of the various measuring devices within the circuit. Inset (B') shows a detailed view of the bioreactor and the configuration used for the biofilm growth experiments.

The water and the nutrient streams are mixed just before entering the bioreactor to prevent biofilm formation. It is a common issue in biofilm experiments that contaminations occur in areas where they should not, for example before the bioreactor in the circuit. Previous experiments showed that contaminations can occur up to the point where the nutrients and the water stream are mixed. The main reason why biofilms tend to spread earlier in the circuit is mainly due to chemotaxis (among others e.g. rheotaxis) where bacteria swim against the flow towards a higher chemical gradient. This results in fouling the various measuring devices and sensors such as the oxygen sensors which might give wrong readings. For this reason, the inlet-oxygen sensor is placed before the mixing of the nutrients with the water stream and also the mixing is taking place as close to the bioreactor as possible. In addition, contaminations earlier and later in the circuit can alter the hydrodynamic conditions of the fluid flow, for example biofilm grown at the inlet compartment of the bioreactor can create preferential flow paths before the area of interest, that being the porous medium.

The presence of bubbles can lead to erroneous measurements of differential pressure, oxygen concentrations and absorption signal. Moreover, if air flows in the porous medium or gets trapped inside the porous structure, it can promote biofilm detachment or alter the hydrodynamic conditions by changing the flow paths [100, 196, 269]. Therefore, the elimination of air bubbles is essential in order to ensure the quality of the experimental results. For this, two bubble traps have been installed before and after the porous medium. These bubble traps are essentially hydrophobic PTFE membrane filters that allow for the bubbles to naturally float upwards and be evacuated by passing through the membrane, without letting the liquid phase escape the fluidic circuit.

The whole experimental setup was placed in a homemade, 3-storey workbench that was designed by the IMFT design department, in particular Julien Lefort and Emmanuel Libert. The three compartments accommodate the different parts of the experimental setup according to the different needs. In the bottom compartment, the water tanks as well as the waste tanks are placed. On the outer side of the lower storey, an electrical box is there to control the supply of electricity of the UV-C lamps, but also regulate the illumination times. The second, and main, compartment, held the bioreactor, the gear pumps, the oxygen and pressure sensors, the spectrophotometric and camera cell, and the nutrient and biocide flasks. Finally, the upper compartment contains the control unit of the oxygen sensors, the spectrophotometer and the light source used for the absorption measurements and image acquisition.

3D-printing For all the 3D-printed parts of the experimental setup, two different methods of additive manufacturing have been extensively used. For the porous medium and several other parts, the SLA also known as stereolithography technique was used. The process includes a UV laser as a light source to selectively cure the polymer resin that is initially in a liquid form. For this, the DWS 29J+ 3D printer was used that is located in LAAS (Laboratory of Architecture and Analysis of Systems). Regarding the porous medium, the commercial name of the resin used for this part is DS3000. It is a semi-transparent, acrylic resin used originally for dental transplants and that has been proven to be an ideal 3D scaffold for growing biofilms due to its biocompatibility. For the spectrophotometric cell and the camera cell, the resin DL260 was used. This resin is an acrylic based polymer mixed with silica and aluminum oxide and, when photopolymerized, provides pieces with a higher surface hardness than DS3000. Furthermore, this resin is opaque, a property that is exploited specifically for the spectrophotometric cell where stray light should be eliminated.

The combination of the printer and these resins offers a relatively high resolution of 30 to 40 µm in the X and Y direction and 10 to 100 µm in the Z direction. At the end of the printing process, the pieces need to be post-treated and more specifically to evacuate the unpolymerized resin located in the crevices by using a mix of organic solvents such as isopropanol and ethanol in the case of DS3000 and acetone in the case of DL260. A combination of washing by using a syringe to displace the resin located in the micro-sized pores and a sonication bath, facilitates the process. For the case of the DS3000 porous media, an extra step of post processing is required where the pieces are exposed for half an hour under 405 nm light. During this step, any leftover resin is polymerized which diminishes the surface cytotoxicity caused by unpolymerized resin.

A second additive manufacturing method, known as multi jet printing (MJP) has been used for the bulkier pieces of the experimental setup. In this case, the printer ProJet MJP 2500 Plus (3D systems) located at IMFT was used with an ABS-like material as the main material (VisiJet M2R-TN) and a support resin that is removed in the post-processing step (VisiJet M2 SUP). This technique offers the advantage that larger pieces can be fabricated with relatively lower precision (32 µm per layer). The printer uses a wax scaffold to support free-hanging structures that is removed in an oven at 80 °C during the post processing step. Further cleaning can be achieved by short ultra-sound bath cycles in warm water. The whole thermal dewaxing procedure can last up to three days depending on the complexity of the structure. A base was fabricated to keep the bioreactor in place in a horizontal position throughout the experiment (fig. 7.1). The form of the base is such that it fits perfectly around the body of the bioreactor and therefore ensures that it stays in place. The dimensions of the base were carefully calculated so that the quartz windows of the bioreactor are perfectly aligned with the bactericidal UV-C LEDs.

All the above mentioned 3D models were designed using the computer-aided design (CAD) software SolidWorks v2016 of Dassault Systems, a well established software in the mechanical engineering domain.

7.1.2 Gear pumps

For all the experiments, three gear pumps are used to supply the different liquids/solutions to the bioreactor. Most experiments concerning biofilm growth in the meso-scale use either peristaltic pumps [61], drip-fed columns [434] or pressure driven pumps [245]. Drip-fed columns is an easy way of roughly regulating the flow without the need for any special device but it is not adapted for our application since the flow rates should be precisely controlled in a closed-aseptic environment. Peristaltic pumps use flexible tubing fixed in a circular casing where a rotor periodically compresses the tube in order to induce the fluid flow. This technique traditionally produces oscillations in the flow rate.

A similar principle, but improved version of peristaltic pumps in respect these fluctuations, are the gear pumps, which were also used in this experimental setup. These pumps generate a low pulsation, highly precise flow. They dispense at a high precision the lowest volumes in micro-liter range. These pumps are suitable for dosage of low viscosity liquids such as deionised water, watery solutions, methanol, solvents, oil and lubricants.

The operation principle of the gear pumps is as follows. The pump contains two eccentrically-mounted rotors. Both rotors, are intermeshed with their cycloid gearing. As a result a system of several sealed pumping chambers exists at all times. With a tooth ratio of 6 to 7, the resulting number of chambers is six (fig. 7.2). The shaft of the micro annular gear pump is connected to the internal rotor and is powered by a precisely controlled electric motor. The external rotor is mounted and is driven by the internal rotor. As the rotors turn around their offset axes, the volume of the pumping chambers increases on the induction side and simultaneously decreases on the delivery side of the pump. A homogeneous and low-pulsation flow rate is generated between the kidney-shaped inlet and outlet which also combines several pumping chambers at the same time. The pump's conveying direction is reversible.

Two different types of gear pumps were used, each with an adapted flow rate range according to the needs of the supplied stream. For the water stream, the pump that is used (mzr-2921x1, HNP Mikrosysteme) could provide a flow rate from 0.03 up to 18 mL/min. For the nutrients and the biocide stream, the two pumps (mzr-2521x1, HNP Mikrosysteme) could provide a flow rate range of 0.15 - 9 mL/min. The lower values of both ranges could only be achieved with adequate precision only with a special module that is provided by the manufacturer. For the mid to high range, the precision is 1 % CV (coefficient of variation). These pumps can work within a differential pressure range of 0 - 3 bars for the mzr-2921x1 and 0 - 1.5 bars for the mzr-2521x1, liquid temperature range of -20 to 60 °C and viscosity range of 0.3 - 100 mPa·s. The interior mechanism of both types of pumps is made out of wear-resistant tungsten carbide while the main body is made of graphite-reinforced PTFE. Both of the materials appear to be inert when in contact with all the liquids used in this setup.

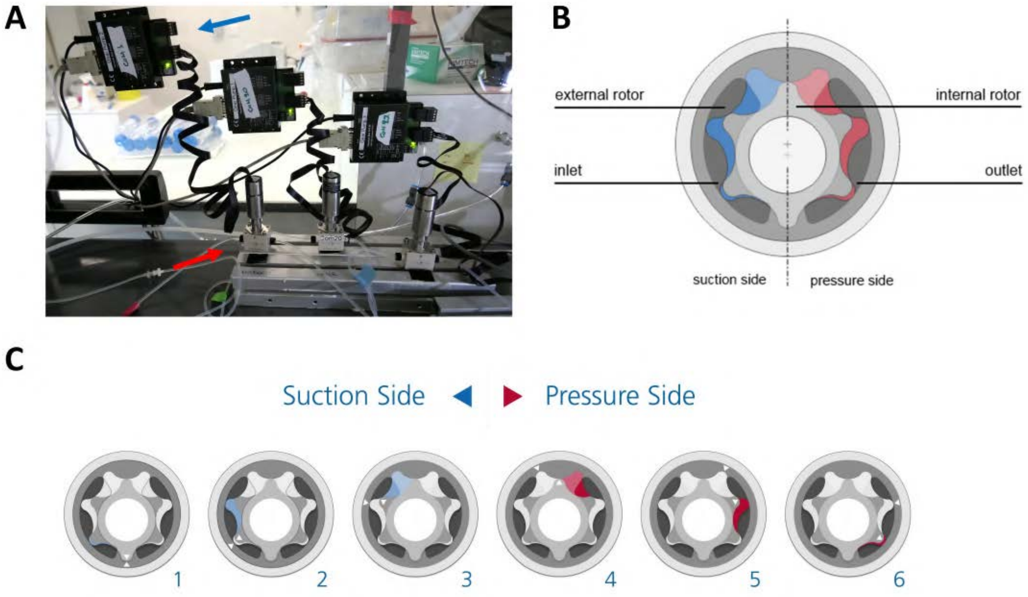

Figure 7.2: (A) Three gear pumps connected to their control units (mzr-2521x1 and mzr-2921x1, HNP Mikrosysteme). Red arrow indicates one of these pumps which is connected to a control unit indicated by the blue arrow. (B) Internal components of the gear pump. (C) Operation principle of micro annular gear pumps. Note in the figure that the arrows indicate the position of two teeth of the inner and outer rotors, highlighting their difference in phase during operation.

7.1.3 Water reservoirs

The water reservoirs were designed and constructed at the laboratory. Each one consists of a 70 cm transparent Lexan tube of internal diameter of 20 cm which translates to roughly 20 l of stored water. This allows for an experiment at 2 mL/min to run for more than three days without the need for a refill. In order to prevent contaminations, the tank is equipped with a bactericidal UV-C lamp which continuously irradiates UV-C light throughout the whole experiment. The Lexan material was specifically chosen for its resistance to UV light. The lamps are working at 16 W (from UV-technik GmbH), satisfying by far the required 10.5 μW/s·cm^2 for the germicidal effect to take place.

The amount of oxygen provided is enough to reach over-saturation level in the water. Normally fresh water can withhold about 8.5 mg/l of dissolved oxygen at 25 °C. Temporarily, oxygen concentrations can go higher than the saturation point, but since this is a thermodynamically unstable state, oxygen concentration will gradually fall back to the saturation value. To make sure that oxygen concentrations are relatively stable at the bioreactor's inlet, a mixture of pressurized air and oxygen is bubbled through a ceramic stone placed inside the tank. The provided mixture over-saturates the liquid in oxygen but the oxygen-permeable, silicon tubing that is used to transfer the water from the tank to the bioreactor, is long enough to allow excess oxygen to diffuse out of the circuit. The oxygenation of the water tanks is performed one day prior to the launching of the experiment for about one hour. By letting the water to sit for an hour, we make sure that the amount of dissolved gas in the liquid will reach an equilibrium. To make sure that oxygen concentration is homogeneous in the bulk of the liquid, a small aquarium pump is used to continuously stir the ultra-pure water.

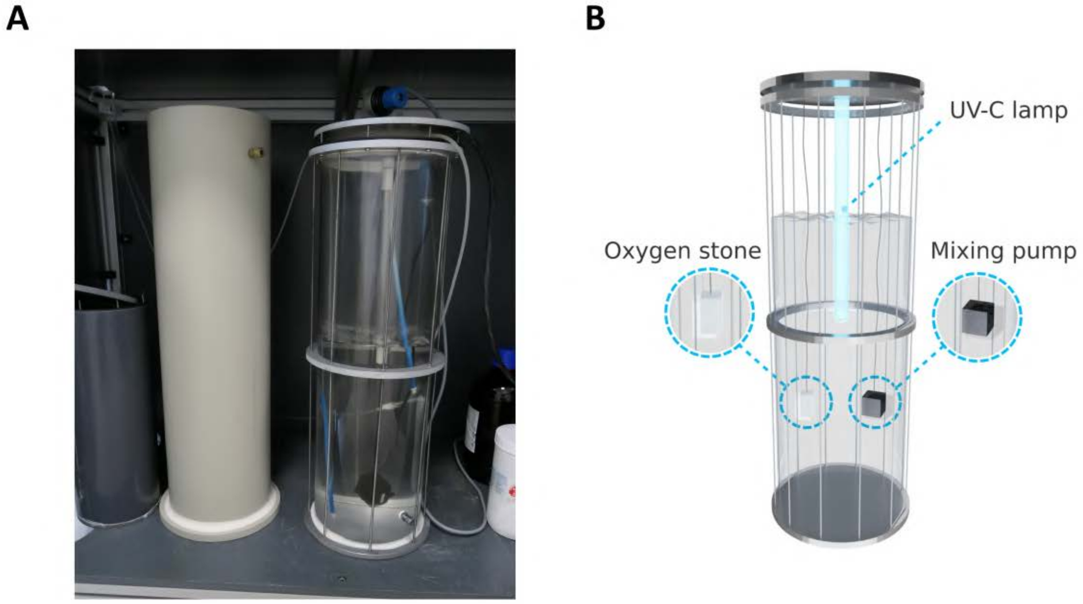

Figure 7.3: (A) The waste and the water tank. (B) The 20 L water tank is equipped with a bactericidal UV-C lamp, O_2 bubbling and constant stirring.

7.1.4 Differential pressure sensors

The differential pressure sensors (Series PD-33X, Keller) (fig. 7.4) have a single silicon diaphragm in their interior, which is pressurized from both sides and measures the pressure difference directly. This design enables them to measure small pressure differences even at an extremely high line pressure. The transmitters use digital compensation with a mathematical model to achieve accuracy of 0.05 % FS (percentage of full scale) – in the temperature range from 10 to 40 °C. The device is also measuring the ambient temperature. The pressure sensors were cleaned with soap and disinfected with ethanol before and after each experiment.

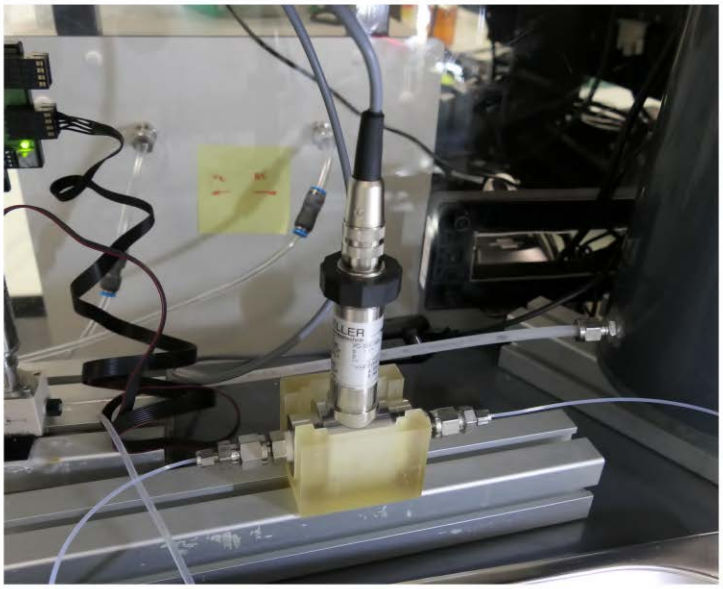

Figure 7.4: The differential pressure sensor (Series PD-33X, Keller).

7.1.5 Dissolved oxygen sensors

To probe the oxygen consumption of the bacteria within the porous medium, two O_2 sensors were used (FTCH-PSt1, Presens), one before the porous medium, that was measuring the dissolved O_2 levels in the water stream, and one after the porous medium, measuring O_2 levels of the effluent stream after the biocide injection. The oxygen sensors are housed in a flow-though cell shaped like a T-cell (fig. 7.5). The volume inside the cell is about 310 µL, the O_2 measurement range is from 0 to 22.5 mg/l of dissolved O_2 and the resolution of the measurement is dependent on the oxygen concentration. For the oxygen levels measured in this work, the resolution of the probes is about ±0.04 mg/l. Inside the cell, the sensor's tip is located. This tip has a diameter of less than 50 µm, on the edge of which, there is a membrane with a luminophore.

The operation principle is based on the effect of dynamic luminescence quenching by molecular oxygen (fig. 7.5). In the absence of oxygen, the control unit, emits light at 633 nm that is directed to the sensor tip through a glass fiber. The luminophore is briefly in an excited state due to the absorption of the light and eventually releases the additional energy in the form of light of different wavelength, putting it back to its ground state. In the presence of oxygen, the interaction between the luminophore in its excited state and the quencher (oxygen) results in radiationless deactivation, a process that is called collisional or dynamic quenching. After collision, energy transfer takes place from the excited indicator molecule to oxygen which consequently is transferred from its ground state (triplet state) to its excited singlet state. As a result, the indicator molecule does not emit luminescence and the measurable luminescence signal decreases.

Prior to commencing with the experiments, the oxygen sensors were calibrated by performing a two-point calibration. A 100 % saturated oxygen solution was prepared by bubbling pressurized air into a bottle filled with 100 mL of DI water for 15 minutes and then the solution was left with an

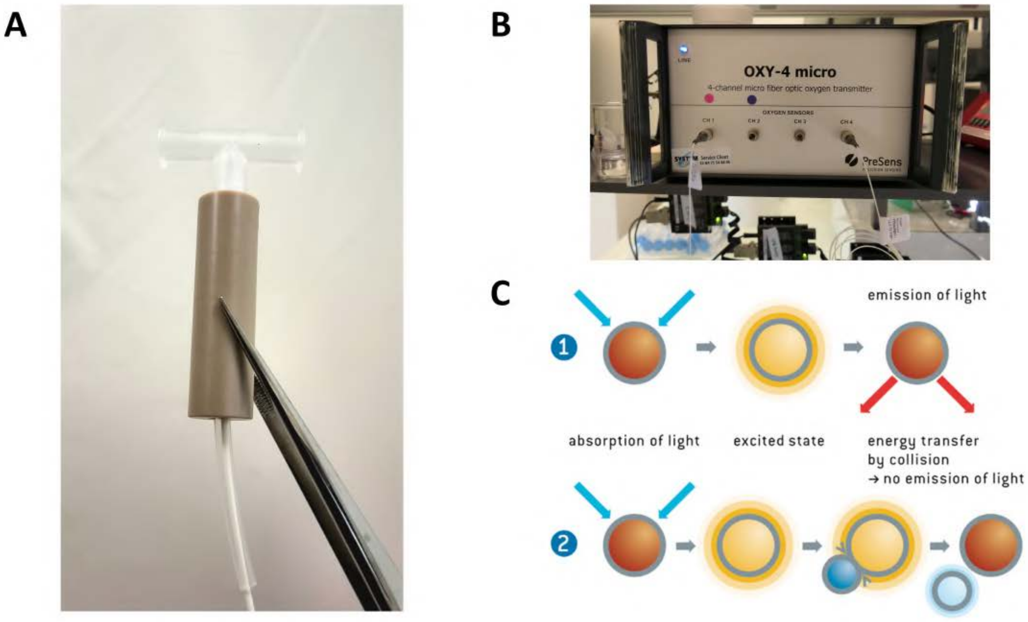

Figure 7.5: (A) The T-shaped, flow-through, oxygen probe (FTCH-PSt1, Presens) (B) The 4-channelled control unit of the oxygen sensors (C) Principle of dynamic quenching of luminescence by molecular oxygen: (C1) Luminescence process in absence of oxygen (C2) Deactivation of the luminescent indicator molecule by molecular oxygen.

open lid under magnetic stirring to ensure that there is no over-saturation in oxygen. An oxygen-free water solution was prepared by dissolving 1 g of sodium sulfite (Na_2SO_3) and 50 µL of cobalt nitrate solution (500 mM $Co(NO_3)_2$ in 100 mL of water. The bottle was closed and shaken for several minutes to dissolve the sodium sulfite and ensure the water is oxygen-free.

7.1.6 Spectrophotometric cell

Spectrophotometric measurements of fluid streams provide information about the contents of the stream, for example to measure the optical density of a stream loaded with biomass, perform tracing tests with colored dyes through the system to study the hydrodynamic properties such as retention times and breakthrough curves, or use it to detect solid/semi-solid objects passing through the stream. In this work, the spectrophotometric cells are mainly used to study the biofilm detachment events by detecting biofilm patches that flow through the effluent stream of the bioreactor.

The module consists of two OceanOptics spectrophotometers, a temperature regulating unit, two 3D-printed cells and a Zeiss light source with two outlets. After the 3D printing of the cells, two quartz glasses are mounted on each one of the cells, on each side of the main flow channel using a UV-C cured glue (fig. 7.6D). The printed part also features threaded luer connectors on each side to easily integrate to the fluidic circuit as needed. The cells are designed to have a light path of 20 mm. The light source was originally destined to be used with a Zeiss microscope to perform brightfield imaging and therefore the light intensity was not perfectly constant for the time scales used for our experiments (3-4 days) and therefore, continuous spectrophotometric measurements would be erroneous. Two procedures were implemented to ensure the stability of the light source intensity prior to each experiment. Firstly, the light source was turned on for an extended duration prior to the experiment to allow for stabilization. Secondly, the intensity of the light source was directly measured in parallel with the spectrophotometric measurements of the effluent stream. In order to accomplish that, the configuration of the setup was as follows: two 3D printed cells were used one on each outlet of the light source. For each cell, the optic fiber of the spectrophotometer is fixed on the one side of the cell, while the tip of the light source probe is placed on the other side (fig. 7.6E). One cell was connected to the fluidic circuit to be measured for its OD while the other one was directly measuring the light intensity of the source without being connected to the fluidic circuit. Like so, the signal obtained from the reference cell, is used as a baseline for the calculation of the absorption, eliminating any erroneous signal due to source light intensity fluctuations.

In an effort to further stabilize the spectrophotometric measurement signal, a secondary fluidic circuit was implemented in order to control the temperature of the spectrophotometers since it was observed that temperature has an important effect on the measured light intensity (fig. 7.7).

This fluidic circuit consisted of a thermoregulated water bath (Heto CBN 8-30), a series of tubing, four aluminum heat exchange plates (Kafuty) and a homemade set of thermocouples. Each of these plates measured 40×80×12 mm and four of them were used to sandwich the two spectrophotometers as in plate:spectrophotometer:two plates side by side:spectrophotometer:plate (see fig. 7.6A) . The plates were connected in series to the temperature regulated water bath through a series of tubes. The bath, that had a capacity of 8 liters of water, was set to keep the temperature constant at 15 °C. The flow rate of the water was manually regulated through tighting and untighting a valve and therefore no precise flow rate was set. The temperature of each spectrophotometer was obtained by attaching two thermocouples on each device. A thermal paste was applied to ensure contact between the device and the thermocouple. The variation of the temperature appeared to be less than half a degree Celsius which is appears to be insignificant for this specific application as we will see later on (fig. 8.3).

For the acquisition, the light intensity of the source was fixed so that the received light does not over-saturate any of the two spectrophotometers. The light sources appeared to be rather too powerful for the sensitivity of the spectrophotometers, saturating the measuring devices even at the lowest intensity setting of the source and the lowest exposure time setting for the photometers. Therefore an additional optical density filter (Neutral Filter 0.25OD, Zeiss) was mounted on the light source that would allow for approximately 56 % of the incoming light to go through and out of the source (transmission). The

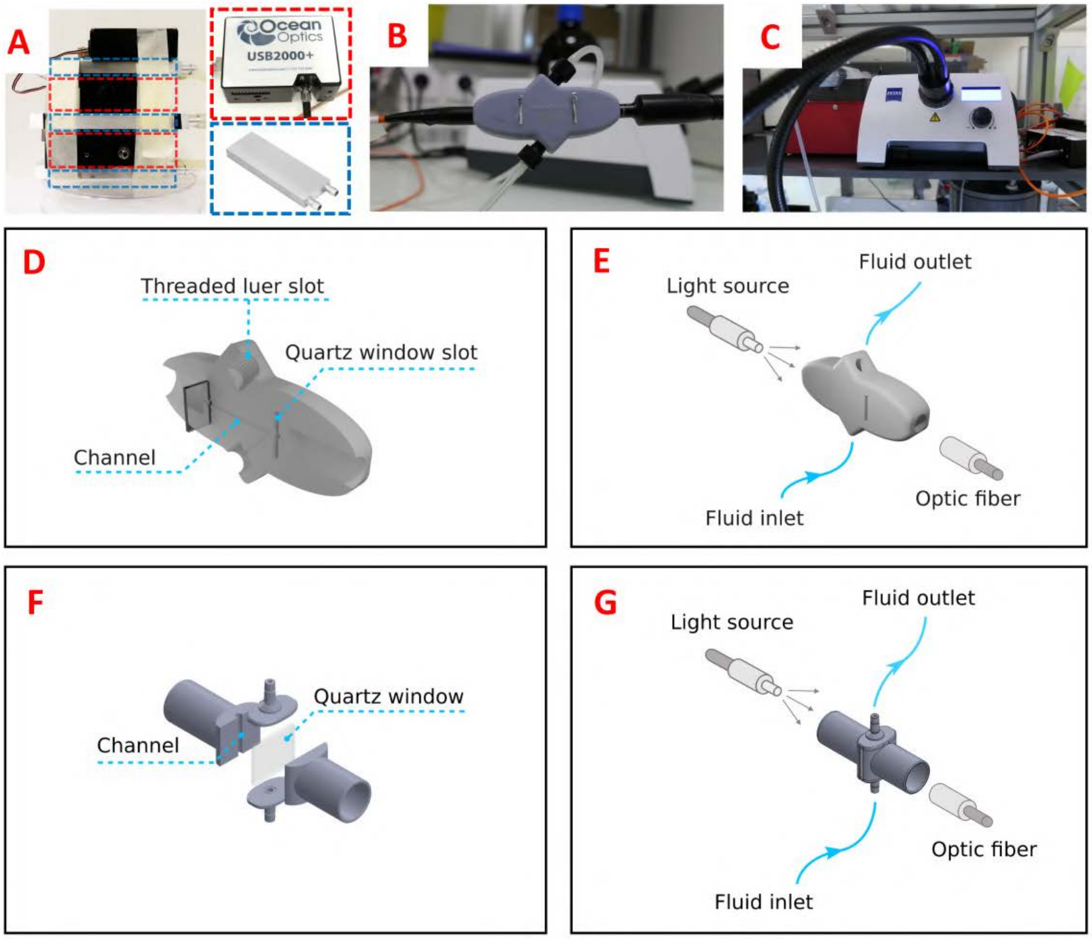

Figure 7.6: (A) The two ocean optics USB2000+ spectrophotometers used in the experimental setup nested in between three heat transfer plates. (B) The 3D-printed spectrophotometric flow cell connected to the fluidic circuit (tubes on the top and the bottom) with the optic fiber of the spectrophotometer attached on the left side and the lightsource outlet on the right side. (C) The white light source that was used in the experimental setup was a Zeiss CL 9000 LED light. (D) Internal structure elementes of the 3D-printed flow cell used for the spectrophotometric measurements. (E) Schematic of the configuration of the spectrophotometric cell module. (F) and (G) present an alternative design of the spectrophotometric cell with a light path of 1 mm. This design was not used for the following experiments.

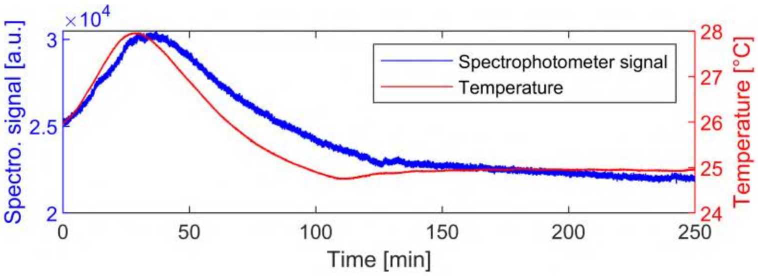

Figure 7.7: Preliminary test for thermoregulation of spectrophotometers. The spectrophotometer's signal is following the trend of the surrounding temperature with a small lag. For this test, the lightsource signal was directly measured without any obstacles on the lightpath.

light intensity was recorded at approximately 0.1 s interval with no averaging of the values, a boxcar width of 10, at 600 nm wavelength.

Alternative designs of the spectrophotometric cell were used and tested in this study. The design chosen that is described above, which has a path length of 20 mm was selected for its ability to effectively capture biofilm patches that passed through the cell due to its high retention time. Another design with a very short light path length of 1mm was developed for OD measurements on the effluent stream (fig. 7.6F,G). This configuration minimized the impact of particles passing through the cell, due to the short retention time. However, the short light path resulted in overexposure of the light, making it unsuitable for the sensors used in this study. Despite this limitation, the long path cell provided valuable insights into biofilm behavior, and the short path cell offered potential for future research under the appropriate conditions.

Both spectrophotometers were measuring the raw light intensity and the measured absorption was calculated later on according to the following equation.

$$A\left(t\right) = log_{10}\left(\frac{I(t) - I_{dark}}{I(t=0) - I_{dark}} \times \frac{I^{ref}(t=0) - I^{ref}_{dark}}{I^{ref}(t) - I^{ref}_{dark}}\right)$$

where $A\left(t\right)$ is the calculated absorption, I_{dark} and I^{ref}_{dark} is the light intensity signals of the main and the reference spectrophotometers in the absence of light, I_0 and I^{ref}_0 is the initial light intensity received by the main and the reference spectrophotometers and I and I^{ref} the light intensity data of the two spectrophotometers.

7.1.7 Camera cell

Biofilm development under flow is a dynamic process with a strong competition between growth and detachment. We therefore designed a cell that can be used to image biofilm patches that detach from within the porous medium and analyze the dynamics of this detachment. This module is meant to be installed at the effluent stream, after the biocide injection to ensure that there is no biofilm colonization on the cell that would perturbate the measurements. The whole module (fig. 7.8) consists of a 3D-printed flow cell, a camera (PCO edge, PCO GmbH) and a light source (Olympus KL 2500 LED). The flow cell is fabricated using one 3D printed part directly glued (NOA81, Norland) to two quartz windows. The printed part also features threaded luer connectors on each side to easily integrate to the fluidic circuit as needed. As biofilm patches flow through the flow cell (3D-printed with two quartz windows), they are captured by the camera through a dark field imaging approach. During the acquisition process, 2×2 binning was employed utilizing the camera with a resolution of 2000×400 pixels and a pixel size of approximately 9 µm/pixel. This technique effectively reduced the size of the data obtained, enabling longer acquisition times while also increasing video contrast. It is important to note that the use of 2×2 binning resulted in a reduction of video resolution by a factor of 4. However, for the purposes of this study, the impact on the resolution is not significant in respect to the detection and measurement of the outflowing biofilm patches. In order to further optimize the contrast of the images, adjustments were made to the exposure time and light source intensity for each experiment. While the camera's exposure time was set at 100 ms - a carefully considered compromise between achieving high contrast images and avoiding overexposure - the final acquisition frequency was slightly increased to approximately 165 ms, which may be attributed to communication delays between the camera and computer. These adjustments were critical for obtaining optimal image quality and provided greater precision and accuracy in the experimental results.

To increase the contrast and better capture the biofilm patches flowing out of the bioreactor the following approach was implemented. The light source was placed behind the camera cell with a certain angle so that the camera, which was placed directly in front of the cell would not receive all the light emitted by the source, but rather the portion of light that is reflected by the object passing through the cell (fig. 7.8). Like so, the edges of the biofilm patches are highlighted and adequate contrast is obtained in between the liquid phase and the biofilm. In addition, by performing a 2×2 binning during acquisition, we reduced the size of the data files while increasing the contrast of the images. On the other hand, by performing a binning, the resolution of the images was decreased by a factor of four but the high initial resolution of the camera allowed us to make that compromise.

7.1.8 Bubble traps

Air bubble formation is a common phenomenon throughout the system, especially when the fluid stream is at the dissolved oxygen saturation levels when injected into the system. These bubbles can perturbate the various measurements but also promote biofilm detachment when they flow through the porous medium. The designed bubble trap module can be used wherever needed throughout the fluidic circuit. A central element of this module is the hydrophobic PTFE membrane filter with 0.45 µm size pores. When the filter is placed upwards, passing bubbles are naturally flowing towards the membrane and due to its hydrophobic nature, the bubbles are evacuated from the fluidic circuit without leakage. The filter membrane can be directly fixed onto the bioreactor, at one of its inlets/outlets, but it can also be placed wherever it is needed throughout the microfluidic circuit by adding a secondary, 3D-printed element to the module. This element, is a 3D-printed part that is designed with one vertical fluidic inlet on the bottom, one horizontal fluidic outlet, an outlet on the top where the membrane filter is fixed and a compartment in the middle to amplify the trapping effect of the bubble trap module (fig. 7.10).

7.1.9 UV-C lamp and LEDs

The bioreactor used in this study had a rectangular opening on each side, one for inlet and the other for outlet, both of which were covered with quartz windows. These windows enabled constant illumination of UV-C bactericidal light to confine the biofilm within the porous medium. In most of the experiments, the light was provided using the same type of UV-C lamps as the ones used for water disinfection in water tanks (UV-technik GmbH). This lamp was inserted in a black, opaque tube with two holes to direct the light towards the bioreactor windows (fig. 7.9A). The lamps were working at 16 W. However, we designed an alternative UV-C system, which used UV-C LEDs with a emitting light spectrum centered at 275 nm. The LEDs were assembled on a PCB circuit, which was mounted on a fan to prevent overheating (fig. 7.9B,C). The PCB was linked to a homemade control unit that could simultaneously control four LEDs either through the unit directly or by using the designated software (fig. 7.9D). Due to their sensitive nature to high temperatures, which could lead to inconsistencies in light intensity and relatively short life, we preferred to utilize UV-C lamps to ensure experimental consistency. In both cases, the light sources were fixed in place in front of the bioreactor by fabricating an adapted, 3D-printed support.

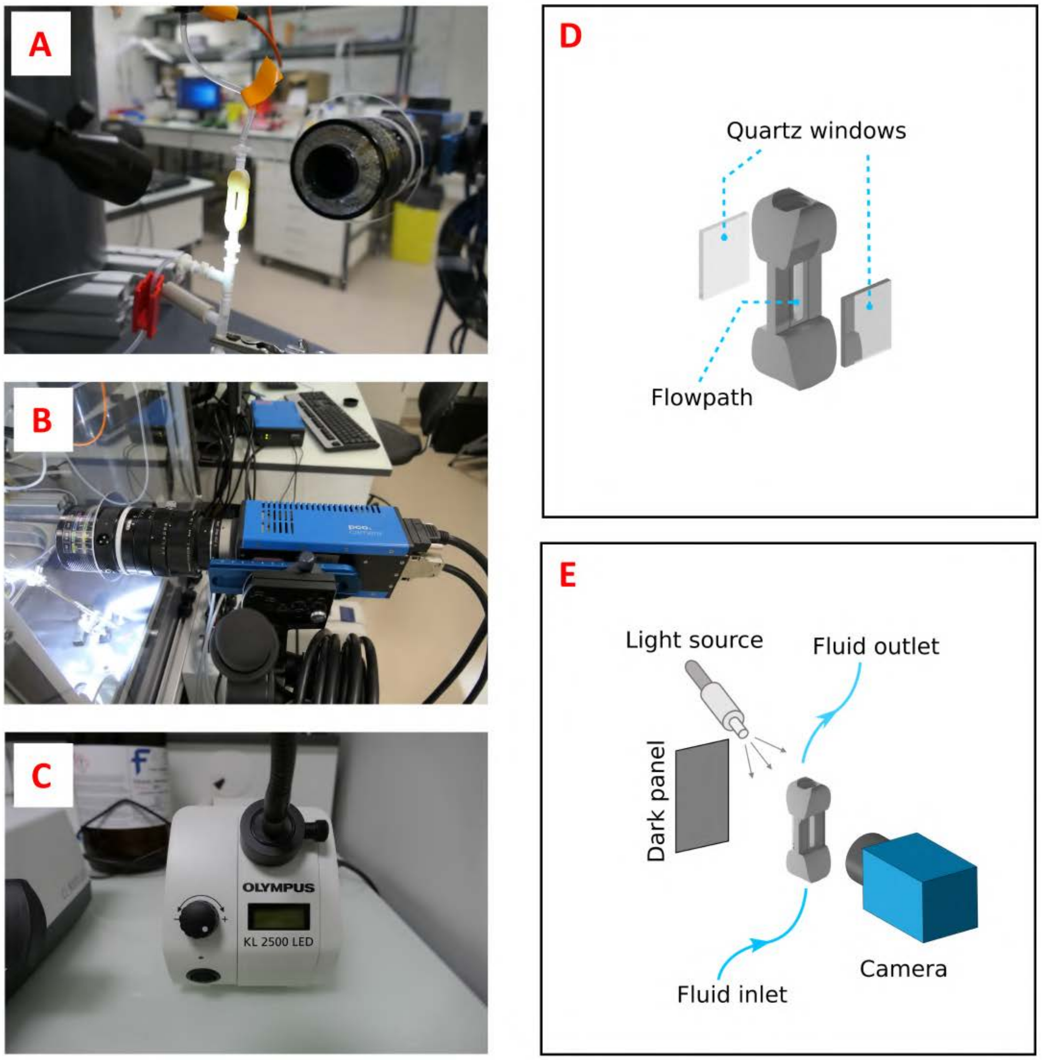

Figure 7.8: (A) Photograph of the camera cell in the middle with the light source on the left and the camera on the right. (B) The camera used for this module, is a high-sensitive and high resolution PCO camera that allowed high contrast imaging at a rate of about 15 images per second. (C) The light source is an Olympus KL 2500 white LED. (D) Schematic of the 3D-printed camera cell used to capture biofilm detachment events at the outlet of the bioreactor. (E) Positioning of the light source and the camera in respect to the cell. The light source is positioned with an angle facing the cell so that the interface between the biofilm patches and the liquid phase is highlighted.

Figure 7.9: (A) shows the UV-C lamp with the arrows indicating the position of the openings on the protective tube. (B) and (C) are the back and front view of the homemade UV-C LED systems. (D) is the control unit used with the UV-C LEDs.

7.1.10 Mixer module

In the low Reynolds number regime that dominates micro-devices, mixing can be challenging and lead to unwanted heterogeneities. A 3D-printed fluidic module was implemented to ensure proper mixing of two streams wherever needed throughout the experimental setup, for example to mix nutrients with water or to mix a colored dye with water for breakthrough curves. The design process involved creating several prototypes and testing various geometries. Initially, we experimented with designs integrated into the inlet compartment of the bioreactor, for example, a multiple-layer, fine mesh with each layer's mesh rotated by 45°. It was concluded that this design is inefficient as the mixing part was not long enough to promote mixing. Next, we designed a separate mixer module using a well-established design used in chemical engineering mixing processes that is known as "Kenics mixer", which proved to be much more effective. However, the mixer's geometry posed difficulties for degassing and sterilization prior to experimentations, and the trapped air bubbles would cause issues later on in the experiment. Ultimately, we landed on a double helicoidal mixer design for the bioreactor.The mixer consists of two helicoidal channels of 1mm in diameter each, one spinning clockwise and one anti-clockwise, with multiple meeting points forcing the fluid flowing through to mix (fig. 7.10). The design was tested by mixing a blue, water-soluble dye and water. With a length as short as 10 cm, the mixer was able to provide adequate mixing (fig. 7.10).

7.2 The bioreactor

7.2.1 General

The bioreactor played a crucial role in the fluidic circuit as it contained the biofilm being studied. It served as the location where all the biological, chemical, and physical reactions occurred, including the metabolism of nutrients, oxygen consumption, reproduction, and EPS excretion by bacteria. The interplay between hydrodynamics and biofilm development in porous media was the primary subject of investigation, and the bioreactor had the challenging task of providing a substrate for biofilm growth while integrating the various elements/measuring devices of the experimental setup. For that, the bioreactor was designed in three parts (fig. 7.11). The central part hosts the porous substrate where biofilm growth takes place. The inlet and the outlet compartments are modifiable and are designed for connection to the various fluidic modules and measuring devices. Examples of such modules include

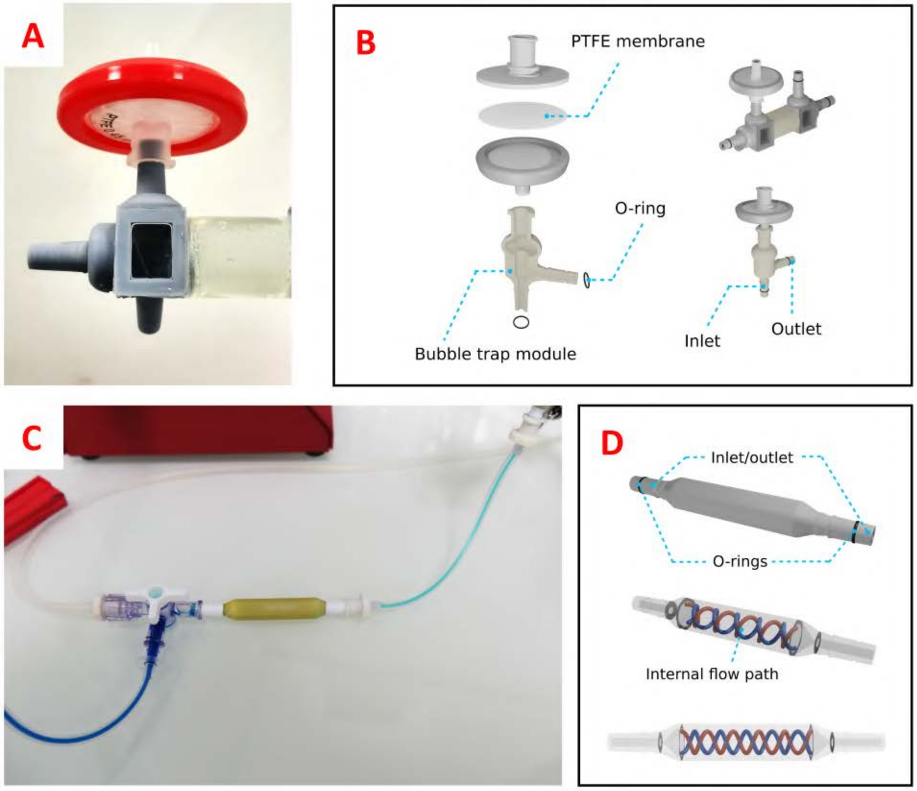

Figure 7.10: (A) A typical configuration where a hydrophobic, PTFE membrane filter is vertically mounted onto the inlet compartment of the bioreactor to act as a bubble trap. (B) The PTFE membrane filter can be mounted either on a separate, 3D-printed, bubble trap module to be integrated anywhere on the fluidic circuit (B left) or directly mounted onto the bioreactor (B top-right). (C) Two streams, one containing a blue dye and another containing water meet just before the mixer module. The mixer ensures proper mixing of the two streams, as observed from the stream exiting the mixer module. The mixer module's internal structure is illustrated in (D), featuring double helicoidal tubes that rotate in opposite directions and intersect at various points.

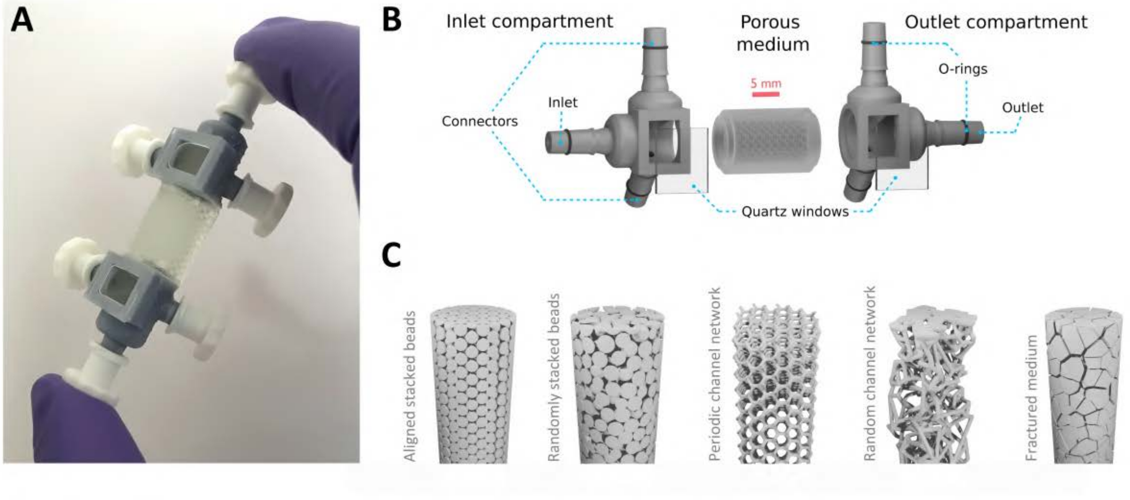

Figure 7.11: (A) Photograph of the micro-bioreactor. (B) The bioreactor split in three parts: inlet, outlet compartment and porous medium. (C) Various types of porous media that can be integrated in the middle part of the bioreactor.

water/nutrient and biocide injection inlets, bubble traps, connectors to differential pressure sensors and oxygen sensors. Each part is printed using a different 3D printing technique, adapted to the needs of each component.

Inlet and outlet compartments The two compartments of the bioreactor (fig. 7.11), attached on the two ends of the porous medium, are designed to accommodate mainly the fluid inlets and outlets, but also serve to attach various fluidic and instrumentation modules. These parts are equipped with luer connectors, which have been designed to be fitted with nitrile rubber o-rings (3.2 mm ID, 4.2 mm OD) to facilitate easy and reliable connection and detachment of the various modules and measuring devices. This feature proved especially beneficial during the bioreactor's initial inoculation phase, where bacteria were injected and the inlets/outlets of the bioreactor had to be sealed in a leak-proof manner. The luer connectors with o-rings contributed to the overall success of the experiment by ensuring a secure and leak-proof setup, while also minimizing the risk of errors.

Nutrients and oxygenated water come in at the inlet compartment, flow through the porous medium and then directed out of the bioreactor from the outlet compartment. Both inlet and outlet compartments have connectors for the pressure sensor that measures the differential pressure developed within the porous medium. Both compartments are equipped with one rectangular opening in each side, covered with a quartz window. This design allows for the continuous illumination of both compartments with bactericidal UV-C light and therefore for the confinement of bacterial development within the limits of the porous medium. The effective UV-C dose exerted by the UV-C lamps passing through the quartz windows is about 13.6 W/m^2, enough to ensure the elimination of biofilm growth .

For the fabrication of 3D pieces using the MJP technique, we used a ProJet MJP 2500 plus (3D Systems) with the resin VisiJet M2R-TN as the main printing material and VisiJet M2 SUP as the support wax material. The printing resolution is about 32 µm per layer. After being printed, all the pieces were placed in the oven at 70 °C for at least one day or until all of the support material was removed.

7.2.2 The porous media

Conventional porous media such as packed beds, sand, and pellets have limitations in their reproducibility, as their arrangement can vary depending on the size and location of each grain. This lack of consistency can generate uncertainties and hinder the analysis of phenomena involving porous structures. To overcome the limitations of conventional porous media and enhance their reproducibility, researchers have turned to 3D printing techniques such as Stereolithography (SLA) and Multi Jet Printing (MJP). These techniques enable the fabrication of complex and precise porous structures with reproducible geometries and properties, which can be customized for specific applications. The flexibility of these techniques allows for the design of various types of porous structures, which in turn allows for the study of different types of systems with varying hydrodynamic environments.

Here we explore the possibilities of the technique by 3D printing various types of porous structures and compare them. Figure 7.11 shows example porous structures that were fabricated: periodic and irregular channeled networks, aligned and randomly stacked beads and finally fractured media. For fabrication, both stereolithography (SLA) and multi jet printing (MJP) were implemented. The SLA technique (resolution down to 30 µm (X,Y) and 10 µm in Z direction) was found to be optimal for 3D-printing channeled networks with channel diameters down to 300 µm, while it was possible to 3D-print bead-like structures only by using the MJP technique (resolution down to 32 µm in Z direction) due to the fact that in certain regions, beads are freely hanging in space and therefore a support material is needed. For the same reason, fractured media are thought to be optimally printed using the MJP technique.

Design of porous structures The aligned and the random bead packing structures were designed using the open source software Blender [133]. In both cases, the beads used for the construction of the porous architecture were designed to be 1mm in diameter. More particularly, random bead packing was generated by simulating falling 1mm-diameter beads in a beaker using Blender. The random channel network, with channels of varying orientation and length, was created from a homemade code 40 that designed for control various parameters, such as node connectivity and density, range of channel length, minimum angle between channels, and removal of border "dead-end" channels. Originally used for brain vascular networks, this code was modified for the current study to generate a channel network with a target channel diameter of 200 µm and a connectivity of 3 for each node. The code produced a binary tiff image stack that was thresholded using Avizo to reproduce the 3D volume The periodic network was modeled after a Laves graph [91] with a target channel diameter of 300 µm, each edge of length 700 µm and a connectivity of 3 for each node. It was designed as a spatial graph comprising of vertices and edges and then transformed into a binarized tiff stack using a homemade Python script. A 3D surface was finally extracted from the tiff stack using Avizo software.

Microfabrication using SLA and MJP SLA microfabrication was performed using a DWS 29J+ (DWS Systems) printer. The resin used (DS3000) is a semi-transparent biocompatible acrylic resin (DWS Systems). The 3D printing method, combined with this resin, offers a relatively high resolution of 30 to 40 µm in the X and Y direction and 10 to 100 µm in the Z direction. The pieces were post-treated with ethanol and isopropanol to evacuate the unpolymerized resin from within the crevices and they were further cured with UV light at 405 nm for 30 minutes to ensure the full polymerization of the resin and minimize cytotoxicity. Structures were printed using the following parameters for the main body of the 3D pieces: indentation 0.01, hatching 0.04, Z-compensation 0.12, laser speed 5800 and contour 0. The parameter “contour” controls the extra layers of material that are added to the surface of the 3D printed structure. Increasing the number of layers, provides a smoother surface but tends to produce oversized structures and wider crevices. Keeping contour to 0, slightly undervalues the size of material-filled structures. For the fabrication of 3D pieces using the MJP technique, we used a ProJet MJP 2500 plus (3D Systems) with the resin VisiJet M2R-TN as the main printing material and VisiJet M2 SUP as the support wax material. The printing resolution is about 32 µm per layer. After being printed, all the pieces were placed in the oven at 70 °C for at least one day or until all of the support material was removed.

Characterization of 3D-printed porous structures We used X-ray computed microtomography to characterize the four different porous media designs after microfabrication. The aligned bead packing was made of beads of 1mm in diameter and a theoretical porosity, based on a body centered cubic packing arrangement, of 31.98 %. The 3D printed fabrication using SLA resulted in a porosity of about 36 %, as measured after processing X-ray tomography images. A few pore throats were clogged with the resin as the structure contains overhanging regions that inevitably produce errors due to the lack of a support material in SLA. For comparison, the random bead packing structure with an initial porosity of 37.45 % had an actual porosity of about 30 % when printed with MJP. X-ray tomography analysis further revealed that some of the pores were clogged with the support material that could not be removed. The third porous structure was a periodic channel network modeled after a Laves graph. The theoretical porosity was calculated to be 8.56 % and channel diameter of 300 µm but the 3D printed version using SLA resulted in a porosity of 10.57 % and channel diameter around 315±18 µm. The last porous structure was the random channel network with a theoretical porosity of 9.79 % and a channel diameter of 200 µm but the printing resulted in a porosity of about 11 % and an approximate channel diameter of 250 µm.

Both SLA and MJP can be used to print the porous structure, with respective advantages and disadvantages. The most important difference is the use of a support material for MJP, which eliminates problems associated with overhanging parts, but makes it difficult to thoroughly extract the support material from the porous medium after printing. Overall, the MJP technique seemed to be more adapted for geometries that exhibit overhanging structures such as the beads and the fractured porous media, while SLA is optimized for low-porosity porous media where limited pore space needs to be free from support materials and unpolymerized resins. In addition, it has been observed that MJP therefore resulted in slightly lower permeabilities compared to the initial design. We obtained slightly higher porosities and larger channel diameters with SLA but with a level of correspondence between the design and the printed structure that was sufficient for our purposes. Our primary goal was indeed to show the feasibility of fabricating our bioreactors, with pores in the microfluidic range, using widely accessible printing techniques. If required, a more accurate correspondence may be obtained by optimizing e.g. printing parameters, equipment and cleaning procedures after printing for MJP. One fundamental aspect, however, was consistency between printings. When performing replicate experiments of biofilm development, it is important to minimize the variability due to changes in the structure. For the periodic channel network that will be used in the remainder of this work, we estimated a standard deviation of 18 micrometers of the diameter of the channels. The estimation was obtained by measuring the diameter of several channels from three µCT datasets of the same empty porous medium printed in different batches. The measurement was performed on the binarized image stacks. As we will see, this is negligible compared to the effect of biofilm.

7.2.3 Permeability

Darcy's Law is a fundamental principle in fluid mechanics that describes the flow of fluids through porous media, such as rocks, soils, or filters. Darcy's Law states that the rate of fluid flow through a porous medium is proportional to the gradient of the hydraulic head (pressure) and the permeability of the medium. The mathematical formula for Darcy's Law in absence of gravitational forces and in a homogeneously permeable medium, is:

$$v = -\frac{k}{\mu L}\Delta p \tag{7.1}$$

where v is the velocity of the fluid through the porous medium in m/s, k the permeability in m^2, μ the dynamic viscosity of the fluid in Pa·s and Δp the pressure drop over a given distance L. The velocity is equal to $v = Q/A$ where Q is the volumetric flow rate in m^3/s and A is the cross-sectional area of the medium in m^2. According to the convention that fluids move from regions of high pressure to regions of low pressure, the definition of the flux employs a negative sign. The permeability can thus be deducted both as:

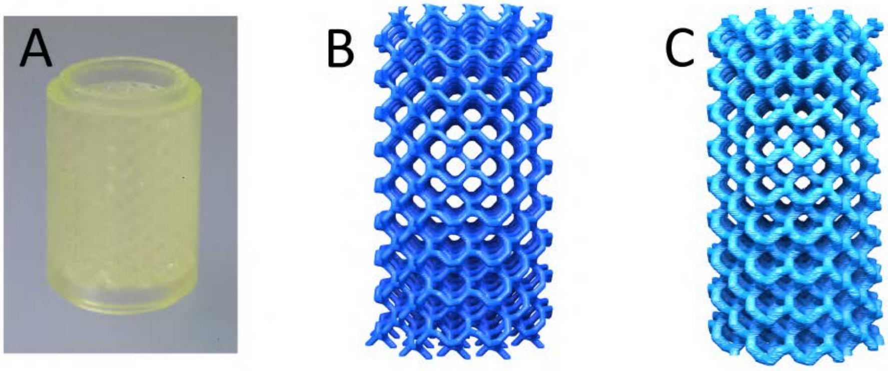

Figure 7.12: (A) Central part of the micromodel with the 3D printed (SLA) porous substrate for biofilm growth. The 3D printed part measures 16 mm from top to bottom. (B) 3D visualization of the .stl file initially used for printing. The channel diameters were designed to be 300 µm. (C) X-ray microtomography 3D reconstruction of the printed sample. The resulting diameters were estimated at 315 ± 18 µm.

$$k = \frac{Q\mu L}{A\Delta p} \tag{7.2}$$

$$\Delta p = \frac{L\mu}{kA}Q \tag{7.3}$$

As stated earlier, the porous medium selected to investigate the intricacies of biofilm growth dynamics in the rest of this chapter, is the periodic channel network. The initial permeability of a porous medium was determined experimentally by measuring the differential pressure at several flow rates using a gear pump. The experiment was carried out by first setting the flow rate to zero and zeroing the measuring device of the differential pressure as part of calibration. Then, several different flow rates were imposed, and the corresponding differential pressures were recorded. A linear fit was performed on the data to extract the initial permeability of the system using eq. 7.3 considering a dynamic viscosity as that of water at 25 °C, $\mu = 0.8891$ mPa·s, a cross section area of the porous medium of $A = 50.24$ mm^2 and a distance between the inlet and the outlet of the porous medium of $L = 14$ mm. The permeability of the empty porous medium was found to be $k_0 = 4.68 \cdot 10^{-11}$ m^2.

7.2.4 Hydrodynamic parameters

T-shaped flow cells equipped with fiber optic probes were used to measure the concentration of the dissolved oxygen before and after the porous medium. This allowed us to measure the oxygen consumption of the microorganisms. The inlet dissolved oxygen (DO) sensor was placed between the gear pump providing the water stream and the T-connector where the nutrients are introduced, so that to avoid potential colonization of the sensor by the bacteria. As a reminder, nutrients and ultra-pure water were separated to prevent biofilm from forming earlier in the system. In addition, in preliminary experiments it has been observed that biofilm formation can take place even up to the mixing point of the nutrients and the main stream. Placing the sensor just before the mixing point, minimizes the probability of biofouling and provides an accurate measurement of the oxygen levels at the inlet. To confirm that the advection time was consistently shorter than the backwards diffusion of nutrient (in the direction opposite to the main flow), we calculated the Péclet number according to the following formula:

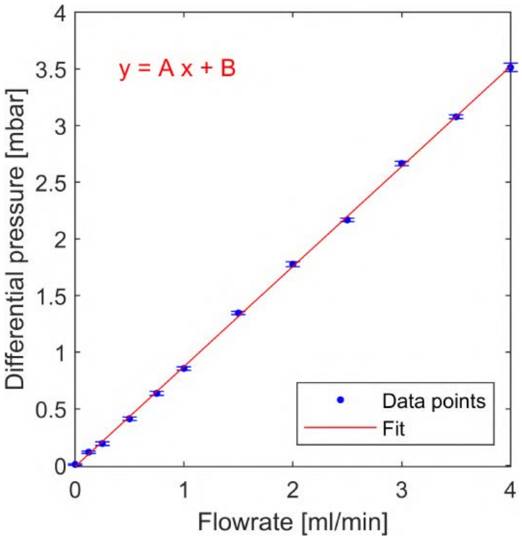

Figure 7.13: The permeability of an empty porous medium was determined by imposing the flow rate using a gear pump and reading the differential pressure between the inlet and the outlet of the bioreactor. The obtained data were fitted onto a linear model (A = 0.88287, B = -0.0093614, $R^2 = 0.999$) and the initial permeability was extracted according to eq 14.1. The initial permeability of the system was found to be $k_0 = 4.68 \cdot 10^{-11}$ m^2.

$$Pe = \frac{\tau_D}{\tau_A} \tag{7.4}$$

where τ_D, the diffusion time and τ_A the advection time are equal to:

$$\tau_D = \frac{L^2}{D} \tag{7.5}$$

$$\tau_\mathrm{A} = \frac{L}{V} \tag{7.6}$$

L is the distance over which diffusion is investigated (here we consider $L = 10^{-3}$ m), D is the diffusivity coefficient (taken as 10^{-9} m/s as this is the typical order of magnitude for water) and V is the fluid velocity. It can therefore be deducted that $\tau_D = 10^3$ s. In addition, if we consider the smallest possible fluid velocity and therefore the largest cross-sectional area in the system (that being the inlet/outlet compartment of the bioreactor) we have $A = \pi \left(r^2\right) = 50.24$ mm^2 and therefore, for a volumetric flow rate of 0.1 mL/min, a velocity of $V = 3.32 \cdot 10^{-5}$ m/s. We can therefore calculate $\tau_\mathrm{A} \simeq 30\ s$ and $Pe \ggg 1$. This suggests that the diffusion process in the direction opposite to the flow will not occur at a fast enough rate to offset advection within the bioreactor.

7.3 Strain preparation and bioreactor inoculation

Bacterial culture was initiated using *Pseudomonas aeruginosa* PAO1 strain (ATCC 15692 GFP). The bacterial strain was retrieved from a -80 °C stock and subsequently incubated in 20 mL of Brain Heart Infusion broth (BHI, Merck, 37.5 mg/mL) containing ampicillin (300 µg/mL) for one night, under conditions of 30 °C and 180 RPM. On the following day, the solution was diluted until an optical density of 0.5 at 600 nm (OD600) was achieved to ensure uniform starting conditions for the biofilm growth. The bioreactor inoculation procedure commenced with the injection of ethanol (≈10 mL) to create a sterile environment while purging air bubbles from the porous medium. Sterilized BHI solution

Figure 7.14: Reservoirs containing the concentrated solution of nutrients (BHI) on the left and the biocide solution (Tergazyme) on the right. The solutions were supplied into the system using a pair of gear pumps.

(37.5 mg/mL) containing ampicillin (300 µg/mL) was subsequently injected (10 mL) to displace the ethanol, followed by 10 mL of the inoculum. Once the inoculation was completed, the bioreactor's inlet and outlet were sealed, and it was placed in the incubator for one hour. After the elapse of one hour, the bioreactor is connected to the main fluidic circuit of the setup and the experiment commences.

7.4 Setting up the experimental setup

A typical biofilm growth experiment lasted for a week. The day before starting the experiment, all the materials, glass flasks and tubings that are to be used for the experimental setup, were cleaned and autoclaved (121 °C for 15 min) and a new bacterial culture was prepared according to the protocol described in the next section. To further ensure a sterile environment a biocide solution (Tergazyme 5.5% g/l, Alconox) was prepared to be injected directly at the outlet compartment, neutralizing planktonic bacteria and biofilm patches flowing out of the porous medium. This biocide solution is an enzyme-active detergent that contains a mixture of anionic surfactants and protease enzyme. A UV-C lamp was used to illuminate the water tank from which water was supplied to the system. A second UV-C lamp placed in front of the quartz windows located at the inlet and outlet compartments of the bioreactor, ensured that biofilm growth is taking place only in the middle part of the bioreactor. Finally, the nutrient solution (BHI, 37.5 % w/w) contained 300 µg/mL of the antibiotic Ampicillin, an antibiotic to which the bacterial strain used in this experiment is resistant. The camera and the spectrophotometric cells were designed with threaded luer fittings to directly connect to the tubing since no unplugging was needed for both modules after the commencing of data acquisition. The tubing used for all the experiments was Novosil silicon flexible tubing (0.75 mm ID, 1.5 mm OD) apart from the one used with the differential pressure sensors (PTFE ID 0.56 mm, OD 1.07 mm). Prior to each experiment, the tubings attached to each side of the pressure sensor, were filled with water and were sealed until the commencing of the experiment, when they were attached on the two bottom inlets of the bioreactor.

8 Data processing and analysis

8.1 Univariate analysis

8.1.1 Differential pressure curves

In order to gain insights into the behavior of the biofilm growth process, we employed various analytical techniques. Firstly, we utilized a moving average and standard deviation calculation to analyze the pressure data and identify any potential trends. This allowed us to identify global patterns and detect any fluctuations that could be indicative of changes in the biofilm growth process. Additionally, permeability evolution was determined and illustrated in fig. 8.1. This was obtained from the differential pressure data and the previously calculated initial permeability of the empty porous medium, using a modified form of Darcy's equation (eq. 8.1) that incorporates the initial permeability of the porous medium,

$$k(t) = \frac{Q\mu L}{A\Delta p(t)} \tag{8.1}$$

$$\frac{k(t)}{k(t=0)} = \frac{\frac{\cancel{Q\mu L}}{\cancel{A}\Delta p(t)}}{\frac{\cancel{Q}\mu L}{\cancel{A}\Delta p(t=0)}} \Rightarrow \tag{8.2}$$

$$\frac{k(t)}{k(t=0)} = \frac{\Delta p(t=0)}{\Delta p(t)} \tag{8.3}$$

The same values of viscosity, porous medium length and cross-section were used as the ones given in section 7.2.4. In addition, we considered that the total flow rate is $Q = 2$ mL/min.

Figure 8.1 shows the differential pressure measurements of biofilm growth in a periodic channeled network at a flow rate of 2 mL/min during 104 hours. The moving average and the corresponding standard deviation over 10 hours is also plotted to illustrate a global trend.

Upon initial inspection of the plot, it is evident that there is no discernible activity in the first 38 hours regarding biofilm production, indicating a lag phase where the bacteria are adapting to their new surroundings, multiplying, and secreting the extracellular polymeric substances (EPS) matrix. This lack of activity is also reflected in the absence of any significant changes in the effective permeability of the porous medium. However, in the subsequent 30 hours, there is a sharp increase in the mean pressure, accompanied by a notable rise in differential pressure. After this initial surge, the pressure reaches a pseudo steady state, exhibiting periodic oscillations that suggest the clogging and reopening of certain pores, potentially indicating preferential flow pathways. Notably, the standard deviation (which is represented by the shaded area around the mean pressure on the plot) increases significantly while the mean pressure remains relatively stable (fig. 8.1). Finally, the permeability shows a drop of approximately two orders of magnitude, from $4{\cdot}10^{-10}$ to $3{\cdot}10^{-12}$ m^2.

8.1.2 Oxygen data analysis

An analysis of the obtained oxygen data was performed in order to have an insight on the metabolic activity of the bacterial biofilm. Oxygen data at the inlet and at the outlet were obtained every 15 min. The oxygen concentration at the outlet was subtracted from the oxygen concentration at the inlet in order to obtain the their difference which would correspond to the oxygen consumption that is taking place within the limits of the porous medium. The moving average of the resulting curve was calculated over a time span of 10 h to eliminate local fluctuations and have a better idea of the global oxygen consumption trend.

The experiment showed that the oxygen consumption by bacteria increased steadily from the start and reached its peak value at time $x_0 = 52.9$ h. This indicates that the metabolic activity of the bacteria was also steadily increasing during that time. However, even at the peak of the oxygen consumption, the differential pressure was at its steepest point, suggesting that biofilm production was

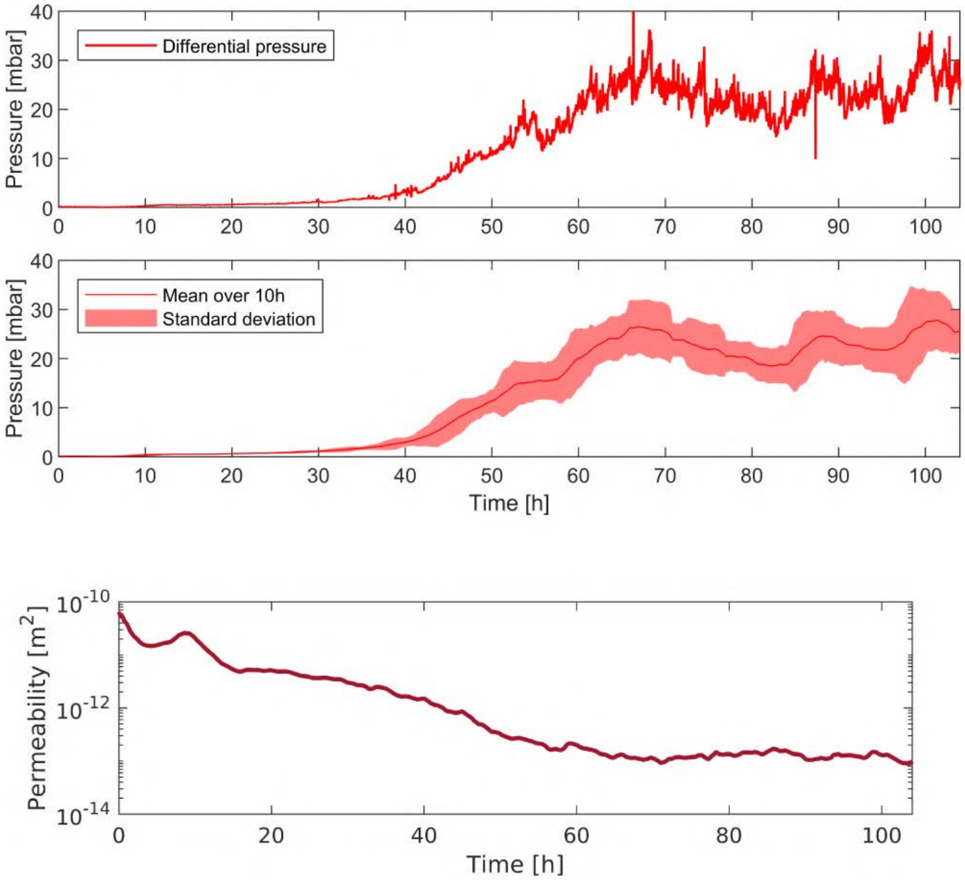

Figure 8.1: Pressure sensor measurements. (Top) is the raw data obtained from the differential pressure sensor for biofilm grown at 2 mL/min. (Middle) The moving mean curve was calculated over 10 h of data. The shaded area represents the moving standard deviation of the data for the same time interval. 95.4 % of the data fall into that area (two standard deviations). (Bottom) The calculated permeability according to eq. 8.3. The resulting data were further treated and smoothed out using a moving average over one hour.

still ongoing despite the stagnation in the metabolic activity of the bacteria. These findings suggest that the biofilm production by bacteria is a complex and dynamic process, which can continue even when the metabolic activity of bacteria seems to have reached its maximum level.

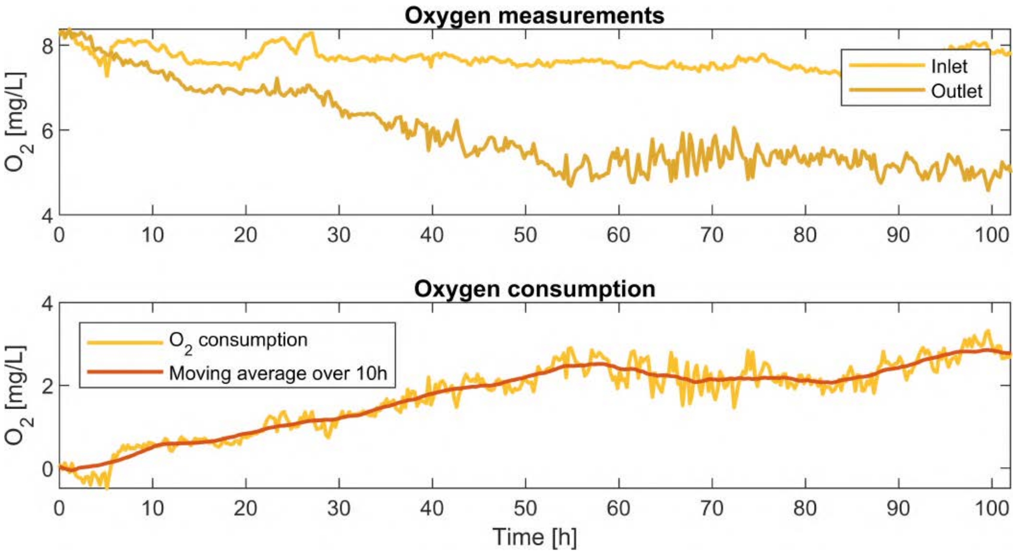

Figure 8.2: Oxygen sensor measurements. Top figure shows the raw oxygen concentrations obtained at the inlet and at the outlet of the bioreactor. Bottom figure shows the oxygen concentration difference between inlet and outlet (oxygen consumption). The moving average over 10 h is plotted to demonstrate the global trend.

8.1.3 Temperature data

Temperature was measured using a homemade thermocouple device that was equipped with several probes, two of which were attached to the spectrophotometers to verify that they are properly thermoregulated, while a third one was left to measure the ambient temperature of the experimental setup. The device was fabricated by the technical team of the lab and no calibration was needed. The ambient temperature obtained showed some periodic cycles that are thought to be due to the room temperature regulation of the laboratory (fig. 8.3). It should be noted that the lab was located in the hospital of Purpan and the heating of the rooms was centrally regulated. This had an effect on the experimental setup's temperature. The whole experimental setup, including the sensors, was located inside a closed transparent storey which prevented heat exchange through advection with the outside environment. Therefore, the heat produced inside the storey (from the UV-C lamps for example) tended to increase the overall temperature. As a result, the temperature would occasionally exceed 32 °C. The temperature readings from the spectrophotometers appeared to be quite stable, only fluctuating by about 1 °C at most, which suggests that the cooling system was functioning well. However, the temperature readings of the water bath were slightly higher than the set temperature of 15 °C, hovering around 17 °C. This implies that some heat exchange might have been occurring through the tubing before the cooling water reached the heat exchanging plates, decreasing the efficacy of the cooling system.

P. aeruginosa is a mesophilic organism, growing with an optimal temperature range of 20-42 °C which falls within the temperatures used in this study. However gene expression related to the production of various exopolysaccharides such as algD and pelA has been shown that is affected by similar temperature changes [221] with the strain PAO14 decreasing its overall exopolysaccharide production when temperature increases from 25 to 37 °C. Therefore, thermoregulation of the system would potentially contribute to the stability of the measurements such as differential pressure and oxygen consumption.

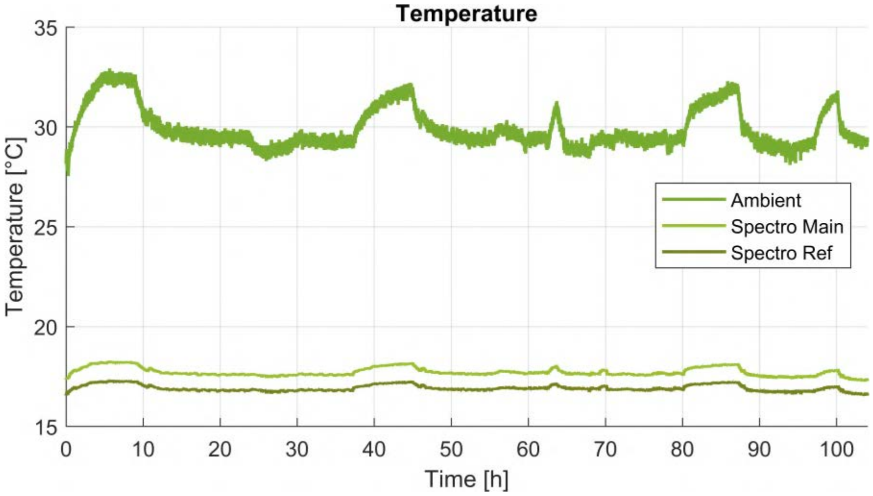

Figure 8.3: Temperature measurements. The temperature of the two spectrophotometers was measured to ensure that the devices were properly thermoregulated. Ambient temperature appears to have some periodic patterns that are related to the temperature regulation of the laboratory room.

8.1.4 Spectrophotometric measurments data analysis

As previously described, in order to conduct the required measurements, we utilized two spectrophotometers and a light source with two outlets. The first spectrophotometer was directly attached onto one of the light source outlets to serve as a reference for measuring the light intensity fluctuations of the source. For the second spectrophotometer, we mounted its optic fiber on another homemade 3D-printed spectrophotometric cell, with the other outlet of the light source on the opposite side of the cell. Throughout the acquisition process, the light intensity of the source was maintained at a fixed level to ensure that neither of the two spectrophotometers was over-saturated. We recorded the light intensity at an approximate interval of 0.1 seconds, without any averaging of the values, and with a boxcar width of 10, at a wavelength of 600 nm.

We then determined the absorption from the light intensity data, according to the following equation (eq. 8.4),

$$A\left(t\right) = log_{10}\left(\frac{I(t) - I_{dark}}{I(t=0) - I_{dark}} \times \frac{I^{ref}(t=0) - I^{ref}_{dark}}{I^{ref}(t) - I^{ref}_{dark}}\right) \tag{8.4}$$

where A represents the calculated absorption, I_{dark} and I^{ref}_{dark} represent the light intensity signals of the main and reference spectrophotometers in the absence of light, and I_0 and I_0^{ref} are the initial light intensities received by the main and reference spectrophotometers, respectively. The light intensity data from the two spectrophotometers are represented by I and I^{ref}. The first term nested in the logarithm in eq. 8.4 corresponds to the standard expression of absorption while the second term, corresponds to the correction of the signal by considering the cell that is measuring the light source intensity as a reference. Therefore, we eliminate the fluctuations in the main spectrophotometric signal that are due to the fluctuations of the light source.

To extract meaningful information from our signal, we applied a baseline correction approach. We initially smoothed the signal using a moving average filter, considering 10 neighboring datapoints, to obtain the baseline. By subtracting this baseline from the main signal, we effectively eliminated any persistent trends in the data, revealing only the sharp peaks that represent the changes in the signal. This approach allowed us to highlight the dynamic changes in the signal, rather than the actual measurement of absorption. We hypothesized that persistent trends are due to the fact that biofilm patches are stuck within the cell and that the sharp peaks detected in the signal corresponded

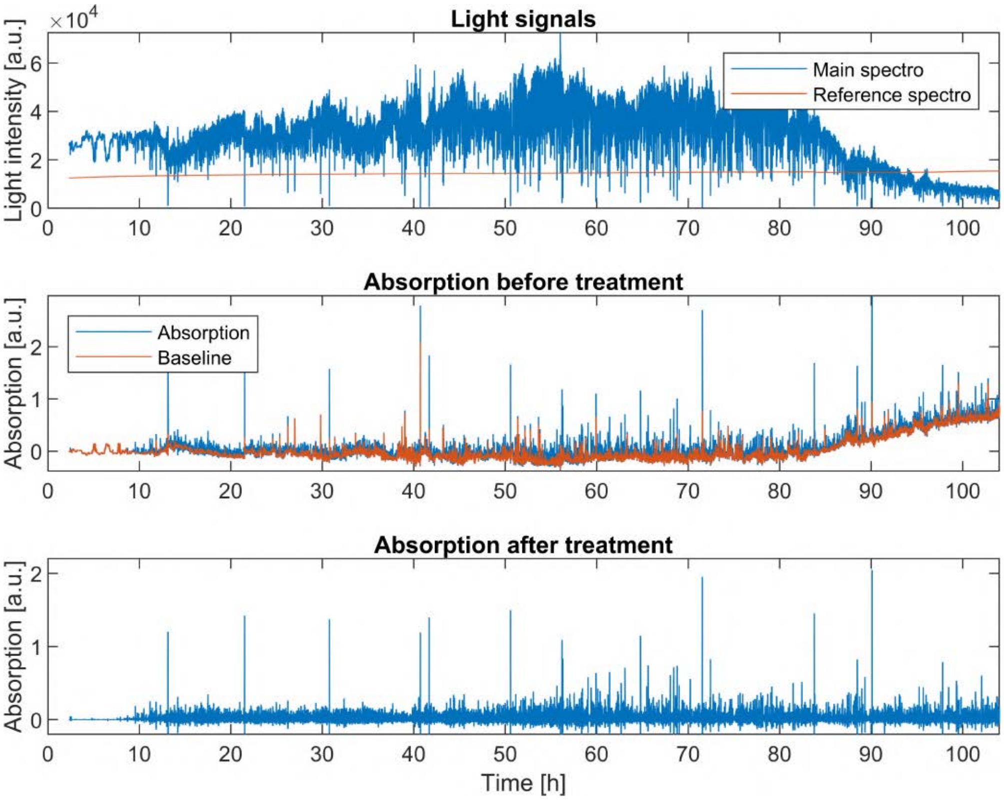

Figure 8.4: Spectrophotometric cell measurements. Top figure shows the raw data obtained from the reference and the main cells. The middle plot shows the absorption calculated according to eq. 8.4 from the two above signals. The baseline is subtracted from the absorption signal to remove persitent trends such as the increase after 85h and the result is plotted in the bottom figure.

to brief passage of biofilm patches. By applying this baseline correction approach, we were able to isolate the relevant changes in the signal which would provide more meaningful insights into the biofilm detachment dynamics.

8.1.5 Camera data analysis

The videos obtained from the camera were exported as tiff image stacks and were processed using a homemade MatLab script. The image sequences were rotated, and the area of interest was cropped in order to keep only the main flow channel of the cell. The image stacks were then thresholded and the mean pixel value of each frame was measured. To exclude the pixels corresponding to the main grayscale histogram peak at the beginning of the experiment and consider them as background, a threshold value of 10000 was chosen.

To remove trends in the signal caused by persistent biofilm patches stuck in the camera cell, the same baseline removal approach was employed once more. The signal's baseline was calculated using the moving average method, considering 10 neighboring data points, and was then subtracted from the main signal. In order to locate the signal peaks, the 'findpeaks' function in MATLAB was utilized by tuning several parameters, such as a minimum peak prominence of 0.02 and a minimum peak height of 0.005. The chosen parameters were lenient, allowing even the smallest peaks in the signal to be considered. Finally, the known size of the channel width (0.826 μm^2/pixel) was used to correlate the pixel number to the biofilm patch area in each frame, resulting in the determination of the biofilm patch size.

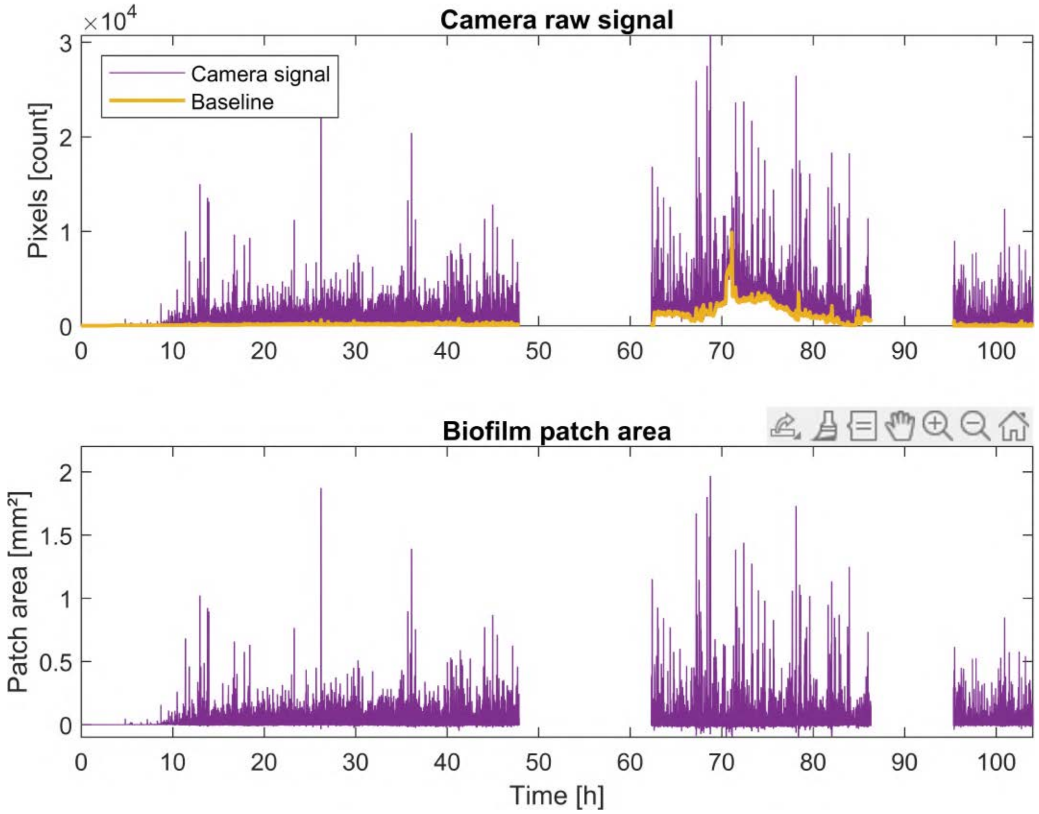

Figure 8.5: Camera cell measurements. Top figure shows the curve obtained after the analysis of the camera videos. The continuous video acquisition was not possible due to hardware limitations therefore three videos were obtained for the different phases of the experiment. The baseline was subtracted from the signal to remove persistent trends related to biofilm patches stuck in the cell (e.g. around 72 h). The resulting curve with each peak corresponding to the size of the biofilm patch going through the cell, is plotted in the bottom.

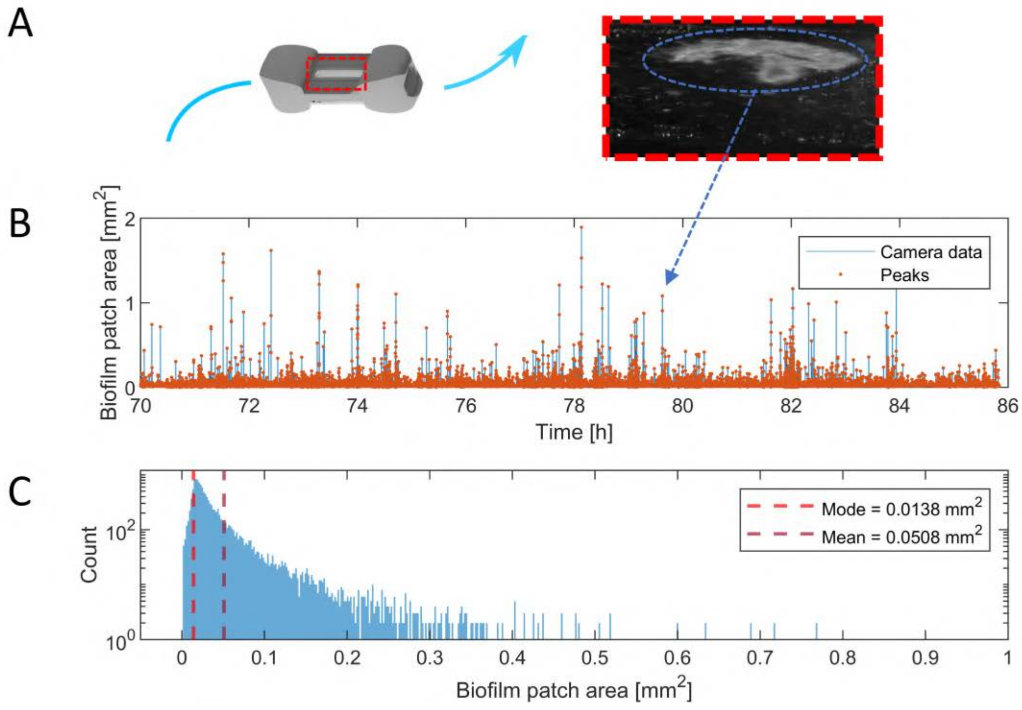

Figure 8.6: Camera peak analysis. (A) The camera is focused on the middle part of the transparent flow cell. An example frame where a biofilm patch goes through this flow path is shown on the right. This patch corresponds to a peak in the obtained data (B). Those data are manipulated so that they correspond to the area occupied by each biofilm patch on each frame of the video. After locating each peak, a histogram showing the distribution of the size corresponding to those peaks, is plotted (C).

After analyzing the patch sizes during the third phase of biofilm growth, from $t_1 = 70$ h to $t_2 = 86$ h, we observed that the mean biofilm patch size was around 0.05 mm^2. This size represents only a small fraction of the entire camera window, which measures 20 mm^2 (2×10 mm). The camera cell thus demonstrates remarkable sensitivity.

Despite this sensitivity, it is important to note that the obtained distribution of patch sizes was heavily influenced by the peak selection algorithm. While we applied this algorithm with relaxed parameters to include all small peaks, a threshold was applied, excluding patches that are less than 0.005 mm^2 wide. In addition, biofilm patches in each frame were not differentiated from one another therefore the height of the given signal can potentially correspond to several individual patches that are captured on the same frame since all the pixels of each frame were used to calculate the camera signal. This is a potential source of error that could be bypass by further analyzing the camera frames using specific ROI segmenting software powered by AI or particle tracking algorithms.

8.2 Cross-correlation analysis for camera and spectrophotometric cell data

Cross-correlation analysis is a statistical technique used to measure the similarity between two sets of data as a function of the time lag applied to one of them. In other words, it involves calculating the degree of similarity between two signals over a range of time delays or lags. The output of a cross-correlation analysis is a correlation function that provides information on the time delay and magnitude of the correlation between the two signals. In this study, we employed cross-correlation analysis on the data obtained from both the camera and spectrophotometric cells. The purpose was to synchronize the peaks observed in both signals, which were a result of the biofilm patches flowing through both modules. However, since the two cells were connected in series, with the camera cell connected prior to the spectrophotometric cell at the effluent stream of the bioreactor, a peak would appear first at the camera cell signal and then at the spectrophotometric cell. Aligning the two signals in time is essential to facilitate the reading and comparison of these signals.

Cross-correlation analysis was performed between the data obtained from the spectrophotometric measurements and the camera cell from time $t_1 = 68$ h to time $t_2 = 86$ h from the beginning of the experiment. This time period was chosen as it is the third phase of biofilm growth and therefore biofilm detachment events occur at their highest frequency. In addition, during that phase we expect both signals to behave in a similar way, with peaks appearing whenever a biofilm patch goes through each respective module. Prior to performing the analysis on the signals, a resampling had to take place so that both datasets have the same number of equally-spaced datapoints spanning across the same time period. Given that the camera data had an acquisition period of $T = 0.065$ s (sampling frequency $f = 15.38$ s^{-1}), and the spectrophotometric data an acquisition period of $T = 0.1$ s (sampling frequency $f = 10$ s^{-1}), we chose to sample both sets of data at a rate of 0.065 s, oversampling spectrophotometric data rather than undersampling camera data which would result in a loss of critical information.

After analyzing the data, it appears that a shift of 85.9 seconds yields a high level of agreement between the graphs captured by the camera and the spectrophotometric data. This time shift corresponds to the transport of biofilm patches from one cell to the other as the outlet of the micromodel was first connected to the camera cell and then, after a 30 cm tubing distance, to the spectrophotometric cell. This observation is quite reasonable and indicates that both modules are quite sensitive.

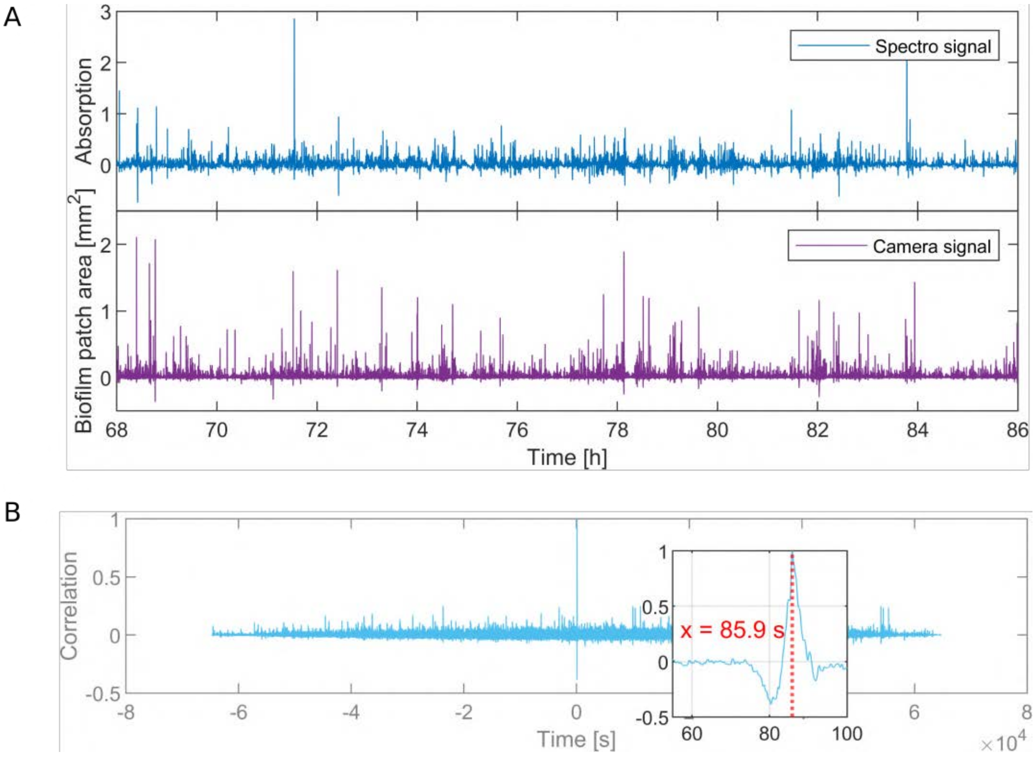

Figure 8.7: Cross-correlation analysis. (A) Data obtained through the spectrophotometric and camera cells were treated and a cross-correlation analysis was performed. The correlation between the two signals is given in (B) where strong correlation can be observed at $x = 85.9$ seconds.

8.3 Control experiment

To validate the results of previous experiments and better understand the impact of biofilm growth on the measured parameters, a control experiment was conducted. The experiment replicated all the parameters of the previous experiments, including a total flow rate of 2 mL/min, injection of the same biocide solution (Tergazyme) at the same location, and the use of all the measuring devices (differential pressure, oxygen, spectrophotometric and camera cell measurements). However, no bacterial culture inoculation occurred at the beginning of the experiment and no nutrients were supplied during the experiment to prevent biofilm contamination. All the measuring instrumentation, such as differential pressure, oxygen, spectrophotometric, and camera, was put in place. It is worth noting that the control experiment lasted for around 70 hours and during this time, no biofilm growth was observed in the system. For comparison, in a typical biofilm growth experiment, where the bioreactor is initially inoculated with a bacterial solution, an increase in pressure due to biofilm growth was typically observed after approximately 35 hours.

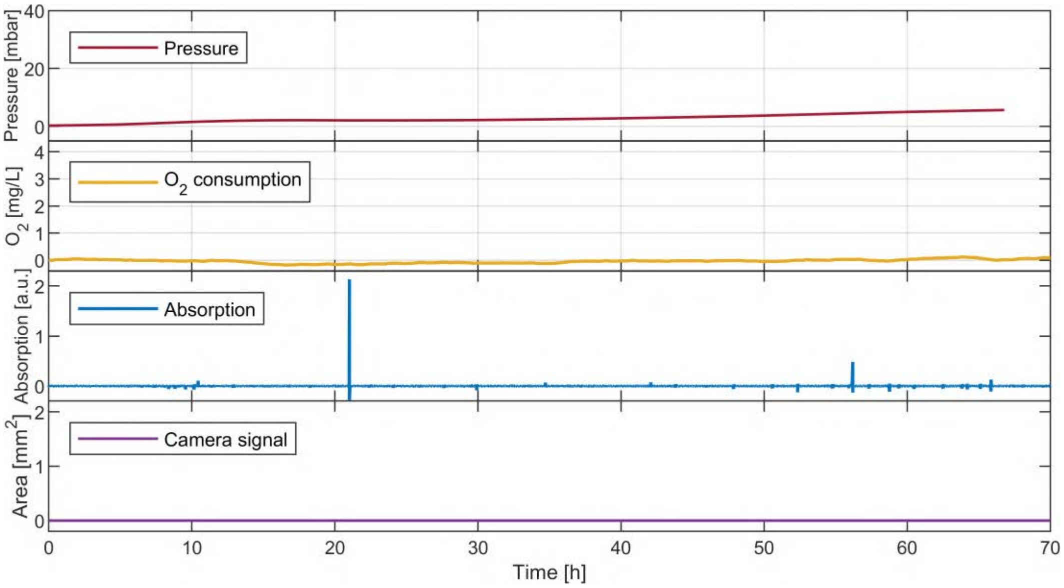

Figure 8.8: Control experiment results. Pressure/oxygen/spectrophotometric and camera module measurements are shown in that order from top to bottom. The typical experimental protocol was implemented but without any biofilm inoculation of the bioreactor taking place. The y axis scaling is kept the same as in corresponding previous figures for comparison. The few peaks present in the spectrophotometric measurements are thought to be air bubbles that made it through the bubble traps into the spectrophotometric module.

During that time, a slight increase in pressure from 0 to about 6 mbar was observed. This would account for about 6 % of the maximum pressure reached by a typical experiment during the same time. The oxygen consumption was constant at 0 mg/mL, an indication that no bacterial activity took place within the limits of the micromodel. The absorption measurements, obtained through the spectrophotometric cell, show two peaks, one at about 21 h and one at 56 h. Based on the absence of fluctuations in pressure and oxygen readings, it is presumed that the observed peaks in the data correspond to the passage of air bubbles through the experimental cell. This indicates that only two bubbles made it through during the 70-hour experiment, which is considered a successful outcome. Moreover, this suggests that infrequent bubbles do not adversely affect the rest of the measurements. The camera cell data, in contrast, shows a flat line, which could be interpreted in two ways. One possibility is that the air bubbles that passed through the spectrophotometric cell were generated after the camera cell (which precedes the spectrophotometric cell), potentially at a threaded junction and therefore did not affect the camera cell. Alternatively, it is possible that the camera cell measurements are overall less sensitive than the spectrophotometric cell measurements.

9 Versatility and limitations of the system

The experimental setup has a crucial advantage in its versatility, which allows for precise control over multiple mechanical and biochemical parameters related to biofilm growth. This level of control can be exploited to explore various aspects of colonization by adapting the experimental conditions to address specific research questions. As such, the setup provides a valuable tool for conducting a diverse range of experiments related to biofilm formation and control. To illustrate, we present below several potential experiments that could be conducted using this adaptable setup.

9.1 Changing the experimental conditions

9.1.1 Biochemical conditions

The setup could be potentially used in various different ways in respect to the biochemical conditions implemented. For example the same test can be performed using different strains of bacteria to determine their colonization capacity under constant flow rate. Furthermore, by using the complete range of gear pumps flow rates ($\sim 0.2 - 10$ mL/min) for the supply of nutrients, temporal biofilm growth curves can be drawn to identify the point where nutrient availability is overtaken by shear rate. This can be achieved by altering the nutrient concentration or by feeding a customized nutrient solution to promote the secretion of specific byproducts. The bioreactor can be modified to introduce a tracer or other substances, such as pollutants, and breakthrough curves can be generated using an adapted device to analyze tracer absorption by the microorganisms. Furthermore, the effluent stream can be sampled or monitored for total (TOC) and dissolved organic carbon (DOC) to determine the extent of bacterial nutrient consumption. Finally, various types of analytic techniques can be used for example high pressure liquid chromatography (HPLC) or gas chromatography (GC) coupled with mass spectrometry (MS) to identify specific byproducts at the effluent.

9.1.2 Hydrodynamic conditions

The micro-fluidic gear pumps used in this study, not only offer a wide range of flow patterns but also allow for completely customized flow patterns through coding. The potential experiments that can be carried out using different flow patterns are numerous. For instance, oscillatory flow, which is known to influence the proliferation of living organisms such as endothelial cells [172], yeasts [183], and human marrow stromal cells [258], could be experimented with using different frequencies and amplitudes on bacteria. Such experiments could lead to solutions for clogging of biofilters or better understanding of prosthetic and orthopaedic infections. Additionally, intermittent backward flow could be implemented to evaluate its impact on effective permeability and could potentially be a solution for auto-regulation of clogging in biofilters.

9.1.3 Porous medium characteristics

Our experimental setup is particularly versatile when it comes to 3D printing porous media. We have demonstrated that with this setup, a wide variety of structures can be created, each with its own unique hydrodynamic environment. For instance, we could print a porous medium with varying channel diameter and varying orientations to the main direction of the flow. Such variations would result in a wide distribution of hydrodynamic parameters, making this experimental setup a valuable tool for investigating the complex fluid dynamics of porous media. Additionally, a simplified porous medium design could focus on analyzing one aspect at a time, such as utilizing a solid block with only two pores (one narrow and one larger) to observe the temporal colonization of each pore. Furthermore, the 3D printing material of the porous medium could be chemically altered or post-treated to tune the bacterial initial adhesion rate and therefore perform relevant studies. Finally, the bioreactor can be customized to accommodate non-printed porous media, such as biological tissue or other biomedical materials requiring assessment of bacterial colonization.

9.2 Limitations

9.2.1 3D printing limitations

SLA and MJP are two specific 3D printing techniques that can be employed to print porous structures, each with their own unique advantages, disadvantages, and limitations. A fundamental difference between the two methods is the requirement for support material during MJP printing, which can lead to difficulties in completely removing the support material from the printed porous medium, ultimately resulting in lower permeabilities compared to the original design. While SLA can produce slightly higher porosities and larger channel diameters, consistency between design and print may not always be satisfactory for specific applications. Although the primary aim of this study was to demonstrate the feasibility of fabricating bioreactors with microfluidic pores using readily available 3D printing techniques, it is important to note that there are inherent limitations to both SLA and MJP printing methods, notable SLA can hardly print successfully a structure with overhanging parts, while MJP is not adapted to print microfluidic channels with a certain diameter due to the fact that a sacrificial material is used and cannot be easily evacuated. Optimizing printing parameters and cleaning procedures may improve the accuracy of the printed structure, but it is essential to consider the limitations of these techniques when designing and fabricating porous structures.

9.2.2 Technical limitations

During the experimental process, certain technical limitations were encountered. Specifically, the gear pumps used had a limited working range. The upper limit ($\sim$ 10 mg/mL) of the mzr-2921x1 pump model, was more than adequate for our application and the lower limit of the mzr-2521x1 model was estimated to be around 0.02 mL/min. However, using the gear pumps at their lower working limit proved to be a challenge as the pumps were less consistent for low flow rates, making it difficult to accurate dispense liquid volumes of the various solutions even after calibration. While a supplementary module could have been obtained from the supplier to improve flow rate regulation, it was eventually deemed unnecessary for the selected flow rates used during the experiments (0.2 mL/min for the nutrients and the biocide solutions).

In addition, in the course of the experiment, it was observed that the light source utilized for spectrophotometric measurements proved too powerful for the spectrophotometers, resulting in oversaturation of the sensors even when the light source was adjusted to its lowest setting of 2 % and the exposure time was reduced to the minimum value of 1 ms. The custom-made module utilized for this process had been composed of elements that were not originally designed to be used in conjunction. Specifically, the light source was intended for use in brightfield microscopy on a Zeiss Axiozoom microscope, explaining the excessive light intensity that was too much for the sensors to handle. This issue was resolved by integrating a neutral optical density filter on the light source, with an OD 0.25 which would reduce the incoming light to about half of its original intensity (Transmission $\sim$ 56 %).

9.2.3 Difficulties encountered

During the course of this thesis, the experimental setup was constantly developed and optimized. The original experimental setup was inherited from a previous thesis project (Anne Edith Larue, "Experimental methodologies to explore 3D development of biofilms in porous media" [246]) and since then numerous modifications were implemented. Notably, the bioreactor design went through more than 10 major versions in the effort to integrate new experimental modules, measuring devices and fluidic elements. The broader fluidic circuit was gradually expanded to accommodate the desired sensors and hydrodynamics, with experiments being continuously run to address any issues encountered along the way. For example, it was observed that biofilm was developing before and after the porous medium, which was affecting the hydrodynamic conditions reaching the porous structure and therefore the quartz window design had to be optimized, accommodating wider windows that would provide no "blind spots" when it was targeted with UV-C rays. Extra care was taken when the UV-C lamp was positioned so that, even from the very first moment of inoculation, the inlet and outlet compartments are clean from biofilm contaminations. Nonetheless, on the matter of biofilm colonization throughout the system, modules such as the spectrophotometric and camera cells were often colonized with bacterial biofilm perturbating each respective measurement. This biofilm was not actively growing, meaning that the chemical conditions were not favorable for it to grow since a biocide solution was injected at the outlet of the bioreactor. However, whenever flow-advected biofilm was mechanistically stuck in such modules, it would sometimes passively grow by retaining other biofilm patches that would pass by through the same tubing.

On the one hand, one significant advantage of this experimental setup is its versatility in terms of integration of extra modules. On the other hand, this characteristic appeared to be a challenge. This multi-element workbench was heavily depending on several apparatus working in parallel, each with specific requirements. The success of every experiment depended on the efficiency of each instrument, and any human error or machine failure, would result in a discarded experiment. Typically, the experiments lasted around 3 to 4 days, with the probability of an error increasing with time. Such unpredictable issues include power failures, insufficient storage space and memory during acquisition, faulty measurements due to moving of the setup. During this work, all the machine-induced, technical errors were addressed and tackled. Predictive maintenance was implemented in order to further control several of these issues and ensure the reproducibility of the experimental results. Maintenance would include regular re-calibration of the instruments and sensors, as well as replacing the silicone tubings and the o-rings used throughout the system for each experiment. The multi-part bioreactor was tested for air-tightness prior to each experiment and extra glue was applied on the joints if needed.

Another inconvenience that arose was the alignment of the camera cell relative to the PCO camera. This camera had a fixed working distance with a very limited margins for focal plane adjustment. The camera cell was fixed in place using a support equipped with crocodile clips. Therefore manual adjustment of the distance between the camera and the camera cell was needed in order to obtain a focused image. This resulted in a human-related error which would affect the results of the camera cell measurements. In practice though, the high resolution of the camera, combined with the adequate light provided by the source, gave a good contrast, minimizing errors related to sub-optimal camera focus.

A recurring challenge encountered during our experiments was the presence of air bubbles inside the bioreactor. The water tanks were the most common source of air bubbles, particularly when they were oxygenated beyond their saturation point or when the ambient temperature rose, which lowered the solubility of gas in the liquid, leading to the formation of bubbles. Since the bioreactor's material is hydrophobic, the bubbles could not easily navigate through its porous structure. In some cases, bubbles from the nutrient feeding pump would remain stagnant just before the bioreactor for hours, disturbing the flow properties that reached the porous medium. In addition to this, it should be noted that the hydrophobic membrane filters used here as bubble traps, tended to leak after prolonged periods of usage. To remedy this, new bubble traps were used for each experiment at the inlet and at the outlet of the bioreactor. Extra bubble trap modules were sometimes used just after the water supplying gear pump to ensure the absence of bubbles.

The main drawback of the workbench was that it required a significant amount of preparation time to launch an experiment, especially for the sake of reproducibility. It was crucial to ensure that the initial conditions of every experiment were the same, which necessitated the proper setting of protocols for every aspect, from inoculating the bioreactor with a similar cell concentration to achieving the same concentration of dissolved oxygen by bubbling the reservoirs for an identical amount of time. To launch a two-day experiment, a minimum of 1 day of preparation prior to the experiment and 1 day of cleaning post-experiment were needed, and the launching process itself was taking several hours. Due to the substantial amount of time required for efficient running and the large amount of unpredictable factors, only one bioreactor could be launched at one time even though up to two bioreactors could be potentially run in parallel.

9.3 Proposed technical improvements

Continuous refinement of an experimental workbench is essential. Therefore, this section aims to suggest technical improvements to be considered in order to further enhance the system's capabilities.

Since air bubbles are a significant issue of this setup, a more robust type of membrane filters could be implemented to increase the efficacy of the bubble traps. In addition, more bubble trap modules should be used throughout the fluidic system wherever it is deemed useful.

The water reservoirs were crafted from transparent Lexan tubes, which unfortunately seemed to acquire a yellowish hue after each experiment. It's believed that the UV-C lights used in the experiments may have caused this discoloration. To mitigate this, the tanks were thoroughly cleansed with soap to remove any residual tint after each experiment. Nonetheless, the material of the tanks should be reconsider and even more inert alternatives to UV-C light should be considered.

Integrating a thermoregulating system would be highly advantageous, as it would eliminate potential biases associated with room air conditioning and would allow to explore the effect of temperature on biofilm growth in porous media. Temperature has been proven to have a significant effect on the exopolysaccharide production of specific P. aeruginosa strains with production decreasing while temperature increasing within the range of 20 to 37 °C [221]. Finally, as temperature was found to have a significant impact on both the oxygen sensors and spectrophotometers, implementing temperature control within the experimental setup would effectively eradicate issues related to these measuring devices.

Research has shown that the characteristics of the 3D printing material used for microfluidic devices have a considerable impact on the adhesion properties of cells and, consequently, on cell proliferation rates [327]. This finding is particularly significant for biofilm control studies in porous media, as the properties of the 3D printing material can be precisely tuned to adjust bacterial adhesion. Therefore, exploiting this knowledge can enable the development of microfluidic devices with tailored surfaces that can effectively modulate bacterial adhesion and biofilm formation.

10 Conclusions

In conclusion, in this part we demonstrated the capabilities of a pioneering porous micromodel technology that enables the study of bacterial biofilms under flow conditions. This novel approach employs a modular "lego-like" design, utilizing 3D printed modules that can be easily assembled to create diverse three-dimensional geometries and topologies of pore networks tailored to specific experiments. The central micromodel module contains a 3D printed porous medium for biofilm growth, allowing for precise control of the architecture, including flow channels with fine diameters. In addition, we demonstrated the capabilities and limitations of two 3D-printing techniques, notably MJP and SLA and how they can be used to 3D-print various proposed geometries. Furthermore, the micromodel is equipped with instrumentation to measure important parameters such as differential pressure, oxygen consumption, optical density, and biofilm detachment through camera monitoring of the effluent stream. We illustrate the versatility and utility of this system by investigating the dynamics of growth and detachment of Pseudomonas aeruginosa biofilms in an example experiment. This innovative micromodel technology opens up new ways for studying biofilm behavior in a controlled and dynamic manner, with potential applications in various fields including microbiology, biotechnology, and environmental science.

Part III

Study on the interplay of hydrodynamics and biofilm growth in porous media

11 Introduction

The study of biofilm growth within porous media is of great significance as biofilms can greatly affect the hydrodynamic parameters of the system. By analyzing and interpreting data obtained from previously presented biofilm growth experiments, we can have an idea of the biofilm growth and detachment patterns. In addition, by performing X-ray imaging on biofilm-inoculated porous media and comparing it with data obtained from scanning empty porous media, we can gain a better understanding of the impact of biofilm growth on the porosity and biomass distribution within the porous structures. Additionally, by performing CFD simulations, we can gain insight into how biofilm growth affects the hydrodynamic parameters of the system, such as pressure and velocity fields, and how flow heterogeneities affect the growth and distribution of biofilms within the porous media. CFD, or Computational Fluid Dynamics, is a numerical method that uses computer simulations to study and analyze the behavior of fluids in various applications, including aerodynamics, combustion, weather prediction, and biomedical engineering, by solving the governing equations of fluid flow using computational techniques. This knowledge can help to develop more effective strategies for managing and controlling biofilm growth within porous media [390], ultimately improving the efficiency of processes that rely on porous media for their operation.

In this section, we will direct our attention solely to the periodic channel network porous medium which features a hydrodynamic landscape that is easier to define, rendering this structure particularly well-suited for investigating the growth of biofilms within porous media. We will further analyze and interpret data obtained through the use of the experimental setup described in part II (chapter 7). We will focus on the characterization of the biofilm detachment events occurring during 4 days of biofilm growth in the aforementioned porous medium using techniques such as Fourier transform analysis and wavelet coherence analysis. Furthermore, we will investigate how biofilm growth affects the porosity and biomass distribution within the porous structures and how it influences the pressure and velocity fields of the system. To achieve this, we will analyze and interpret data obtained from X-ray imaging of both biofilm-inoculated and empty porous media. Additionally, we will perform CFD simulations to gain insights into the hydrodynamic parameters of the system before and after biofilm inoculation of the pore space. We will compare the results obtained from X-ray tomography with the experimental results obtained in part II and CFD results to gain a comprehensive understanding of how biofilm growth impacts the hydrodynamic parameters of the periodic channel network porous medium.

12 Analysis of biofilm growth data

12.1 Definition of growth phases

For the data obtained from a typical biofilm growth experiment, three phases were defined according to the evolution of the differential pressure. The phase of biofilm growth was determined through fitting the data to the logistic function, as we hypothesized that the growth of the biofilm would follow a sigmoid curve. This approach has been previously used in similar biofilm studies in porous media [373]. By accurately identifying the growth phase of the biofilm, we were able to gain a better understanding of its behavior and tailor our experimental approach accordingly. The logistic function has the following form (eq. 12.1)

$$f(t) = \frac{\overline{\Delta P}}{1 + e^{-\frac{t-t_1}{\tau}}} \tag{12.1}$$

where $\overline{\Delta P}$ is the supremum of the values of the function, t_1 the value of the function's midpoint ($f(t_1) = \frac{\overline{\Delta P}}{2}$) and τ the logistic growth characteristic time. To separate between the different growth phases, we defined t_0 as the timepoint where the curve is at 5 % of its maximum value ($f(t_0) = \frac{5}{100}\overline{\Delta P}$) and it represents the transition from phase I to phase II of biofilm growth. In addition, t_2 is the time point where the function is at 95 % of its maximum value ($f(t_2) = \frac{95}{100}\overline{\Delta P}$) and it denotes the beginning

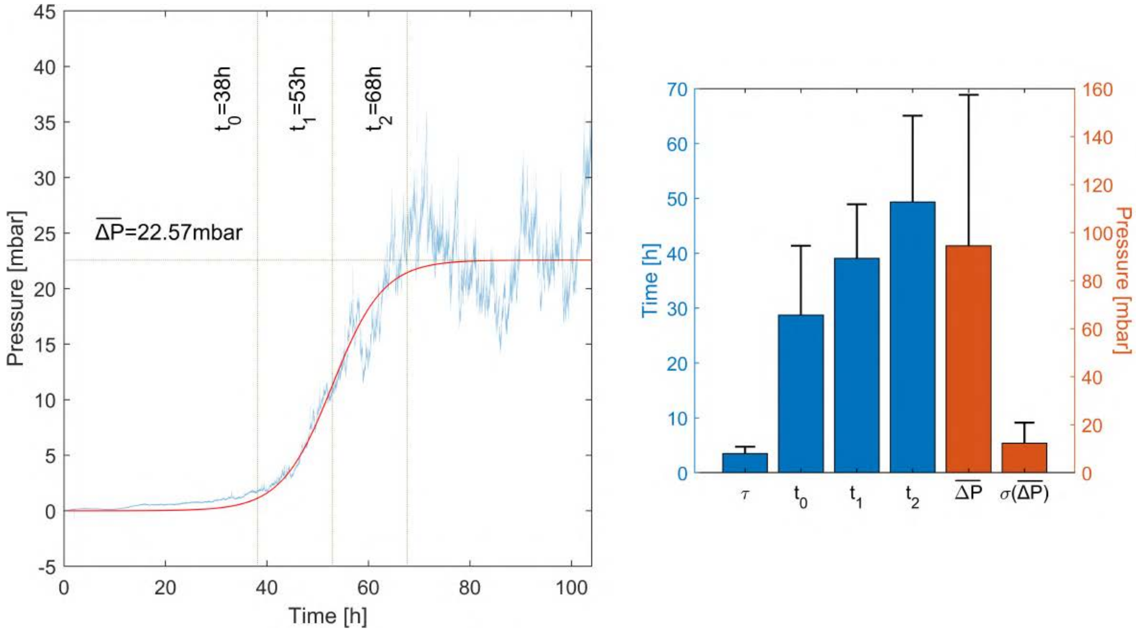

Figure 12.1: (A) Example of fitting differential pressure data to the logistic function (eq. 12.1). The data presented here are the ones obtained during the experiment presented in part II. (B) Comparison of the fitting parameters on differential pressure data of n = 7 independent experiments. The error bars represent one standard deviation from the mean value of each parameter. $\overline{\Delta P}$ is the average differential pressure at phase III of biofilm growth, t_1 is the value of the function's midpoint, τ is the logistic growth characteristic time of the curve,t_0 the time when biofilm growth transitions from phase I to phase II and t_2 the transitioning time from phase II to phase III. Finally, the standard deviation of the phase III differential pressure fluctuations is noted as $\sigma\left(\overline{\Delta P}\right)$. About 68 % of the pressure data points fall within one standard deviation of the mean.

of phase III of biofilm growth. The data from several experiments (n = 7) were analyzed using the same method, and statistical parameters were subsequently derived.

While figure 12.1 shows the results of only one experiment, the global behavior was similar for n = 7 independent experiments where biofilm was grown under identical conditions. The data shown in fig. 12.1A are the ones obtained during the experiment presented in part II of the thesis. The vertical lines in the figure indicate the transition points of the three phases of biofilm growth as defined by t_0 and t_2. The centerpoint of the pressure increase during the second phase of biofilm growth, as defined by the logistics curve fitting, is at $t_1 = 52.9$ h while the characteristic time is $\tau = 5$ h. Mean pressure fluctuation was found to be $\overline{\Delta P} = 22.57$ mbar implying that the pressure levels reached at the steady state (phase III) are relatively low compared to similar experiment (fig. 12.1B).

Applying the same logic for n = 7 experiments we can have a better idea of biofilm's behavior. The determination of biofilm growth phase through curve fitting showed that transition time between phase I and II of biofilm growth is $t_0 = 28.75 \pm 9.13$ h while transition time between phases II and II is $t_2 = 49.35 \pm 14.53$ h. Additionally, the standard deviation of the phase III differential pressure fluctuations was calculated for each experiment individually and it was found to be $\sigma(\overline{\Delta P}) = 12.34$ mbar while the mean differential pressure during the same period was $\overline{\Delta P} = 94.53$ mbar. This implies that 95 % of the pressure fluctuation datapoints are diverging by no more than 25 mbars from mean differential pressure. Biofilm development in porous media flow thus never seems to reach a steady-state.

12.2 Signification of the different growth phases

Here we will re-introduce the experimental data obtained through the experiments presented in part II with the consideration of the previously-defined growth phases. This will allow us to correlate datasets and better understand the behavior of biofilm growth in porous media. Figure 12.2 shows the differential pressure and oxygen measurements, as well as the absorption and camera data. We observed three distinct phases in the evolution of the differential pressure, which we quantified by fitting the logistic growth curve to the data (approach previously used e.g. in [373]). Phase 1 (from 0 to about $t_0 = 38$ h) is a lag phase where bacteria attached to the porous substrate during the incubation start growing and increase oxygen consumption, but without significantly affecting the hydrodynamics and thus the effective permeability of the porous medium. Absorption data show a progressive increase in the amplitude and frequency of fluctuations, suggesting a range of detachment events as bacteria develop. In the second phase, which ranges from about $t_0 = 38$ to $t_2 = 68$ h, the biomass is sufficient to induce a steep increase in the pressure difference ($\tau = 5$ h with τ the characteristic time in the logistic growth) across the porous medium. Oxygen consumption peaks and then stabilizes, while fluctuations in absorption due to biofilm detachment keep increasing further compared to phase 1. The third phase, starting at approximately $t_2 = 68$ h, corresponds to a form of permanent regime where pressure is dominated by important fluctuations, but the plateau differential pressure is relatively stable ($\overline{\Delta P} \approx 23\ mbar$). As previously stated, the global behavior was similar for n = 7 independent experiments where biofilm was grown under identical conditions.

The oxygen consumption measurements is in a good agreement with the differential pressure measurements with an inflection point at 55 h. More specifically, the results demonstrate a steady increase in oxygen consumption up to the inflection point throughout phase I and half of phase II, after which the slope of the curve changes, and the consumption tends to remain relatively constant, resembling a plateau rather than an increase during phase III. The spectrophotometric and camera data indicate minimal or no biofilm production or detachment activity at the beginning while peaks appear later on in both, indicating that biofilm production and detachment starts as early as within 10 first hours of the experiment. Frequency analysis will be performed on both camera and spectrophotometric in the following paragraphs.

12.2.1 Fourier transform analysis of camera and spectrophotometric cell data

Fourier Transform Analysis is a mathematical technique used to analyze signals and data sets that vary over time. The technique is based on the idea that any complex waveform can be expressed as a sum of simpler, periodic waveforms of different frequencies. The Fourier transform can provide insights into the frequency content of a signal, allowing identification of the frequencies at which a signal is repeating or oscillating. This is particularly useful for analyzing signals with periodic or cyclical components. By applying Fourier transform analysis to a signal, we can obtain information about the amplitude, phase, and frequency of the constituent sinusoidal components that make up the signal. This can help identify repeating patterns or frequencies of interest, which can provide insights into the underlying phenomena that generated the signal.

To analyze the spectrophotometric and camera data, the fast Fourier transform algorithm for discrete Fourier transform analysis (DFT) in MatLab was utilized. Specifically, the data obtained between $t_1 = 68$ h to $t_2 = 86$ h was selected for analysis, as this time range falls within the phase III of biofilm growth previously defined. This time period is of particular interest as it is associated with the study of biofilm detachment events during a dynamic equilibrium. By focusing on this specific period, the analysis was able to provide more targeted and accurate insights into the dynamics of biofilm growth and detachment. The data in both cases were resampled to make sure that they are equally spaced and have a constant sampling rate along the sampling period. The sampling rate was chosen as that of the highest rate between the two datasets, being $f = 15.38$ s^{-1} (or acquisition period $T = 0.065$ s). This showed predominant wave components with periods ranging from 4 to 13 minutes for the camera data and 7 to 23 minutes for the camera cell. This suggests that important biofilm detachment events occur approximately in cycles every 4 to 23 minutes at the late stage of

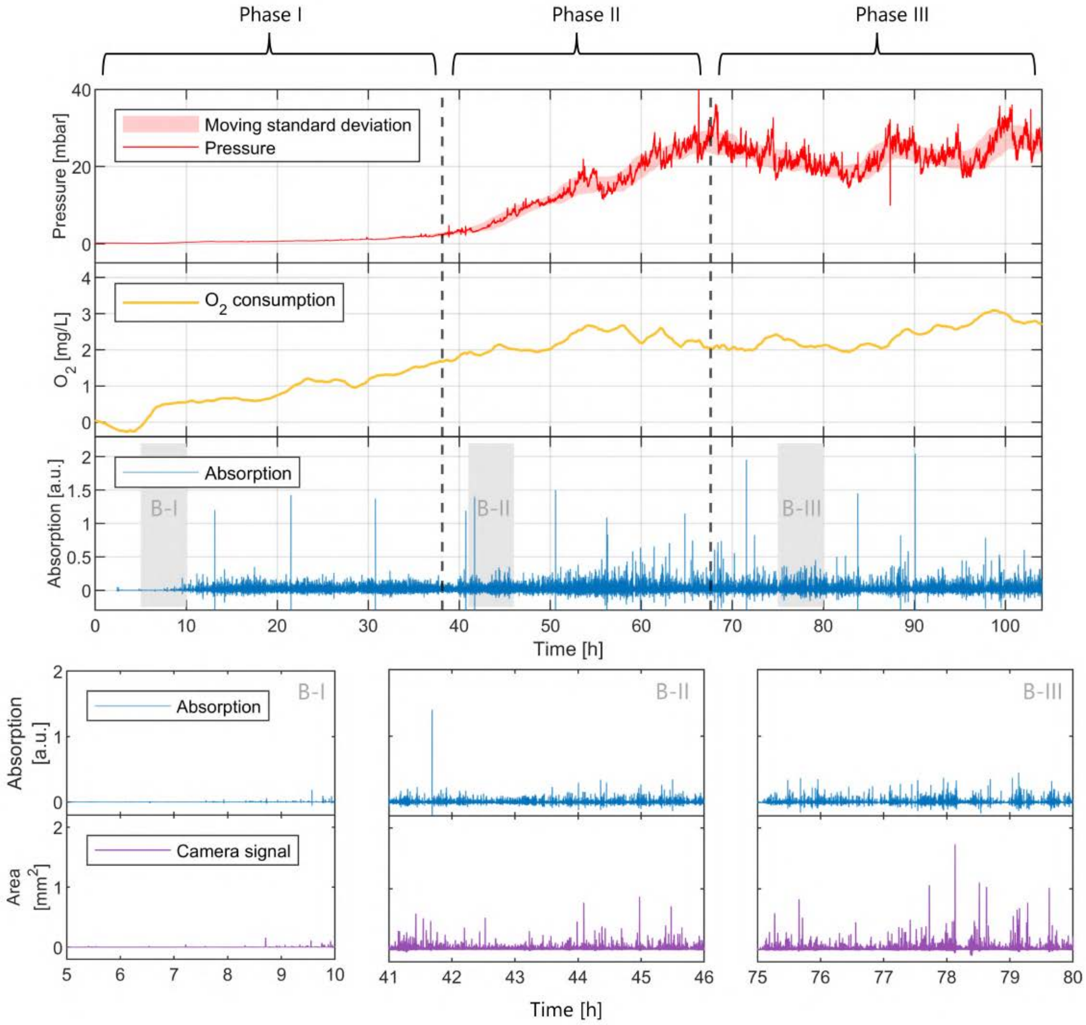

Figure 12.2: Biofilm development experiment. Pressure/oxygen/spectrophotometric/camera measurements of a typical biofilm growth experiment performed using the setup presented part II of this thesis. The biofilm growth experiment is separated in three distinct phases in respect to the evolution of the differential pressure. The pressure moving standard deviation was calculated over 10␣h of data. For each one of the biofilm growth phases, short videos were taken with the camera module (B-I, B-II and B-III) and were compared to the continuous spectrophotometric data. Initially, no peaks are observed in both camera and spectrophotometric signal indicating that no biofilm detachment is taking place. As the experiment progresses, peak frequency increases. The camera signal is correlated to the area in the video occupied by moving-through biofilm patches giving an indication about their size.

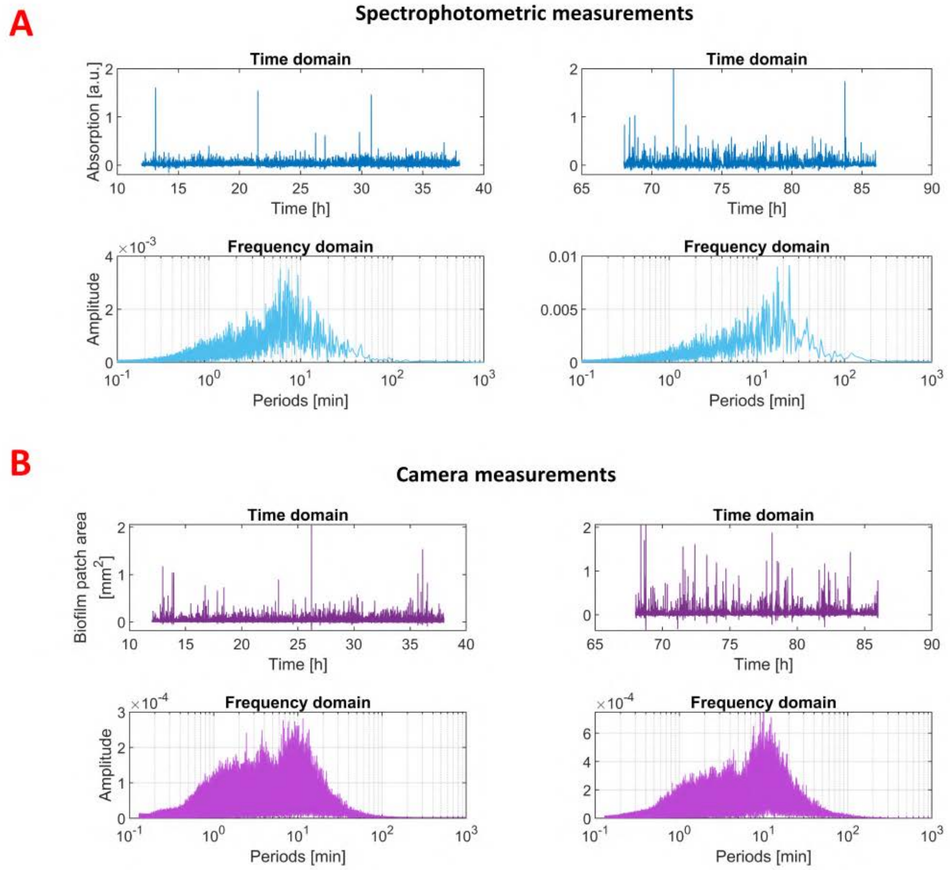

Figure 12.3: Fourier transform analysis of the spectrophotometric measurements (A) and camera cell measurements (B) for an early and a late stage time window.

biofilm growth. However conclusions should be drawn with caution as several factors can affect the analysis. To begin with, the amplitude of the predominant frequencies in the frequency domain is influenced by the amplitude of the peaks in the original signals. However, these peaks may not always accurately reflect the true situation and may not correspond well with the size of the biofilm patches being analyzed. For example two small biofilm patches captured in the same frame in the camera cell, are represented as one large peak rather than two small ones, therefore introducing an error in the analysis.

12.2.2 Wavelet coherence analysis of camera and spectrophotometric cell data

Wavelet analysis is a mathematical tool used for analyzing and processing signals, particularly in time-frequency analysis. The fundamental idea behind wavelet analysis is to decompose a signal into a set of wavelets, which are functions that are localized both in time and frequency domains [432]. Wavelet analysis differs from Fourier analysis, which represents a signal as a sum of complex sinusoidal functions with fixed frequencies. The ability of wavelets to capture localized features in a signal makes them more suitable for analyzing signals with non-stationary characteristics, such as those with sudden changes or transient behavior. In contrast, Fourier analysis is more suitable for analyzing stationary signals with well-defined frequency components.

Wavelet analysis can be performed using different types of wavelets, each with its own characteristics and properties. Some commonly used wavelets include the Haar wavelet, the Daubechies wavelet, and the Morlet wavelet. The choice of wavelet depends on the specific application and the desired properties of the wavelet transform, such as its time and frequency resolution and its ability to capture specific features in the signal [312, 453]. For example, wavelet analysis has been previously used to approximate a method to model biofilm under steady state kinetics [304]. The wavelet used in that work is the Chebyshev wavelet.

Taking this technique one step further, we have wavelet coherence analysis, which is a technique used in signal processing and time-frequency analysis to measure the degree of similarity between two signals as a function of time and frequency. It is a form of cross-spectral analysis that allows for the detection of significant relationships between two signals at different scales [243]. Wavelet coherence analysis uses the wavelet transform to decompose two signals into a set of wavelets with different scales and positions. The coherence between the two signals is then calculated by computing the cross-spectrum of the wavelet coefficients and normalizing it by the individual spectra of each signal. The resulting coherence measure varies between 0 and 1, with values close to 1 indicating a strong correlation between the two signals. Wavelet coherence analysis is particularly useful for analyzing non-stationary signals that exhibit time-varying relationships between different frequency components [476]. This analysis can provide valuable insights into the dynamics of complex systems by identifying significant relationships between different signals at different time and frequency scales [150]. It can also be used to study the propagation of signals in time and space, as well as the synchronization of different oscillatory processes in physiological systems [333].

Three time ranges were selected, one for each of the three growth phases of biofilm. For each time range, the global wavelet spectrum, also known as scalogram, was drawn (right-side plot in fig. 12.4A,B,C). If a vertical slice through a wavelet plot, is a measure of the local spectrum, then a horizontal slice is the time-averaged wavelet correlation magnitude for a specific wavelet width (time span). Performing the same calculation for all the wavelet widths (y axis of wavelet plots in fig. 12.4) one can obtain the global wavelet spectrum over the whole time range. The colorscale in a typical coherence scalogram represents the magnitude of coherence between compared data ranges. It should be noted that the wavelet width corresponds to the period indicated in min on the y axis in fig. 12.4 which is also linked to the wavelet's frequency. Hereafter, in order to avoid confusion, we will refer to the different wavelet frequencies/periods as widths.

It can be observed that for each phase, similar ranges of frequencies show, locally, high correlation. For example in fig. 12.4A there is an agreement in terms of global frequencies between camera and spectrophotometric measurements. For example, if we consider the most predominant peaks of the

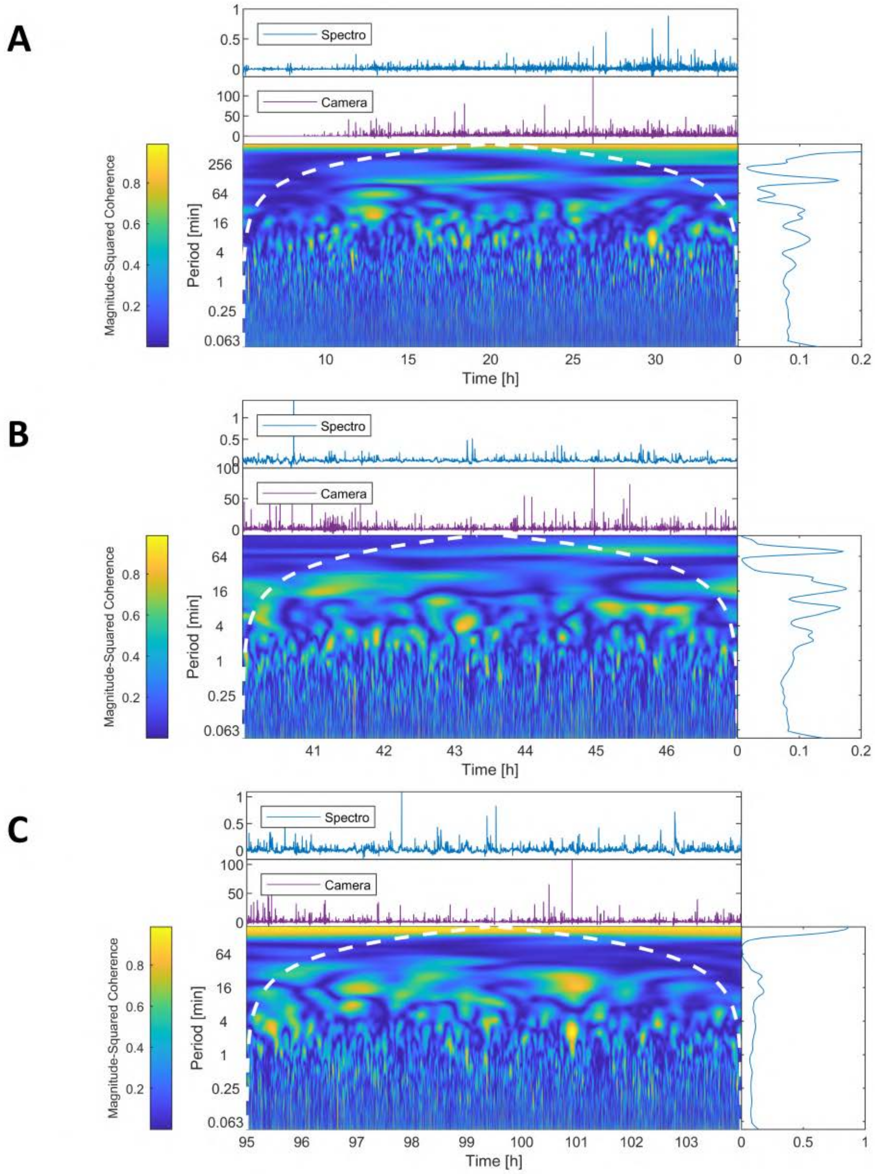

Figure 12.4: Wavelet coherence analysis. Each scalogram represents a different time period of the experiment. (A) corresponds to 0 - 36 h (Phase I), (B) to 40 - 47 h (Phase II) and (C) to 95 - 104 h (Phase III). For each scalogram, the spectrophotometric and camera signals that are compared are shown on top while the global wavelet spectrum is shown in the right. The white dotted line indicates the significance border indicating that data spanning further outward should not be considered. The colorbar indicated the magnitude of the coherence between the two signals.

global wavelet spectra, correlation can be observed at wavelets with a period of 14 min and 19 min both for the fig. 12.4B and C data. However, the correlation is only local throughout time with wider wavelets being positively correlated in longer time ranges while short-width wavelets showing less consistent correlation. This observation is inherent to the method. In addition, during the initial phase (fig. 12.4A) two major peaks are observed in the global wavelet spectrum, at 12 min and at ~100 min. The peak corresponding to high periods is excluded due to the fact that it corresponds to data that are beyond the limits of the significance borders (dotted white line). During that phase, both the spectrophotometric and camera signals show that initially there is little to no activity in terms of biofilm production and detachment which corresponds to the lack of coherence in wide wavelets. Discussion of these results will be provided later on in section 12.3. Overall wavelet analysis seems to be a promising method to identify typical behaviors of biofilm growth in porous media as it allows to differentiate frequency patterns in time and therefore in different biofilm growth phases. However further analysis should be considered.

12.3 Discussion

12.3.1 Clogging vs differential pressure/biofilm detachment

Clogging induced by biofilm growth in porous media can lead to large changes in the pressure drop and the permeability. Our results are consistent with this with pressure drop that varied from several mbars in the empty structure to tens of mbars in the porous media colonized by biofilms. Pressure fluctuations due to the presence of bacteria have been more rarely observed. It has been shown that *Leuconostoc mesenteroides* biofilms [409] can generate such fluctuations, with a mechanism based on plugging and plug-propagation through the porous structure. The authors show that this effect is closely related to the production of dextran and its mechanical properties. *P. aeruginosa* cannot produce dextran and pressure fluctuations in our case are much smaller in amplitude, so that the mechanism inducing these fluctuations is likely different. Recent microfluidic experiments [239] have shown that a competition between growth and shear-induced detachment can generate pressure fluctuations in the same amplitude range for *Bacillus subtilis* biofilms. Opening of flow paths is driven by shear stress causing rupture, while closing results from an increase in the volume of the biomass due to growth. Because pressure fluctuations in our case are also associated with peaks in the spectrophotometric and camera cells, we hypothesize that our observations result from a similar mechanism where the porous medium is saturated in biomass with a stable oxygen consumption but with constant production and flow-induced detachment of biofilm. The fact that our structure is 3D with a topology different from that of microfluidic experiments shows that this phenomenon is not specific to 2D systems and may be ubiquitous in applications.

Comparison with analogous 2D system An equivalent 2D, porous, micro-model was developed by Gabriel Ramos Peroni, post-doc in our team, in order to perform similar experiments in biofilm inoculated 2D porous media. The experimental setup comprised of the porous geometry that was embedded in a microfluidic chip and a pressure pump (Fluigent MFCS-EZ) coupled with a flow meter (Fluigent Flow Unit S) used to supply the needed nutrients (BHI, 37.5 mg/mL, Ampicillin, 300 µg/mL). The microfluidic chip consisted of two mixing zones and a honeycomb channel network (fig. 12.5A), with each channel having a cross section of 100 × 100 µm. The mixing zones on the left and right of the hexagonal network were constantly illuminated with bactericidal UV-C light that would prevent biofilm growth. The flowrate of the pumps was set to 2 µL/min and was regulated by a feedback loop between the pump and the flowmeter where pressurized air was applied in the airtight nutrient container in order to main the set flowrate (fig. 12.5B).

The bacterial strain of *P. aeruginosa* used here is the same as the one used for the 3D-printed bioreactor experiments (PAO1). Image acquisition is performed every hour with an inverted microscope (Nikon Eclipse Ti2-E) using a 4x objective (Plan Fluor 0.13 NA) and an exposure time of 80 ms. For these images, a light source (Lumencor Sola light engine SM at 10%) filtered by a cube (Nikon filter cube GFP-3035D) is exciting the green fluorescence protein produced by the bacteria (GFPmut3).

In figure 12.5D it can be observed that there are fluctuations in pressure, which is an observation we have with the 3D micromodel experiments. Similar biofilm-induced, pressure fluctuations have been reported in similar works [239, 409]. The exact mechanism that gonverns these fluctuations is still unknown, yet it is believed that this intermittency is caused by the competition between microbial growth, which leads to the closure of preferential flow paths, and biofilm compression and rupture, which govern their opening. As biomass clogs a pore channel, it causes the flow path to be diverted and consequently differential pressure builds up. As more and more pores become clogged, a significant amount of pressure can build up, leading to an abrupt declogging event. These major, pressure-drop events are commonly considered to be caused by this pressure-induced mechanisms. However, it is important to note that shear stress can also induce biofilm detachment events, which can lead to small, local pressure fluctuations.

The global power spectrum of a wavelet analysis performed on the whole dataset (fig. 12.5) revealed that a reoccuring event has a period of 1.2, 2.4 and 7 hours implying that major detachment event occures periodically on those times. A rough estimation of the time it takes for the bacteria to fully clog a channel of the 2D experimental setup showed that it takes about 5 hours. The estimation was performed by simply considering bacteria as space-filling disks (diameter of 1 µm) that grow expodentially with a doubling time of 30 minutes. The bacteria would continue to grow until they would fill up the whole cross-section area of a channer (100 × 100 µm). The wavelet analysis and the time estimation showed characteristic times of the same order of magnitude. However, regarding the estimation, no EPS matrix production was considered and the effect of the flow was not taken into account. In the case of experiments in 3D, Fourier analysis highlighted the minor pressure drop events that occured in the timescale of several minutes to almost half an hour. More precisely, the camera cell data gave frequencies of less than ten minutes in period and spectrophotometric cell data showed several predominant frequencies with a period in between ten minutes and half an hour. These methods tend to accentuate these small detachment events as for example, the camera cell is capturing even the slightest biofilm patch that is detaching from within the porous medium. The datasets that were analyzed were 18 hours long in the case of late stage biofilm growth, enough time to capture repeating patterns of several hours. However, no such frequencies were featured in the frequency domain. This would suggest that in the case of 3D porous media, pressure-driven, significant biofilm detachment events are less prominent than in the case of the 2D system and that shear induced minor detachment events dominate the landscape. This could be potentially explained by the different pore connectivity in the two systems. In both systems, when a channel is clogged due to biomass accumulation, flow is redirected towards neighboring channels. However in the case of 2D, the available flow paths are limited compared to 3D which offers more versatility in terms of possible flow paths therefore when a channel is declogged due to pressure, the pressure drop tends to be larger and more important in the 2D case rather than in 3D. Unfortunatelly, the wavelet analysis performed on the same data, could not give any indication about repeating events in timescales of 4 hours and more because the time windows on which the analysis was applied was relatively narrow.

12.3.2 Clogging vs oxygen consumption

The relationship between bioclogging and oxygen consumption in a porous system with biofilm growth can vary depending on several factors, including the type of microorganisms present in the biofilm, the environmental conditions, and the availability of oxygen. In general, biofilms are known to consume oxygen as part of their metabolic processes [427], which can lead to decreased oxygen availability in the pores of the porous system. This can result in decreased oxygen diffusion into the biofilm and the surrounding porous media, leading to anoxic or anaerobic conditions within the biofilm and the surrounding environment. Bioclogging can further exacerbate oxygen consumption in a porous system with biofilm growth. As the biofilm accumulates and occupies the pores of the system, it can reduce the transport of oxygen into the biofilm and the surrounding media, resulting in increased oxygen consumption by the biofilm to sustain its metabolic activities. This can lead to increased bioclogging

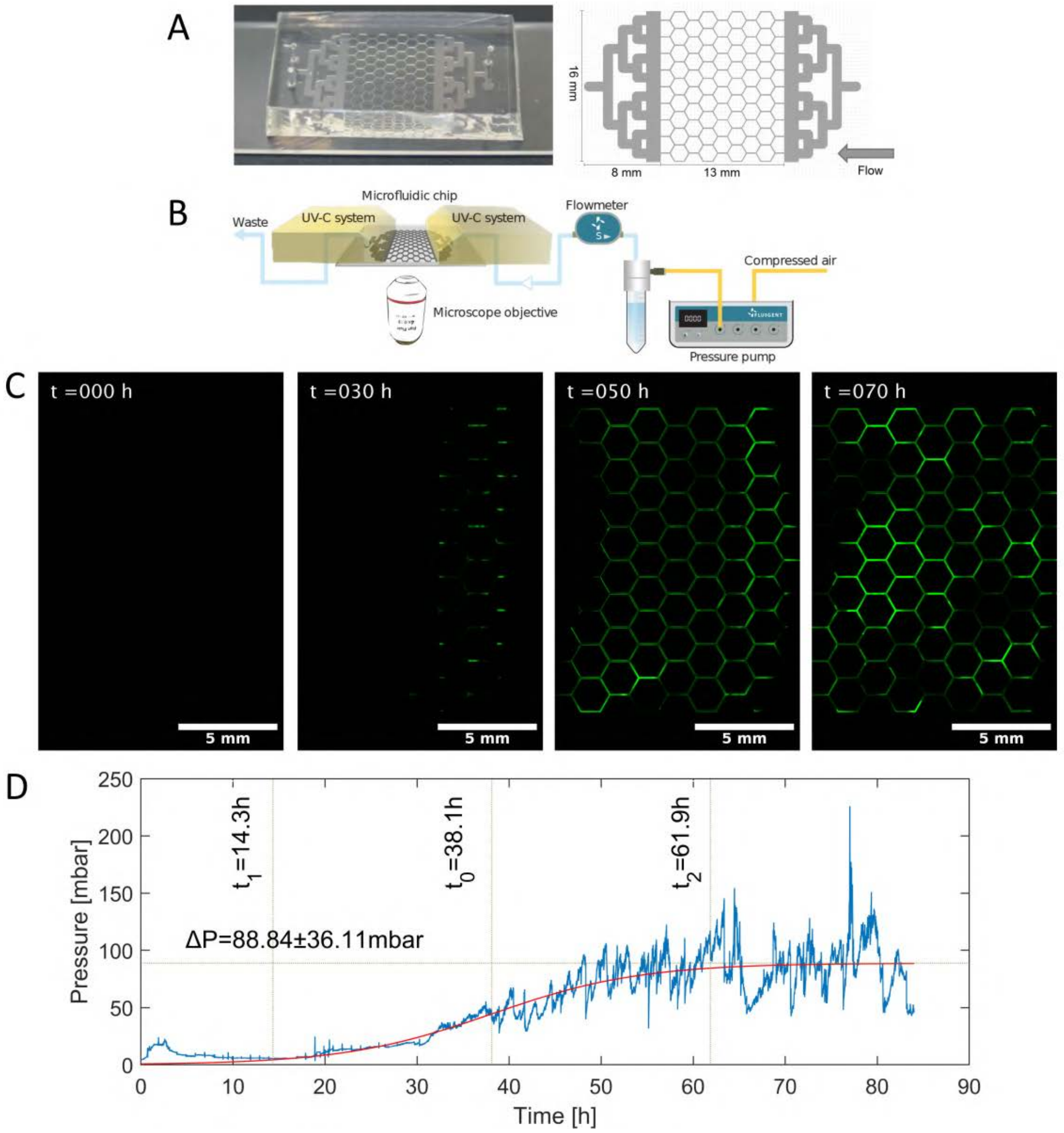

Figure 12.5: Microfluidic analogous, 2D system. (A) Microfluidic chip. On the left, we present a picture of the micro-patterned PDMS plasma bonded directly to a glass slide. On the right, the schematic shows the different regions: the mixing zones (inlet and outlet) and the hexagonal network channels. (B) Schematics of the fluidic system. A constant flowrate is imposed through the microfluidic chip using a pressure pump coupled with a flow meter. Two UV-C systems irradiate both the inlet and outlet of the chip during the total duration of the experiment. (C) Fluorescence images at different stages of biofilm growth indicate the biomass distribution throughout the porous medium. (D) Analysis of the pressure data indicate similar fluctuation patterns compared to the 3D micromodel that was previously showed.

and further reduction of oxygen availability in the system, potentially leading to enhanced anaerobic processes, such as denitrification or sulfate reduction, depending on the specific microorganisms present in the biofilm.

In our experiment, results showed that there is no global, oxygen limitation since the oxygen concentration at the outlet was not zero. However, local oxygen limitations might occur nonetheless. When part of the porous medium is clogged, it could imply that another portion may be deprived of oxygen and nutrients. It's important to note that the relationship between bioclogging and oxygen consumption can be complex and may also depend on other factors, such as the availability of other electron acceptors or the presence of alternative metabolic pathways in the biofilm. Additionally, biofilms can exhibit different growth patterns and characteristics depending on the specific conditions and microorganisms involved. To investigate these transportation phenomena, one possible approach would be to conduct CFD simulations using original datasets or carry out microfluidic experiments with spatially resolved oxygen sensors. Overall, a detailed understanding of the specific biofilm system and its environmental conditions is necessary to accurately assess the relationship between bioclogging and oxygen consumption in a particular porous system.

13 Biomass distribution in the porous medium

13.1 Porous structure characteristics

In studying the growth of biofilms within porous media, it is crucial to consider the structural characteristics of the medium. Porous media, such as periodic channel networks, are composed of interconnected channels that create a complex geometry, which plays a significant role in the hydrodynamics of the system. In this study, we focus on a periodic channel network porous medium, inspired by what is known as Laves network or Laves graph [91].

A channeled network modeled after the Laves network is a complex and highly interconnected structure composed of a series of interconnected channels that meet on nodes, at an angle of 120°. Each node of this graph has a connectivity of 3 meaning that three channels are connected to each node. However, this is not always the case considering the finite dimensions of the 3D-printed graph. The connectivity of channels within the porous medium is a crucial factor that impacts the hydrodynamic properties of the medium. Specifically, the border effects, which are caused by the unique connectivity of channels near the outermost boundary of the medium, can have a significant impact on the transport and distribution of substances within the medium. In the context of this work, the border effects refer to the fact that channels at the outermost boundary of the porous medium exhibit a connectivity of 2 at each node, while channels in the bulk of the medium have a connectivity of 3. Understanding the role of border effects is important for accurately predicting the behavior of biofilms within the porous medium, as the connectivity of channels near the boundaries can impact the transport and distribution of nutrients and other substances necessary for biofilm growth.

The porous medium consists of two types of channels in respect to their orientations. Channels perpendicular to the main flow direction (ChA) and channels angled at 45° relative to the main flow direction (ChB) create distinct hydrodynamic landscapes that can impact the growth and distribution of biofilms within the medium (fig. 13.1). The orientation of a channel can significantly affect its hydrodynamic parameters. Channels oriented perpendicular to the main flow direction tend to experience negligible velocities, while channels angled relative to the main flow direction facilitate the formation of high-velocity, helicoidal flow patterns. Additionally, the shape of the channel cross-section can also impact its hydrodynamic properties. For example, channels with circular cross-sections tend to exhibit more uniform flow patterns, while channels with non-circular cross-sections can induce secondary flows and turbulence.

In this study, we fabricated a 3D-printed porous medium with specific geometrical features. The porous medium had a diameter of 8mm and a vertical length of 14mm in the Z direction. The channels within the medium had a diameter of 300 µm and a length of 700 µm. In total, the porous medium contained 39 ChB channels at both the inlet and outlet regions. For a flow rate of 2 mL/min, we calculated that the mean fluid velocity in each of these channels is about 12.1 mm·s^{-1} while the Reynolds number is close to 4. The initial permeability of the porous medium was experimentally found equal to 5.26·10^{-11} m^2 as described in the previous chapter.

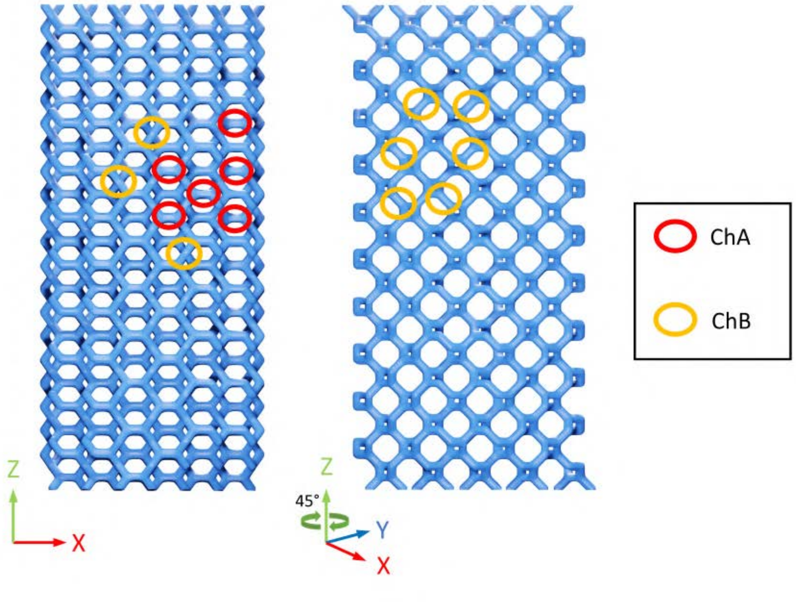

Figure 13.1: (A) The porous structure contains two types of channels. Channels A are positioned perpendicularly to the main flow direction while channels B are at 45° from the main flow direction. The view on the right (A) is rotated 45° around the Z axis in respect to the view on the left.

13.2 Biofilm growth and staining protocol

Preparation of biofilm inoculated bioreactor In order to perform X-ray imaging, the same procedure to grow biofilm in porous micro-bioreactors was applied as described in the previous chapter (section 7.3). Ideally, these biofilm growth experiments were carried out for a period of 3 to 4 days before proceeding with the staining protocol and the X-ray imaging. In the experiment described hereafter, biofilm was grown in a bioreactor similar to the one used for the biofilm growth experiments, presented in Part II of this work. Biofilm was cultured within this bioreactor under carefully controlled conditions for three days, enough to reach the third phase of growth. At the end of that phase, the gear pumps were stopped, the tubings were carefully unplugged to avoid introducing any air bubbles, and the inlets/outlets were plugged with luer stops. Only the inlet and outlet designated for the contrast agent injection were left unplugged for the staining protocol. By following this protocol, we were able to ensure the integrity of the biofilm and obtain high-quality X-ray images of the biofilm for further analysis.

Injection of $BaSO_4$ contrast agent Before the experiment, the contrast agent was prepared according to the protocol described in the thesis of Anne Edith Larue [246], using a combination of commercially available medical-grade barium sulfate suspension (Micropaque, Guerbet) and low-gelling temperature agarose from Sigma-Aldrich. The low-gelling temperature agarose was selected to enable the injection of the contrast agent in liquid form. The contrast agent was introduced into the bioreactor in liquid form at 37 °C and its polymerization was then triggered by cooling the sample between at around 10 °C. Once polymerized, the hydrogel remained solid due to a hysteresis effect until its melting point (approximately 50 °C), which allowed for X-ray CMT imaging at room temperature without causing depolymerization.

The gel solution was made by combining 0.2 g of agarose powder with 10 mL of bacterial culture medium in an Erlenmeyer flask, resulting in a 2 % (w/v) concentration. The mixture was sterilized and the agarose dissolved by autoclaving at 121 °C. After autoclaving, barium sulfate suspension was added to the non-polymerized gel to achieve a 50 % (w/w) concentration in the final solution. To carry out this manipulation, the density of the barium sulfate suspension was previously determined. For this the wright of known volumes of the $BaSO_4$ solutions were repeatedly measured using a precision balance.

The barium sulfate particles had a size of approximately 1 micrometer and were insoluble in water. The stock product had a concentration of 1 gram per milliliter of barium sulfate. To eliminate barium sulfate aggregates, the mixture was vortexed and filtered using a vacuum pump with 30 µm nylon filters. The solution was treated under a sonication bath for 5 min to further ensure the small size of the particles. The final concentration of barium sulfate in the contrast agent was around 30 % w/w, slightly reduced by the filtration process. The contrast agent was placed in a sterile centrifuge tube and left to rest in a 40 °C water bath. Just prior to injection, the centrifuge tube was thoroughly shaken to prevent the settlement of barium sulfate, then degassed in a vacuum bell jar and loaded into a sterile syringe.

The injection of the contrast agent was as follows. The syringe containing the contrast agent was carefully connected to the flow cell to avoid introducing any bubbles. The injection was performed at a flow rate 10 times slower than the growth flow rate, in order not to promote sloughing (0.2 mL/min). After the effluent turned white due to the presence of barium sulfate, the bioreactor main inlet and outlet were sealed with luer stoppers. The bioreactor was then refrigerated at 4 °C for 15 minutes to quickly solidify the gel and prevent sedimentation of the barium sulfate particles and the bioreactor was transferred to the Institute of Fluid Mechanics of Toulouse where the X-ray tomography setup was located.

13.3 X-ray imaging protocol and data processing

Imaging protocol All of the X-ray imaging of the various porous structures as well as that of the biofilm inoculated bioreactors was performed with the same scanning parameters. The X-ray tomography setup (EasyTom XL 150, RX Solutions) was equipped with a sealed-tube X-ray source (Micro 150, RX Solutions) capable of delivering 75 W maximum power. Only the middle part (porous medium) of the bioreactor was imaged. The imaging was performed at 60 kV tube voltage and 165 µA tube current with a frame rate of 2 images per second and averaging 8 images per projection. By adjusting the position of the sample relative to the source and the sensor, a voxel size of 9 µm was achieved.

Prior to commencing, the detector was calibrated by measuring the signal received in the absence of x-rays and the signal received from the source with no sample hindering the photons in between. During the acquisition a full rotation of the sample was performed and at the end of the acquisition, reference images were taken to verify that the sample was not moved during the acquisition. The software of the X-ray tomographer offered some post-treatment options for the projection datasets. It performed a geometrical correction by comparing the reference images with the main acquisition images to verify that the sample was not moved. Circular artifacts were removed automatically, the tomographs were recreated using the "filtered backprojection" method and they stacks were exported as .tiff image stacks.

The filtered backprojection algorithm works by first applying a mathematical filter to the projections to remove any noise or artifacts that may be present. This filtered data is then back-projected through the object to reconstruct the image. During the backprojection step, the filtered data is traced back along each ray to determine the contribution of each point in the object to the projection. The process is repeated for all projection angles, and the resulting data is combined to create a 3D image of the object. This technique is the most commonly used technique in CT medical imaging.

Post-processing of µCT datasets Two data sets of images were obtained for each bioreactor experiment, 1) one prior to biofilm inoculation (DS1), when the bioreactor was completely empty and 2) one at the end of a typical biofilm growth experiment (DS2) where the bioreactor is inoculated with biofilm. The raw datasets were post-processed using a combination of Amira-Avizo v2022 (ThermoFisher) [2] and IPSDK v3.2 (Reactiv'IP) [187] software. Firstly, the image stack DS2 was translated and rotated in X, Y and Z directions so that it is aligned with the DS1 of the empty bioreactor. This was done by utilizing the *Image Registration* module provided by Avizo. A non-local means filter (search window 21, local neighborhood 5, similarity value 0.6) was applied to the DS2 dataset. The grayscale histograms of the two whole datasets are given in fig. 13.2. It can be seen that two distinct peaks can be identified, suggesting a relatively straightforward segmentation in case of manual thresholding. However, to obtain more consistent results, image segmentation was performed on both datasets using a human-trained machine learning algorithm implemented by IPSDK [187]. By binarizing the DS1 dataset, the bioreactor material was obtained while by segmenting the DS2 dataset, the biofilm phase was differentiated from the liquid/bioreactor material phase. By subtracting the binarized datasets, three distinct phases were identified: biofilm, liquid phase and solid bioreactor material phase. The porosity of the porous medium was considered as

$$\varphi = V_{pores}/V_{tot} \tag{13.1}$$

where φ is the porosity of the medium, V_{pores} is the volume of the pores and V_{tot} the total volume of the porous medium. Here the total volume was taken as a cylinder of length of 14mm and a diameter of 8mm while the pore volume was extracted from the respective µCT dataset through image analysis.

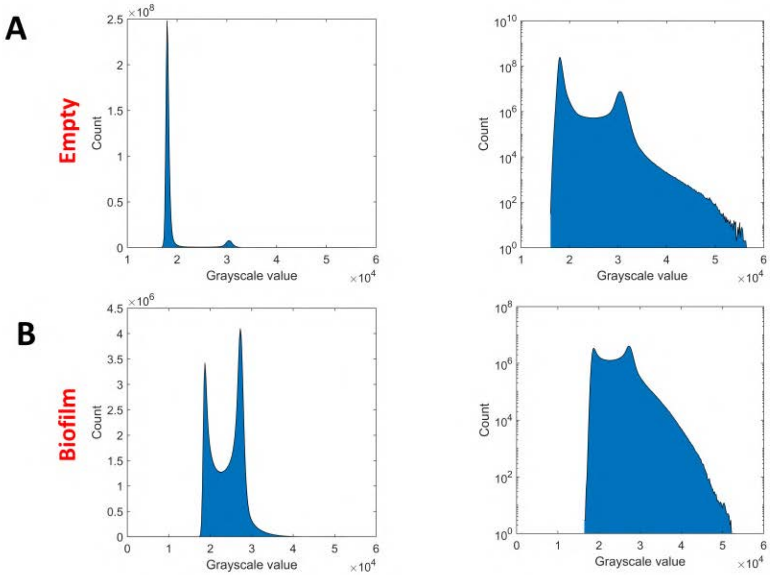

Figure 13.2: Grayscale histograms of empty (DS1) and biofilm inoculated (DS2) bioreactors after application of a non-local means filter on the second one.

Channel-specific analysis of µCT datasets Next, the percentage of biomass occupation was calculated for channels ChA and channels ChB separately. To do that, the binarized X-ray image stacks of empty (DS1) and biofilm inoculated (DS2) bioreactors were used. A projection on the XY plane, of the each dataset was obtained and the resulting image was properly rotated around the Z axis so that channels ChA are orthogonal to the primary axes. The pixel values were integrated both in the x and y direction and the resulting curves were plotted (fig. 13.3A, blue curves). There curves had a characteristic wave-like pattern where the "wells" correspond to the uni-directional sum of the pixel values of ChA channels. Then, by using the *findpeaks* algorithm in MatLab, the coordinates of the centers of the channels were extracted, by locating the local minima of each of these curves. Considering that these projections have a pixel size of 9 µm, and that the area of interest of each channel is 300µm long, stripes of 32 pixels in length were cut aligned with the center of each channel, so that ChA channels are isolated in the X and Y direction. The biomass occupation percentage was extracted by summing up all the pixel values of the biofilm inoculated channels in each direction and dividing that number to the sum of the empty porous medium pixels. In order to obtain the biomass occupation percentage in ChB channels, a projection of the same image stacks (DS1 and DS2) on the XZ plane was calculated. Then the resulting images were rotated around the Y axis by 45° so that the channels of interest (ChB) are orthogonal to the main axes (fig. 13.3B). For the rest, the same procedure was followed as before.

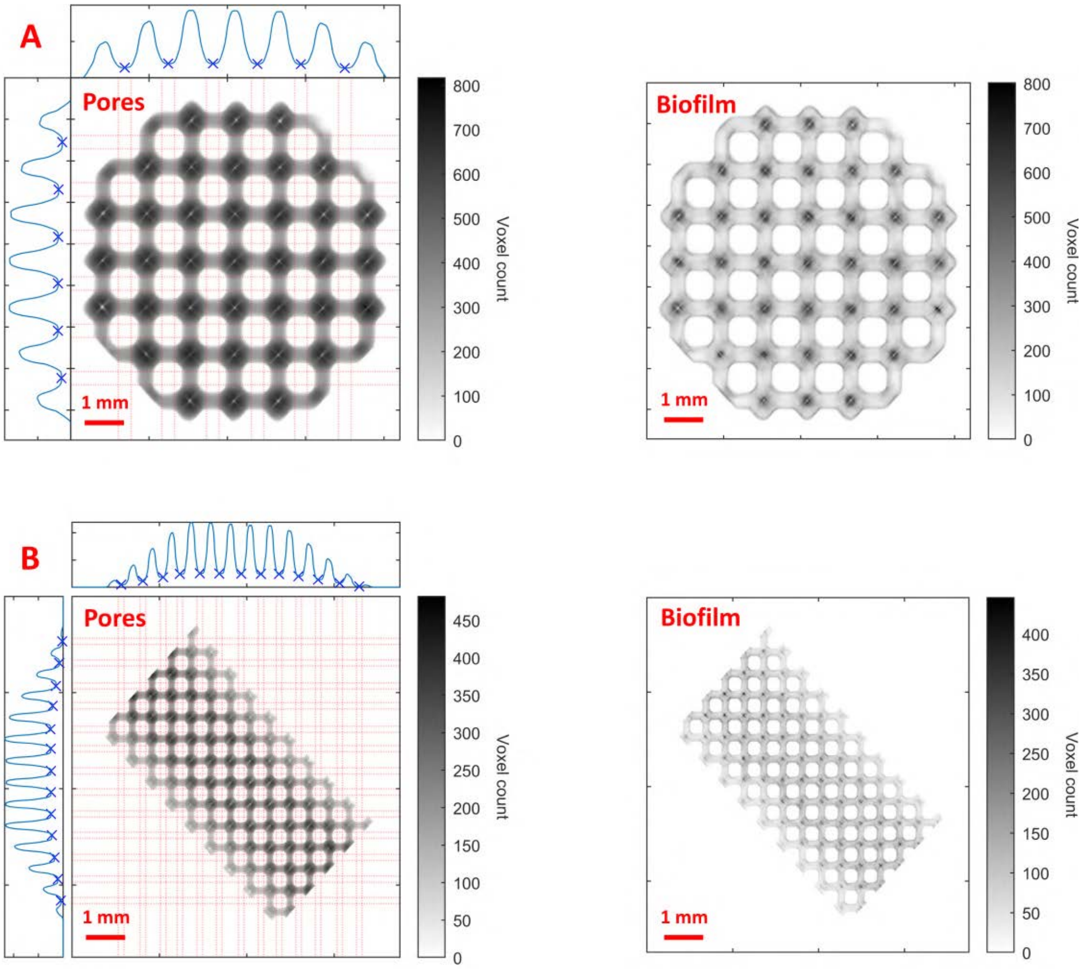

Figure 13.3: Analysis of projections of binarized image stacks obtained through X-ray tomography. The biomass percentage in channels ChA was obtained by projecting the image stack on the XY plane (A) for both empty (DS1) and biofilm inoculated datasets (DS2) while the same information for channels ChB was obtained by calculating the projection on the XZ plane and rotating the image 45 °C (B). Then the regions occupied by the corresponding channels were isolated and the percentage was calculated according to the procedure described in 13.3. The blue curves represent the pixel integration profile of the corresponding pictures in the X and Y direction. The red dotted lines indicate the limits of the regions containing the channels in the X and Y direction.

13.4 Results

In this study, two datasets of images were obtained for each bioreactor experiment. The first dataset (DS1) was acquired prior to biofilm inoculation when the bioreactor was not inoculated with biofilm, and the second dataset (DS2) was acquired at the end of a typical biofilm growth experiment where the bioreactor was inoculated with biofilm. After post processing the raw data, the porosity change from DS1 to DS2 was determined to be 15.11 %, with the porosity decreasing from 32.21 % to 17.10 % due to biofilm growth. Channels ChA and ChB were analyzed to determine the biomass distribution within the porous medium. The results showed that ChA channels were occupied by 41.47 % by biofilm, while ChB channels were occupied by 54.33 %.

The observed differences in the biofilm occupancy levels between channels ChA and ChB suggest that there may be distinct hydrodynamic conditions in these two channels. These differences in the hydrodynamic environment could affect the accumulation of biomass due to various physical forces or the differential transport phenomena that occur in the channels. The significant reduction in the porosity of the biofilm-inoculated porous medium by 15.11 % also supports the idea that biofilm formation is a dynamic process that is influenced by environmental factors. Overall, these findings suggest that the hydrodynamic environment in channels ChA and ChB may play a crucial role in the growth and development of biofilms, and further studies are warranted to investigate this relationship in more detail. Additional discussion will be provided later on.

14 Effect of biofilm formation to the hydrodynamic environment of the porous medium

14.1 Setting up CFD parameters

Understanding the fluid flow and transport properties in these complex porous media is crucial. An additional layer of complexity is added since biofilm is grown inside the pore space, altering the hydrodynamic environment. To better understand the hydrodynamic conditions of this particular structure, CFD simulations were conducted on both an empty porous structure and a biofilm-inoculated porous medium thanks to Omar Mohtari, PhD that run the simulations through CALIMP on the Olympe supercomputer. To generate the mesh for these simulations, we used X-ray tomography to generate the image stacks of an empty bioreactor (DS1) and a bioreactor inoculated with biofilm (DS2), with the latter being injected with $BaSO_4$ to increase contrast. The resulting image stacks were processed using binarization techniques to extract the pore space and liquid phase from DS1 and DS2, respectively. The contrast injection process as well as the imaging protocol is detailed in paragraphs 13.2 and 13.3 respectively.

We simulated the flow in the porous network by solving the incompressible Navier-Stokes equations with no-slip & no-penetration conditions for liquid/solid and liquid/biofilm interfaces. Flow resulted from imposing the velocity at the inlet ($v_{in} = 6.17 \cdot 10^{-4}$ m/s) and a pressure at the outlet ($P_{out} = 0$ Pa). An "extra" rectangle of thickness of 0.5 mm was designed at the inlet to evenly distribute the imposed velocity and better reflect real conditions (fig. 14.1A). The imposed velocity was selected so that the volumetric flow rate is the same as the one imposed during the biofilm growth experiments described in part II ($Q = 2$ mL/min). Space discretization was based on the Marker-and-Cell (MAC) scheme [309] with the unknown velocities evaluated on the faces of mesh elements and the pressure unknowns at the center of each element. The whole 3D domain, including the solid, was discretized using a uniform grid with a local refinement of level 2 near the fluid-solid interface (fig. 14.1B). Non-conforming local refinement was obtained [76] by cutting each edge into 2 equal parts and thus each face and cube into 4 parts. The finest mesh had a number of cells of about 6 millions. No-slip & no-penetration conditions were approximated by adding a penalization term in the momentum transport equation [214], a standard approach to computing flows with obstacles [46, 51]. The penalization was 0 in the liquid, so as to recover the Navier-Stokes equations, and -10^{10} times the velocity inside the solid to obtain negligible velocities. Error estimations and numerical efficiency were previously established in [13]. Time discretization was based on a fractional-step of pressure-correction [152].

The solver was implemented in the CALIF3S platform [330] developed at the French Institut de Radioprotection et de Sûreté Nucléaire (IRSN). Parallel computations were executed on the CALMIP supercomputer Olympe, based on a domain decomposition approach with METIS (4.0.3) graph partitioner and the OpenMPI (3.1.5) library. At each iteration, the linear system arising from the prediction step was solved using the Generalized Minimal Residual Method. The projection step was solved using the classical conjugate gradient method with an initial stop criterion at 10^{-6}. Stationary state is attained after approximately 300 iterations. The mesh had approximately 25 million mesh cells and required one hour of computation on 288 processors.

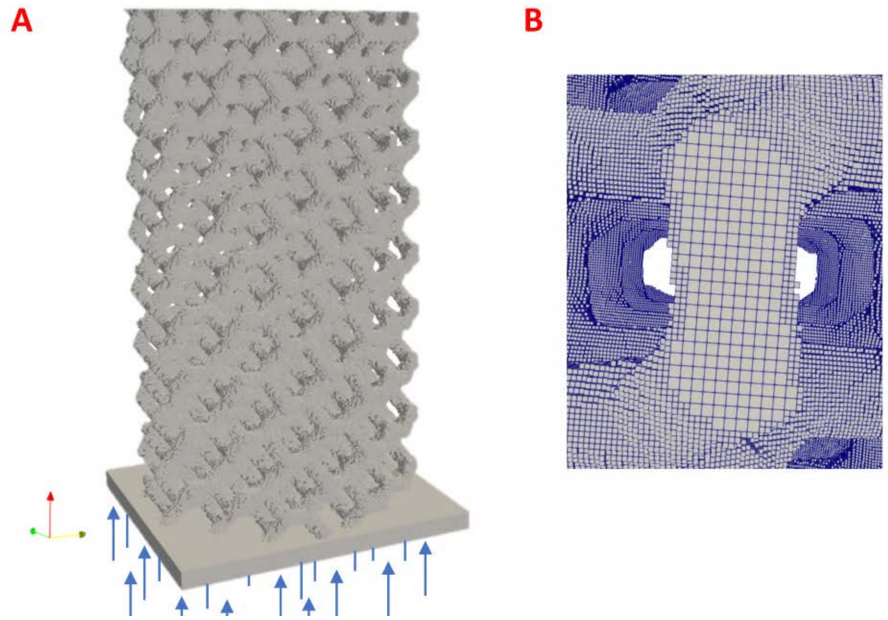

Figure 14.1: (A) Simulation mesh of an empty porous medium, including an additional rectangle at the bottom to ensure that the imposed fluid velocity is homogeneous at the inlet of the porous medium. (B) Cross-sectional detail highlighting the mesh refinement near the edges.

14.2 Global CFD results

Studying the effect of biofilm formation on the hydrodynamic environment of a porous medium is crucial to optimize various processes that rely on porous media. Biofilms can significantly alter the hydrodynamic parameters of a system, including pressure and velocity fields, which in turn affects the growth and distribution of biofilms within the porous structure. Therefore, the impact of biofilm growth on the hydrodynamic environment of a porous medium was investigated through CFD simulations of the steady state flow. As a reminder to the reader, the empty porous medium, modeled after the laves network, was used for the following simulations to get an insight of the hydrodynamic environment experienced by the biofilm but also to demonstrate the capabilities of the 3D printed porous medium. At a first glance on the results, the velocity field in the case of an empty porous medium appeared to have an axisymmetric profile along each channel, characteristic of Poiseuille flow with velocity being zero on the faces of the porous structure and maximum on the center of the channels (fig. 14.2). Some channels at the inlet and at the outlet side of the porous structure appeared to have somewhat elevated pressure due to boundary effects, since their connectivity to neighboring channels is lower than that of channels in the middle of the structure. Upon comparing the velocity field of the empty porous medium to that of the biofilm-inoculated porous medium, it is apparent that the velocity field in the biofilm case is more heterogeneous, as expected given the wide distribution of pore sizes. Furthermore, the velocities in the biofilm-inoculated porous medium appear to reach higher values, at least locally.

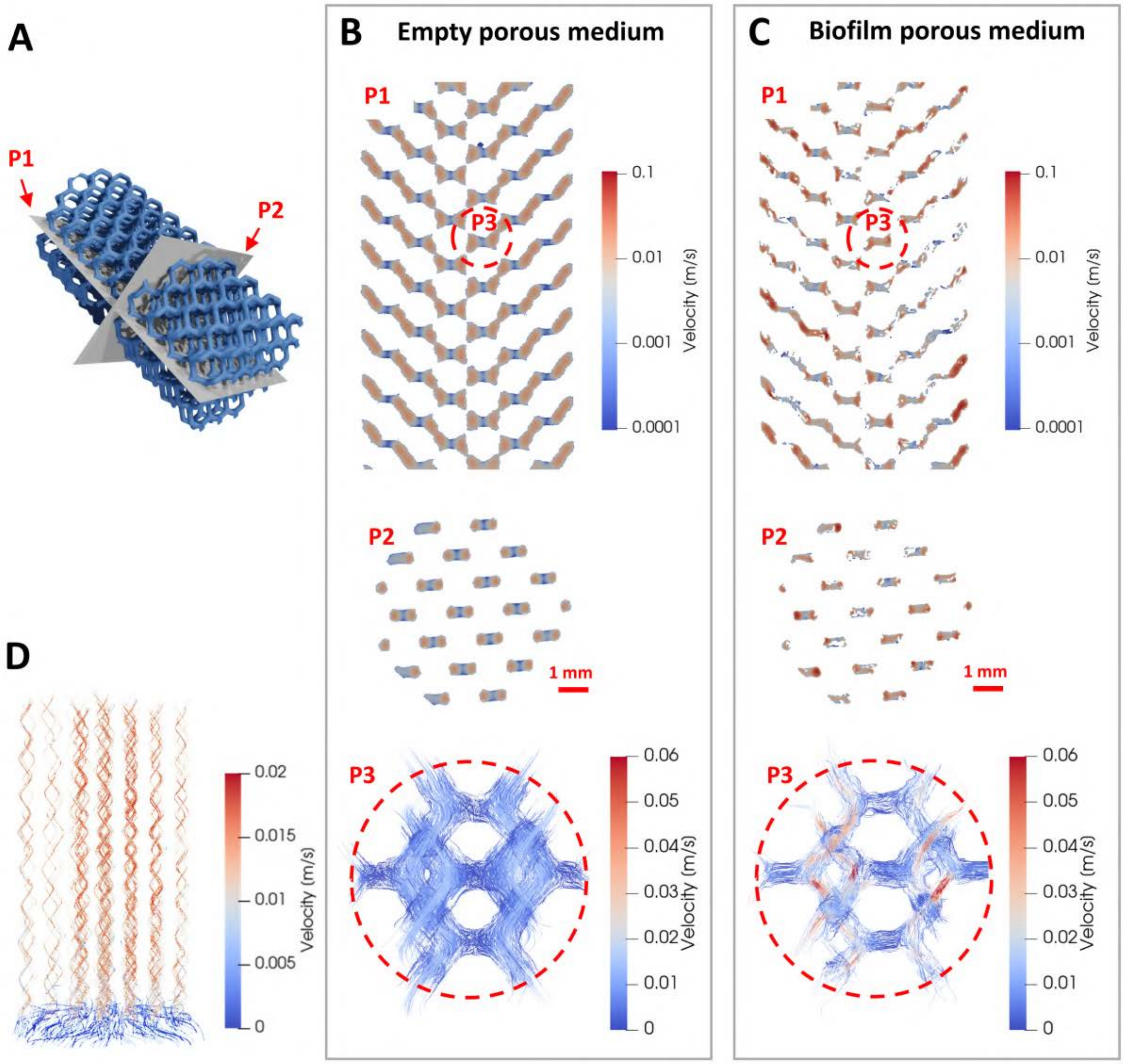

Figure 14.2: CFD simulation results. (A) A schematic of the two planes visualized is shown on the left. (B-C)The center and right scheme show the field of velocity's magnitude for the empty and the biofilm-inoculated porous medium. (D) Visualization of streamlines generated for 1000 particles introduced at the inlet. The empty porous medium dataset was used.

Furthermore, we utilized the velocity field of the empty porous medium to generate the streamlines. A streamline is a curve that is tangent to the velocity vector of a fluid flow at every point in the flow field. Streamlines are useful tools for visualizing fluid flows and can provide information on the direction of the flow field at various points within the flow field. By tracing streamlines in a steady-state fluid flow, one can visualize the flow path of a fluid particle as it moves through the flow field. Streamlines can also be used to determine the location of stagnation points, regions of recirculating flow, and areas of flow separation within a flow field. Notably, by drawing the streamlines for 1000 particles introduced at the inlet of the empty porous medium, it can be clearly demonstrated how channels ChB act as preferential paths with considerably higher velocities compared to those of channels ChA. A particle would rarely enter a ChA channel since velocities are negligible. Drawing streamlines on the biofilm inoculated bioreactor proved to be a channel due to technical difficulties. More precisely, the elements of the mesh.

The resulting probability density functions (PDFs) of the following parameters (Velocity and shear stress) provide valuable insights into the hydrodynamic conditions in the biofilm-inoculated porous media. In fig. 14.3 the PDFs of different hydrodynamic parameters such as velocity, pressure, and shear stress are plotted for all the elements in a dataset. We compared the PDFs of an empty porous structure and a biofilm-inoculated porous medium to investigate the effect of biofilm growth on the hydrodynamics. The probability density functions (PDFs) for velocity components in the X and Y directions exhibit positive and negative values, as expected due to the system's relative uniaxial symmetry across the Z-axis and the main flow being along the Z-axis. Biofilm inoculation results in a higher distribution of velocity magnitudes, as well as the component Z of the velocity. This increase is attributed to biofilm growth restricting the pore space, resulting in smaller cross sections and an increase in velocity. Moreover, the shear stress after biofilm inoculation reaches higher values, with some high-end values being more than 10 times larger than before (500 Pa vs 5000 Pa).

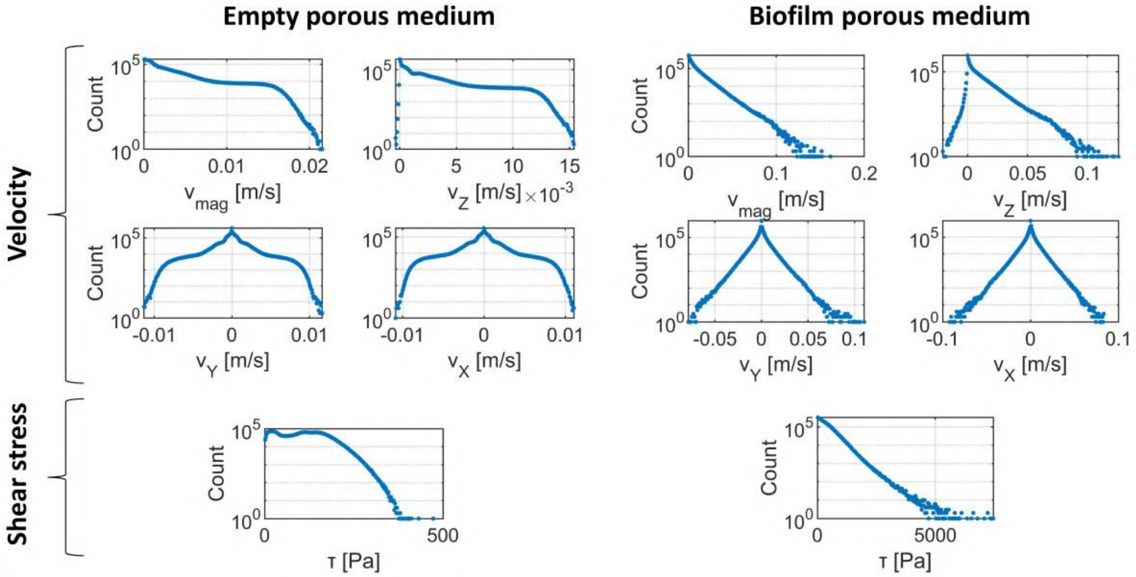

Figure 14.3: Probability density functions (PDFs) of the simulated parameters for the datasets of the empty and the biofilm inoculated porous media. The parameters plotted are the magnitude of the velocity, the three components of the velocity in X,Y and Z directions and the shear stress. It should be noted that here the Z direction is along the length of the porous medium, from the inlet towards the outlet. The presence of biofilm widens the distribution of fluid velocities towards higher values. In addition, by having a look at the z component of velocity, we see that biofilm causes a small degree of backflow (negative values of v_z component) that is not present in an empty porous medium. Finally, the maximum shear stress value is increased from 500 Pa to 5000 Pa when biofilm is present in the porous medium.

14.3 Channel-specific analysis of CFD results

Distinguishing between channels ChA and ChB is essential for gaining a comprehensive understanding of the fluid flow and transport properties in the porous medium. Channels ChA are perpendicular to the flow direction, while channels ChB follow the direction of the flow. Consequently, these two types of channels experience different hydrodynamic environments. By extracting the velocity, pressure, and shear stress parameters separately for ChA and ChB channels from the CFD simulations, we can gain a better understanding of how these properties vary with channel orientation and how they contribute to the overall flow behavior and transport properties of fluids in the porous medium. This was done in a similar way as the one described in section 13.3. To begin with, the parameters (velocity's XYZ components, magnitude, pressure and shear stress) were exported as a .csv with their corresponding coordinates in space.

To extract the parameters based on their location, the porous structure was aligned in the same manner as described before and two projections (XY, XZ) were generated onto a single plane. The projections were rotated accordingly and the channels were located using the same methodology as before. By doing so, we were able to extract the parameters for the elements situated in ChA and ChB channels separately. Box plots were utilized to visualize the distribution of velocities and shear stresses in channels ChA and ChB, as well as in the empty and biofilm-inoculated porous medium.

We also examine the spatial distribution of these parameters within the porous media to gain a better understanding of the hydrodynamic environment. More specifically, as described in section 14.3, the velocities, shear stresses and pressures were analyzed for channels ChA and ChB separately. Channels ChB experience higher velocities compared to ChA in both empty and biofilm-inoculated porous media, consistent with the observed streamlines (fig. 14.2B). After biofilm inoculation, an increase in velocity occurred in both channel types. A similar pattern is observed for the shear stress.

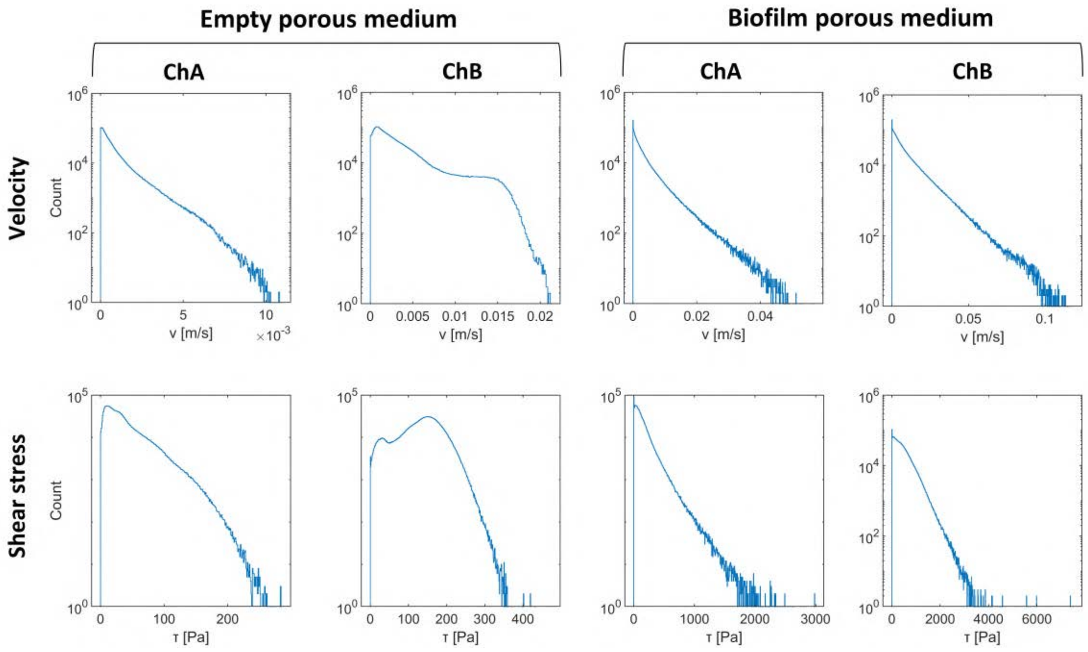

Figure 14.4: Probability density functions (PDFs) of the simulation extracted parameters (Velocity, Shear stress, Pressure) in ChA and ChB channels for the datasets of the empty and the biofilm inoculated porous media. The velocity here refers to the velocity magnitude.

14.4 Calculation of permeability

The permeability of the empty porous media as well as that of the biofilm inoculated bioreactor, were calculated from Darcy's law of permeability:

$$v = -\frac{k}{\mu L}\Delta p \tag{14.1}$$

where v is the fluid velocity in m/s, k the permeability in m^2, μ the dynamic viscosity of the fluid in Pa·s and Δp the pressure drop in Pa over a given distance L in m. The permeability was calculated by considering that $v = 6.17{\cdot}10^{-4}$ m/s which is the imposed velocity, $L = 12.93$ mm being the length of the mesh from top to bottom and $\mu = 1$ mPa·s the dynamic viscosity of water at 25 °C. The differential pressure between the inlet and the outlet of the porous medium from the simulations, was found to be $\Delta p = 32.13$ Pa in the case of an empty porous medium and $\Delta p = 359.25$ Pa for the biofilm inoculated bioreactor.

Finally the calculation of permeabilities using the simulation data yielded the following results: For the empty porous medium, the permeability was equal to $k_0^{sim} = 2.48{\cdot}10^{-10}$ m^2 while for the biofilm inoculated bioreactor dataset, the permeability was calculated equal to $k_f^{sim} = 2.22{\cdot}10^{-11}$ m^2 indicating a 91.0 % decrease. Here we will remind the reader that according to an experiment performed to determine the initial permeability of the porous medium (section 7.2.3) the permeability was found $k_0^{exp} = 4.68{\cdot}10^{-11}$ m^2 while the biofilm growth experiments (section 8.1.1) showed a final permeability of about $k_f^{exp} = 1.5{\cdot}10^{-13}$ m^2 at the end of the experiment, a drop in permeability of 99.7%. Differences in both the initial permeability and the subsequent decrease in permeability appear evident when experimental and simulation permeability values are compared. This can be attributed to several factors. First of all, the bioreactor scanned and used for obtaining the mesh used for CFD, is not the same as the one used for the biofilm growth experiments therefore small defaults on the porous medium geometries due to 3D-printing can have an impact on its permeability. Parameters such as the cleanliness of the unpolymerized, 3D-printing resin or the wearing of the tank containing it, may affect the quality of the resulting porous medium after printing. In addition, segmentation of the obtained X-ray datasets can slightly vary due to the fact that segmentation of the datasets was performed using a machine learning image processing software (IPSDK, section 13.3). Since the segmentation model used to extract the mesh for the CFD was trained by a human, it may contain errors and inconsistencies. It should be noted also that the theoretical porosity of the medium is 8.6 %, while the scanned porosity was found to be 10.6 %. It has been indeed observed that the channels are slightly larger in diameter (315 ± 18 µm instead of 300 µm) which would explain the porosity and the permeability increase. Any slight variations in the above mentioned parameters could lead to errors in the calculation of permeability. Thus, it is evident that the accuracy of the permeability calculation is highly dependent on the precision of the segmentation model, as well as the accuracy of the printing procedure. Finally, the experiments revealed a notably more significant decrease in permeability compared to the simulations. The dataset used for simulations involved the introduction of a viscous contrast agent ($BaSO_4$) into the bioreactor, a known facilitator of biofilm detachment [61, 100]. This process was expected to ultimately lead to increased permeability, as a decrease in biomass within the pores correlates with higher permeability. On the other hand, in the experimental setup, the bioreactor remained undisturbed throughout the duration of the experiment. Consequently, the undisturbed proliferation of biofilm and subsequent pore clogging led to a notably greater decrease in permeability.

14.5 Correlation of the hydrodynamic environment to biomass distribution in the porous medium

Studying the relationship between biofilm growth and the hydrodynamic environment in porous media is crucial for a comprehensive understanding of the impact of biofilms. In this section, we analyze the correlation between hydrodynamic parameters and biofilm distribution in a periodic channel network porous medium. By analyzing channel-specific velocity and shear stress using CFD and biomass distribution using X-ray tomography, one main observation can be made. Our findings showed that channels with high velocities and shear stresses, such as ChB, had a higher percentage of biomass compared to channels with negligible velocities like ChA. Fig. 14.5 illustrates the distribution of velocities and shear stresses in different channels. These results demonstrate the influence of the hydrodynamic environment on biofilm formation and distribution within porous media.

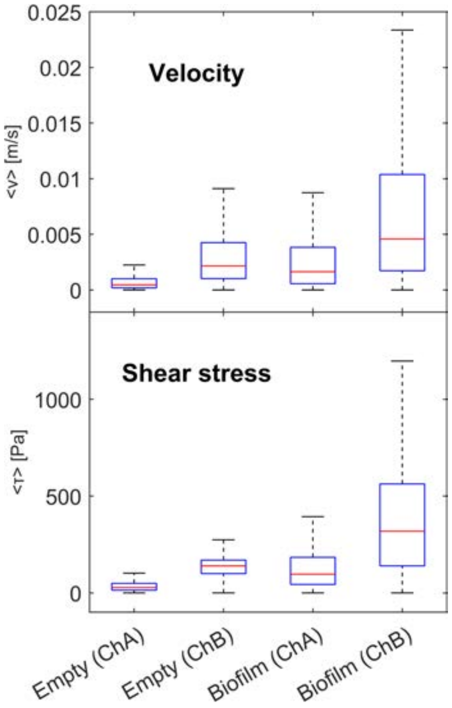

Figure 14.5: Boxplot of the velocity and shear stress distributions in channels ChA and ChB for an empty and a biofilm-inoculated porous medium as obtained by CFD simulations. The red lines indicate the median of the distribution, the boxes represent the 50 % of the values and the whiskers extend to the most extreme data points .

14.6 Discussion

It is known from literature that biofilm distribution in porous media is influenced by various parameters that can be physical (shear stress, flowrate, pore geometry etc.), chemical (nutrient concentration, oxygen availability, presence of inhibitors etc) and biological (microbial strain) [30, 102, 103, 167, 278]. In particular, hydrodynamic parameters are very important for shaping biofilm distribution in porous media. The flow rate and shear stress can affect the attachment, detachment, and distribution of biofilm in a porous medium [24, 35, 62, 67]. The shear stress can physically remove the biofilm from the surface or cause it to detach due to mechanical forces [234], while the flow rate can affect the nutrient and oxygen transport to the biofilm [427]. The Reynolds and Péclet numbers can also have a significant impact on the biofilm distribution, as they affect the flow behavior and mixing in the porous medium, which in turn affects the transport of nutrients and oxygen to the biofilm [14, 35].

Beyond these consideration on the dynamics of biofilm development, studies have also shown that varying shear stress levels can impact the composition, diversity, and dynamics of biofilm bacterial communities, as well as decrease biofilm diversity and slow down biofilm maturation [345]. In one study where biofilm growth in 3D porous media were studied, a local analysis revealed wide distributions of wall shear stresses and concentration boundary layer thicknesses [62] when biomass accumulates in the porous medium. The spatial distribution of the biofilm patches uncovered that the wall shear stresses controlled the biofilm development. However making more global deductions regarding the effect of shear stress on biofilm growth in porous media has proven to be a challenging task due to the coupling of all the aforementioned parameters. For example, the same study [62], and others [441] suggest that biofilms tend to form more readily in low shear regions, which is in contrasts with our experimental observations. Nevertheless, it is important to acknowledge that the hydrodynamic conditions in these studies vary from ours since different flowrates and porous geometries are used. On the other hand, biofilm growth in porous media had a similar effect on the distribution of shear stresses and velocities in [62] with biofilm inducing a spreading of shear stress and velocities towards higher values.

Additionally, the mechanical properties of the biofilm and the effect of both hydrodynamic and growth conditions must be taken into account to predict detachment, as detachment is a major process determining the physical structure and microbial functionalities of biofilms [311]. The density and cohesion of biofilms have been reported to increase with shear stress, and the application of shear stress may result both in detachment and compression [311]. This finding is in line with the observed behavior of biofilm in our experiments. In addition, it has been shown that biofilm thickness increased with apparent surface organic loading rate (SOLR), while biofilm density increased with both SOLR and shear stress [313].

Overall, biofilm growth in porous media plays a major role in shaping the hydrodynamic environment and the transport dynamics within a porous medium by enhancing anomalous characteristics, such as intermittent behavior of Lagrangian velocities, solute spreading in breakthrough curves, and solute retention. This change in the hydrodynamic environment has in turn an effect on biofilm growth and vice versa.

15 Conclusions

In this work, we focused on studying the growth of biofilms within a periodic channel network porous medium modeled after the Laves graph. We further analyzed biofilm growth data of 7 independent biofilm growth experiments obtained according to the protocol described in part II, using Fourier analysis and wavelet coherence analysis in order to try to decipher the biofilm behavior and identify biofilm detachment patterns. In addition, we used X-ray imaging (µCT) to compare data obtained from biofilm-inoculated porous media with data obtained from scanning empty porous media. By analyzing the porosities and biomass distribution within the porous structures and performing CFD simulations, we gained a better understanding of how biofilm growth affects the hydrodynamic parameters of the system, such as pressure and velocity fields. Finally we observed that regions within the porous medium that experience higher velocities and therefore higher shear stresses exhibit higher biomass percentages than those in low-shear-stress regions. It was concluded that the biofilm adjusts its growth in response to unfavorable high shear stress regions in order to gain access to increased nutrient availability. These results are of great significance as they provide valuable insights into the hydrodynamic parameters that impact biofilm growth in porous media.

It is important to study the effect of biofilm growth on the hydrodynamic environment of a porous medium because biofilms can significantly alter the hydrodynamic parameters, such as pressure and velocity fields, within the porous medium. This, in turn, can impact the efficiency of processes such as filtration and bioremediation that rely on porous media for their operation. By analyzing the hydrodynamic environment, we can gain insights into how biofilm growth affects the performance of porous media-based systems and develop more effective strategies for managing and controlling biofilm growth. The fact that biofilms do not create uniform films but rather heterogeneous structures in porous media is consistent with a broad range of studies [240, 441]. This is because biofilm development results from complex coupling mechanisms between flow, transport phenomena, bacterial behavior and biofilm growth. Biofilm development can, for instance, lead to fouling and to the formation of both preferential flow pathways [62, 322] with large flows and areas that are deprived of nutrients. Biofilm can also induce modifications of flow and transport properties, such as anomalous dispersion [380]. These modifications can then feedback upon the development of biofilms, for example by modifying shear stress and detachment patterns, with different organisms expected to respond differently. Due to these couplings, it has proven difficult to understand what drives biofilm development in porous media flows and to derive general principles. For instance, results in [441] and [62] suggest that biofilms may develop preferentially in low shear regions, which is not the case in our experiments. Our technology, combined with X-ray tomography and CFD, provides a way to explore the dynamics of biofilm development in virtually any porous structure in controlled conditions with embedded instrumentation highlighting its potential as a tool for similar studies. It therefore represents a unique platform to study these couplings in 3D geometries.

Part IV

Investigating the potential of gold nanoparticles as x-ray tomography contrast agents

16 Introduction

Over the past decade, X-ray microtomography has gained attention as a powerful tool for imaging biofilms in 3D porous media. This technique enables the visualization of the biofilm structure and its spatial distribution within opaque 3D substrates at the mesoscale with a high resolution – usually several micrometers. However, the primary challenge arises from the fact that biofilms are mainly composed of water, estimated to be more than 80 % of the biofilm [484], and develop in aqueous conditions. The X-ray absorption contrast tomography principle is based on the fact that different phases of a sample attenuate X-rays in a different way. Therefore, differentiating between the biofilm phase and the liquid phase in between them is a difficult task, given that both phases consist mainly of water. To overcome this limitation, the predominant approach is the use of a contrast agents to stain either the liquid or the biofilm phase to distinguish one from the other.

Previously proposed contrast agents Several contrast agents for biofilm X-ray imaging have been proposed. Iltis et al. have used silver-coated hollow microspheres to outline the interface between the biofilm and the liquid phase [186] (fig. 16.1C). This approach creates contrast only at the fluid/biofilm interface, with often particles that are unevenly distributed which makes it difficult to delineate between the phases. Davit et al. [100] proposed the use of a barium sulfate ($BaSO_4$) suspension to increase the absorption of the liquid phase, a method that is now established [303, 348] (fig. 16.1A). One issue is that $BaSO_4$ is heavy, so that sedimentation is fast and can result in concentration gradients and blur artifacts upon imaging. This problem can be solved by either using highly concentrated solutions which would provide adequate contrast or use lower concentrations combined with low-gelling point agarose to completely eliminate sedimentation [245]. Another issue is that the concentrations necessary to obtain good contrast in lab X-ray CMT leads to inconvenient rheological properties of the solution, in particular a large viscosity that may induce biofilm detachment [348] depending on the mechanical properties of the biofilm, the porous medium and the flow rate of introduction. Another approach from du Roscoat et al. suggests the use of 1-chloronaphthalene (CN) as a less viscous alternative to the barium sulfate suspension [191, 348] (fig. 16.1B). In a slightly different way, Carrel et al. have been continuously feeding the bioreactor with iron sulfate ($FeSO_4$) throughout the experiment in order for the contrast agent to be evenly distributed within the biofilm [61] (fig. 16.1D). While this technique eliminates issues related to biofilm detachment due to shear stress during contrast agent injection, it showed that Fe(II) oxidizes quite rapidly to Fe(III), a less soluble form of iron, promoting flocculation. In the same study, they compared their results with the use of $BaSO_4$ pointing out that the latter method shows significant lesser biofilm volume, implying that through the injection of the viscous solution of $BaSO_4$ biofilm is detaching. However, it is important to note that the injection of

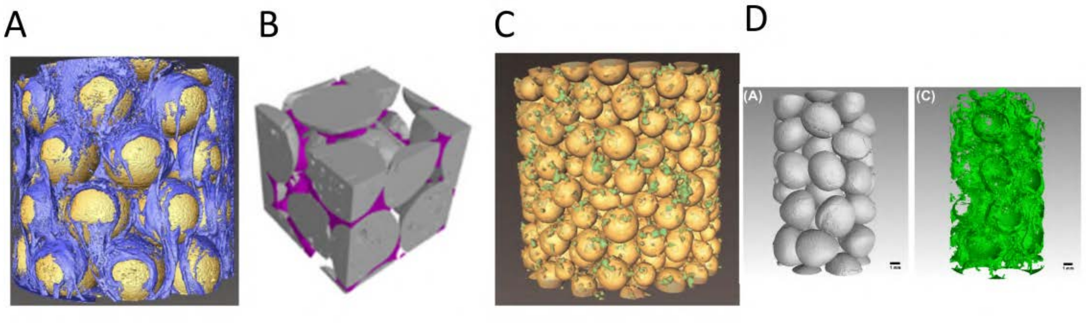

Figure 16.1: Previously suggested contrast agents (A) Barium sulfate [100, 245] (B) 1-chloronaphthalene [348] (C) Silver-coated hollow microspheres [186] (D) Iron sulfate [61].

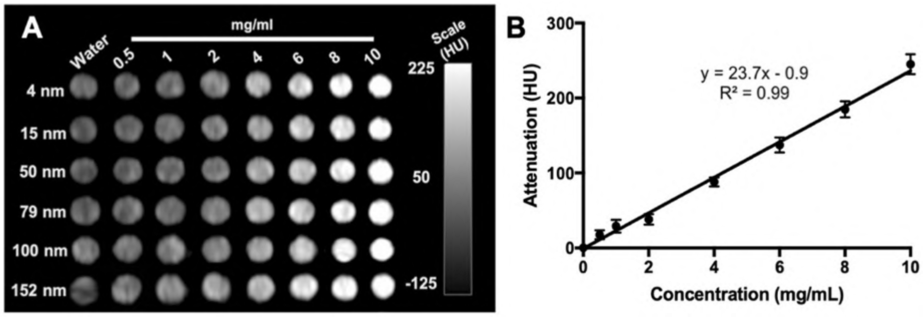

Figure 16.2: (A) Various concentrations and sizes of gold nanoparticle solutions were scanned to demonstrate their X-ray attenuation capabilities. (B) X-ray attenuation changes versus concentration for 50 nm AuNP Image adapted from [109].

$BaSO_4$was performed sequentially, after the initial imaging with Fe(II) as the contrast agent. The time delay between the two injections may have rendered the biofilm more prone to detachment, which could have impacted the results. On the same idea, even though 1-chloronaphtalene is an oily, significantly less viscous contrast agent, without sedimentation phenomena, appeared to fail to fill every pore space throughout the porous medium and also the toxicity of the substance towards the biofilm is considered high. All the above mentioned contrast agents are useful within a limited scope and can only be used for their respective applications. Therefore, there is a need for designing a versatile and universal CT contrast agent that would eliminate the limitations of each aforementioned technique.

Potential of gold nanoparticles as a novel contrast agent Here, we explored a novel family of contrast agents based on gold nanoparticles. Gold nanoparticles (AuNPs) coated with ligands have shown promising potential as X-ray contrast agents in medical imaging [159]. Gold has a high X-ray attenuation coefficient, as demonstrated by Dong et al. [109] (fig. 16.2), making it an ideal material for enhancing contrast in X-ray images of biological tissues, fluids [57, 403], and potentially bacteria [145]. The selective attachment of ligand-coated AuNPs to bacteria can be achieved through careful ligand selection, such as using Concanavalin-A (conA) which is known for its cell-binding properties [15]. Functionalized AuNPs, such as those coated with collagen-binding adhesion proteins, have been used in vivo to enhance contrast in computed tomography (CT) images, specifically targeting collagen within myocardial scars for improved vascular imaging of coronary arteries [211]. These ligand-coated gold nanoparticles offer a novel approach for X-ray contrast enhancement in medical imaging, with potential advantages in selective targeting, improved image quality, and enhanced diagnostic capabilities in various biomedical applications.

In this work... In this section, we begin by performing first test to calibrate the gold concentration to the grayscale levels in the obtained X-ray tomographs as has been previously demonstrated by [109]. These tests were performed by preparing solutions of several concentrations of homemade, phosphene-stabilized gold nanoparticles. Later on, we continue by testing another type of non-functionalized contrast agent consisting of commercial, highly concentrated gold nanoparticles (namely AuroVist). In these tests, we tried to get an insight on the interaction of these particles on bacterial biofilm patches and test their potential as a contrast agent. The staining was performed in 1.5 mL Eppendorf flasks that contained mature, previously-grown biofilm patches, so as to perform a quick test. The next step was to test commercial, functionalized gold nanoparticles that would specifically target the biofilm matrix. The staining strategy involves using two reagents for contrast agent staining. The first reagent is a Concanavalin-A (ConA) / biotin conjugate that binds to the biofilm matrix's extracellular polymeric substances (EPS) and provides biotin sites. The second reagent is a Streptavidin-functionalized gold nanoparticle solution, which binds to the biotinylated EPS matrix through a strong and irreversible

Streptavidin-biotin covalent bond. Initially, the newly developed protocol is tested on biofilm patches in Eppendorf flasks to confirm its efficacy. Once validated, the protocol is then applied to biofilm-inoculated bioreactors, where the biofilm is grown for several days following the procedure outlined in part II.

The chapter is divided into two main sections. The first section presents experiments conducted on non-functionalized AuNPs. Initially, the contrast provided by x-ray tomography was calibrated with simple, phosphene coated AuNPs. Next, the interaction of commercial, highly concentrated AuNPs with biofilm in flasks was investigated to gain insight into their behavior. The second section focuses on functionalized gold nanoparticles that could attach specifically to the biofilm matrix. Firstly, their interaction with biofilm in eppendorf flasks was examined, and then they were tested in the biofilm inoculated bioreactor micro-model. The preliminary results indicate that AuNPs have great potential as a candidate for use as an x-ray contrast agent.

17 Non-functionalized gold nanoparticles

17.1 Contrast-AuNP Concentration calibration

The contrast given by a material is directly related to the x-ray attenuation coefficient of that material. This coefficient can be described as

$$\mu = \frac{\rho Z^4}{AE^3} \tag{17.1}$$

where ρ is the density of the material, Z is the atomic number, A is the atomic mass and E is the X-ray energy. Attenuation is often measure in Hounsfield units (HU), normalized to the attenuation of water. The Hounsfield unit (HU) scale is a linear transformation of the original linear attenuation coefficient measurement into one in which the radiodensity of distilled water at standard pressure and temperature (STP) is defined as 0 Hounsfield units (HU), while the radiodensity of air at STP is defined as -1000 HU. In a voxel with average linear attenuation coefficient μ, the corresponding HU value is therefore given by

$$HU = 1000 \times \frac{\mu - \mu_{water}}{\mu_{water} - \mu_{air}}. \tag{17.2}$$

It is evident from equation 17.1 that the energy of the X-ray scan impacts the attenuation coefficient. Since the X-ray tube's energy output is typically not constant across experiments, even with the same parameters, the grayscale values of an image cannot be directly compared.However, by converting the attenuation coefficient into Hounsfield unit scale, provides a rough calibration and therefore allows for the comparison of scans with different scanning parameters.

Experimental procedure The experimental procedure involved testing unfunctionalized, phosphene-stabilized gold nanoparticles that were fabricated at IMRCP laboratory in Toulouse, through a collaboration with Christophe Coudret and Diana Ciuculescu. The initial solution provided had a concentration of 0.7 mg/mL and a particle diameter of about 14 nm. To prepare various concentrations, the initial solution was centrifuged at 500 rcf (relative centrifugal force) for 15 minutes, resulting in a clear supernatant and a pellet of AuNP at the bottom of the flask. To concentrate the solution, 9/10ths of the supernatant volume were carefully removed with a pipette, ensuring that the AuNPs were not agitated and remained at the bottom of the flask. Consecutive solutions were then prepared by dissolving the concentrated AuNPs in DI water resulting in the concentrations given in fig. 17.1. The solutions were then prepared to be scanned through the X-ray tomographer. Regarding the acquisition parameters, the middle focal spot was used with tube voltage and tube current set to 70 kV and 428 µA respectively, resulting in a tube power of 30 W. The frame rate was set to 3 images per second averaging over 6 images. The resulting voxel size was 14.06 µm.

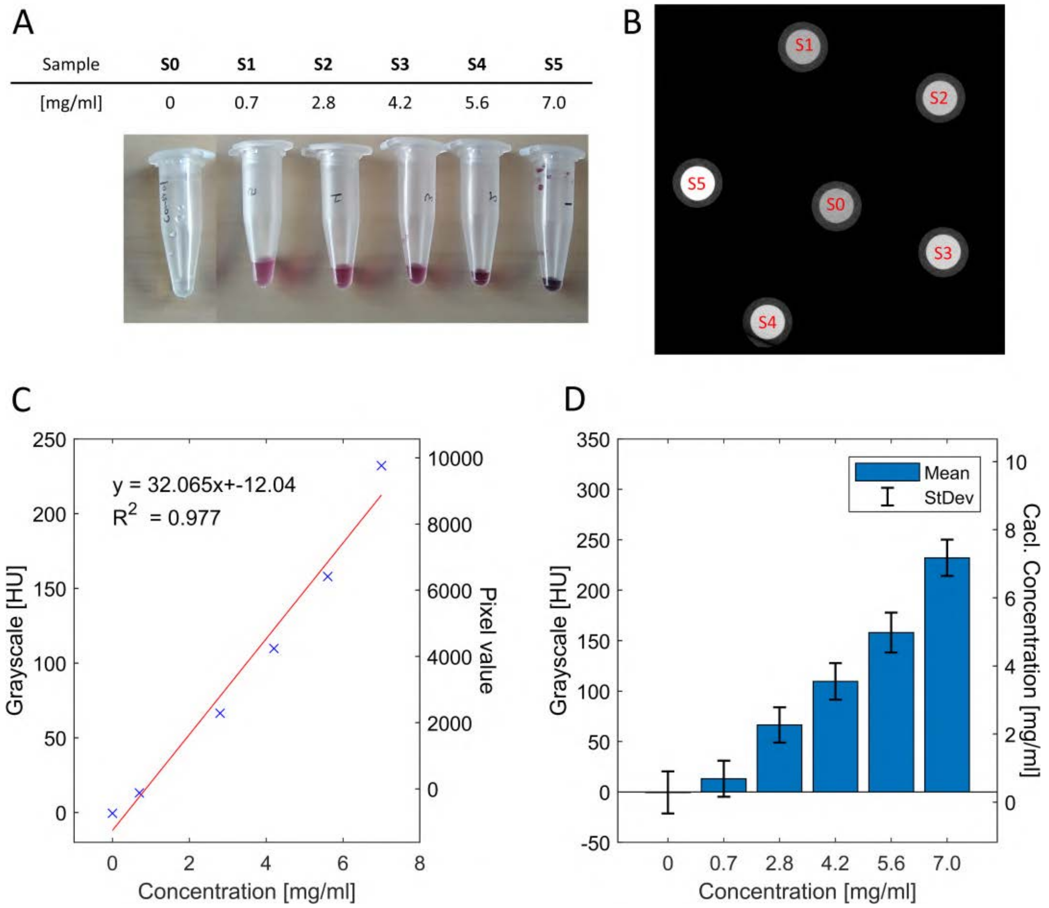

Figure 17.1: (A) Six solutions were prepared for this test with concentrations ranging from 0 to 7 mg/mL. (B) An image slice obtained through X-ray tomography demonstrating the different X-ray attenuations of the solutions. (C) The AuNP concentration is linearly correlated to the mean pixel grayscale value for each of the solutions in (B). The grayscale can be converted in Hounsfield units since the grayscale levels of water and air are also measured. (D) The calculated gold concentration can be verified after the calibration and conversion in Hounsfield units is performed.

Image analysis and results For the analysis of the data, one slice from the image stack was used as the solutions were homogeneous throughout the bulk of their volume. For the image analysis, a combination of MatLab and ImageJ were used. Initially, for each solution, a circular ROI was selected so that the pixels corresponding to the solution are cropped and the mean pixel value was obtained. One solution (S0) in the experiment consisted of pure water, while the space between the scanned flasks contained air. As a result, grayscale values were obtained for both air and water, which enabled the correlation of grayscale values to Hounsfield units. This was achieved by conducting linear fitting of the data, considering that in the Hounsfield scale, water corresponds to 0_HU and air corresponds to -1000_HU (fig. 17.1C). Furthermore a bar plot was drawn that would link each solution to a calculated gold concentration using the previously performed calibration. The standard deviation in grayscale levels obtained for each solution indicate the uncertainty of the method meaning that calculating the local gold concentration using X-ray tomography can result in a significant error. This uncertainty is related to the scanning parameters and the technical characteristics of the X-ray setup such as resolution of the X-ray detector and energy fluctuations of the X-ray source.

17.2 Diffusion of AuNPs in biofilm

The tests were conducted using non-functionalized commercial gold nanoparticles (AuNPs), specifically the AuroVist brand provided by Nanoprobes. These nanoparticles were provided at an unusually high concentration of 200 mg/mL, which is significantly higher than similar nanoparticle solutions provided by other companies. Due to their high concentration, the AuNPs provided relatively strong contrast when used in X-ray tomography. They are also advertised as having low toxicity, with an LD50 (median lethal dose) > 5 g/kg, making them suitable for in vivo, bloodstream injection and imaging in mice. Furthermore, these nanoparticles exhibit low viscosity, similar to water, making them easy to manipulate and inject.

Experimental procedure The bacterial culture was initiated using *Pseudomonas aeruginosa* PAO1 strain (ATCC 15692 GFP). The bacterial strain was retrieved from a -80 °C stock and subsequently incubated in 20 mL of Brain Heart Infusion broth (BHI, Merck, 37.5 mg/mL) containing ampicillin (300 µg/mL) for 3 nights since a thick biofilm is needed for this experiment, under conditions of 30 °C and 180 RPM. On the day of the experiment, biofilm patches were carefully removed from the flask and distributed into four separate 1.5 mL Eppendorf flasks. To prepare for imaging, four distinct solutions of AuroVist gold nanoparticles were prepared, with two solutions containing nanoparticles with a diameter of 1.9 nm and the remaining two solutions containing nanoparticles with a diameter of 15 nm. For both groups of different AuNP sizes, two concentrations were tested, one with low Au concentration of 3.2 mg/mL and one at 8 mg/mL (fig. 17.2A). One mL of each solution was poured directly into the erlenmeyer flask containing the biofilm patches. The flasks were placed in the incubator at 30 °C for 30 min and then were taken to the X-ray tomographer which would allow another 45 min for the particles to interact with biofilm before imaging.

For he x-ray imaging, the samples were mounted on a homemade support to ensure that they do not move during x-ray acuisition. The characteristics of the x-ray tomography system have been previously detailed in paragraph 13.3. For the acquisition, the middle focal spot was used with tube voltage and tube current set to 70 kV and 428 µA respectively, resulting in a tube power of 30 W. The frame rate was set to 3 images per second averaging over 6 images. The resulting voxel size was 14.06 µm. After the acquisition, samples 3 and 4 (AuroVist 15 nm diameter) were washed multiple times with deionised water by pouring out the nanoparticle-infused liquid and reintroducing pure water until the solution was clear. The samples were rescaned using the same scanning parameters to investigate wether or not washing would be useful for improving the biofilm contrast in case NPs diffuse into the biofilm matrix.

Image analysis and results All the datasets, before and after washing were treated in the same way. Prior to any image analysis, no filters were applied since the aim of this analysis is not to binarize or threshold the biofilm phase, rather to compare the contrast given by each solution. For each solution, an area of interest was defined on a slice normal to the Z axis that did not appear to contain any biofilm, and the mean pixel value with standard deviations was calculated. These areas were either on the bottom or towards the air-liquid interface where the main mass of the biofilm was found. We believe that in the case of concentrated solutions the density of the bulk of the liquid is higher than that of biofilm as the nanoparticle concentration is lower in the biofilm, making the biofilm float. The opposite effect is observed for the case of low concentration solutions. In addition, the minimum and the maximum pixel value were noted for the whole bulk of the liquid. This allowed us to identify the phase that the gold nanoparticles are staining.

According to what was discussed previously in this section, the contrast given off by a material is is dependent on the density of the atoms of the material (eq. 17.1). Therefore, theoretically, solutions S1-S3 and S2-S4 shoud have the same contrast, be it in HU or grayscale pixel values, given that they were both obtained during the same acquisition. Their difference in contrast is therefore attributed to the fact that in order to perform the dilution of the AuNPs from the stock solution, very small volumes of nanoparticle solution had to be handled implying that a small deviation of the pippeted volume can result in significant changes in respect to the final concentration. Nonetheless an overall patern can be

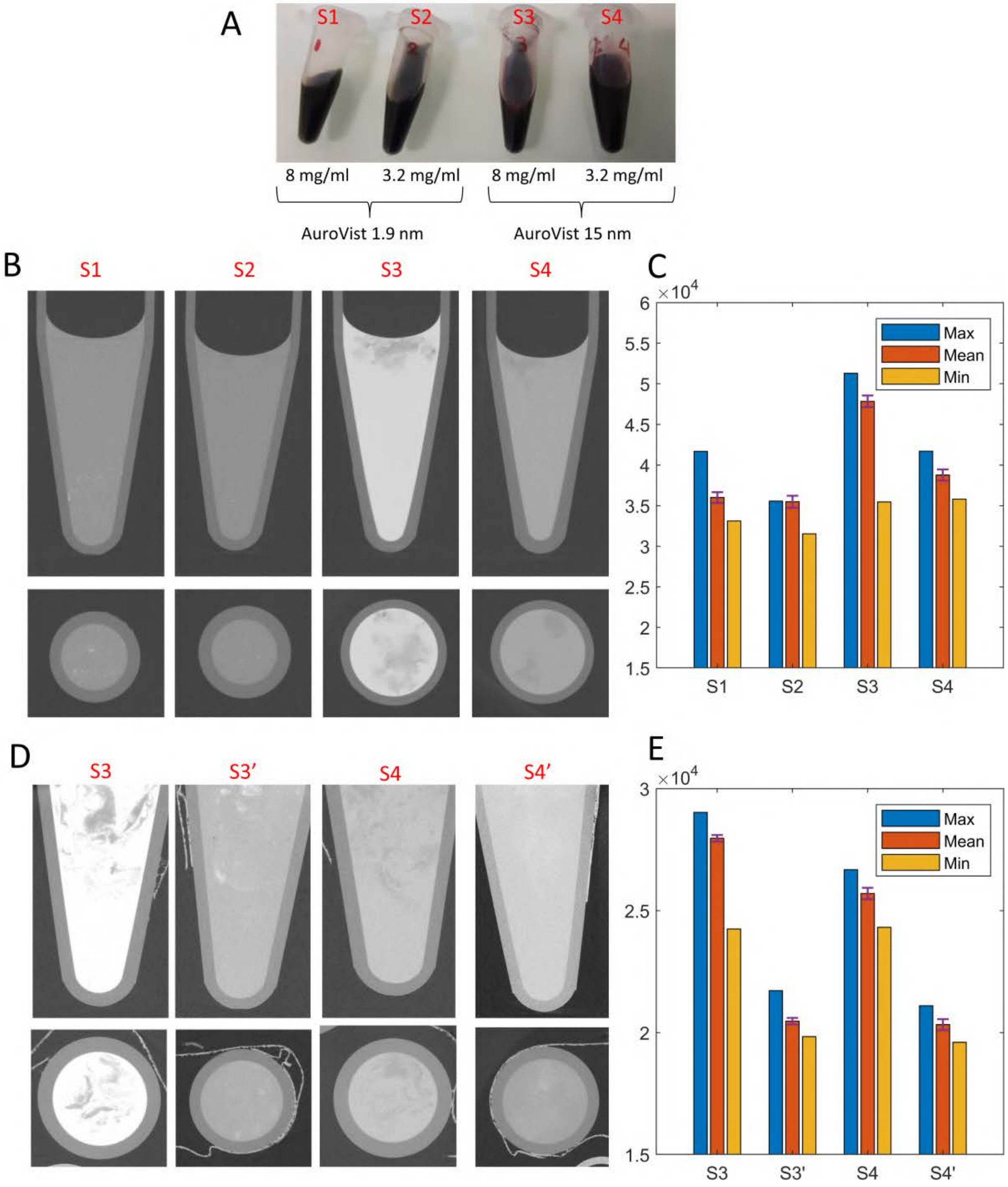

Figure 17.2: (A) Four different AuroVist solutions were prepared using nanoparticles of 1.9 and 15 nm in diameter. Two concentrations were tested, 8 and 3.2 mg/mL. (B) X-ray tomograph vertical and horizontal slices of each of the solutions prepared with their grayscale measurements (C) on a ROI obtained from an area that does not contain biofilm (bulk of the liquid). (D) X-ray tomograph vertical and horizontal slices of solutions S3 and S4, before and after washing (S3' and S4') with their corresponding grayscale measurement levels (E) on a ROI that does not contain biofilm.

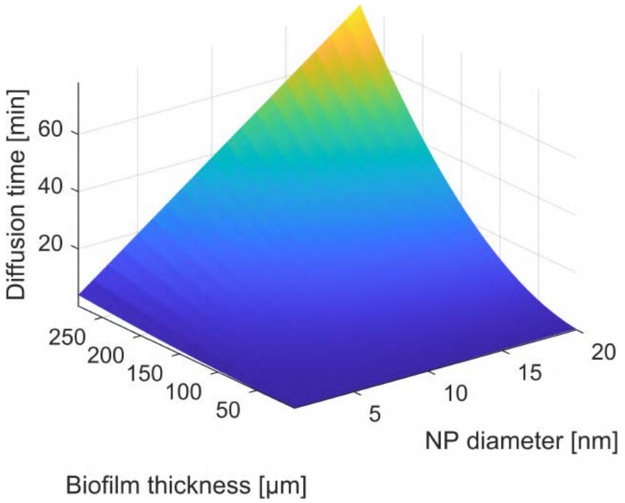

Figure 17.3: Nanoparticle diffusion time calculations using the Stokes-Einstein equation (eq. 17.3)

observed where concentrated solutions give higher bulk contrast and smaller nanoparticle sizes tend to penetrate the matrix.

Regarding the size of the AuNPs, looking at fig. 17.2B it can be seen that in solution S1 (1.9 nm, 8 mg/mL), it is the biofilm that stands out as the high intensity pixels while in solution S3 (15 nm, 8 mg/mL) biofilm corresponds to the darker pixels. This is an indication that in the case of smaller diameter AuNPs, the nanoparticles penetrate into and concentrate within the biofilm while larger diameters do not diffuse as easily into the biofilm. The same effect is observed for the lower concentration solutions (S2 and S4) but with less contrast since gold quantity is lower. Furthermore, washing of the stained biofilms with water in order to remove unbound particles seemed to affect the final result in terms of contrast. Solution S3 (15 nm, 8 mg/mL) in fig. 17.2D, shows biofilm as darker pixels while after washing (S3') pixels corresponding to biofilm appear brighter than the bulk. Suggesting that part of the AuNPs that were injected, indeed diffused into the biofilm matrix, therefore when the bulk liquid was washed, AuNP concentration was higher within biofilm. The same effect can be observen for solution S4 and S4' however it is less pronounced since the AuNP concentration was lower in that case.

17.3 Diffusion calculation

In order to have an idea of the time it takes for the nanoparticles to penetrate the biofilm matrix, we calculated the diffusion coefficient of a spherical particle through a liquid using the Stokes–Einstein equation:

$$D = \frac{k_B T}{3\pi\eta d} \tag{17.3}$$

where D is the diffusion coefficient, k_B the Boltzmann constant ($1.38 \cdot 10^{-23}$ J·K^{-1}), T the absolute temperature, η the dynamic viscosity and d the diameter of the spherical particle. Here we considered that the temperature is $37\_{}^{\circ}C$ since this is the temperature that was used when the protocol was applied and we made the rough assumption that the dynamic viscosity of biofilm is 0.3 times the viscosity of water, therefore 0.002307 Pa·s. The calculations were performed for a range of diameters from 1 to 20 nm. Furthermore, the diffusion time was calculated for a range of biofilm thicknesses, l, ranging from 20 to 300 µm, according to eq:

$$t = \frac{l^2}{2D} \tag{17.4}$$

Based on the observation of the fig. 17.3, it is suggested that the diffusion of gold nanoparticles through the biofilm matrix is highly dependent on their size. Smaller particles have higher diffusion coefficients and, therefore, can penetrate the biofilm matrix more easily than larger particles. Moreover, the diffusion time of nanoparticles through the biofilm increases with increasing biofilm thickness. These findings suggest that the size of the nanoparticles is a crucial parameter that should be considered when designing experiments to study nanoparticle diffusion in biofilms. Overall, the Stokes-Einstein equation provides a useful tool for estimating the diffusion coefficient and diffusion time of nanoparticles in biofilms, which can aid in the design and optimization of experiments aimed at investigating the interactions between nanoparticles and biofilms. However, the results presented here provide a rough estimation of the diffusion time since the value of the viscosity is assumed to be 0.3 times the viscosity of water.

18 Functionalized gold nanoparticles

18.1 Working principle and characteristics

The contrast agent staining procedure includes the use of two reagents. The first of the two reagents is a concanavalin-A (ConA) / biotin conjugate (Prod. Catalogue C2272, Sigma Aldrich) that would bind onto the EPS and provide free biotin sites. Concanavalin A (ConA) is a lectin (carbonhydrate-binding protein) originally extracted from the jack-bean (*Canavalia ensiformis*). It binds specifically to certain structures found in various sugars, glycoproteins and glycolipids, mainly internal and nonreducing terminal α-D-mannosyl and α-D-glucosyl groups that are present in the biofilm matrix. The second reagent is the Streptavidin - functionalized gold nanoparticle solution (Prod. Catalogue CF11, Nanopartz) that was readily supplied by Nanopartz company at 4 °C. The nanoparticles measure 10nm in diameter and approximately 4 molecules of streptavidin are fixed on each particle according to the quality test performed by the company. Streptavidin is a lectin whose homo-tetramers have an extraordinarily high affinity for biotin (also known as vitamin B7 or vitamin H). With a dissociation constant (K_d) on the order of $K_d \approx 10^{-14}$ mol/l [149], the binding of biotin to streptavidin is one of the strongest non-covalent interactions known in nature. The idea is that these particles would bind onto the biotinylated EPS matrix through this strong and irreversible Streptavidin-biotin covalent bond. Furthermore, the particles were additionally functionalized with a fluorophore, Rhodamine, which would potentially allow us to observe the particles under fluoresence microscopy. However, this additional functionality of the particles was not exploited in this work. As indicated in the technical sheet that came with the particles, the provided solution contained $2.48 \cdot 10^{14}$ nanoparticles per mL and were loaded with 6 mg/mL of gold with a size dispersity of less than 15%.

18.2 Preliminary functionalized AuNP tests

The method for assessing the binding potential of functionalized gold nanoparticles on biofilm in eppendorf tubes involves several steps (fig. 18.2A). Initially, 10 mL of BHI nutrient solution is taken in an autoclaved erlenmeyer flask and inoculated with the *P. aeruginosa* strain stock solution, which is kept at -80 °C, under aseptic conditions in a fume hood. The flask is incubated for three days to allow for the formation of a thick biofilm. A portion of this biofilm is transferred into an eppendorf flask with 0.5 mL of BHI.

Next, a 1 mg/mL solution of ConA-biotin is prepared from the stock solution, and 0.5 mL is poured into the flask. The solution is then placed in the incubator at 37 °C for half an hour to ensure proper binding of the biotinylated concanavalinA. Then, 0.1 mL of the Nanopartz solution containing gold at a concentration of 6 mg/mL is added directly to the flask. The solution is again placed in the incubator at 37 °C for half an hour. After this time, the solution appears clear with dark red/black biofilm

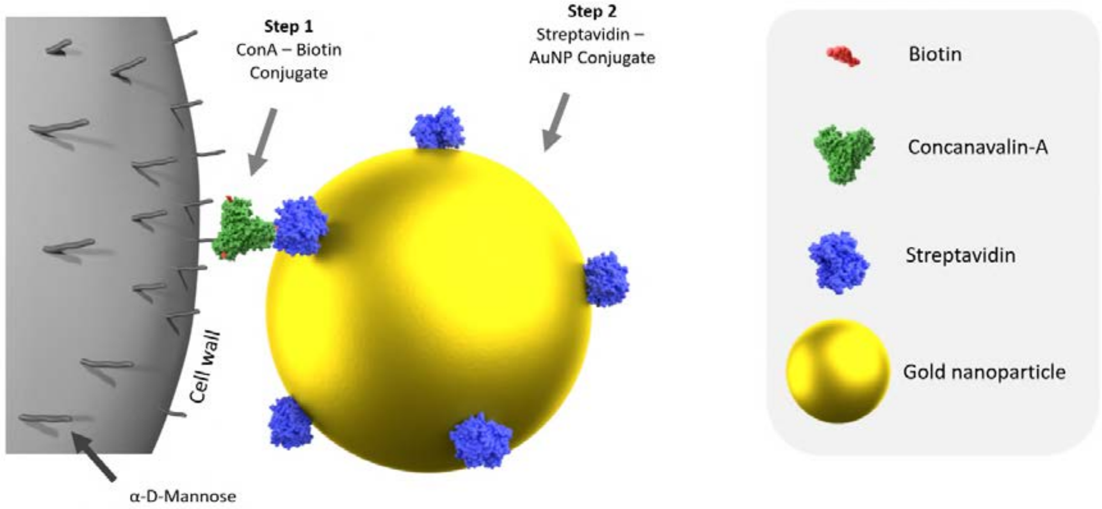

Figure 18.1: Nanopartz binding mechanism in two steps. Initially, the biotinylated ConA binds onto polysaccharites present onto the biofilm matrix providing site to where Streptavidin functionalized AuNPs would bind.

flocculates concentrated at the bottom of the flask (fig. 18.2B). The experimental solution was then taken to the X-ray tomographer, and a typical acquisition was performed using the same parameters as before (section 17.1). The X-ray tomographs obtained from our imaging method displayed a high level of contrast (fig. 18.2C), enabling easy and straightforward binarization of the stack through simple thresholding. This process allowed for a clear overview of the biofilm's volume occupancy (fig. 18.2D).

A flask containing DI water was scanned during the same acquisition, which aided in determining the pixel intensities in Hounsfield units. Prior calibration experiments enabled the correlation between the concentration of gold and contrast in µCT tomographs, which was used to map the gold concentration in the current dataset. During these previous experiments, the Hounsfield scale was also correlated to gold concentration, allowing the transformation of grayscale values to a spatial map of gold concentration in the present study (fig. 18.2E). By statistically analysing the pixel values of one slice of the dataset, it has been observed that there is a broad distribution of gold concentrations. This heterogeneity also suggests that gold has locally accumulated onto the biofilm matrix through the selective binding mechanism of the particles. The initial gold nanoparticle solution was concentrated at 6 mg/mL and was later diluted about tenfold when injected into the eppendorf flask which would have resulted in poor contrast. However the Au concentration distribution histogram suggests that locally, the Au concentration can reach more than 10 mg/mL.

As a final remark, it should be noted that the X-ray tomography setup used for this study provided adequate resolution and contrast to perform quantitative analysis of the samples, allowing for the distinction of biofilm as a separate phase, but qualitative results such as the ones presented in fig. 18.2E,F should be considered with caution. The variation of grayscale values of pixels representing homogeneous phases, such as in the DI water flask, are in the order of hundreds which results in important uncertainty. This variation is due to the noise which is inherent to the experimental setup and the acquisition parameters used here.

18.3 Functionalized AuNPs in porous media

In this experimental procedure, we aim to investigate the performance of functionalized gold nanoparticles (AuNPs) as a contrast agent in a more realistic environment. Specifically, we will utilize a porous micro-bioreactor to cultivate biofilm, and then introduce the AuNPs to the system to enable

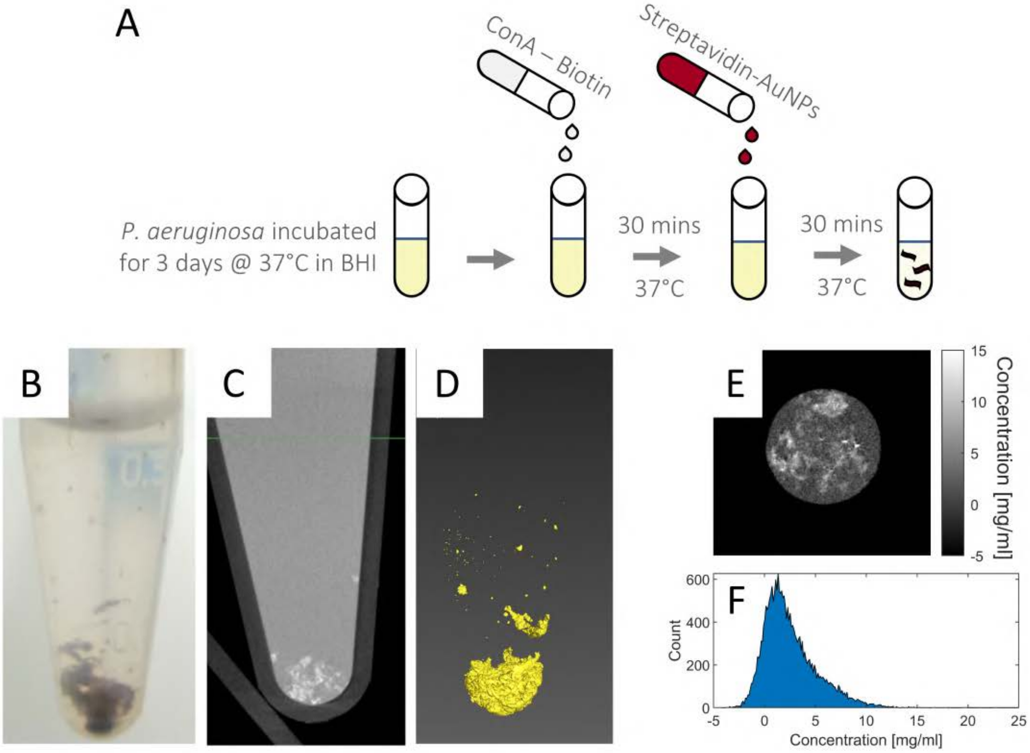

Figure 18.2: (A) Schematic of the biofilm staining protocol with functionalized AuNPs in eppendorf tubes. (B) Visual examination of the samples after the staining procedure suggested that AuNPs binded onto the biofilm matrix. Even though the functionalized AuNP solution had a deep red color, the final solution was clear with the gold accumulated on the biofilm patches. (C) µCT vertical slice of the tube, showing the contrast of the AuNPs. (D) Volume reconstruction of the AuNPs in space through simple segmentation of the high intensity pixels of the µCT datasets. (E) A horizontal slice of the µCT dataset. The pixel values were calibrated and translated in HU units and subsequently to Au concentration using the previously obtained calibration data (section 17.1). (F) The histogram of the pixel intensities (and therefore Au concentrations) indicate a relatively wide distribution of concentrations. The histogram correspond to the circular area of the slice shown in (E).

high-resolution X-ray imaging of the biofilm. The use of AuNPs as a contrast agent has shown great potential in various biomedical applications [57, 73, 79]. However, testing their efficacy in a more complex and dynamic environment, such as a microbioreactor, is crucial to develop more sophisticated and adaptable contrast agents.

18.3.1 Bioreactor preparation

To facilitate X-ray imaging, we followed the same protocol outlined in the previous chapter to cultivate biofilm in porous micro-bioreactors (section 7.3). The biofilm was grown under precisely controlled conditions for three days, allowing it to reach the third phase of growth. At the end of this phase, we stopped operation of the gear pumps and unplugged the tubing with caution to avoid introducing air bubbles. Subsequently, we plugged the inlets and outlets with luer stops, leaving only the designated inlet and outlet for contrast agent injection unplugged for the staining protocol.

18.3.2 Injection protocol

The AuNP staining procedure took place in three steps. Initially, a diluted solution of Concanavalin-A and biotin conjugate was introduced to the bioreactor, to stain polysaccharides present on the biofilm matrix. The solution was prepared by diluting part of the stock solution in brain-heart infusion broth (BHI) to end up with 1 mL solution containing 1 mg/mL of ConA/Biotin conjugate (C2272, Sigma-Aldrich). This solution was slowly injected into the bioreactor using a syringe pump at a flowrate 40 times lower than the growth flowrate (0.05 mL/min) in order not to promote biofilm detachment. The injection was thus slow and it took about 20 mins. The bioreactor was then placed in the incubator at 37 °C for another 40 minutes before proceeding to the next step to ensure proper binding.

The second step of the staining process includes the preparation and injection of the AuNP solution. For that, 0.15 mL of a solution of Streptavidin-functionalized gold nanoparticles of 10 nm in diameter provided by Nanopartz (CF11-10-RHO-FS-DIH-250) were diluted 1:10 volumes in BHI resulting in a final solution of 1.5 mL. Similarly to the previous step, the solution was injected with a syringe pump at a flowrate of 0.05 mL/min. The solution appears deep red in color, allowing for visual verification that it has properly saturated the inlet and outlet compartments of the bioreactor and has reached the outlet. The bioreactor was then moved in the incubator at 37 °C for 40 mins to ensure proper binding of the AuNPs onto the biofilm matrix.

The final step involves the washing of the bioreactor with BHI at 37.5 mg/mL, so as to remove any unbound reagents from the system. The washing procedure was carried out at a flow rate of 0.05 mL/min, using at least 4 mL of washing solution, which is two times the dead volume of the bioreactor. This approach ensured a comprehensive and effective washing. The inlets and outlets of the bioreactor were sealed and it was transferred at the x-ray tomographer.

18.3.3 Imaging protocol

The same scanning parameters were used for all x-ray imaging of the contrasted bioreactors. The characteristics of the equipment used to perform the scanning are detailed in paragraph (13.3). Imaging was only conducted on the middle part (porous medium) of the bioreactor. The x-ray source had to be preheated prior to launching the acquisition. For the imaging process, the x-ray generator tube was set to 60 kV tube voltage and 165 µA tube current resulting in 10 W of source tube power. The small focal point was used to obtain the best resolution possible. No filter was used in front of the x-ray source. The x-ray sensor obtained 1120 projection images per turn with a frame rate of 2 images per second, and 8 images per projection were averaged. A voxel size of 9 µm was achieved by adjusting the position of the sample relative to the source and sensor. Prior to scanning, the X-ray tomographer was calibrated according to the procedure described in section 13.3 and the typical image, post-processing, software tools provided by the manufacturer, were applied.

18.3.4 Data post-processing

A standardized procedure was employed for processing all datasets. Initially, a simple despeckle filter was utilized to reduce noise in the raw data, followed by the cropping of a rectangular region of interest (ROI) encompassing the entire porous medium located in the central section of the bioreactor. The grayscale histograms of the complete datasets were then obtained from this ROI. Subsequently, a machine learning model was trained to binarize the image stacks, thereby enabling the differentiation of pixels corresponding to biofilm. These pixels were on the high-end of the grayscale histogram. This approach allowed for the accurate and consistent identification of biofilm within the datasets. The binarized stacks were used to extract the biomass percentage profile along the Z axis within each bioreactor. The number of pixels corresponding to biofilm phase in each slice was determined and divided by the total number of pore pixels, therefore resulting in the fraction of the pore space occupied by biofilm.

18.3.5 Results

As discussed in the introduction, the x-ray source intensity of the tomographer is not constant. Therefore the grayscale values shown in (A) cannot be directly compared for each one of the three experiments performed even though their experimental parameters were identical. Despite this variability, the histograms of the bioreactor material consistently exhibit a small quantity of dark pixels, which could correspond to bubbles trapped on the top and bottom of the porous medium 18.3A). The predominant peak of the histograms corresponds to the gray bioreactor material, while the wide distribution of high-intensity pixels corresponds to gold nanoparticles, and by extension, the biofilm.

When comparing the histograms and images of gold nanoparticles to $BaSO_4$ (fig. 13.2), it is apparent that the gold nanoparticles give off less contrast at this concentration 1.13 mg/mL compared to the concentration of $BaSO_4$ used in this study(fig. 18.3B). The staining is also found to be non-homogeneous throughout the body of the porous medium, suggesting the presence of preferential flow paths (fig. 18.3C). Areas where the contrast agent did not reach are likely due to clogged pores, rendering parts of the porous structure inaccessible. Nonetheless, biomass accumulation appears to be concentrated in channels type ChA, with a pattern showing that biomass tends to accumulate towards the inlet of the bioreactor. If we consider that the staining properly stained the biofilm phase, even partially, this biomass distribution could be due to the higher availability of nutrients and oxygen at the inlet or an error in staining. These observations were based on visual inspection and column volumetric fractions.

19 Discussion

In this chapter, we have highlighted the potential of gold nanoparticles as contrast agents for X-ray imaging of biofilms in porous media. It has been demonstrated that functionalized gold nanoparticles can be used in combination with the experimental setup presented in the previous parts of the thesis. However, the image stacks showed a partial/incomplete staining of the biomass (fig. 18.3). While keeping in mind that functionalized AuNPs can easily stain small portions of biofilm that is wetted all-around with the NP solution, as shown in section 18.2 (fig. 18.2), staining biofilm in complex 3D structures has proven to be challenging. Even though the staining did not serve its initial purpose of indicating the biomass distribution throughout the whole porous medium, it did highlight the preferential flow paths by staining biofilm that is in contact with fresh nutrients and the main flow. This is interesting by itself as this gives us an insight on how biofilm growth shapes the pore space and giving us information about the percentage of "active" biofilm.

Moreover, it has been demonstrated that AuNP diffusion times are strongly affected by the size of the particles and biofilm thickness as can be seen in section 17.2 (fig. 17.2). Biofilm layering can become quite thick and reach several mm from the surface, rendering AuNP diffusion virtually impossible due to extremely long diffusion timescales. Both the issue with long diffusion times and inaccessible regions

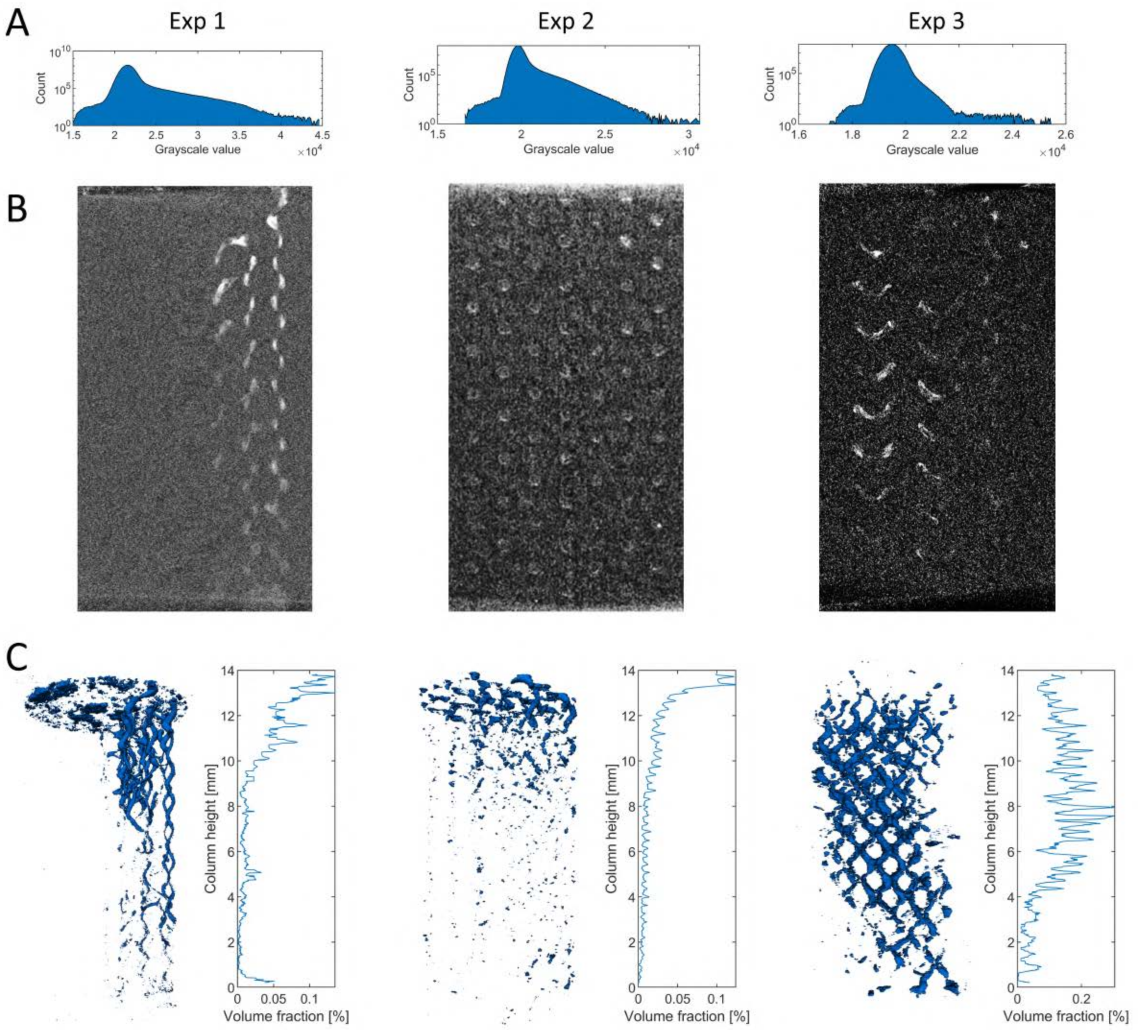

Figure 18.3: Comparison of the results of three replicate experiments where functionalized AuNPs were used to examine their potential use as contrast agents for biofilm visualization. (A) The grayscale histograms for each corresponding dataset show similar trends with a main peak corresponding to the bioreactor material and a broad distribution of brighter pixels, corresponding to what is thought to be biofilm. (B) An example slice of the obtained µCT datasets is shown. The distribution of bright pixels is highly inhomogeneous. The reconstructed volume of the biofilm after machine-learning powered segmentation, is shown in (C) alongside with the percentage of biofilm occupation profile from top to bottom.

due to bioclogging can be potentially circumvented by continuously injecting a contrast agent from the beginning of an experiment. This would ensure the even distribution of AuNPs throughout the bulk of the biofilm. Preliminary tests, performed by Clara Toulouze, PhD candidate and part of our laboratory team, using homemade, citrate stabilized gold nanoparticles have shown promising results. This approach could also significantly lower the cost of staining as non-functionalized AuNPs tend to be cheaper than functionalized ones, for the same amount of atomic gold used.

In this discussion, we will furthermore present the merits of AuNPs as contrast agents, including their high atomic number and electron density, which enhance X-ray attenuation and enable clear visualization of structures in samples. Additionally, we highlight the versatility of surface chemistry of AuNPs, which allows for the incorporation of other imaging contrast agents, resulting in multimodal imaging. However, we also acknowledge the challenges related to the use of AuNPs, such as their toxicity, stability, and potential impact on biofilm structures. These challenges must be carefully considered when evaluating the suitability of AuNPs as contrast agents for X-ray imaging of biofilms.

19.1 Advantages of AuNPs

Size and shape The analysis carried out in this work demonstrates that the size of nanoparticles is a crucial factor influencing their diffusion through the biofilm matrix. As smaller nanoparticles have higher diffusion coefficients, they can penetrate the biofilm matrix more easily compared to larger ones. In addition, the diffusion time of nanoparticles increases with the biofilm thickness. These findings emphasize the significance of considering the particle size while designing experiments to study the interactions between nanoparticles and biofilms. The utilization of the Stokes-Einstein equation can be a valuable tool in estimating the diffusion coefficient and time of nanoparticles in biofilms, thereby aiding the optimization of such experiments.

Furthermore, there have been conflicting reports on the role of AuNP size in their contrast generation for CT. In one study researchers concluded that smaller spherical AuNPs exhibit greater x-ray attenuation [213]. In another study, researchers synthesized AuNP of different sizes and investigated their contrast generation with various imaging systems [109]. They found no statistically significant difference in CT contrast generation among different AuNP sizes, but observed a significant effect of size on the diagnostic utility of AuNP. Specifically, smaller AuNP had longer blood circulation times while larger AuNP accumulated in the liver and spleen more rapidly.

Contrast Gold nanoparticles have emerged as a promising contrast agent for X-ray tomography due to their high atomic number and electron density, resulting in strong X-ray attenuation. It has been previously demonstrated that gold nanoparticles provide a relatively high contrast even at relatively low concentrations [109]. This property leads to a high contrast-to-noise ratio, enabling clear visualization of structures in a sample.

One technique used to enhance the contrast of gold nanoparticles is through the use of the K-shell value of gold. The K-shell is the innermost electron shell of an atom, and when excited by X-rays, it results in characteristic X-ray emissions that are specific to the element. Gold has a unique K-shell value, allowing for the enhancement of the contrast of gold nanoparticles in X-ray tomography. This method involves selecting X-ray energies that correspond to the K-shell value of gold, resulting in the enhancement of the X-ray attenuation of gold nanoparticles and improving their visualization in a sample.

Functionalization Gold nanoparticles (AuNPs) can potentially serve as a suitable contrast agent for 3D biofilm imaging due to their unique physicochemical properties. They can be easily synthesized with various sizes, shapes, and surface properties, making them highly customizable for specific imaging applications. AuNPs can also be functionalized with targeting ligands such as peptides and antibodies, allowing them to selectively bind to specific components of the biofilm matrix for enhanced imaging specificity or provide them with specific functionalities by binding active molecules (e.g. fluorophores).

In this instance, we developed a technique that targets the biofilm matrix by utilizing Concancavalin-A's strong affinity to α-D-mannose and α-D-glucose molecules that are abundant in the matrix. This lectin has been extensively utilized in biochemistry and cell biology to identify glycan structures on tissues, as well as isolate and examine glycoproteins. As a result, we aimed to bind gold nanoparticles to the biofilm matrix through this strategy.

The versatility of gold nanoparticles in terms of surface chemistry has led scientists to consider further applications for them. For instance, these nanoparticles can be easily designed to incorporate other imaging contrast agents, such as rare earth metals and dyes [270]. This approach enables the specific binding of contrast agents to particular sites, resulting in what is referred to as multimodal imaging. By employing this technique, multiple objects in the same sample can be distinguished with greater accuracy and precision.

In addition, it is possible to facilitate the passive trapping of AuNPs within the biofilm matrix by adjusting the surface chemistry of the particles. This approach involves rendering the AuNPs inert instead of functionalizing them, thus enabling physical investigations of the biofilm. For instance, monitoring the brownian motion of the AuNPs immobilized within the biofilm can yield valuable information regarding the biofilm's mechanical characteristics [336].

19.2 Challenges

There are, however, several challenges associated with the use of functionalized gold nanoparticles in X-ray tomography.

Stability One challenge is ensuring that the nanoparticles are stable and do not aggregate, which could lead to inaccurate imaging. Commercial gold nanoparticles such as Nanopartz come with a proprietary coating layer, referred to as "polymer/metal spacer" that is supposedly keeps the nanoparticles stabilized and functioning in time. AuroVist commercial gold nanoparticles give no indication of the stabilizing agent used, even though it is implied that one is used. On the other hand, the homemade, phosphene capped gold nanoparticles that were prepared at IMRCP, were relatively unstable, shifting their color from deep red to a hue of blue, an indication that aggregation took place. However, due to the phosphene covering the surface of the particles, this phenomenon is reversible and the AuNPs can be re-dispersed by a simple sonication. Preliminary tests showed that this aggregation can occur during the staining procedure within a bioreactor resulting in inhomogeneous contrast. However, if the overall contrast given by the particles throughout the biofilm phase is adequate, the inhomogeneities do not pose a problem. For a comparison, a similar phenomenon of sedimentation is observed with the $BaSO_4$ contrast agent that has not been mixed with thickening agents such as agarose.

Cytotoxicity/Biocompatibility Another challenge is optimizing the concentration of the nanoparticles to ensure good contrast without causing toxicity to the cells within the biofilm. AuroVist nanoparticles claim that 200 mg/mL of their product injected into mice gives 1800 HU in blood vessels with no toxicity issues. They indicate that the median lethal dose for gold is LD50 $>$ 5.0 g Au/kg of body. Indeed, various studies highlighted the low cytotoxicity citrate capped AuNPs [86, 445] which render them ideal for in vivo studies but further studies suggest that AuNPs can be strategically used to target and eliminate biofilms [3, 365]. There are also studies that indicate that gold nanoparticles can be taken up by bacteria without causing toxicity [38]. On the other hand, other studies have shown that biosynthesized gold nanoparticles can be effective against P. aeruginosa [401], inhibiting growth even at concentrations as low as 50 µg/mL [7]. All in all, their cytotoxicity depends on several parameters such as their size [306], concentration and surface functionalization [398] and therefore, further studies are needed.

Cost to contrast ratio When considering contrast agents, $BaSO_4$ is an economical option despite requiring a minimum concentration of about 30 % w/v for optimal results. On the other hand, functionalized AuNPs are significantly more expensive, requiring a higher concentration to achieve the desired contrast. As a reminder, here the solution injected had a concentration of 1.13 mg/mL. For comparison, non-functionalized AuNPs such as the commercial AuroVist, fall within a mid-range cost and they are supplied in high concentrations. The stock solution provided by the company had a concentration of 40 mg/mL. Finally, the homemade, phosphene-stabilized AuNPs were the most cost efficient gold nanoparticles but with a trade-off of inconsistencies from batch to batch and the fact that even though it is possible to synthesize large quantities, it is challenging to fabricate concentrated solutions. Overall, the use of functionalized gold nanoparticles as a contrast agent in X-ray tomography shows promising results for improving the accuracy of biofilm imaging. However, further research is needed to optimize the properties of the nanoparticles and to evaluate their safety and efficacy in vivo.

20 Conclusion

In this chapter, we explored the potential use of non-functionalized and functionalized gold nanoparticles (AuNPs) as contrast agents for X-ray imaging of biofilms. We conducted a series of experiments to investigate the imaging capabilities of AuNPs in the visualization of biofilm structures. We demonstrate that gold nanoparticles present a promising option for the development of novel x-ray tomography contrast agents for imaging biofilms. The high atomic number of gold provides excellent contrast for imaging biological materials, and the ability to functionalize the particles with targeting molecules could allow for specific imaging of biofilms. Additionally, the small size of gold nanoparticles allows for deeper penetration into biological tissues, making them an attractive option for biological imaging applications. However, further studies are needed to optimize the size, surface chemistry, and targeting of the nanoparticles to maximize their efficacy for biofilm imaging. With continued research and development, functionalized gold nanoparticles could become a valuable tool for the non-invasive imaging of biofilms and improve our understanding of these complex microbial communities.

Overall, the results of these experiments demonstrate the utilization potential of the 3D printed system as well as the potential of the AuNPs as a novel approach to contrast enhancing. On the one hand, non-functionalized, commercial gold nanoparticles offer a relatively cheap solution for staining the liquid phase of similar systems but with the drawback of low selectivity of the particles for the stained phase. On the other hand, functionalized gold nanoparticles provide a more expensive but also more sophisticated and expensive solution with a lot of potential regarding the provided contrast. The main advantages of this newly proposed approach is the versatility of the surface functionalization of the novel contrast agent that could potentially allow for a development of a “library” of μCT contrast agents for staining biological samples, adapted for each specific application.

Part V

General conclusion and perspectives

This work has contributed to the field of biofilm studies in two major ways. The first is the development of a highly modular experimental setup comprising of an innovative 3D-printed bioreactor technology and a fluidic circuit with various measuring and parameter controling units, to monitor the biofilm growth dynamics in porous media and investigate the influence of various biochemical and mechanical parameters on biofilm development. The experimental setup allowed for the real-time tracking of the evolution of differential pressure and permeability along the porous medium, O_2 consumption, and biofilm detachment events under controlled hydrodynamical environment using spectrophotometry and direct observation of the effluent stream using a camera. Statistical analysis and post-processing of the data identified specific detachment patterns with different frequencies depending on the growth phase. This methodology enables investigation of the influence of mechanical and biochemical parameters on the colonization of various porous media. By controlling biofilm growth environmental factors, biofilm development can be investigated with only one varying parameter, such as bacterial strain, porous medium, pressure, flow rate, differential pressure, nutrient composition, or concentration.

In addition to the previously mentioned methodology, we can further enhance our understanding of the hydrodynamic environment within the porous substrate by combining it with X-ray imaging and CFD techniques. X-ray tomography was used with a well-established contrast agent protocol for 3D biofilm imaging to determine the spatial distribution of biomass within the pore space. Furthermore, CFD simulations were performed on a mesh fabricated from these X-ray tomography data and on a mesh corresponding to an empty bioreactor, providing a better view of the hydrodynamic environment, including fluid velocity and shear stress, within the selected porous structure. Through further analysis, we discovered a correlation between these parameters and biomass distribution, indicating that biomass tends to develop in high shear areas.

The second contribution is related to the potential use of gold nanoparticles (AuNPs) as a novel contrast agent for biofilm visualisation using µCT. First we studied the potential use of non-functionalized comercial AuNPs and we correlated the contrast given off in X-ray tomographs to the gold concentration using homemade, phosphene stabilized AuNPs. The efficiency of biofilm staining using the non-functionalized AuNPs showed a strong dependence on the size of the particles as well as the injected concentration. Smaller particles tended to diffuse within the biofilm matrix while larger ones did not penetrate the matrix as much suggesting that these larger particles could be used as a contrast agent for staining the liquid phase around the biofilm rather the biofilm itself. Additionally, functionalized, commercial AuNPs were tested, implementing a more sophisticated mechanism to bind onto biofilm components through an adapted surface functionalization. The developed staining protocol included two steps, first biotinylating specific polysaccharites present on the matrix and then injection/interraction of the Streptavidin-functionalized AuNPs with the biotinylated sites. X-ray imaging revealed that these nanoparticles accumulate onto the biofilm matrix providing an enhanced contrast relative to the one provided by the initially injected AuNP solution. Ultimately, the nanoparticles were tested on biofilm grown within the bioreactor setup mentioned earlier, in order to assess their viability as a tool for imaging biofilms in porous media. Although this approach was successful in producing sufficient contrast to differentiate between the biofilm and liquid phases, the resulting biomass visualization indicated that the staining was not uniformly distributed throughout the entirety of the porous medium. However, the resulting image stacks highlighted the creation of preferential paths with only the "active" biofilm (biofilm in direct contact with the liquid phase) being stained. Overall, the preliminary tests carried out in this study on the use of AuNPs as a contrast agent for X-ray imaging of biofilms have shown promising results. However, it is important to note that further and more extensive studies are required to fully understand the potential of AuNPs as a contrast agent for biofilm imaging in porous media.

In conclusion, this thesis has presented a comprehensive and innovative approach for studying biofilms in porous media. By developing a modular experimental setup and utilizing advanced imaging techniques, we were able to gain valuable insights into the dynamics of biofilm growth and its interactions with the surrounding environment. Our findings have significant implications for the design of effective strategies for controlling and managing biofilms in various settings. Moreover, our investigation into the potential use of gold nanoparticles as a contrast agent for biofilm visualization using µCT has shown promising results. This opens up new possibilities for non-invasive, high-resolution imaging of biofilms in complex structures, which could have important applications in fields such as microbiology, environmental science, and biotechnology.

Bibiography

References

[1] I. Gilan (Orr), Y. Hadar, and A. Sivan. "Colonization, Biofilm Formation and Biodegradation of Polyethylene by a Strain of Rhodococcus Ruber". In: *Applied Microbiology and Biotechnology* 65.1 (July 2004), pp. 97–104. ISSN: 1432-0614. DOI: `10.1007/s00253-004-1584-8`. (Visited on 04/07/2023).

[2] *3D Visualization & Analysis Software - FR*. https://www.thermofisher.com/fr/fr/home/electron-microscopy/products/software-em-3d-vis/3d-visualization-analysis-software.html. (Visited on 02/25/2023).

[3] Sundos S. I. Abdalla et al. "Antibacterial and Anti-Biofilm Biosynthesised Silver and Gold Nanoparticles for Medical Applications: Mechanism of Action, Toxicity and Current Status". In: *Current Drug Delivery* 17.2 (Feb. 2020), pp. 88–100. DOI: `10.2174/1567201817666191227094334`.

[4] Soumya El Abed et al. *Scanning Electron Microscopy (SEM) and Environmental SEM: Suitable Tools for Study of Adhesion Stage and Biofilm Formation*. IntechOpen, Mar. 2012. ISBN: 978-953-51-0092-8. DOI: `10.5772/34990`. (Visited on 12/19/2022).

[5] Miguel A. Acosta et al. "Fluorescent Microparticles for Sensing Cell Microenvironment Oxygen Levels within 3D Scaffolds". In: *Biomaterials* 30.17 (June 2009), pp. 3068–3074. ISSN: 01429612. DOI: `10.1016/j.biomaterials.2009.02.021`. (Visited on 01/08/2023).

[6] Morten Alhede et al. "Combination of Microscopic Techniques Reveals a Comprehensive Visual Impression of Biofilm Structure and Composition". In: *FEMS Immunology & Medical Microbiology* 65.2 (July 2012), pp. 335–342. ISSN: 0928-8244. DOI: `10.1111/j.1574-695X.2012.00956.x`. (Visited on 11/01/2021).

[7] Syed Ghazanfar Ali et al. "Biosynthesis of Gold Nanoparticles and Its Effect against Pseudomonas Aeruginosa". In: *Molecules* 27.24 (Jan. 2022), p. 8685. ISSN: 1420-3049. DOI: `10.3390/molecules27248685`. (Visited on 04/14/2023).

[8] Cristina Isabel Amador et al. "High-Throughput Screening Alternative to Crystal Violet Biofilm Assay Combining Fluorescence Quantification and Imaging". In: *Journal of Microbiological Methods* 190 (Nov. 2021), p. 106343. ISSN: 0167-7012. DOI: `10.1016/j.mimet.2021.106343`. (Visited on 04/05/2023).

[9] Reza Amin et al. "3D-printed Microfluidic Devices". In: *Biofabrication* 8.2 (June 2016), p. 022001. ISSN: 1758-5090. DOI: `10.1088/1758-5090/8/2/022001`. (Visited on 03/14/2023).

[10] Sajjad Al-Amshawee and Mohd Yusri Bin Mohd Yunus. "Geometry of Biofilm Carriers: A Systematic Review Deciding the Best Shape and Pore Size". In: *Groundwater for Sustainable Development* 12 (Feb. 2021), p. 100520. ISSN: 2352-801X. DOI: `10.1016/j.gsd.2020.100520`. (Visited on 01/31/2023).

[11] N. D. Andryushchenko et al. "Sorption Characteristics of Materials of the Filtration Barrier in Upper Aquifers Contaminated with Radionuclides". In: *Radiochemistry* 59.4 (July 2017), pp. 414–424. ISSN: 1608-3288. DOI: `10.1134/S1066362217040154`. (Visited on 03/15/2023).

[12] Maria Joseph Angelaalincy et al. "Biofilm Engineering Approaches for Improving the Performance of Microbial Fuel Cells and Bioelectrochemical Systems". In: *Frontiers in Energy Research* 6 (2018). ISSN: 2296-598X. (Visited on 03/13/2023).

[13] Philippe Angot, Charles-Henri Bruneau, and Pierre Fabrie. "A Penalization Method to Take into Account Obstacles in Incompressible Viscous Flows". In: *Numerische Mathematik* 81.4 (Feb. 1999), pp. 497–520. ISSN: 0945-3245. DOI: `10.1007/s002110050401`. (Visited on 03/09/2023).

[14] Pietro de Anna et al. "Mixing and Reaction Kinetics in Porous Media: An Experimental Pore Scale Quantification". In: *Environmental Science & Technology* 48.1 (Jan. 2014), pp. 508–516. ISSN: 0013-936X. DOI: `10.1021/es403105b`. (Visited on 12/09/2022).

[15] A. R. Archibald and H. E. Coapes. "The Interaction of Concanavalin A with Teichoic Acids and Bacterial Walls." In: *The Biochemical journal* 123.4 (1971), pp. 665–667. ISSN: 02646021. DOI: `10.1042/bj1230665`.

[16] Anthony K. Au et al. "3D-Printed Microfluidics". In: *Angewandte Chemie International Edition* 55.12 (Mar. 2016), pp. 3862–3881. ISSN: 14337851. DOI: `10.1002/anie.201504382`. (Visited on 03/14/2023).

[17] Jayde A. Aufrecht et al. "Pore-Scale Hydrodynamics Influence the Spatial Evolution of Bacterial Biofilms in a Microfluidic Porous Network". In: *PLOS ONE* 14.6 (June 2019), e0218316. ISSN: 1932-6203. DOI: `10.1371/journal.pone.0218316`. (Visited on 01/27/2022).

[18] Jose M. Ayuso et al. "A Role for Microfluidic Systems in Precision Medicine". In: *Nature Communications* 13.1 (June 2022), p. 3086. ISSN: 2041-1723. DOI: `10.1038/s41467-022-30384-7`. (Visited on 09/20/2022).

[19] Niels Bagge et al. "Dynamics and Spatial Distribution of Beta-Lactamase Expression in Pseudomonas Aeruginosa Biofilms". In: *Antimicrobial Agents and Chemotherapy* 48.4 (Apr. 2004), pp. 1168–1174. ISSN: 0066-4804. DOI: `10.1128/AAC.48.4.1168-1174.2004`.

[20] Perrin Baker et al. "Exopolysaccharide Biosynthetic Glycoside Hydrolases Can Be Utilized to Disrupt and Prevent Pseudomonas Aeruginosa Biofilms". In: *Science Advances* 2.5 (May 2016), e1501632. ISSN: 2375-2548. DOI: `10.1126/sciadv.1501632`.

[21] Christiane Baschien et al. "In Situ Detection of Freshwater Fungi in an Alpine Stream by New Taxon-Specific Fluorescence in Situ Hybridization Probes". In: *Applied and Environmental Microbiology* 74.20 (Oct. 2008), pp. 6427–6436. ISSN: 1098-5336. DOI: `10.1128/AEM.00815-08`.

[22] B. L. Bassler, M. Wright, and M. R. Silverman. "Multiple Signalling Systems Controlling Expression of Luminescence in Vibrio Harveyi: Sequence and Function of Genes Encoding a Second Sensory Pathway". In: *Molecular Microbiology* 13.2 (July 1994), pp. 273–286. ISSN: 0950-382X. DOI: `10.1111/j.1365-2958.1994.tb00422.x`.

[23] Tom J. Battin et al. "The Ecology and Biogeochemistry of Stream Biofilms". In: *Nature Reviews Microbiology* 14.4 (Apr. 2016), pp. 251–263. ISSN: 1740-1534. DOI: `10.1038/nrmicro.2016.15`. (Visited on 11/03/2021).

[24] R. N. Bearon and A. L. Hazel. "The Trapping in High-Shear Regions of Slender Bacteria Undergoing Chemotaxis in a Channel". In: *Journal of Fluid Mechanics* 771 (May 2015), R3. ISSN: 0022-1120, 1469-7645. DOI: `10.1017/jfm.2015.198`. (Visited on 04/07/2023).

[25] A. Beaudoin and J.-R. de Dreuzy. "Numerical Assessment of 3-D Macrodispersion in Heterogeneous Porous Media". In: *Water Resources Research* 49.5 (2013), pp. 2489–2496. ISSN: 1944-7973. DOI: `10.1002/wrcr.20206`. (Visited on 04/04/2023).

[26] Iwona B Beech and Jan Sunner. "Biocorrosion: Towards Understanding Interactions between Biofilms and Metals". In: *Current Opinion in Biotechnology* 15.3 (June 2004), pp. 181–186. ISSN: 0958-1669. DOI: `10.1016/j.copbio.2004.05.001`. (Visited on 04/07/2023).

[27] Iwona B Beech et al. "The Use of Atomic Force Microscopy for Studying Interactions of Bacterial Biofilms with Surfaces". In: *Colloids and Surfaces B: Biointerfaces* 23.2 (Feb. 2002), pp. 231–247. ISSN: 0927-7765. DOI: `10.1016/S0927-7765(01)00233-8`. (Visited on 12/19/2022).

[28] Michael R. Behrens et al. "Open-Source, 3D-printed Peristaltic Pumps for Small Volume Point-of-Care Liquid Handling". In: *Scientific Reports* 10.1 (Jan. 2020), p. 1543. ISSN: 2045-2322. DOI: `10.1038/s41598-020-58246-6`. (Visited on 03/15/2023).

[29] M. A. Benjamin et al. "Changes in Murine Jejunal Morphology Evoked by the Bacterial Superantigen Staphylococcus Aureus Enterotoxin B Are Mediated by CD4+ T Cells". In: *Infection and Immunity* 66.5 (May 1998), pp. 2193–2199. ISSN: 0019-9567. DOI: `10.1128/IAI.66.5.2193-2199.1998`.

[30] Saida Benomar et al. “Nutritional Stress Induces Exchange of Cell Material and Energetic Coupling between Bacterial Species”. In: *Nature Communications* 6.1 (Feb. 2015), pp. 1–10. ISSN: 20411723. DOI: `10.1038/ncomms7283`.

[31] Martin Berger, Qiao Yang, and Andreas Maier. “X-Ray Imaging”. In: *Medical Imaging Systems: An Introductory Guide*. Ed. by Andreas Maier et al. Cham (CH): Springer, 2018. ISBN: 978-3-319-96519-2 978-3-319-96520-8. (Visited on 01/03/2023).

[32] E. Berkenpas, P. Millard, and M. Pereira da Cunha. “Detection of Escherichia Coli O157:H7 with Langasite Pure Shear Horizontal Surface Acoustic Wave Sensors”. In: *Biosensors & Bioelectronics* 21.12 (June 2006), pp. 2255–2262. ISSN: 0956-5663. DOI: `10.1016/j.bios.2005.11.005`.

[33] Y. Bernabé, M. Li, and A. Maineult. “Permeability and Pore Connectivity: A New Model Based on Network Simulations”. In: *Journal of Geophysical Research: Solid Earth* 115.B10 (2010). ISSN: 2156-2202. DOI: `10.1029/2010JB007444`. (Visited on 04/04/2023).

[34] Katharina Besemer et al. “Architectural Differentiation Reflects Bacterial Community Structure in Stream Biofilms”. In: *The ISME Journal* 3.11 (Nov. 2009), pp. 1318–1324. ISSN: 1751-7370. DOI: `10.1038/ismej.2009.73`. (Visited on 03/15/2023).

[35] Haluk Beyenal and Zbigniew Lewandowski. “Internal and External Mass Transfer in Biofilms Grown at Various Flow Velocities”. In: *Biotechnology Progress* 18.1 (2002), pp. 55–61. ISSN: 1520-6033. DOI: `10.1021/bp010129s`. (Visited on 01/29/2023).

[36] Tapomoy Bhattacharjee and Sujit S. Datta. “Bacterial Hopping and Trapping in Porous Media”. In: *Nature Communications* 10.1 (Dec. 2019), pp. 1–9. ISSN: 20411723. DOI: `10.1038/s41467-019-10115-1`.

[37] Tapomoy Bhattacharjee et al. “Chemotactic Migration of Bacteria in Porous Media”. In: *Biophysical Journal* 120.16 (Aug. 2021), pp. 3483–3497. ISSN: 0006-3495. DOI: `10.1016/j.bpj.2021.05.012`. (Visited on 12/29/2022).

[38] Nataniel Białas et al. “Bacteria (E. Coli) Take up Ultrasmall Gold Nanoparticles (2 Nm) as Shown by Different Optical Microscopic Techniques (CLSM, SIM, STORM)”. In: *Nano Select* 3.10 (2022), pp. 1407–1420. ISSN: 2688-4011. DOI: `10.1002/nano.202200049`. (Visited on 04/14/2023).

[39] Barry J. F. Biggs, Vladimir I. Nikora, and Ton H. Snelder. “Linking Scales of Flow Variability to Lotic Ecosystem Structure and Function”. In: *River Research and Applications* 21.2-3 (2005), pp. 283–298. ISSN: 1535-1467. DOI: `10.1002/rra.847`. (Visited on 01/03/2023).

[40] Nicole Billings et al. “The Extracellular Matrix Component Psl Provides Fast-Acting Antibiotic Defense in Pseudomonas Aeruginosa Biofilms”. In: *PLOS Pathogens* 9.8 (Aug. 2013), e1003526. ISSN: 1553-7374. DOI: `10.1371/journal.ppat.1003526`. (Visited on 09/13/2019).

[41] Wolfgang Birkfellner. *Applied Medical Image Processing: A Basic Course*. Second edition. Boca Raton: CRC Press, Taylor & Francis Group, 2014. ISBN: 978-1-4665-5557-0.

[42] Andrew Bissett et al. “Metabolic Microenvironmental Control by Photosynthetic Biofilms under Changing Macroenvironmental Temperature and pH Conditions”. In: *Applied and Environmental Microbiology* 74.20 (Oct. 2008), pp. 6306–6312. DOI: `10.1128/AEM.00877-08`. (Visited on 01/07/2023).

[43] Sara M Bjork and Haakan N Joensson. “Microfluidics for Cell Factory and Bioprocess Development”. In: *Current Opinion in Biotechnology*. Analytical Biotechnology 55 (Feb. 2019), pp. 95–102. ISSN: 0958-1669. DOI: `10.1016/j.copbio.2018.08.011`. (Visited on 03/27/2023).

[44] Marcel Bogers, Ronen Hadar, and Arne Bilberg. “Additive Manufacturing for Consumer-Centric Business Models: Implications for Supply Chains in Consumer Goods Manufacturing”. In: *Technological Forecasting and Social Change* 102 (Jan. 2016), pp. 225–239. ISSN: 0040-1625. DOI: `10.1016/j.techfore.2015.07.024`. (Visited on 03/14/2023).

[45] Thomas Böhm et al. “Quantitative Synchrotron X-ray Tomography of the Material-Tissue Interface in Rat Cortex Implanted with Neural Probes”. In: *Scientific Reports* 9.1 (May 2019), p. 7646. ISSN: 2045-2322. DOI: `10.1038/s41598-019-42544-9`. (Visited on 12/21/2022).

[46] O. Boiron, G. Chiavassa, and R. Donat. “A High-Resolution Penalization Method for Large Mach Number Flows in the Presence of Obstacles”. In: *Computers & Fluids* 38.3 (Mar. 2009), pp. 703–714. ISSN: 0045-7930. DOI: `10.1016/j.compfluid.2008.07.003`. (Visited on 03/09/2023).

[47] Anuja Bokare et al. “Herringbone-Patterned 3D-Printed Devices as Alternatives to Microfluidics for Reproducible Production of Lipid Polymer Hybrid Nanoparticles”. In: *ACS Omega* 4.3 (Mar. 2019), pp. 4650–4657. DOI: `10.1021/acsomega.9b00128`. (Visited on 03/15/2023).

[48] Niels P. Boks et al. “Forces Involved in Bacterial Adhesion to Hydrophilic and Hydrophobic Surfaces”. In: *Microbiology* 154.10 (Oct. 2008), pp. 3122–3133. ISSN: 1350-0872, 1465-2080. DOI: `10.1099/mic.0.2008/018622-0`. (Visited on 01/29/2023).

[49] Simona Bottero et al. “Biofilm Development and the Dynamics of Preferential Flow Paths in Porous Media”. In: *Biofouling* 29.9 (2013), pp. 1069–1086. ISSN: 08927014. DOI: `10.1080/08927014.2013.828284`.

[50] Gilles Brackman et al. “Use of Quorum Sensing Inhibitors to Interfere with Biofilm Formation and Development in Burkholderia Multivorans and Burkholderia Cenocepacia”. In: *Research in Microbiology* 160.2 (Mar. 2009), pp. 144–151. ISSN: 0923-2508. DOI: `10.1016/j.resmic.2008.12.003`. (Visited on 04/07/2023).

[51] Ch.-H. Bruneau and P. Fabrie. “Effective Downstream Boundary Conditions for Incompressible Navier–Stokes Equations”. In: *International Journal for Numerical Methods in Fluids* 19.8 (1994), pp. 693–705. ISSN: 1097-0363. DOI: `10.1002/fld.1650190805`. (Visited on 03/09/2023).

[52] Esther Bullitt and Lee Makowski. *Structural Polymorphism of Bacterial Adhesion Pili*. Vol. 373. Jan. 1995. DOI: `10.1038/373164a0`.

[53] Noa Burshtein et al. “3D-printed Glass Microfluidics for Fluid Dynamics and Rheology”. In: *Current Opinion in Colloid & Interface Science*. Rheology 43 (Oct. 2019), pp. 1–14. ISSN: 1359-0294. DOI: `10.1016/j.cocis.2018.12.005`. (Visited on 03/14/2023).

[54] Matthew S. Byrd et al. “Direct Evaluation of Pseudomonas Aeruginosa Biofilm Mediators in a Chronic Infection Model”. In: *Infection and Immunity* 79.8 (Aug. 2011), pp. 3087–3095. DOI: `10.1128/IAI.00057-11`. (Visited on 04/07/2023).

[55] Matthew S. Byrd et al. “Genetic and Biochemical Analyses of the Pseudomonas Aeruginosa Psl Exopolysaccharide Reveal Overlapping Roles for Polysaccharide Synthesis Enzymes in Psl and LPS Production”. In: *Molecular Microbiology* 73.4 (Aug. 2009), pp. 622–638. ISSN: 1365-2958. DOI: `10.1111/j.1365-2958.2009.06795.x`.

[56] Peng Cai et al. “Soil Biofilms: Microbial Interactions, Challenges, and Advanced Techniques for Ex-Situ Characterization”. In: *Soil Ecology Letters* 1.3 (Dec. 2019), pp. 85–93. ISSN: 2662-2297. DOI: `10.1007/s42832-019-0017-7`. (Visited on 03/13/2023).

[57] Quan-Yu Cai et al. “Colloidal Gold Nanoparticles as a Blood-Pool Contrast Agent for X-ray Computed Tomography in Mice”. In: *Investigative Radiology* 42.12 (Dec. 2007), pp. 797–806. ISSN: 0020-9996. DOI: `10.1097/RLI.0b013e31811ecdcd`.

[58] Nicky C. Caiazza and George A. O’Toole. “SadB Is Required for the Transition from Reversible to Irreversible Attachment during Biofilm Formation by Pseudomonas Aeruginosa PA14”. In: *Journal of Bacteriology* 186.14 (July 2004), pp. 4476–4485. ISSN: 0021-9193. DOI: `10.1128/JB.186.14.4476-4485.2004`.

[59] Leire Caizán-Juanarena et al. “3D Biofilm Visualization and Quantification on Granular Bioanodes with Magnetic Resonance Imaging”. In: *Water Research* 167 (Dec. 2019), p. 115059. ISSN: 18792448. DOI: `10.1016/j.watres.2019.115059`.

[60] M. Carrel et al. “Pore-Scale Hydrodynamics in a Progressively Bioclogged Three-Dimensional Porous Medium: 3-D Particle Tracking Experiments and Stochastic Transport Modeling”. In: *Water Resources Research* 54.3 (Mar. 2018), pp. 2183–2198. ISSN: 19447973. DOI: `10.1002/2017WR021726`.

[61] Maxence Carrel et al. “Biofilm Imaging in Porous Media by Laboratory X-Ray Tomography: Combining a Non-Destructive Contrast Agent with Propagation-Based Phase-Contrast Imaging Tools”. In: *PLoS ONE* 12.7 (July 2017), e0180374. ISSN: 19326203. DOI: `10.1371/journal.pone.0180374`.

[62] Maxence Carrel et al. “Biofilms in 3D Porous Media: Delineating the Influence of the Pore Network Geometry, Flow and Mass Transfer on Biofilm Development”. In: *Water Research* 134 (May 2018), pp. 280–291. ISSN: 18792448. DOI: `10.1016/j.watres.2018.01.059`.

[63] Sarah L. Castro et al. “Induction of Attachment-Independent Biofilm Formation and Repression of Hfq Expression by Low-Fluid-Shear Culture of Staphylococcus Aureus”. In: *Applied and Environmental Microbiology* 77.18 (Sept. 2011), pp. 6368–6378. DOI: `10.1128/AEM.00175-11`. (Visited on 04/12/2023).

[64] Giulia Ceriotti et al. “Morphology and Size of Bacterial Colonies Control Anoxic Microenvironment Formation in Porous Media”. In: *Environmental Science & Technology* 56.23 (Dec. 2022), pp. 17471–17480. ISSN: 0013-936X. DOI: `10.1021/acs.est.2c05842`. (Visited on 12/29/2022).

[65] R. Cesareo. “X-Ray Physics: Interaction with Matter, Production, Detection”. In: *La Rivista del Nuovo Cimento* 23.7 (July 2000), pp. 1–231. ISSN: 1826-9850. DOI: `10.1007/BF03548887`. (Visited on 12/22/2022).

[66] Peter Chahales and David G. Thanassi. “Structure, Function, and Assembly of Adhesive Organelles by Uropathogenic Bacteria”. In: *Microbiology Spectrum* 3.5 (Oct. 2015). ISSN: 2165-0497. DOI: `10.1128/microbiolspec.uti-0018-2013`.

[67] Jiangfan Chang et al. “The Impact of Hydrodynamic Shear Force on Adhesion Morphology and Biofilm Conformation of Bacillus Sp.” In: *Ocean Engineering* 197 (Feb. 2020), p. 106860. ISSN: 00298018. DOI: `10.1016/j.oceaneng.2019.106860`.

[68] W. G. Characklis and K. E. Cooksey. “Biofilms and Microbial Fouling”. In: *Advances in Applied Microbiology* 29.C (Jan. 1983), pp. 93–138. ISSN: 00652164. DOI: `10.1016/S0065-2164(08)70355-1`.

[69] Susmita Chatterjee et al. “Atomic Force Microscopy in Biofilm Study”. In: *Microscopy* 63.4 (Aug. 2014), pp. 269–278. ISSN: 2050-5698. DOI: `10.1093/jmicro/dfu013`. (Visited on 12/19/2022).

[70] Niladri Chattopadhyay et al. “Design and Characterization of HER-2-Targeted Gold Nanoparticles for Enhanced X-radiation Treatment of Locally Advanced Breast Cancer”. In: *Molecular Pharmaceutics* 7.6 (Dec. 2010), pp. 2194–2206. ISSN: 1543-8384. DOI: `10.1021/mp100207t`.

[71] Chengpeng Chen et al. “3D-printed Microfluidic Devices: Fabrication, Advantages and Limitations—a Mini Review”. In: *Analytical Methods* 8.31 (Aug. 2016), pp. 6005–6012. ISSN: 1759-9679. DOI: `10.1039/C6AY01671E`. (Visited on 03/14/2023).

[72] Guanghao Chen et al., eds. *Biological Wastewater Treatment: Principles, Modeling and Design*. Second. IWA Publishing, July 2020. ISBN: 978-1-78906-036-2. DOI: `10.2166/9781789060362`. (Visited on 11/08/2022).

[73] Wen-Jie Chen, Karthikeyan Kandasamy, and Yu-Chie Chen. “Functional Gold Nanoparticles as Sensing Probes for Concanavalin A and as Imaging Agents for Cancer Cells”. In: *ACS Applied Nano Materials* 2.6 (June 2019), pp. 3348–3357. ISSN: 2574-0970, 2574-0970. DOI: `10.1021/acsanm.9b00220`. (Visited on 02/14/2020).

[74] Xianchuan Chen et al. “Sinking of Floating Plastic Debris Caused by Biofilm Development in a Freshwater Lake”. In: *Chemosphere* 222 (May 2019), pp. 856–864. ISSN: 18791298. DOI: `10.1016/j.chemosphere.2019.02.015`. PMID: `30743237`.

[75] Kuan-Chen Cheng, Ali Demirci, and Jeffrey M. Catchmark. “Advances in Biofilm Reactors for Production of Value-Added Products”. In: *Applied Microbiology and Biotechnology* 87.2 (June 2010), pp. 445–456. ISSN: 1432-0614. DOI: `10.1007/s00253-010-2622-3`. (Visited on 11/08/2022).

[76] Eric Chénier et al. “An Extension of the MAC Scheme to Locally Refined Meshes: Convergence Analysis for the Full Tensor Time-Dependent Navier–Stokes Equations”. In: *Calcolo* 52.1 (Mar. 2015), pp. 69–107. ISSN: 0008-0624, 1126-5434. DOI: `10.1007/s10092-014-0108-x`. (Visited on 03/09/2023).

[77] Martin R. Chénier et al. “Impact of Seasonal Variations and Nutrient Inputs on Nitrogen Cycling and Degradation of Hexadecane by Replicated River Biofilms”. In: *Applied and Environmental Microbiology* 69.9 (Sept. 2003), pp. 5170–5177. DOI: `10.1128/AEM.69.9.5170-5177.2003`. (Visited on 03/15/2023).

[78] Kathryn E. Cherny and Karin Sauer. “Pseudomonas Aeruginosa Requires the DNA-Specific Endonuclease EndA To Degrade Extracellular Genomic DNA To Disperse from the Biofilm”. In: *Journal of Bacteriology* 201.18 (Sept. 2019), e00059–19. ISSN: 1098-5530. DOI: `10.1128/JB.00059-19`.

[79] Peter Chhour et al. “Labeling Monocytes with Gold Nanoparticles to Track Their Recruitment in Atherosclerosis with Computed Tomography”. In: *Biomaterials* 87 (May 2016), pp. 93–103. ISSN: 1878-5905. DOI: `10.1016/j.biomaterials.2016.02.009`.

[80] Alessandro Chiadò et al. “A Modular 3D Printed Lab-on-a-Chip for Early Cancer Detection”. In: *Lab on a Chip* 20.3 (2020), pp. 665–674. DOI: `10.1039/C9LC01108K`. (Visited on 04/05/2023).

[81] Hyunah Cho, Udayabhanu Jammalamadaka, and Karthik Tappa. “Nanogels for Pharmaceutical and Biomedical Applications and Their Fabrication Using 3D Printing Technologies”. In: *Materials* 11.2 (Feb. 2018), p. 302. ISSN: 1996-1944. DOI: `10.3390/ma11020302`. (Visited on 03/14/2023).

[82] Oana Ciofu et al. “Antimicrobial Resistance, Respiratory Tract Infections and Role of Biofilms in Lung Infections in Cystic Fibrosis Patients”. In: *Advanced Drug Delivery Reviews* 85 (May 2015), pp. 7–23. ISSN: 1872-8294. DOI: `10.1016/j.addr.2014.11.017`.

[83] Rolf Clackdoyle and Michel Defrise. “Tomographic Reconstruction in the 21st Century”. In: *IEEE Signal Processing Magazine* 27.4 (July 2010), pp. 60–80. ISSN: 1558-0792. DOI: `10.1109/MSP.2010.936743`.

[84] Kelly M. Colvin et al. “PelA Deacetylase Activity Is Required for Pel Polysaccharide Synthesis in Pseudomonas Aeruginosa”. In: *Journal of Bacteriology* 195.10 (May 2013), pp. 2329–2339. ISSN: 1098-5530. DOI: `10.1128/JB.02150-12`.

[85] Kelly M. Colvin et al. “The Pel and Psl Polysaccharides Provide Pseudomonas Aeruginosa Structural Redundancy within the Biofilm Matrix”. In: *Environmental Microbiology* 14.8 (Aug. 2012), pp. 1913–1928. ISSN: 1462-2920. DOI: `10.1111/j.1462-2920.2011.02657.x`.

[86] Ellen E. Connor et al. “Gold Nanoparticles Are Taken Up by Human Cells but Do Not Cause Acute Cytotoxicity”. In: *Small* 1.3 (2005), pp. 325–327. ISSN: 1613-6829. DOI: `10.1002/smll.200400093`. (Visited on 04/01/2023).

[87] Jacinta Conrad and Ryan Poling-Skutvik. “Confined Flow: Consequences and Implications for Bacteria and Biofilms”. In: *Annual Review of Chemical and Biomolecular Engineering* 9 (June 2018). DOI: `10.1146/annurev-chembioeng-060817-084006`.

[88] J. William Costerton, ed. *The Biofilm Primer*. Vol. 1. Springer Series on Biofilms. Berlin, Heidelberg: Springer Berlin Heidelberg, 2007. ISBN: 978-3-540-68021-5. DOI: `10.1007/b136878`. (Visited on 09/17/2019).

[89] Laura M. Coughlan et al. "New Weapons to Fight Old Enemies: Novel Strategies for the (Bio)Control of Bacterial Biofilms in the Food Industry". In: *Frontiers in Microbiology* 7 (2016), p. 1641. ISSN: 1664-302X. DOI: `10.3389/fmicb.2016.01641`.

[90] Marjorie M. Cowan, Tessie M. Warren, and Madilyn Fletcher. "Mixed-Species Colonization of Solid Surfaces in Laboratory Biofilms". In: *Biofouling* 3.1 (Feb. 1991), pp. 23–34. ISSN: 10292454. DOI: `10.1080/08927019109378159`.

[91] H. S. M. Coxeter. "On Laves' Graph Of Girth Ten". In: *Canadian Journal of Mathematics* 7 (1955/ed), pp. 18–23. ISSN: 0008-414X, 1496-4279. DOI: `10.4153/CJM-1955-003-7`. (Visited on 02/25/2023).

[92] Katharine Z. Coyte et al. "Microbial Competition in Porous Environments Can Select against Rapid Biofilm Growth". In: *Proceedings of the National Academy of Sciences* 114.2 (Jan. 2017), E161–E170. ISSN: 0027-8424, 1091-6490. DOI: `10.1073/pnas.1525228113`. (Visited on 09/29/2021).

[93] Stephanie Crone et al. "The Environmental Occurrence of Pseudomonas Aeruginosa". In: *APMIS* 128.3 (2020), pp. 220–231. ISSN: 1600-0463. DOI: `10.1111/apm.13010`. (Visited on 04/07/2023).

[94] Alexandra Csapai et al. "3D Printed Microfluidic Bioreactors Used for the Preferential Growth of Bacterial Biofilms through Dielectrophoresis". In: *Micromachines* 13.9 (Sept. 2022), p. 1377. ISSN: 2072-666X. DOI: `10.3390/mi13091377`. (Visited on 03/14/2023).

[95] Alfred B. Cunningham et al. "Subsurface Biofilm Barriers for the Containment and Remediation of Contaminated Groundwater". In: *Bioremediation Journal* 7.3-4 (July 2003), pp. 151–164. ISSN: 1088-9868. DOI: `10.1080/713607982`. (Visited on 03/25/2023).

[96] Sophie E. Darch et al. "Spatial Determinants of Quorum Signaling in a Pseudomonas Aeruginosa Infection Model". In: *Proceedings of the National Academy of Sciences of the United States of America* 115.18 (May 2018), pp. 4779–4784. ISSN: 1091-6490. DOI: `10.1073/pnas.1719317115`.

[97] Sudipta Dash et al. "Probing the Surface-Attached In Vitro Microbial Biofilms with Atomic Force (AFM) and Scanning Probe Microscopy (SPM)". In: *Analytical Methodologies for Biofilm Research*. Ed. by Moupriya Nag and Dibyajit Lahiri. Springer Protocols Handbooks. New York, NY: Springer US, 2021, pp. 223–241. ISBN: 978-1-07-161378-8. DOI: `10.1007/978-1-0716-1378-8_10`. (Visited on 11/01/2021).

[98] D G Davies, A M Chakrabarty, and G G Geesey. "Exopolysaccharide Production in Biofilms: Substratum Activation of Alginate Gene Expression by Pseudomonas Aeruginosa". In: *Applied and Environmental Microbiology* 59.4 (Apr. 1993), pp. 1181–1186. DOI: `10.1128/aem.59.4.1181-1186.1993`. (Visited on 01/22/2023).

[99] D G Davies and G G Geesey. "Regulation of the Alginate Biosynthesis Gene algC in Pseudomonas Aeruginosa during Biofilm Development in Continuous Culture." In: *Applied and Environmental Microbiology* 61.3 (Mar. 1995), pp. 860–867. ISSN: 0099-2240. (Visited on 01/22/2023).

[100] Y. Davit et al. "Imaging Biofilm in Porous Media Using X-ray Computed Microtomography". In: *Journal of Microscopy* 242.1 (Apr. 2011), pp. 15–25. ISSN: 00222720. DOI: `10.1111/j.1365-2818.2010.03432.x`.

[101] Marcia de Almeida Monteiro Melo Ferraz et al. "3D Printed Mold Leachates in PDMS Microfluidic Devices". In: *Scientific Reports* 10.1 (Jan. 2020), p. 994. ISSN: 2045-2322. DOI: `10.1038/s41598-020-57816-y`. (Visited on 03/15/2023).

[102] Pietro de Anna et al. "Chemotaxis under Flow Disorder Shapes Microbial Dispersion in Porous Media". In: *Nature Physics* 17.1 (Jan. 2021), pp. 68–73. ISSN: 1745-2481. DOI: `10.1038/s41567-020-1002-x`. (Visited on 01/27/2022).

[103] Pietro de Anna et al. "Flow Intermittency, Dispersion, and Correlated Continuous Time Random Walks in Porous Media". In: *Physical Review Letters* 110.18 (May 2013), p. 184502. DOI: `10.1103/PhysRevLett.110.184502`. (Visited on 09/13/2019).

[104] Dirk de Beer, Paul Stoodley, and Zbigniew Lewandowski. “Measurement of Local Diffusion Coefficients in Biofilms by Microinjection and Confocal Microscopy”. In: *Biotechnology and Bioengineering* 53.2 (1997), pp. 151–158. ISSN: 1097-0290. DOI: `10.1002/(SICI)1097-0290(19970120)53:2<151::AID-BIT4>3.0.CO;2-N`. (Visited on 12/20/2022).

[105] A Demirci, A L Pometto III, and K-L G Ho. “Ethanol Production by Saccharomyces Cerevisiae in Biofilm Reactors”. In: *Journal of Industrial Microbiology and Biotechnology* 19.4 (Oct. 1997), pp. 299–304. ISSN: 1367-5435, 1476-5535. DOI: `10.1038/sj.jim.2900464`. (Visited on 04/07/2023).

[106] Anna Depetris et al. “Automated 3D Optical Coherence Tomography to Elucidate Biofilm Morphogenesis Over Large Spatial Scales”. In: *JoVE (Journal of Visualized Experiments)* 150 (Aug. 2019), e59356. ISSN: 1940-087X. DOI: `10.3791/59356`. (Visited on 11/01/2021).

[107] Navdeep Kaur Dhami, M. Sudhakara Reddy, and Abhijit Mukherjee. “Biomineralization of Calcium Carbonate Polymorphs by the Bacterial Strains Isolated from Calcareous Sites”. In: *Journal of Microbiology and Biotechnology* 23.5 (2013), pp. 707–714. ISSN: 1017-7825. DOI: `10.4014/jmb.1212.11087`. (Visited on 11/03/2021).

[108] L. Di Gregorio et al. “Unravelling the Core Microbiome of Biofilms in Cooling Tower Systems”. In: *Biofouling* 33.10 (Nov. 2017), pp. 793–806. ISSN: 0892-7014. DOI: `10.1080/08927014.2017.1367386`. (Visited on 04/07/2023).

[109] Yuxi C. Dong et al. “Effect of Gold Nanoparticle Size on Their Properties as Contrast Agents for Computed Tomography”. In: *Scientific Reports* 9.1 (Oct. 2019), p. 14912. ISSN: 2045-2322. DOI: `10.1038/s41598-019-50332-8`. (Visited on 11/01/2021).

[110] Rodney M. Donlan. *Biofilms: Microbial Life on Surfaces*. Vol. 8. Centers for Disease Control and Prevention (CDC), 2002. DOI: `10.3201/eid0809.020063`.

[111] Helen Downie et al. “Transparent Soil for Imaging the Rhizosphere”. In: *PLoS ONE* 7.9 (Sept. 2012). Ed. by Malcolm Bennett, e44276. ISSN: 1932-6203. DOI: `10.1371/journal.pone.0044276`.

[112] J.A. Downing et al. “Global Abundance and Size Distribution of Streams and Rivers”. In: *Inland Waters* 2.4 (Jan. 2012), pp. 229–236. ISSN: 2044-2041. DOI: `10.5268/IW-2.4.502`. (Visited on 01/31/2023).

[113] Anna Dragoš and Ákos T. Kovács. *The Peculiar Functions of the Bacterial Extracellular Matrix*. Vol. 25. Elsevier Ltd, Apr. 2017. DOI: `10.1016/j.tim.2016.12.010`.

[114] Knut Drescher et al. “Biofilm Streamers Cause Catastrophic Disruption of Flow with Consequences for Environmental and Medical Systems”. In: *Proceedings of the National Academy of Sciences* 110.11 (Mar. 2013), pp. 4345–4350. ISSN: 0027-8424, 1091-6490. DOI: `10.1073/pnas.1300321110`. (Visited on 09/17/2019).

[115] James A. Driscoll, Steven L. Brody, and Marin H. Kollef. “The Epidemiology, Pathogenesis and Treatment of Pseudomonas Aeruginosa Infections”. In: *Drugs* 67.3 (Feb. 2007), pp. 351–368. ISSN: 1179-1950. DOI: `10.2165/00003495-200767030-00003`. (Visited on 04/02/2023).

[116] Bang Du et al. “Flagellar Motility Mediates Early-Stage Biofilm Formation in Oligotrophic Aquatic Environment”. In: *Ecotoxicology and Environmental Safety* 194 (May 2020), p. 110340. ISSN: 10902414. DOI: `10.1016/j.ecoenv.2020.110340`.

[117] Bin Duan and Min Wang. “Selective Laser Sintering and Its Application in Biomedical Engineering”. In: *MRS Bulletin* 36.12 (Dec. 2011), pp. 998–1005. ISSN: 1938-1425, 0883-7694. DOI: `10.1557/mrs.2011.270`. (Visited on 03/14/2023).

[118] Ravindra Duddu, David L. Chopp, and Brian Moran. “A two-dimensional continuum model of biofilm growth incorporating fluid flow and shear stress based detachment”. In: *Biotechnology and Bioengineering* 103.1 (2009), pp. 92–104. ISSN: 1097-0290. DOI: `10.1002/bit.22233`. (Visited on 04/07/2023).

[119] Todd A. Duncombe, Augusto M. Tentori, and Amy E. Herr. “Microfluidics: Reframing Biological Enquiry”. In: *Nature Reviews Molecular Cell Biology* 16.9 (Sept. 2015), pp. 554–567. ISSN: 1471-0080. DOI: `10.1038/nrm4041`. (Visited on 03/27/2023).

[120] Braden C. Dunsmore, Catherine J. Bass, and Hilary M. Lappin-Scott. “A Novel Approach to Investigate Biofilm Accumulation and Bacterial Transport in Porous Matrices”. In: *Environmental Microbiology* 6.2 (2004), pp. 183–187. ISSN: 1462-2920. DOI: `10.1046/j.1462-2920.2003.00546.x`. (Visited on 01/31/2023).

[121] Deborah Elenter et al. “Influence of Detachment on Substrate Removal and Microbial Ecology in a Heterotrophic/Autotrophic Biofilm”. In: *Water Research* 41.20 (Dec. 2007), pp. 4657–4671. ISSN: 0043-1354. DOI: `10.1016/j.watres.2007.06.050`. (Visited on 04/07/2023).

[122] Ariadni Elmaloglou et al. “Microfluidic Study in a Meter-Long Reactive Path Reveals How the Medium’s Structural Heterogeneity Shapes MICP-induced Biocementation”. In: *Scientific Reports* 12.1 (Nov. 2022), p. 19553. ISSN: 2045-2322. DOI: `10.1038/s41598-022-24124-6`. (Visited on 12/29/2022).

[123] Philippe Emge et al. “Resilience of Bacterial Quorum Sensing against Fluid Flow”. In: *Scientific Reports* 6.1 (Sept. 2016), p. 33115. ISSN: 2045-2322. DOI: `10.1038/srep33115`. (Visited on 09/02/2022).

[124] L. R. Evans and A. Linker. “Production and Characterization of the Slime Polysaccharide of Pseudomonas Aeruginosa”. In: *Journal of Bacteriology* 116.2 (Nov. 1973), pp. 915–924. ISSN: 0021-9193. DOI: `10.1128/jb.116.2.915-924.1973`.

[125] P. Fera et al. “Seasonal Variations in Bacterial Colonisation of Stainless Steel Aluminium and Polycarbonate Surfaces in a Seawater Flow System”. In: *Biofouling* 1.3 (Mar. 1989), pp. 251–261. ISSN: 10292454. DOI: `10.1080/08927018909378112`.

[126] Hans Curt Flemming, Thomas R. Neu, and Daniel J. Wozniak. *The EPS Matrix: The "House of Biofilm Cells"*. Vol. 189. American Society for Microbiology Journals, Nov. 2007. DOI: `10.1128/JB.00858-07`.

[127] Hans Curt Flemming et al. *Biofilms: An Emergent Form of Bacterial Life*. Vol. 14. Nature Publishing Group, Sept. 2016. DOI: `10.1038/nrmicro.2016.94`.

[128] Hans-Curt Flemming and Stefan Wuertz. “Bacteria and Archaea on Earth and Their Abundance in Biofilms”. In: *Nature Reviews Microbiology* 17.4 (Apr. 2019), pp. 247–260. ISSN: 1740-1534. DOI: `10.1038/s41579-019-0158-9`. (Visited on 11/03/2021).

[129] Hans-Curt Flemming et al. “The Biofilm Matrix: Multitasking in a Shared Space”. In: *Nature Reviews Microbiology* (Sept. 2022). ISSN: 1740-1526, 1740-1534. DOI: `10.1038/s41579-022-00791-0`. (Visited on 01/12/2023).

[130] Hans-Curt Flemming et al. “Who Put the Film in Biofilm? The Migration of a Term from Wastewater Engineering to Medicine and Beyond”. In: *npj Biofilms and Microbiomes* 7.1 (Jan. 2021), pp. 1–5. ISSN: 2055-5008. DOI: `10.1038/s41522-020-00183-3`. (Visited on 01/12/2023).

[131] Madilyn Fletcher and G. I. Loeb. “Influence of Substratum Characteristics on the Attachment of a Marine Pseudomonad to Solid Surfaces”. In: *Applied and Environmental Microbiology* 37.1 (Jan. 1979), pp. 67–72. ISSN: 0099-2240. DOI: `10.1128/aem.37.1.67-72.1979`.

[132] Roseanne M. Ford and Ronald W. Harvey. “Role of Chemotaxis in the Transport of Bacteria through Saturated Porous Media”. In: *Advances in Water Resources*. Biological Processes in Porous Media: From the Pore Scale to the Field 30.6 (June 2007), pp. 1608–1617. ISSN: 0309-1708. DOI: `10.1016/j.advwatres.2006.05.019`. (Visited on 03/15/2023).

[133] Blender Foundation. *Blender.Org - Home of the Blender Project - Free and Open 3D Creation Software*. (Visited on 02/25/2023).

[134] Bo Frølund et al. “Extraction of Extracellular Polymers from Activated Sludge Using a Cation Exchange Resin”. In: *Water Research* 30.8 (Aug. 1996), pp. 1749–1758. ISSN: 00431354. DOI: `10.1016/0043-1354(95)00323-1`.

[135] Riccardo Funari and Amy Q. Shen. “Detection and Characterization of Bacterial Biofilms and Biofilm-Based Sensors”. In: *ACS sensors* 7.2 (Feb. 2022), pp. 347–357. ISSN: 2379-3694. DOI: `10.1021/acssensors.1c02722`.

[136] M. Parvinzadeh Gashti et al. “A Microfluidic Platform with pH Imaging for Chemical and Hydrodynamic Stimulation of Intact Oral Biofilms”. In: *Lab on a Chip* 16.8 (Apr. 2016), pp. 1412–1419. ISSN: 1473-0189. DOI: `10.1039/c5lc01540e`.

[137] Steffen Geisel, Eleonora Secchi, and Jan Vermant. “The Role of Surface Adhesion on the Macroscopic Wrinkling of Biofilms”. In: *eLife* 11 (June 2022). Ed. by Raymond E Goldstein and Aleksandra M Walczak, e76027. ISSN: 2050-084X. DOI: `10.7554/eLife.76027`. (Visited on 12/28/2022).

[138] S. U. Gerbersdorf and S. Wieprecht. “Biostabilization of Cohesive Sediments: Revisiting the Role of Abiotic Conditions, Physiology and Diversity of Microbes, Polymeric Secretion, and Biofilm Architecture”. In: *Geobiology* 13.1 (Jan. 2015), pp. 68–97. ISSN: 14724677. DOI: `10.1111/gbi.12115`. (Visited on 01/25/2023).

[139] Krist V. Gernaey et al. “Monitoring and Control of Microbioreactors: An Expert Opinion on Development Needs”. In: *Biotechnology Journal* 7.10 (Oct. 2012), pp. 1308–1314. ISSN: 1860-7314. DOI: `10.1002/biot.201200157`.

[140] Aamir Ghafoor, Iain D. Hay, and Bernd H. A. Rehm. “Role of Exopolysaccharides in Pseudomonas Aeruginosa Biofilm Formation and Architecture”. In: *Applied and Environmental Microbiology* 77.15 (Aug. 2011), pp. 5238–5246. DOI: `10.1128/AEM.00637-11`. (Visited on 01/04/2023).

[141] Kirandeep K. Gill, Zhengchun Liu, and Nuno M. Reis. “Fast Prototyping Using 3D Printed Templates and Flexible Fluoropolymer Microcapillary Films Offers Enhanced Micromixing in Immobilised (Bio)Catalytic Reactions”. In: *Chemical Engineering Journal* 429 (Feb. 2022), p. 132266. ISSN: 1385-8947. DOI: `10.1016/j.cej.2021.132266`. (Visited on 04/05/2023).

[142] Erin S. Gloag et al. “Viscoelastic Properties of Pseudomonas Aeruginosa Variant Biofilms”. In: *Scientific Reports* 8.1 (June 2018), p. 9691. ISSN: 2045-2322. DOI: `10.1038/s41598-018-28009-5`.

[143] Rn Glud et al. “Oxygen Dynamics at the Base of a Biofilm Studied with Planar Optodes”. In: *Aquatic Microbial Ecology* 14 (1998), pp. 223–233. ISSN: 0948-3055, 1616-1564. DOI: `10.3354/ame014223`. (Visited on 01/08/2023).

[144] C. C. Goller and Tony Romeo. “Environmental Influences on Biofilm Development”. In: *Bacterial Biofilms*. Ed. by Tony Romeo. Current Topics in Microbiology and Immunology. Berlin, Heidelberg: Springer, 2008, pp. 37–66. ISBN: 978-3-540-75418-3. DOI: `10.1007/978-3-540-75418-3_3`. (Visited on 04/05/2023).

[145] Ana González et al. “Optical and Tomography Studies of Water-Soluble Gold Nanoparticles on Bacterial Exopolysaccharides”. In: *Journal of Applied Physics* 126.5 (Aug. 2019), p. 053101. ISSN: 10897550. DOI: `10.1063/1.5090879`.

[146] C. González et al. “Efficient Nutrient Removal from Swine Manure in a Tubular Biofilm Photo-Bioreactor Using Algae-Bacteria Consortia”. In: *Water Science and Technology* 58.1 (July 2008), pp. 95–102. ISSN: 0273-1223, 1996-9732. DOI: `10.2166/wst.2008.655`. (Visited on 04/12/2023).

[147] Myriam Graba et al. “Effect of Near-Bed Turbulence on Chronic Detachment of Epilithic Biofilm: Experimental and Modeling Approaches”. In: *Water Resources Research* 46.11 (2010). ISSN: 1944-7973. DOI: `10.1029/2009WR008679`. (Visited on 04/12/2023).

[148] Beatrice Grasland et al. “Bacterial Biofilm in Seawater: Cell Surface Properties of Early-attached Marine Bacteria”. In: *Biofouling* 19.5 (Oct. 2003), pp. 307–313. ISSN: 0892-7014. DOI: `10.1080/0892701031000121041`. (Visited on 04/07/2023).

[149] N. Michael Green. “Avidin”. In: *Advances in Protein Chemistry*. Ed. by C. B. Anfinsen, John T. Edsall, and Frederic M. Richards. Vol. 29. Academic Press, Jan. 1975, pp. 85–133. DOI: `10.1016/S0065-3233(08)60411-8`. (Visited on 02/05/2023).

[150] A. Grinsted, J. C. Moore, and S. Jevrejeva. “Application of the Cross Wavelet Transform and Wavelet Coherence to Geophysical Time Series”. In: *Nonlinear Processes in Geophysics* 11.5/6 (Nov. 2004), pp. 561–566. ISSN: 1023-5809. DOI: `10.5194/npg-11-561-2004`. (Visited on 04/02/2023).

[151] Bethany C. Gross et al. “Polymer Coatings in 3D-Printed Fluidic Device Channels for Improved Cellular Adherence Prior to Electrical Lysis”. In: *Analytical chemistry* 87.12 (June 2015), pp. 6335–6341. ISSN: 0003-2700. DOI: `10.1021/acs.analchem.5b01202`. (Visited on 03/14/2023).

[152] J.L. Guermond, P. Minev, and Jie Shen. “An Overview of Projection Methods for Incompressible Flows”. In: *Computer Methods in Applied Mechanics and Engineering* 195.44-47 (Sept. 2006), pp. 6011–6045. ISSN: 00457825. DOI: `10.1016/j.cma.2005.10.010`. (Visited on 03/09/2023).

[153] N. Guignot, A. King, and E. Boulard. “Synchrotron X-Ray Computed Microtomography for High Pressure Science”. In: *Journal of Applied Physics* 127.24 (June 2020), p. 240901. ISSN: 0021-8979. DOI: `10.1063/5.0008731`. (Visited on 12/21/2022).

[154] Morgan Guilbaud et al. “Proteomic Response of Pseudomonas Aeruginosa PAO1 Adhering to Solid Surfaces”. In: *Frontiers in Microbiology* 8 (2017), p. 1465. ISSN: 1664-302X. DOI: `10.3389/fmicb.2017.01465`.

[155] Kajal Gupta et al. “Antimicrobial Tolerance of Pseudomonas Aeruginosa Biofilms Is Activated during an Early Developmental Stage and Requires the Two-Component Hybrid SagS”. In: *Journal of Bacteriology* 195.21 (Nov. 2013), pp. 4975–4987. ISSN: 1098-5530. DOI: `10.1128/JB.00732-13`.

[156] Suvidha Gupta, Sanjay B. Pawar, and R. A. Pandey. “Current Practices and Challenges in Using Microalgae for Treatment of Nutrient Rich Wastewater from Agro-Based Industries”. In: *Science of The Total Environment* 687 (Oct. 2019), pp. 1107–1126. ISSN: 0048-9697. DOI: `10.1016/j.scitotenv.2019.06.115`. (Visited on 07/01/2019).

[157] Callum Guttridge et al. “Biocompatible 3D Printing Resins for Medical Applications: A Review of Marketed Intended Use, Biocompatibility Certification, and Post-Processing Guidance”. In: *Annals of 3D Printed Medicine* 5 (Mar. 2022), p. 100044. ISSN: 2666-9641. DOI: `10.1016/j.stlm.2021.100044`. (Visited on 03/15/2023).

[158] Max Hackbarth et al. “Monitoring and Quantification of Bioelectrochemical Kyrpidia Spormannii Biofilm Development in a Novel Flow Cell Setup”. In: *Chemical Engineering Journal* 390 (June 2020), p. 124604. ISSN: 1385-8947. DOI: `10.1016/j.cej.2020.124604`. (Visited on 11/01/2021).

[159] J F Hainfeld et al. “Gold Nanoparticles: A New X-ray Contrast Agent”. In: *The British Journal of Radiology* 79.939 (Mar. 2006), pp. 248–253. ISSN: 0007-1285. DOI: `10.1259/bjr/13169882`. (Visited on 12/02/2021).

[160] Victoria L. Hand et al. “Experimental Studies of the Influence of Grain Size, Oxygen Availability and Organic Carbon Availability on Bioclogging in Porous Media”. In: *Environmental Science & Technology* 42.5 (Mar. 2008), pp. 1485–1491. ISSN: 0013-936X. DOI: `10.1021/es072022s`. (Visited on 12/29/2022).

[161] Martin C. Hansen et al. "Assessment of GFP Fluorescence in Cells of Streptococcus Gordonii under Conditions of Low pH and Low Oxygen Concentration". In: *Microbiology* 147.5 (2001), pp. 1383–1391. ISSN: 1465-2080. DOI: `10.1099/00221287-147-5-1383`. (Visited on 03/15/2023).

[162] Susse Kirkelund Hansen et al. "Evolution of Species Interactions in a Biofilm Community". In: *Nature* 445.7127 (Feb. 2007), pp. 533–536. ISSN: 1476-4687. DOI: `10.1038/nature05514`. (Visited on 04/07/2023).

[163] Likai Hao et al. "Mapping of Heavy Metal Ion Sorption to Cell-Extracellular Polymeric Substance-Mineral Aggregates by Using Metal-Selective Fluorescent Probes and Confocal Laser Scanning Microscopy". In: *Applied and Environmental Microbiology* 79.21 (Nov. 2013), pp. 6524–6534. ISSN: 0099-2240, 1098-5336. DOI: `10.1128/AEM.02454-13`. (Visited on 01/08/2023).

[164] Akshay K. Harapanahalli et al. *Chemical Signals and Mechanosensing in Bacterial Responses to Their Environment*. Vol. 11. Public Library of Science, Aug. 2015. DOI: `10.1371/journal.ppat.1005057`.

[165] Dustin Harris et al. "Real-Time Monitoring of Calcification Process by Sporosarcina Pasteurii Biofilm". In: *Analyst* 141.10 (May 2016), pp. 2887–2895. ISSN: 1364-5528. DOI: `10.1039/C6AN00007J`. (Visited on 01/07/2023).

[166] Rasika M. Harshey. "Bacterial Motility on a Surface: Many Ways to a Common Goal". In: *Annual Review of Microbiology* 57.1 (Oct. 2003), pp. 249–273. ISSN: 0066-4227, 1545-3251. DOI: `10.1146/annurev.micro.57.030502.091014`. (Visited on 03/15/2023).

[167] Raimo Hartmann et al. *Emergence of Three-Dimensional Order and Structure in Growing Biofilms*. Vol. 15. Nature Publishing Group, Mar. 2019. DOI: `10.1038/s41567-018-0356-9`.

[168] Iain D. Hay et al. "Bacterial Biosynthesis of Alginates". In: *Journal of Chemical Technology & Biotechnology* 85.6 (2010), pp. 752–759. ISSN: 1097-4660. DOI: `10.1002/jctb.2372`. (Visited on 01/05/2023).

[169] Iain D. Hay et al. "Microbial Alginate Production, Modification and Its Applications". In: *Microbial Biotechnology* 6.6 (Nov. 2013), pp. 637–650. ISSN: 1751-7915. DOI: `10.1111/1751-7915.12076`.

[170] Yun Heacock-Kang et al. "Spatial Transcriptomes within the Pseudomonas Aeruginosa Biofilm Architecture". In: *Molecular Microbiology* 106.6 (Dec. 2017), pp. 976–985. ISSN: 1365-2958. DOI: `10.1111/mmi.13863`.

[171] Hanaa M. Hegab, Ahmed ElMekawy, and Tim Stakenborg. "Review of Microfluidic Microbioreactor Technology for High-Throughput Submerged Microbiological Cultivation". In: *Biomicrofluidics* 7.2 (Apr. 2013), p. 021502. ISSN: 1932-1058. DOI: `10.1063/1.4799966`. (Visited on 11/08/2022).

[172] G. Helmlinger et al. "Effects of Pulsatile Flow on Cultured Vascular Endothelial Cell Morphology". In: *Journal of Biomechanical Engineering* 113.2 (May 1991), pp. 123–131. ISSN: 0148-0731. DOI: `10.1115/1.2891226`.

[173] Johannes Hemmerich et al. "Microbioreactor Systems for Accelerated Bioprocess Development". In: *Biotechnology Journal* 13.4 (2018), p. 1700141. ISSN: 1860-7314. DOI: `10.1002/biot.201700141`. (Visited on 06/22/2022).

[174] Paul Heo et al. "Highly Reproducible Physiological Asymmetric Membrane with Freely Diffusing Embedded Proteins in a 3D-Printed Microfluidic Setup". In: *Small* 15.21 (2019), p. 1900725. ISSN: 1613-6829. DOI: `10.1002/smll.201900725`. (Visited on 03/15/2023).

[175] Joris Heyman et al. "Stretching and Folding Sustain Microscale Chemical Gradients in Porous Media". In: *Proceedings of the National Academy of Sciences* 117.24 (June 2020), pp. 13359–13365. DOI: `10.1073/pnas.2002858117`. (Visited on 12/20/2022).

[176] Jason W. Hickman and Caroline S. Harwood. "Identification of FleQ from Pseudomonas Aeruginosa as a C-Di-GMP-responsive Transcription Factor". In: *Molecular Microbiology* 69.2 (July 2008), pp. 376–389. ISSN: 1365-2958. DOI: `10.1111/j.1365-2958.2008.06281.x`.

[177] Marko Hoffmann, Michael Schlüter, and Norbert Räbiger. "Experimental Investigation of Liquid–Liquid Mixing in T-shaped Micro-Mixers Using μ-LIF and μ-PIV". In: *Chemical Engineering Science*. Fluid Mixing VIII International Conference 61.9 (May 2006), pp. 2968–2976. ISSN: 0009-2509. DOI: `10.1016/j.ces.2005.11.029`. (Visited on 11/03/2021).

[178] Niels Høiby. "A Short History of Microbial Biofilms and Biofilm Infections". In: *APMIS* 125.4 (2017), pp. 272–275. ISSN: 1600-0463. DOI: `10.1111/apm.12686`. (Visited on 01/12/2023).

[179] Niels Høiby et al. "Antibiotic Resistance of Bacterial Biofilms". In: *International Journal of Antimicrobial Agents* 35.4 (Apr. 2010), pp. 322–332. ISSN: 1872-7913. DOI: `10.1016/j.ijantimicag.2009.12.011`.

[180] Jiapeng Hou et al. "Bacterial Density and Biofilm Structure Determined by Optical Coherence Tomography". In: *Scientific Reports* 9.1 (Dec. 2019). ISSN: 20452322. DOI: `10.1038/s41598-019-46196-7`.

[181] Junxian Hou et al. "An Experimental Study of pH Distributions within an Electricity-Producing Biofilm by Using pH Microelectrode". In: *Electrochimica Acta* 251 (Oct. 2017), pp. 187–194. ISSN: 0013-4686. DOI: `10.1016/j.electacta.2017.08.101`. (Visited on 01/07/2023).

[182] Shuyu Hou et al. "Microtopographic Patterns Affect Escherichia Coli Biofilm Formation on Poly(Dimethylsiloxane) Surfaces". In: *Langmuir* 27.6 (Mar. 2011), pp. 2686–2691. ISSN: 07437463. DOI: `10.1021/la1046194`.

[183] J. A. Howell, R. W. Field, and Dengxi Wu. "Yeast Cell Microfiltration: Flux Enhancement in Baffled and Pulsatile Flow Systems". In: *Journal of Membrane Science* 80.1 (June 1993), pp. 59–71. ISSN: 0376-7388. DOI: `10.1016/0376-7388(93)85132-G`. (Visited on 03/23/2023).

[184] Stephen M. Hunt et al. "Hypothesis for the Role of Nutrient Starvation in Biofilm Detachment". In: *Applied and Environmental Microbiology* 70.12 (2004), pp. 7418–7425. ISSN: 00992240. DOI: `10.1128/AEM.70.12.7418-7425.2004`.

[185] Ryan C. Hunter and Terry J. Beveridge. "High-Resolution Visualization of Pseudomonas Aeruginosa PAO1 Biofilms by Freeze-Substitution Transmission Electron Microscopy". In: *Journal of Bacteriology* 187.22 (Nov. 2005), pp. 7619–7630. DOI: `10.1128/JB.187.22.7619-7630.2005`. (Visited on 12/19/2022).

[186] Gabriel C. Iltis et al. "Imaging Biofilm Architecture within Porous Media Using Synchrotron-Based X-ray Computed Microtomography". In: *Water Resources Research* 47.2 (Feb. 2011). ISSN: 00431397. DOI: `10.1029/2010WR009410`.

[187] *IPSDK - Software Solution - by Reactiv IP*. (Visited on 04/14/2023).

[188] Yasuhiko Irie et al. "Self-Produced Exopolysaccharide Is a Signal That Stimulates Biofilm Formation in Pseudomonas Aeruginosa". In: *Proceedings of the National Academy of Sciences of the United States of America* 109.50 (Dec. 2012), pp. 20632–20636. ISSN: 1091-6490. DOI: `10.1073/pnas.1217993109`.

[189] Yasuhiko Irie et al. "The Pseudomonas Aeruginosa PSL Polysaccharide Is a Social but Noncheatable Trait in Biofilms". In: *mBio* 8.3 (June 2017), e00374–17. ISSN: 2150-7511. DOI: `10.1128/mBio.00374-17`.

[190] Tetsuya Ishikawa. "Accelerator-Based X-ray Sources: Synchrotron Radiation, X-ray Free Electron Lasers and Beyond". In: *Philosophical Transactions of the Royal Society A: Mathematical, Physical and Engineering Sciences* 377.2147 (June 2019), p. 20180231. DOI: `10.1098/rsta.2018.0231`. (Visited on 12/22/2022).

[191] Tomislav Ivankovic et al. "Development and Evaluation of an Experimental Protocol for 3-D Visualization and Characterization of the Structure of Bacterial Biofilms in Porous Media Using Laboratory X-ray Tomography". In: *Biofouling* 32.10 (Nov. 2016), pp. 1235–1244. ISSN: 10292454. DOI: `10.1080/08927014.2016.1249865`.

[192] Kara D. Jackson et al. "Identification of Psl, a Locus Encoding a Potential Exopolysaccharide That Is Essential for Pseudomonas Aeruginosa PAO1 Biofilm Formation". In: *Journal of Bacteriology* 186.14 (July 2004), pp. 4466–4475. DOI: `10.1128/JB.186.14.4466-4475.2004`. (Visited on 01/05/2023).

[193] A. Jacobs et al. "Kinetic Adhesion of Bacterial Cells to Sand: Cell Surface Properties and Adhesion Rate". In: *Colloids and Surfaces B: Biointerfaces* 59.1 (Sept. 2007), pp. 35–45. ISSN: 09277765. DOI: `10.1016/j.colsurfb.2007.04.008`.

[194] Sara Jägevall, Lisa Rabe, and Karsten Pedersen. "Abundance and Diversity of Biofilms in Natural and Artificial Aquifers of the Äspö Hard Rock Laboratory, Sweden". In: *Microbial Ecology* 61.2 (Feb. 2011), pp. 410–422. ISSN: 1432-184X. DOI: `10.1007/s00248-010-9761-z`. (Visited on 03/15/2023).

[195] Sean A. James, Lydia C. Powell, and Chris J. Wright. "Atomic Force Microscopy of Biofilms—Imaging, Interactions, and Mechanics". In: *Microbial Biofilms - Importance and Applications*. Ed. by Dharumadurai Dhanasekaran and Nooruddin Thajuddin. InTech, July 2016. ISBN: 978-953-51-2435-1 978-953-51-2436-8. DOI: `10.5772/63312`. (Visited on 12/19/2022).

[196] Hongchul Jang, Roberto Rusconi, and Roman Stocker. "Biofilm Disruption by an Air Bubble Reveals Heterogeneous Age-Dependent Detachment Patterns Dictated by Initial Extracellular Matrix Distribution". In: *npj Biofilms and Microbiomes* 3.1 (Mar. 2017), pp. 1–7. ISSN: 2055-5008. DOI: `10.1038/s41522-017-0014-5`. (Visited on 11/10/2022).

[197] Kimberly K. Jefferson, Donald A. Goldmann, and Gerald B. Pier. "Use of Confocal Microscopy To Analyze the Rate of Vancomycin Penetration through Staphylococcus Aureus Biofilms". In: *Antimicrobial Agents and Chemotherapy* 49.6 (June 2005), pp. 2467–2473. DOI: `10.1128/AAC.49.6.2467-2473.2005`. (Visited on 12/20/2022).

[198] Laura K. Jennings et al. "Pel Is a Cationic Exopolysaccharide That Cross-Links Extracellular DNA in the Pseudomonas Aeruginosa Biofilm Matrix". In: *Proceedings of the National Academy of Sciences of the United States of America* 112.36 (Sept. 2015), pp. 11353–11358. ISSN: 1091-6490. DOI: `10.1073/pnas.1503058112`.

[199] Nadia M. Jesús-Pérez and Blanca H. Lapizco-Encinas. "Dielectrophoretic Monitoring of Microorganisms in Environmental Applications". In: *ELECTROPHORESIS* 32.17 (2011), pp. 2331–2357. ISSN: 1522-2683. DOI: `10.1002/elps.201100107`. (Visited on 01/07/2023).

[200] Megan P. Jewell et al. "Luminescent Nanosensors for Ratiometric Monitoring of Three-Dimensional Oxygen Gradients in Laboratory and Clinical Pseudomonas Aeruginosa Biofilms". In: *Applied and Environmental Microbiology* 85.20 (Oct. 2019). Ed. by Andrew J. McBain, e01116–19. ISSN: 0099-2240, 1098-5336. DOI: `10.1128/AEM.01116-19`. (Visited on 01/08/2023).

[201] Ru Jia et al. "Enhanced Biocide Treatments with D-amino Acid Mixtures against a Biofilm Consortium from a Water Cooling Tower". In: *Frontiers in Microbiology* 8 (2017). ISSN: 1664-302X. (Visited on 04/07/2023).

[202] Gaoshan Jing et al. "Development of a Microfluidic Biosensor for Detection of Environmental Mycobacteria". In: *Sensors and Actuators B: Chemical* 123.1 (Apr. 2007), pp. 614–621. ISSN: 0925-4005. DOI: `10.1016/j.snb.2006.07.029`. (Visited on 01/07/2023).

[203] Christopher J. Jones and Daniel J. Wozniak. "Psl Produced by Mucoid Pseudomonas Aeruginosa Contributes to the Establishment of Biofilms and Immune Evasion". In: *mBio* 8.3 (June 2017), e00864–17. ISSN: 2150-7511. DOI: `10.1128/mBio.00864-17`.

[204] Henk M. Jonkers. “Self Healing Concrete: A Biological Approach”. In: *Self Healing Materials*. Ed. by Robert Hull et al. Vol. 100. Dordrecht: Springer Netherlands, 2007, pp. 195–204. ISBN: 978-1-4020-6249-0 978-1-4020-6250-6. DOI: 10.1007/978-1-4020-6250-6_9. (Visited on 08/31/2022).

[205] A. Karimi et al. “Interplay of Physical Mechanisms and Biofilm Processes: Review of Microfluidic Methods”. In: *Lab on a Chip* 15.1 (Dec. 2014), pp. 23–42. ISSN: 1473-0189. DOI: 10.1039/C4LC01095G. (Visited on 11/12/2022).

[206] Shahab Karimifard et al. “Modeling the Impact of Evolving Biofilms on Flow in Porous Media inside a Microfluidic Channel”. In: *Water Research* 188 (Jan. 2021), p. 116536. ISSN: 0043-1354. DOI: 10.1016/j.watres.2020.116536. (Visited on 01/27/2022).

[207] Richard L. Karpel et al. “Design and Characterization of Crotamine-Functionalized Gold Nanoparticles”. In: *Colloids and Surfaces B: Biointerfaces* 163 (Mar. 2018), pp. 1–8. ISSN: 18734367. DOI: 10.1016/j.colsurfb.2017.12.013.

[208] M. Karrabi et al. “Investigation of Hydrodynamic/Biomass Growth Coupling in a Pilot Scale Granular Bioreactor at Low Pore Reynolds Number”. In: *Chemical Engineering Science* 66.8 (Apr. 2011), pp. 1765–1782. ISSN: 00092509. DOI: 10.1016/j.ces.2011.01.010.

[209] Swetha Kasetty et al. “Both Pseudomonas Aeruginosa and Candida Albicans Accumulate Greater Biomass in Dual-Species Biofilms under Flow”. In: *mSphere* 6.3 (June 2021), e00416–21. DOI: 10.1128/mSphere.00416-21. (Visited on 02/01/2023).

[210] Krista M. Kaster et al. “Mechanisms Involved in Microbially Enhanced Oil Recovery”. In: *Transport in Porous Media* 91.1 (Jan. 2012), pp. 59–79. ISSN: 1573-1634. DOI: 10.1007/s11242-011-9833-7. (Visited on 03/13/2023).

[211] Patrick H. Kee and Delia Danila. “CT Imaging of Myocardial Scar Burden with CNA35-conjugated Gold Nanoparticles”. In: *Nanomedicine: Nanotechnology, Biology, and Medicine* 14.6 (Aug. 2018), pp. 1941–1947. ISSN: 15499642. DOI: 10.1016/j.nano.2018.06.003.

[212] Sarah Kerdi et al. “Effect of Localized Hydrodynamics on Biofilm Attachment and Growth in a Cross-Flow Filtration Channel”. In: *Water Research* 188 (Jan. 2021), p. 116502. ISSN: 0043-1354. DOI: 10.1016/j.watres.2020.116502. (Visited on 01/08/2023).

[213] Sara Khademi et al. “Evaluation of Size, Morphology, Concentration, and Surface Effect of Gold Nanoparticles on X-ray Attenuation in Computed Tomography”. In: *Physica Medica* 45 (Jan. 2018), pp. 127–133. ISSN: 1120-1797. DOI: 10.1016/j.ejmp.2017.12.001. (Visited on 04/01/2023).

[214] Khodor Khadra et al. “Fictitious Domain Approach for Numerical Modelling of Navier-Stokes Equations”. In: *International Journal for Numerical Methods in Fluids* 34.8 (Dec. 2000), pp. 651–684. ISSN: 0271-2091, 1097-0363. DOI: 10.1002/1097-0363(20001230)34:8<651::AID-FLD61>3.0.CO;2-D. (Visited on 03/09/2023).

[215] Mohammad Khodaei, Kamran Amini, and Alireza Valanezhad. “Fabrication and Characterization of Poly Lactic Acid Scaffolds by Fused Deposition Modeling for Bone Tissue Engineering”. In: *Journal of Wuhan University of Technology-Mater. Sci. Ed.* 35.1 (Feb. 2020), pp. 248–251. ISSN: 1993-0437. DOI: 10.1007/s11595-020-2250-4. (Visited on 03/14/2023).

[216] Yalda Khosravi et al. “Use of an Oxygen Planar Optode to Assess the Effect of High Velocity Microsprays on Oxygen Penetration in a Human Dental Biofilms In-Vitro”. In: *BMC Oral Health* 20.1 (Dec. 2020), p. 230. ISSN: 1472-6831. DOI: 10.1186/s12903-020-01217-0. (Visited on 01/08/2023).

[217] Dong-Shik Kim and H. Scott Fogler. “Biomass Evolution in Porous Media and Its Effects on Permeability under Starvation Conditions”. In: *Biotechnology and Bioengineering* 69.1 (July 2000), pp. 47–56. ISSN: 1097-0290. DOI: 10.1002/(SICI)1097-0290(20000705)69:1<47::AID-BIT6>3.0.CO;2-N.

[218] Dongkyu Kim et al. "Antibiofouling Polymer-Coated Gold Nanoparticles as a Contrast Agent for in Vivo X-ray Computed Tomography Imaging". In: *Journal of the American Chemical Society* 129.24 (June 2007), pp. 7661–7665. ISSN: 00027863. DOI: `10.1021/ja071471p`.

[219] Minyoung Kevin Kim et al. "Local and Global Consequences of Flow on Bacterial Quorum Sensing". In: *Nature Microbiology* 1.1 (Jan. 2016), p. 15005. ISSN: 2058-5276. DOI: `10.1038/nmicrobiol.2015.5`. (Visited on 07/04/2019).

[220] Soohong Kim et al. "High-Throughput Automated Microfluidic Sample Preparation for Accurate Microbial Genomics". In: *Nature Communications* 8.1 (Jan. 2017), p. 13919. ISSN: 2041-1723. DOI: `10.1038/ncomms13919`. (Visited on 04/07/2023).

[221] Suran Kim et al. "Thermoregulation of Pseudomonas Aeruginosa Biofilm Formation". In: *Applied and Environmental Microbiology* 86.22 (Oct. 2020), e01584–20. DOI: `10.1128/AEM.01584-20`. (Visited on 04/06/2023).

[222] Mary Jo Kirisits et al. "Influence of the Hydrodynamic Environment on Quorum Sensing in Pseudomonas Aeruginosa Biofilms". In: *Journal of Bacteriology* 189.22 (Nov. 2007), pp. 8357–8360. ISSN: 0021-9193. DOI: `10.1128/JB.01040-07`. (Visited on 01/30/2023).

[223] Timothy V. Kirk and Nicolas Szita. "Oxygen Transfer Characteristics of Miniaturized Bioreactor Systems". In: *Biotechnology and Bioengineering* 110.4 (Apr. 2013), pp. 1005–1019. ISSN: 1097-0290. DOI: `10.1002/bit.24824`.

[224] Mikkel Klausen et al. "Biofilm Formation by Pseudomonas Aeruginosa Wild Type, Flagella and Type IV Pili Mutants". In: *Molecular Microbiology* 48.6 (June 2003), pp. 1511–1524. ISSN: 0950-382X. DOI: `10.1046/j.1365-2958.2003.03525.x`.

[225] Mikkel Klausen et al. "Involvement of Bacterial Migration in the Development of Complex Multicellular Structures in Pseudomonas Aeruginosa Biofilms". In: *Molecular Microbiology* 50.1 (Oct. 2003), pp. 61–68. ISSN: 0950-382X. DOI: `10.1046/j.1365-2958.2003.03677.x`.

[226] J. Komlos et al. "Interaction of Klebsiella Oxytoca and Burkholderia Cepacia in Dual-Species Batch Cultures and Biofilms as a Function of Growth Rate and Substrate Concentration". In: *Microbial Ecology* 49.1 (Jan. 2005), pp. 114–125. ISSN: 1432-184X. DOI: `10.1007/s00248-003-1066-z`. (Visited on 11/03/2021).

[227] T. Kone et al. "Impact of Biofilm-Induced Heterogeneities on Solute Transport in Porous Media". In: *Water Resources Research* 50.11 (2014), pp. 9103–9119. ISSN: 1944-7973. DOI: `10.1002/2013WR015213`. (Visited on 04/03/2023).

[228] Hyun Koo et al. *Targeting Microbial Biofilms: Current and Prospective Therapeutic Strategies*. Vol. 15. Nature Publishing Group, Dec. 2017. DOI: `10.1038/nrmicro.2017.99`.

[229] Darren R. Korber et al. "Effect of Laminar Flow Velocity on the Kinetics of Surface Recolonization by Mot+ and Mot-Pseudomonas Fluorescens". In: *Microbial Ecology* 18.1 (July 1989), pp. 1–19. ISSN: 00953628. DOI: `10.1007/BF02011692`.

[230] Maria Kostakioti, Maria Hadjifrangiskou, and Scott J. Hultgren. "Bacterial Biofilms: Development, Dispersal, and Therapeutic Strategies in the Dawn of the Postantibiotic Era". In: *Cold Spring Harbor Perspectives in Medicine* 3.4 (Apr. 2013), a010306. ISSN: 2157-1422. DOI: `10.1101/cshperspect.a010306`.

[231] Y. Kostov et al. "Low-Cost Microbioreactor for High-Throughput Bioprocessing". In: *Biotechnology and Bioengineering* 72.3 (Feb. 2001), pp. 346–352. ISSN: 0006-3592. DOI: `10.1002/1097-0290(20010205)72:3<346::aid-bit12>3.0.co;2-x`.

[232] Sebastian Kreß et al. "3D Printing of Cell Culture Devices: Assessment and Prevention of the Cytotoxicity of Photopolymers for Stereolithography". In: *Materials* 13.13 (Jan. 2020), p. 3011. ISSN: 1996-1944. DOI: `10.3390/ma13133011`. (Visited on 03/15/2023).

[233] M. S. Krishnan et al. "Economic Analysis of Fuel Ethanol Production from Corn Starch Using Fluidized-Bed Bioreactors". In: *Bioresource Technology* 75.2 (Nov. 2000), pp. 99–105. ISSN: 0960-8524. DOI: `10.1016/S0960-8524(00)00047-X`. (Visited on 11/08/2022).

[234] Milos Krsmanovic et al. "Hydrodynamics and Surface Properties Influence Biofilm Proliferation". In: *Advances in Colloid and Interface Science* 288 (Feb. 2021), p. 102336. ISSN: 0001-8686. DOI: `10.1016/j.cis.2020.102336`. (Visited on 12/29/2022).

[235] Felix Krujatz et al. "Additive Biotech—Chances, Challenges, and Recent Applications of Additive Manufacturing Technologies in Biotechnology". In: *New Biotechnology*. European Congress of Biotechnology - ECB 2016 39 (Oct. 2017), pp. 222–231. ISSN: 1871-6784. DOI: `10.1016/j.nbt.2017.09.001`. (Visited on 03/14/2023).

[236] Sherry L. Kuchma, John P. Connolly, and George A. O'Toole. "A Three-Component Regulatory System Regulates Biofilm Maturation and Type III Secretion in Pseudomonas Aeruginosa". In: *Journal of Bacteriology* 187.4 (Feb. 2005), pp. 1441–1454. ISSN: 0021-9193. DOI: `10.1128/JB.187.4.1441-1454.2005`.

[237] Sherry L. Kuchma et al. "BifA, a Cyclic-Di-GMP Phosphodiesterase, Inversely Regulates Biofilm Formation and Swarming Motility by Pseudomonas Aeruginosa PA14". In: *Journal of Bacteriology* 189.22 (Nov. 2007), pp. 8165–8178. ISSN: 1098-5530. DOI: `10.1128/JB.00586-07`.

[238] Michael Kühl, Lars F. Rickelt, and Roland Thar. "Combined Imaging of Bacteria and Oxygen in Biofilms". In: *Applied and Environmental Microbiology* 73.19 (Oct. 2007), pp. 6289–6295. ISSN: 0099-2240, 1098-5336. DOI: `10.1128/AEM.01574-07`. (Visited on 01/08/2023).

[239] Dorothee L. Kurz et al. "Competition between Growth and Shear Stress Drives Intermittency in Preferential Flow Paths in Porous Medium Biofilms". In: *Proceedings of the National Academy of Sciences* 119.30 (July 2022), e2122202119. DOI: `10.1073/pnas.2122202119`. (Visited on 09/01/2022).

[240] Dorothee L. Kurz et al. "Morphogenesis of Biofilms in Porous Media and Control on Hydrodynamics". In: *Environmental Science & Technology* 57.14 (Apr. 2023), pp. 5666–5677. ISSN: 0013-936X. DOI: `10.1021/acs.est.2c08890`. (Visited on 04/13/2023).

[241] Jin Il Kwak and Youn-Joo An. "The Current State of the Art in Research on Engineered Nanomaterials and Terrestrial Environments: Different-scale Approaches". In: *Environmental Research* 151 (Nov. 2016), pp. 368–382. ISSN: 0013-9351. DOI: `10.1016/j.envres.2016.08.005`. (Visited on 04/07/2023).

[242] Annette E. LaBauve and Matthew J. Wargo. "Growth and Laboratory Maintenance of Pseudomonas Aeruginosa". In: *Current Protocols in Microbiology* 25.1 (2012), 6E.1.1–6E.1.8. ISSN: 1934-8533. DOI: `10.1002/9780471729259.mc06e01s25`. (Visited on 04/07/2023).

[243] Jean-Philippe Lachaux et al. "Estimating the Time-Course of Coherence between Single-Trial Brain Signals: An Introduction to Wavelet Coherence". In: *Neurophysiologie Clinique/Clinical Neurophysiology* 32.3 (June 2002), pp. 157–174. ISSN: 0987-7053. DOI: `10.1016/S0987-7053(02)00301-5`. (Visited on 04/02/2023).

[244] Hilary M Lappin-Scott and J William Costerton. "Bacterial Biofilms and Surface Fouling". In: *Biofouling* 1.4 (Sept. 1989), pp. 323–342. ISSN: 0892-7014. DOI: `10.1080/08927018909378120`. (Visited on 04/07/2023).

[245] A. E. Larue et al. "Quantitative 3D Comparison of Biofilm Imaged by X-ray Micro-Tomography and Two-Photon Laser Scanning Microscopy". In: *Journal of Microscopy* 271.3 (Sept. 2018), pp. 302–314. ISSN: 13652818. DOI: `10.1111/jmi.12718`.

[246] Anne Larue. "Experimental Methodologies to Explore 3D Development of Biofilms in Porous Media". These de Doctorat. Toulouse, INPT, Mar. 2018. (Visited on 04/12/2023).

[247] V. Lazarova and J. Manem. “Biofilm Characterization and Activity Analysis in Water and Wastewater Treatment”. In: *Water Research* 29.10 (Oct. 1995), pp. 2227–2245. ISSN: 0043-1354. DOI: `10.1016/0043-1354(95)00054-O`. (Visited on 03/13/2023).

[248] Sigolene Lecuyer et al. “Shear Stress Increases the Residence Time of Adhesion of Pseudomonas Aeruginosa”. In: *Biophysical Journal* 100.2 (Jan. 2011), pp. 341–350. ISSN: 0006-3495. DOI: `10.1016/j.bpj.2010.11.078`. (Visited on 01/26/2023).

[249] Woo Hyoung Lee et al. “Needle-Type Environmental Microsensors: Design, Construction and Uses of Microelectrodes and Multi-Analyte MEMS Sensor Arrays”. In: *Measurement Science and Technology* 22.4 (Mar. 2011), p. 042001. ISSN: 0957-0233. DOI: `10.1088/0957-0233/22/4/042001`. (Visited on 01/07/2023).

[250] Andrew P. Leis et al. “Optically Transparent Porous Medium for Nondestructive Studies of Microbial Biofilm Architecture and Transport Dynamics”. In: *Applied and Environmental Microbiology* 71.8 (Aug. 2005), pp. 4801–4808. ISSN: 00992240. DOI: `10.1128/AEM.71.8.4801-4808.2005`.

[251] Phillip Lemke et al. “Microfluidic Cultivation and Analysis of Productive Biofilms”. In: *Biotechnology and Bioengineering* 118.10 (2021), pp. 3860–3870. ISSN: 1097-0290. DOI: `10.1002/bit.27861`. (Visited on 11/12/2022).

[252] Yannick Lequette and E. P. Greenberg. “Timing and Localization of Rhamnolipid Synthesis Gene Expression in Pseudomonas Aeruginosa Biofilms”. In: *Journal of Bacteriology* 187.1 (Jan. 2005), pp. 37–44. ISSN: 0021-9193. DOI: `10.1128/JB.187.1.37-44.2005`.

[253] D. R. Lester, G. Metcalfe, and M. G. Trefry. “Is Chaotic Advection Inherent to Porous Media Flow?” In: *Physical Review Letters* 111.17 (Oct. 2013), p. 174101. DOI: `10.1103/PhysRevLett.111.174101`. (Visited on 12/27/2022).

[254] Daniel R. Lester, Marco Dentz, and Tanguy Le Borgne. “Chaotic Mixing in Three-Dimensional Porous Media”. In: *Journal of Fluid Mechanics* 803 (Sept. 2016), pp. 144–174. ISSN: 0022-1120, 1469-7645. DOI: `10.1017/jfm.2016.486`. (Visited on 09/12/2022).

[255] Kim Lewis. “Riddle of Biofilm Resistance”. In: *Antimicrobial Agents and Chemotherapy* 45.4 (Apr. 2001), pp. 999–1007. DOI: `10.1128/AAC.45.4.999-1007.2001`. (Visited on 01/04/2023).

[256] Baikun Li and Bruce E. Logan. “Bacterial Adhesion to Glass and Metal-Oxide Surfaces”. In: *Colloids and Surfaces B: Biointerfaces* 36.2 (July 2004), pp. 81–90. ISSN: 09277765. DOI: `10.1016/j.colsurfb.2004.05.006`.

[257] Qian Li and Wolfgang Sand. “Mechanical and Chemical Studies on EPS from Sulfobacillus Thermosulfidooxidans: From Planktonic to Biofilm Cells”. In: *Colloids and Surfaces B: Biointerfaces* 153 (May 2017), pp. 34–40. ISSN: 0927-7765. DOI: `10.1016/j.colsurfb.2017.02.009`. (Visited on 12/19/2022).

[258] Ying Jun Li et al. “Oscillatory Fluid Flow Affects Human Marrow Stromal Cell Proliferation and Differentiation”. In: *Journal of Orthopaedic Research: Official Publication of the Orthopaedic Research Society* 22.6 (Nov. 2004), pp. 1283–1289. ISSN: 0736-0266. DOI: `10.1016/j.orthres.2004.04.002`.

[259] Seng Han Lim et al. “3D Printed Drug Delivery and Testing Systems — a Passing Fad or the Future?” In: *Advanced Drug Delivery Reviews*. 3D-Bioprinting and Micro-/Nano-Technology: Emerging Technologies in Biomedical Sciences 132 (July 2018), pp. 139–168. ISSN: 0169-409X. DOI: `10.1016/j.addr.2018.05.006`. (Visited on 03/14/2023).

[260] Georg Linz et al. “3D-Printed Bioreactor with Integrated Impedance Spectroscopy for Cell Barrier Monitoring”. In: *Advanced Materials Technologies* 6.6 (2021), p. 2100009. ISSN: 2365-709X. DOI: `10.1002/admt.202100009`. (Visited on 03/14/2023).

[261] Justin Liu et al. “Direct 3D-printing of Cell-Laden Constructs in Microfluidic Architectures”. In: *Lab on a Chip* 16.8 (Apr. 2016), pp. 1430–1438. ISSN: 1473-0189. DOI: `10.1039/C6LC00144K`. (Visited on 03/14/2023).

[262] Luting Liu et al. “Understanding the Role of Polymer Surface Nanoscale Topography on Inhibiting Bacteria Adhesion and Growth”. In: *ACS Biomaterials Science and Engineering* 2.1 (Jan. 2016), pp. 122–130. ISSN: 23739878. DOI: `10.1021/acsbiomaterials.5b00431`.

[263] J. T. Locsei and T. J. Pedley. “Run and Tumble Chemotaxis in a Shear Flow: The Effect of Temporal Comparisons, Persistence, Rotational Diffusion, and Cell Shape”. In: *Bulletin of Mathematical Biology* 71.5 (July 2009), pp. 1089–1116. ISSN: 1522-9602. DOI: `10.1007/s11538-009-9395-9`.

[264] Sabrina Lucas, Frédéric Moulin, and Katell Guizien. “Oscillating Grid Mesocosm for Studying Oxygen Dynamics under Controlled Unsteady Turbulence”. In: *Limnology and Oceanography: Methods* 14.1 (2016), pp. 1–13. ISSN: 1541-5856. DOI: `10.1002/lom3.10064`. (Visited on 04/12/2023).

[265] Calvin Lumban Gaol et al. “Investigation of Clogging in Porous Media Induced by Microorganisms Using a Microfluidic Application”. In: *Environmental Science: Water Research & Technology* 7.2 (2021), pp. 441–454. DOI: `10.1039/D0EW00766H`. (Visited on 09/29/2021).

[266] Giuliano Lupini et al. “CARD–FISH and Confocal Laser Scanner Microscopy to Assess Successional Changes of the Bacterial Community in Freshwater Biofilms”. In: *Journal of Microbiological Methods* 86.2 (Aug. 2011), pp. 248–251. ISSN: 0167-7012. DOI: `10.1016/j.mimet.2011.05.011`. (Visited on 12/20/2022).

[267] Luyan Ma et al. “Assembly and Development of the Pseudomonas Aeruginosa Biofilm Matrix”. In: *PLoS pathogens* 5.3 (Mar. 2009), e1000354. ISSN: 1553-7374. DOI: `10.1371/journal.ppat.1000354`.

[268] Luyan Ma et al. “The Roles of Biofilm Matrix Polysaccharide Psl in Mucoid Pseudomonas Aeruginosa Biofilms”. In: *FEMS immunology and medical microbiology* 65.2 (July 2012), pp. 377–380. ISSN: 1574-695X. DOI: `10.1111/j.1574-695X.2012.00934.x`.

[269] Nariman Mahabadi et al. “Gas Bubble Migration and Trapping in Porous Media: Pore-Scale Simulation”. In: *Journal of Geophysical Research: Solid Earth* 123.2 (2018), pp. 1060–1071. ISSN: 2169-9356. DOI: `10.1002/2017JB015331`. (Visited on 04/05/2023).

[270] Matthew M. Mahan and Amber L. Doiron. *Gold Nanoparticles as X-Ray, CT, and Multimodal Imaging Contrast Agents: Formulation, Targeting, and Methodology.* https://www.hindawi.com/journals/jnm/2018/ Review Article. Mar. 2018. DOI: `10.1155/2018/5837276`. (Visited on 06/09/2020).

[271] Bertram Manz et al. “Measuring Local Flow Velocities and Biofilm Structure in Biofilm Systems with Magnetic Resonance Imaging (MRI)”. In: *Biotechnology and Bioengineering* 84.4 (2003), pp. 424–432. ISSN: 1097-0290. DOI: `10.1002/bit.10782`. (Visited on 11/01/2021).

[272] Marco PC Marques and Nicolas Szita. “Bioprocess Microfluidics: Applying Microfluidic Devices for Bioprocessing”. In: *Current Opinion in Chemical Engineering*. Biotechnology and Bioprocess Engineering / Process Systems Engineering 18 (Nov. 2017), pp. 61–68. ISSN: 2211-3398. DOI: `10.1016/j.coche.2017.09.004`. (Visited on 11/12/2022).

[273] Philip D. Marsh, Annette Moter, and Deirdre A. Devine. “Dental Plaque Biofilms: Communities, Conflict and Control”. In: *Periodontology 2000* 55.1 (2011), pp. 16–35. ISSN: 09066713. DOI: `10.1111/j.1600-0757.2009.00339.x`. PMID: 21134226.

[274] Ivan Martin, David Wendt, and Michael Heberer. “The Role of Bioreactors in Tissue Engineering”. In: *Trends in Biotechnology* 22.2 (Feb. 2004), pp. 80–86. ISSN: 0167-7799. DOI: `10.1016/j.tibtech.2003.12.001`.

[275] Kelly J. Martin and Robert Nerenberg. "The Membrane Biofilm Reactor (MBfR) for Water and Wastewater Treatment: Principles, Applications, and Recent Developments". In: *Bioresource Technology.* Membrane Bioreactors (MBRs): State-of-Art and Future 122 (Oct. 2012), pp. 83–94. ISSN: 0960-8524. DOI: `10.1016/j.biortech.2012.02.110`. (Visited on 03/13/2023).

[276] Yoshimi Matsumoto et al. "A Microfluidic Channel Method for Rapid Drug-Susceptibility Testing of Pseudomonas Aeruginosa". In: *PLOS ONE* 11.2 (Feb. 2016), e0148797. ISSN: 1932-6203. DOI: `10.1371/journal.pone.0148797`. (Visited on 04/07/2023).

[277] Tiina Mattila-Sandholm and Gun Wirtanen. "Biofilm Formation in the Industry: A Review". In: *Food Reviews International* 8.4 (Jan. 1992), pp. 573–603. ISSN: 8755-9129. DOI: `10.1080/87559129209540953`. (Visited on 04/07/2023).

[278] Carsten Matz et al. "Biofilm Formation and Phenotypic Variation Enhance Predation-Driven Persistence of Vibrio Cholerae". In: *Proceedings of the National Academy of Sciences of the United States of America* 102.46 (Nov. 2005), pp. 16819–16824. ISSN: 00278424. DOI: `10.1073/pnas.0505350102`.

[279] Jeffrey S. McLean, Ositadinma N. Ona, and Paul D. Majors. "Correlated Biofilm Imaging, Transport and Metabolism Measurements via Combined Nuclear Magnetic Resonance and Confocal Microscopy". In: *The ISME Journal* 2.2 (Feb. 2008), pp. 121–131. ISSN: 1751-7370. DOI: `10.1038/ismej.2007.107`. (Visited on 01/07/2023).

[280] C. M. McLeavy et al. "The Future of CT: Deep Learning Reconstruction". In: *Clinical Radiology* 76.6 (June 2021), pp. 407–415. ISSN: 0009-9260. DOI: `10.1016/j.crad.2021.01.010`. (Visited on 12/23/2022).

[281] Cathy E. McNamee, Nayoung Pyo, and Ko Higashitani. "Atomic Force Microscopy Study of the Specific Adhesion between a Colloid Particle and a Living Melanoma Cell: Effect of the Charge and the Hydrophobicity of the Particle Surface". In: *Biophysical Journal* 91.5 (Sept. 2006), pp. 1960–1969. ISSN: 00063495. DOI: `10.1529/biophysj.106.082420`.

[282] Viraj Mehta and Subha N. Rath. "3D Printed Microfluidic Devices: A Review Focused on Four Fundamental Manufacturing Approaches and Implications on the Field of Healthcare". In: *Bio-Design and Manufacturing* 4.2 (June 2021), pp. 311–343. ISSN: 2522-8552. DOI: `10.1007/s42242-020-00112-5`. (Visited on 03/15/2023).

[283] Judith H. Merritt et al. "SadC Reciprocally Influences Biofilm Formation and Swarming Motility via Modulation of Exopolysaccharide Production and Flagellar Function". In: *Journal of Bacteriology* 189.22 (Nov. 2007), pp. 8154–8164. ISSN: 1098-5530. DOI: `10.1128/JB.00585-07`.

[284] Meenu Mishra et al. "Pseudomonas Aeruginosa Psl Polysaccharide Reduces Neutrophil Phagocytosis and the Oxidative Response by Limiting Complement-Mediated Opsonization". In: *Cellular Microbiology* 14.1 (Jan. 2012), pp. 95–106. ISSN: 1462-5822. DOI: `10.1111/j.1462-5822.2011.01704.x`.

[285] Sandhya Mishra et al. "Biofilm-Mediated Bioremediation Is a Powerful Tool for the Removal of Environmental Pollutants". In: *Chemosphere* 294 (May 2022), p. 133609. ISSN: 0045-6535. DOI: `10.1016/j.chemosphere.2022.133609`. (Visited on 04/07/2023).

[286] M. N. B. Momba et al. "Overview of Biofilm Formation in Distribution Systems and Its Impact on the Deterioration of Water Quality". In: (Jan. 2000). ISSN: 0378-4738. (Visited on 03/13/2023).

[287] Monica Monici. "Cell and Tissue Autofluorescence Research and Diagnostic Applications". In: *Biotechnology Annual Review.* Vol. 11. Elsevier, Jan. 2005, pp. 227–256. DOI: `10.1016/S1387-2656(05)11007-2`. (Visited on 03/13/2023).

[288] A. Monmeyran et al. "Four Species of Bacteria Deterministically Assemble to Form a Stable Biofilm in a Millifluidic Channel". In: *NPJ biofilms and microbiomes* 7.1 (Aug. 2021), p. 64. ISSN: 2055-5008. DOI: `10.1038/s41522-021-00233-4`.

[289] Amaury Monmeyran et al. "The Inducible Chemical-Genetic Fluorescent Marker FAST Outperforms Classical Fluorescent Proteins in the Quantitative Reporting of Bacterial Biofilm Dynamics". In: *Scientific Reports* 8.1 (July 2018), p. 10336. ISSN: 2045-2322. DOI: `10.1038/s41598-018-28643-z`.

[290] Ryan Morgan et al. "BdlA, a Chemotaxis Regulator Essential for Biofilm Dispersion in Pseudomonas Aeruginosa". In: *Journal of Bacteriology* 188.21 (Nov. 2006), pp. 7335–7343. ISSN: 00219193. DOI: `10.1128/JB.00599-06`.

[291] Teresa K Nam et al. "Biofilm Characteristics as Affected by Sand Size and Location in Fluidized Bed Vessels". In: *Aquacultural Engineering* 22.3 (June 2000), pp. 213–224. ISSN: 0144-8609. DOI: `10.1016/S0144-8609(00)00040-6`. (Visited on 12/28/2022).

[292] Thomas R. Neu and John R. Lawrence. "Innovative Techniques, Sensors, and Approaches for Imaging Biofilms at Different Scales". In: *Trends in Microbiology* 23.4 (Apr. 2015), pp. 233–242. ISSN: 18784380. DOI: `10.1016/j.tim.2014.12.010`.

[293] Bella H. Neufeld et al. "Metal–Organic Framework Material Inhibits Biofilm Formation of Pseudomonas Aeruginosa". In: *Advanced Functional Materials* 27.34 (2017), p. 1702255. ISSN: 1616-3028. DOI: `10.1002/adfm.201702255`. (Visited on 04/07/2023).

[294] Cac T. Nguyen et al. "Noninvasive in Vivo Optical Detection of Biofilm in the Human Middle Ear". In: *Proceedings of the National Academy of Sciences* 109.24 (June 2012), pp. 9529–9534. DOI: `10.1073/pnas.1201592109`. (Visited on 04/07/2023).

[295] C. Nicolella, M. C. M. van Loosdrecht, and J. J. Heijnen. "Wastewater Treatment with Particulate Biofilm Reactors". In: *Journal of Biotechnology* 80.1 (June 2000), pp. 1–33. ISSN: 0168-1656. DOI: `10.1016/S0168-1656(00)00229-7`. (Visited on 03/01/2023).

[296] Colleen T. O'Loughlin et al. "A Quorum-Sensing Inhibitor Blocks Pseudomonas Aeruginosa Virulence and Biofilm Formation". In: *Proceedings of the National Academy of Sciences* 110.44 (Oct. 2013), pp. 17981–17986. DOI: `10.1073/pnas.1316981110`. (Visited on 01/30/2023).

[297] P. F. O'Neill et al. "Advances in Three-Dimensional Rapid Prototyping of Microfluidic Devices for Biological Applications". In: *Biomicrofluidics* 8.5 (Sept. 2014), p. 052112. ISSN: 1932-1058. DOI: `10.1063/1.4898632`.

[298] G. A. O'Toole and R. Kolter. "Flagellar and Twitching Motility Are Necessary for Pseudomonas Aeruginosa Biofilm Development". In: *Molecular Microbiology* 30.2 (Oct. 1998), pp. 295–304. ISSN: 0950-382X. DOI: `10.1046/j.1365-2958.1998.01062.x`.

[299] Y. J. Oh et al. "Effects of Substrates on Biofilm Formation Observed by Atomic Force Microscopy". In: *Ultramicroscopy* 109.8 (July 2009), pp. 874–880. ISSN: 0304-3991. DOI: `10.1016/j.ultramic.2009.03.042`. (Visited on 12/19/2022).

[300] Olubukola Oluyombo, Christopher N. Penfold, and Stephen P. Diggle. "Competition in Biofilms between Cystic Fibrosis Isolates of Pseudomonas Aeruginosa Is Shaped by R-Pyocins". In: *mBio* 10.1 (Jan. 2019), e01828–18. ISSN: 2150-7511. DOI: `10.1128/mBio.01828-18`.

[301] Fiorenzo G. Omenetto and David L. Kaplan. "New Opportunities for an Ancient Material". In: *Science (New York, N.Y.)* 329.5991 (July 2010), pp. 528–531. ISSN: 0036-8075. DOI: `10.1126/science.1188936`. (Visited on 08/19/2018).

[302] D. Or et al. "Physical Constraints Affecting Bacterial Habitats and Activity in Unsaturated Porous Media – a Review". In: *Advances in Water Resources*. Biological Processes in Porous Media: From the Pore Scale to the Field 30.6 (June 2007), pp. 1505–1527. ISSN: 0309-1708. DOI: `10.1016/j.advwatres.2006.05.025`. (Visited on 11/03/2021).

[303] Sassan Ostvar et al. "Investigating the Influence of Flow Rate on Biofilm Growth in Three Dimensions Using Microimaging". In: *Advances in Water Resources* 117 (July 2018), pp. 1–13. ISSN: 03091708. DOI: `10.1016/j.advwatres.2018.03.018`.

[304] S. Padma and G. Hariharan. "Wavelet Based Analytical Expressions to Steady State Biofilm Model Arising in Biochemical Engineering". In: *The Journal of Membrane Biology* 249.3 (June 2016), pp. 221–228. ISSN: 1432-1424. DOI: `10.1007/s00232-015-9861-2`. (Visited on 04/06/2023).

[305] H. W. Paerl and J. L. Pinckney. "A Mini-Review of Microbial Consortia: Their Roles in Aquatic Production and Biogeochemical Cycling". In: *Microbial Ecology* 31.3 (1996), pp. 225–247. ISSN: 0095-3628. JSTOR: `25152978`. (Visited on 03/13/2023).

[306] Yu Pan et al. "Size-Dependent Cytotoxicity of Gold Nanoparticles". In: *Small* 3.11 (2007), pp. 1941–1949. ISSN: 1613-6829. DOI: `10.1002/smll.200700378`. (Visited on 04/01/2023).

[307] Joo-Hyeon Park et al. "Extracellular Protease in Actinomycetes Culture Supernatants Inhibits and Detaches Staphylococcusaureus Biofilm Formation". In: *Biotechnology Letters* 34.4 (Apr. 2012), pp. 655–661. ISSN: 1573-6776. DOI: `10.1007/s10529-011-0825-z`. (Visited on 04/07/2023).

[308] G. Pasirayi et al. "Microfluidic Bioreactors for Cell Culturing: A Review". In: *Micro and Nanosystems* 3.2 (), pp. 137–160. (Visited on 11/12/2022).

[309] Suhas V. Patankar. *Numerical Heat Transfer and Fluid Flow*. First. CRC Press, Oct. 2018. ISBN: 978-1-315-27513-0. DOI: `10.1201/9781482234213`. (Visited on 03/09/2023).

[310] Jay Patel et al. "Recent Developments in Microbial Enhanced Oil Recovery". In: *Renewable and Sustainable Energy Reviews* 52 (Dec. 2015), pp. 1539–1558. ISSN: 1364-0321. DOI: `10.1016/j.rser.2015.07.135`. (Visited on 11/12/2022).

[311] Etienne Paul et al. "Effect of Shear Stress and Growth Conditions on Detachment and Physical Properties of Biofilms". In: *Water Research* 46.17 (Nov. 2012), pp. 5499–5508. ISSN: 0043-1354. DOI: `10.1016/j.watres.2012.07.029`. (Visited on 03/26/2023).

[312] Aleksei N. Pavlov et al. "Wavelet Analysis in Neurodynamics". In: *Physics-Uspekhi* 55.9 (Sept. 2012), p. 845. ISSN: 1063-7869. DOI: `10.3367/UFNe.0182.201209a.0905`. (Visited on 04/02/2023).

[313] Yoan Pechaud et al. "Influence of Shear Stress, Organic Loading Rate and Hydraulic Retention Time on the Biofilm Structure and on the Competition between Different Biological Aggregate Morphotypes". In: *Journal of Environmental Chemical Engineering* 10.3 (June 2022), p. 107597. ISSN: 2213-3437. DOI: `10.1016/j.jece.2022.107597`. (Visited on 03/26/2023).

[314] S L Percival et al. "The Effect of Turbulent Flow and Surface Roughness on Biofilm Formation in Drinking Water". In: *Journal of Industrial Microbiology and Biotechnology* 22.3 (Mar. 1999), pp. 152–159. ISSN: 1367-5435, 1476-5535. DOI: `10.1038/sj.jim.2900622`. (Visited on 01/29/2023).

[315] Maria Olivia Pereira et al. "Effect of Flow Regime on the Architecture of a Pseudomonas Fluorescens Biofilm". In: *Biotechnology and Bioengineering* 78.2 (Apr. 2002), pp. 164–171. ISSN: 0006-3592. DOI: `10.1002/bit.10189`.

[316] David Perera-Costa et al. "Studying the Influence of Surface Topography on Bacterial Adhesion Using Spatially Organized Microtopographic Surface Patterns". In: *Langmuir* 30.16 (Apr. 2014), pp. 4633–4641. ISSN: 15205827. DOI: `10.1021/la5001057`.

[317] Lazaro J. Perez et al. "Contributions of Biofilm-Induced Flow Heterogeneities to Solute Retention and Anomalous Transport Features in Porous Media". In: *Water Research* 209 (Feb. 2022), p. 117896. ISSN: 0043-1354. DOI: `10.1016/j.watres.2021.117896`. (Visited on 03/26/2023).

[318] Pablo Perez-Pinera et al. "Synthetic Biology and Microbioreactor Platforms for Programmable Production of Biologics at the Point-of-Care". In: *Nature Communications* 7.1 (July 2016), p. 12211. ISSN: 2041-1723. DOI: `10.1038/ncomms12211`. (Visited on 11/12/2022).

[319] Edgar Peris et al. "Tuneable 3D Printed Bioreactors for Transaminations under Continuous-Flow". In: *Green Chemistry* 19.22 (Nov. 2017), pp. 5345–5349. ISSN: 1463-9270. DOI: `10.1039/C7GC02421E`. (Visited on 03/14/2023).

[320] Alexandre Persat, Howard A. Stone, and Zemer Gitai. "The Curved Shape of Caulobacter Crescentus Enhances Surface Colonization in Flow". In: *Nature Communications* 5.1 (May 2014), p. 3824. ISSN: 2041-1723. DOI: `10.1038/ncomms4824`. (Visited on 01/29/2023).

[321] Alexandre Persat et al. "The Mechanical World of Bacteria". In: *Cell* 161.5 (May 2015), pp. 988–997. ISSN: 0092-8674. DOI: `10.1016/j.cell.2015.05.005`. (Visited on 01/26/2023).

[322] Malgorzata Peszynska et al. "Biofilm Growth in Porous Media: Experiments, Computational Modeling at the Porescale, and Upscaling". In: *Advances in Water Resources* 95 (Sept. 2016), pp. 288–301. ISSN: 03091708. DOI: `10.1016/j.advwatres.2015.07.008`.

[323] Niels Peter Revsbech. "Analysis of Microbial Communities with Electrochemical Microsensors and Microscale Biosensors". In: *Methods in Enzymology*. Vol. 397. Environmental Microbiology. Academic Press, Jan. 2005, pp. 147–166. DOI: `10.1016/S0076-6879(05)97009-2`. (Visited on 01/07/2023).

[324] Olga E. Petrova and Karin Sauer. *Escaping the Biofilm in More than One Way: Desorption, Detachment or Dispersion*. Vol. 30. Elsevier Ltd, Apr. 2016. DOI: `10.1016/j.mib.2016.01.004`.

[325] Adrienne J. Phillips et al. "Potential CO2 Leakage Reduction through Biofilm-Induced Calcium Carbonate Precipitation". In: *Environmental Science & Technology* 47.1 (Jan. 2013), pp. 142–149. ISSN: 0013-936X. DOI: `10.1021/es301294q`. (Visited on 11/03/2021).

[326] Cristian Picioreanu et al. "Determination of Mechanical Properties of Biofilms by Modelling the Deformation Measured Using Optical Coherence Tomography". In: *Water Research* 145 (Nov. 2018), pp. 588–598. ISSN: 18792448. DOI: `10.1016/j.watres.2018.08.070`.

[327] Kati Piironen et al. "Cell Adhesion and Proliferation on Common 3D Printing Materials Used in Stereolithography of Microfluidic Devices". In: *Lab on a Chip* 20.13 (2020), pp. 2372–2382. DOI: `10.1039/D0LC00114G`. (Visited on 04/06/2023).

[328] Mohammad Pousti et al. "Microfluidic Bioanalytical Flow Cells for Biofilm Studies: A Review". In: *Analyst* 144.1 (Dec. 2018), pp. 68–86. ISSN: 1364-5528. DOI: `10.1039/C8AN01526K`. (Visited on 01/07/2023).

[329] Balasankar Meera Priyadarshini, Vishwesh Dikshit, and Yi Zhang. "3D-printed Bioreactors for In Vitro Modeling and Analysis". In: *International Journal of Bioprinting* 6.4 (Aug. 2020), p. 267. ISSN: 2424-7723. DOI: `10.18063/ijb.v6i4.267`. (Visited on 06/09/2022).

[330] *Project Home - CALIF3S - MyGForge*. https://gforge.irsn.fr/#/project/calif3s. (Visited on 04/04/2023).

[331] B. Purevdorj, J. W. Costerton, and P. Stoodley. "Influence of Hydrodynamics and Cell Signaling on the Structure and Behavior of Pseudomonas Aeruginosa Biofilms". In: *Applied and Environmental Microbiology* 68.9 (Sept. 2002), pp. 4457–4464. ISSN: 0099-2240. DOI: `10.1128/AEM.68.9.4457-4464.2002`.

[332] B. Purevdorj-Gage, W. J. Costerton, and P. Stoodley. "Phenotypic Differentiation and Seeding Dispersal in Non-Mucoid and Mucoid Pseudomonas Aeruginosa Biofilms". In: *Microbiology (Reading, England)* 151.Pt 5 (May 2005), pp. 1569–1576. ISSN: 1350-0872. DOI: `10.1099/mic.0.27536-0`.

[333] Yahya T. Qassim et al. "Wavelet Coherence of EEG Signals for a Visual Oddball Task". In: *Computers in Biology and Medicine* 43.1 (Jan. 2013), pp. 23–31. ISSN: 0010-4825. DOI: `10.1016/j.compbiomed.2012.10.008`. (Visited on 04/02/2023).

[334] Ning Qin et al. "Microfluidic Technology for Antibacterial Resistance Study and Antibiotic Susceptibility Testing: Review and Perspective". In: *ACS Sensors* 6.1 (Jan. 2021), pp. 3–21. DOI: `10.1021/acssensors.0c02175`. (Visited on 03/01/2023).

[335] Reverson Fernandes Quero et al. "Understanding and Improving FDM 3D Printing to Fabricate High-Resolution and Optically Transparent Microfluidic Devices". In: *Lab on a Chip* 21.19 (Sept. 2021), pp. 3715–3729. ISSN: 1473-0189. DOI: `10.1039/D1LC00518A`. (Visited on 03/15/2023).

[336] Minhaz Ur Rahman et al. "Microrheology of Pseudomonas Aeruginosa Biofilms Grown in Wound Beds". In: *npj Biofilms and Microbiomes* 8.1 (June 2022), pp. 1–9. ISSN: 2055-5008. DOI: `10.1038/s41522-022-00311-1`. (Visited on 04/13/2023).

[337] Jorge Ramírez-Muñoz et al. "CFD Study of the Hydrodynamics and Biofilm Growth Effect of an Anaerobic Inverse Fluidized Bed Reactor Operating in the Laminar Regime". In: *Journal of Environmental Chemical Engineering* 9.1 (Feb. 2021), p. 104674. ISSN: 2213-3437. DOI: `10.1016/j.jece.2020.104674`. (Visited on 04/12/2023).

[338] Tsiry Rasamiravaka et al. "The Formation of Biofilms by Pseudomonas Aeruginosa: A Review of the Natural and Synthetic Compounds Interfering with Control Mechanisms". In: *BioMed Research International* 2015 (2015), p. 759348. ISSN: 2314-6141. DOI: `10.1155/2015/759348`.

[339] Abigail R. Raveling, Sophia K. Theodossiou, and Nathan R. Schiele. "A 3D Printed Mechanical Bioreactor for Investigating Mechanobiology and Soft Tissue Mechanics". In: *MethodsX* 5 (Jan. 2018), pp. 924–932. ISSN: 2215-0161. DOI: `10.1016/j.mex.2018.08.001`. (Visited on 03/14/2023).

[340] Lukas Richter et al. "Development of a Microfluidic Biochip for Online Monitoring of Fungal Biofilm Dynamics". In: *Lab on a Chip* 7.12 (Nov. 2007), pp. 1723–1731. ISSN: 1473-0189. DOI: `10.1039/B708236C`. (Visited on 01/07/2023).

[341] H. H.M. Rijnaarts et al. "Bacterial Adhesion under Static and Dynamic Conditions". In: *Applied and Environmental Microbiology* 59.10 (1993), pp. 3255–3265. ISSN: 00992240. DOI: `10.1128/aem.59.10.3255-3265.1993`.

[342] Sandra Milena Rincon et al. "Photosynthetic Activity Assessment in Mixotrophically Cultured Chlorella Vulgaris Biofilms at Various Developmental Stages". In: *Algal Research* 38 (Mar. 2019), p. 101408. ISSN: 2211-9264. DOI: `10.1016/j.algal.2019.101408`. (Visited on 01/07/2023).

[343] Rosa Ripa, Amy Q. Shen, and Riccardo Funari. "Detecting *Escherichia Coli* Biofilm Development Stages on Gold and Titanium by Quartz Crystal Microbalance". In: *ACS Omega* 5.5 (Feb. 2020), pp. 2295–2302. ISSN: 2470-1343, 2470-1343. DOI: `10.1021/acsomega.9b03540`. (Visited on 01/08/2023).

[344] Bruce E. Rittmann. "The Significance of Biofilms in Porous Media". In: *Water Resources Research* 29.7 (1993), pp. 2195–2202. ISSN: 1944-7973. DOI: `10.1029/93WR00611`. (Visited on 11/03/2021).

[345] Alice Rochex et al. "Role of Shear Stress on Composition, Diversity and Dynamics of Biofilm Bacterial Communities". In: *Water Research* 42.20 (Dec. 2008), pp. 4915–4922. ISSN: 0043-1354. DOI: `10.1016/j.watres.2008.09.015`. (Visited on 03/26/2023).

[346] Chad I. Rogers et al. "3D Printed Microfluidic Devices with Integrated Valves". In: *Biomicrofluidics* 9.1 (Jan. 2015), p. 016501. ISSN: 1932-1058. DOI: `10.1063/1.4905840`. (Visited on 03/14/2023).

[347] A. -M. Rogues et al. "Contribution of Tap Water to Patient Colonisation with Pseudomonas Aeruginosa in a Medical Intensive Care Unit". In: *Journal of Hospital Infection* 67.1 (Sept. 2007), pp. 72–78. ISSN: 0195-6701. DOI: `10.1016/j.jhin.2007.06.019`. (Visited on 04/07/2023).

[348] S. Rolland du Roscoat et al. "Application of Synchrotron X-ray Microtomography for Visualizing Bacterial Biofilms 3D Microstructure in Porous Media". In: *Biotechnology and Bioengineering* 111.6 (June 2014), pp. 1265–1271. ISSN: 10970290. DOI: `10.1002/bit.25168`.

[349] Sabine Rolland du Roscoat et al. "First Visualisation of Bacterial Biofilms in 3D Porous Media with Neutron Microtomography without Contrast Agent". In: *Journal of Microscopy* 285.1 (2022), pp. 20–28. ISSN: 1365-2818. DOI: `10.1111/jmi.13063`. (Visited on 12/27/2022).

[350] Anna M. Romaní et al. "Microbial Biofilm Structure and Organic Matter Use in Mediterranean Streams". In: *Hydrobiologia* 719.1 (Nov. 2013), pp. 43–58. ISSN: 1573-5117. DOI: `10.1007/s10750-012-1302-y`. (Visited on 04/07/2023).

[351] Valentin Romanov et al. "FDM 3D Printing of High-Pressure, Heat-Resistant, Transparent Microfluidic Devices". In: *Analytical Chemistry* 90.17 (Sept. 2018), pp. 10450–10456. ISSN: 0003-2700. DOI: `10.1021/acs.analchem.8b02356`. (Visited on 03/15/2023).

[352] U. Römling and C. Balsalobre. "Biofilm Infections, Their Resilience to Therapy and Innovative Treatment Strategies". In: *Journal of Internal Medicine* 272.6 (2012), pp. 541–561. ISSN: 1365-2796. DOI: `10.1111/joim.12004`. (Visited on 04/07/2023).

[353] R. Kerry Rowe, Mark D. Armstrong, and D. Roy Cullimore. "Particle Size and Clogging of Granular Media Permeated with Leachate". In: *Journal of Geotechnical and Geoenvironmental Engineering* 126.9 (Sept. 2000), pp. 775–786. ISSN: 1090-0241. DOI: `10.1061/(ASCE)1090-0241(2000)126:9(775)`. (Visited on 12/29/2022).

[354] P. A. Rühs et al. "Studying Bacterial Hydrophobicity and Biofilm Formation at Liquid–Liquid Interfaces through Interfacial Rheology and Pendant Drop Tensiometry". In: *Colloids and Surfaces B: Biointerfaces* 117 (May 2014), pp. 174–184. ISSN: 0927-7765. DOI: `10.1016/j.colsurfb.2014.02.023`. (Visited on 01/08/2023).

[355] Patrick A. Rühs et al. "In-Situ Quantification of the Interfacial Rheological Response of Bacterial Biofilms to Environmental Stimuli". In: *PLOS ONE* 8.11 (Nov. 2013), e78524. ISSN: 1932-6203. DOI: `10.1371/journal.pone.0078524`. (Visited on 01/08/2023).

[356] Kendra P. Rumbaugh and Karin Sauer. "Biofilm Dispersion". In: *Nature Reviews Microbiology* 18.10 (Oct. 2020), pp. 571–586. ISSN: 1740-1534. DOI: `10.1038/s41579-020-0385-0`. (Visited on 01/22/2023).

[357] Roberto Rusconi, Melissa Garren, and Roman Stocker. "Microfluidics Expanding the Frontiers of Microbial Ecology". In: *Annual Review of Biophysics* 43.1 (2014), pp. 65–91. DOI: `10.1146/annurev-biophys-051013-022916`. (Visited on 09/13/2019).

[358] Roberto Rusconi, Jeffrey S. Guasto, and Roman Stocker. "Bacterial Transport Suppressed by Fluid Shear". In: *Nature Physics* 10.3 (Feb. 2014), pp. 212–217. ISSN: 17452481. DOI: `10.1038/nphys2883`.

[359] Cynthia Ryder, Matthew Byrd, and Daniel J Wozniak. "Role of Polysaccharides in Pseudomonas Aeruginosa Biofilm Development". In: *Current Opinion in Microbiology*. Growth and Development 10.6 (Dec. 2007), pp. 644–648. ISSN: 1369-5274. DOI: `10.1016/j.mib.2007.09.010`. (Visited on 01/05/2023).

[360] Sergi Sabater et al. "Stream Biofilm Responses to Flow Intermittency: From Cells to Ecosystems". In: *Frontiers in Environmental Science* 4 (2016). ISSN: 2296-665X. (Visited on 01/12/2023).

[361] Samuel C. Saccomano, Megan P. Jewell, and Kevin J. Cash. "A Review of Chemosensors and Biosensors for Monitoring Biofilm Dynamics". In: *Sensors and Actuators Reports* 3 (Nov. 2021), p. 100043. ISSN: 2666-0539. DOI: `10.1016/j.snr.2021.100043`. (Visited on 01/07/2023).

[362] Luis E. Sáenz de Miera et al. "Effects of Varying CO2 Flows on Bacterial Communities in Mesocosms Created from Two Soils". In: *International Journal of Greenhouse Gas Control* 46 (Mar. 2016), pp. 205–214. ISSN: 1750-5836. DOI: `10.1016/j.ijggc.2016.01.013`. (Visited on 04/12/2023).

[363] Rokas Šakalys, Kiang Wei Kho, and Tia E. Keyes. "A Reproducible, Low Cost Microfluidic Microcavity Array SERS Platform Prepared by Soft Lithography from a 2 Photon 3D Printed Template". In: *Sensors and Actuators B: Chemical* 340 (Aug. 2021), p. 129970. ISSN: 0925-4005. DOI: `10.1016/j.snb.2021.129970`. (Visited on 03/15/2023).

[364] S. Sangetha et al. "In Situ TEM and SEM Studies on the Antimicrobial Activity and Prevention of Candida Albicans Biofilm by Cassia Spectabilis Extract". In: *Micron* 40.4 (June 2009), pp. 439–443. ISSN: 0968-4328. DOI: `10.1016/j.micron.2009.01.003`. (Visited on 04/07/2023).

[365] Madhu Bala Sathyanarayanan et al. "The Effect of Gold and Iron-Oxide Nanoparticles on Biofilm-Forming Pathogens". In: *ISRN microbiology* 2013 (2013), p. 272086. ISSN: 2090-7478. DOI: `10.1155/2013/272086`.

[366] Yoshinori Sato et al. "Effects of Colistin and Tigecycline on Multidrug-Resistant Acinetobacter Baumannii Biofilms: Advantages and Disadvantages of Their Combination". In: *Scientific Reports* 11.1 (June 2021), p. 11700. ISSN: 2045-2322. DOI: `10.1038/s41598-021-90732-3`. (Visited on 04/07/2023).

[367] K. Sauer et al. "Characterization of Nutrient-Induced Dispersion in Pseudomonas Aeruginosa PAO1 Biofilm". In: *Journal of Bacteriology* 186.21 (Nov. 2004), pp. 7312–7326. DOI: `10.1128/JB.186.21.7312-7326.2004`. (Visited on 04/07/2023).

[368] Karin Sauer et al. "The Biofilm Life Cycle: Expanding the Conceptual Model of Biofilm Formation". In: *Nature Reviews Microbiology* 20.10 (Oct. 2022), pp. 608–620. ISSN: 1740-1534. DOI: `10.1038/s41579-022-00767-0`. (Visited on 01/03/2023).

[369] Günter Sauerbrey. "Verwendung von Schwingquarzen zur Wägung dünner Schichten und zur Mikrowägung". In: *Zeitschrift für Physik* 155.2 (Apr. 1959), pp. 206–222. ISSN: 0044-3328. DOI: `10.1007/BF01337937`. (Visited on 01/08/2023).

[370] J. Andy Schaber et al. "Pseudomonas Aeruginosa Forms Biofilms in Acute Infection Independent of Cell-to-Cell Signaling". In: *Infection and Immunity* 75.8 (Aug. 2007), pp. 3715–3721. DOI: `10.1128/IAI.00586-07`. (Visited on 04/07/2023).

[371] Daniel Schäpper et al. "Application of Microbioreactors in Fermentation Process Development: A Review". In: *Analytical and Bioanalytical Chemistry* 395.3 (Oct. 2009), pp. 679–695. ISSN: 1618-2650. DOI: `10.1007/s00216-009-2955-x`.

[372] David Scheidweiler et al. "Trait-Specific Dispersal of Bacteria in Heterogeneous Porous Environments: From Pore to Porous Medium Scale". In: *Journal of The Royal Society Interface* 17.164 (Mar. 2020), p. 20200046. DOI: `10.1098/rsif.2020.0046`. (Visited on 01/27/2022).

[373] David Scheidweiler et al. "Unraveling the Biophysical Underpinnings to the Success of Multispecies Biofilms in Porous Environments". In: *The ISME Journal* 13.7 (July 2019), pp. 1700–1710. ISSN: 1751-7370. DOI: `10.1038/s41396-019-0381-4`. (Visited on 09/29/2021).

[374] Jakob Schmid et al. "A Perfusion Bioreactor System for Cell Seeding and Oxygen-Controlled Cultivation of Three-Dimensional Cell Cultures". In: *Tissue Engineering Part C: Methods* 24.10 (Oct. 2018), pp. 585–595. ISSN: 1937-3384. DOI: `10.1089/ten.tec.2018.0204`. (Visited on 06/22/2022).

[375] A Schramm et al. "Structure and Function of a Nitrifying Biofilm as Determined by in Situ Hybridization and the Use of Microelectrodes". In: *Applied and Environmental Microbiology* 62.12 (Dec. 1996), pp. 4641–4647. DOI: `10.1128/aem.62.12.4641-4647.1996`. (Visited on 01/07/2023).

[376] Tobias Schubeis et al. "Untangling a Repetitive Amyloid Sequence: Correlating Biofilm-Derived and Segmentally Labeled Curli Fimbriae by Solid-State NMR Spectroscopy". In: *Angewandte Chemie International Edition* 54.49 (2015), pp. 14669–14672. ISSN: 1521-3773. DOI: `10.1002/anie.201506772`. (Visited on 04/07/2023).

[377] Dorte Seifert and Peter Engesgaard. "Use of Tracer Tests to Investigate Changes in Flow and Transport Properties Due to Bioclogging of Porous Media". In: *Journal of Contaminant Hydrology* 93.1 (Aug. 2007), pp. 58–71. ISSN: 0169-7722. DOI: `10.1016/j.jconhyd.2007.01.014`. (Visited on 12/27/2022).

[378] Katsutoshi Seki et al. "Moderate Bioclogging Leading to Preferential Flow Paths in Biobarriers". In: *Ground Water Monitoring & Remediation* 26.3 (Aug. 2006), pp. 68–76. ISSN: 10693629. DOI: `10.1111/j.1745-6592.2006.00086.x`. (Visited on 12/27/2022).

[379] Diego O. Serra and Regine Hengge. "Stress Responses Go Three Dimensional - the Spatial Order of Physiological Differentiation in Bacterial Macrocolony Biofilms". In: *Environmental Microbiology* 16.6 (June 2014), pp. 1455–1471. ISSN: 1462-2920. DOI: `10.1111/1462-2920.12483`.

[380] Joseph D. Seymour et al. "Anomalous Fluid Transport in Porous Media Induced by Biofilm Growth". In: *Physical Review Letters* 93.19 (Nov. 2004), p. 198103. DOI: `10.1103/PhysRevLett.93.198103`. (Visited on 11/01/2021).

[381] John W. Shanahan and Michael J. Semmens. "Alkalinity and pH Effects on Nitrification in a Membrane Aerated Bioreactor: An Experimental and Model Analysis". In: *Water Research* 74 (May 2015), pp. 10–22. ISSN: 0043-1354. DOI: `10.1016/j.watres.2014.12.055`. (Visited on 04/12/2023).

[382] H. Shemesh et al. "High Frequency Ultrasound Imaging of a Single-Species Biofilm". In: *Journal of Dentistry* 35.8 (Aug. 2007), pp. 673–678. ISSN: 0300-5712. DOI: `10.1016/j.jdent.2007.05.007`. (Visited on 04/07/2023).

[383] Yi Shen et al. "Flow Directs Surface-Attached Bacteria to Twitch Upstream". In: *Biophysical Journal* 103.1 (July 2012), pp. 146–151. ISSN: 00063495. DOI: `10.1016/j.bpj.2012.05.045`. (Visited on 01/29/2023).

[384] Xiaoxia X. Sheng, Yen Peng Ting, and Simo Olavi Pehkonen. "The Influence of Ionic Strength, Nutrients and pH on Bacterial Adhesion to Metals". In: *Journal of Colloid and Interface Science* 321.2 (May 2008), pp. 256–264. ISSN: 00219797. DOI: `10.1016/j.jcis.2008.02.038`.

[385] Ryotaro Shimizu and Hajime Tanaka. "Impact of Complex Topology of Porous Media on Phase Separation of Binary Mixtures". In: *Science Advances* 3.12 (Dec. 2017), eaap9570. DOI: `10.1126/sciadv.aap9570`. (Visited on 04/04/2023).

[386] Joshua D. Shrout et al. "The Impact of Quorum Sensing and Swarming Motility on Pseudomonas Aeruginosa Biofilm Formation Is Nutritionally Conditional". In: *Molecular Microbiology* 62.5 (2006), pp. 1264–1277. ISSN: 1365-2958. DOI: `10.1111/j.1365-2958.2006.05421.x`. (Visited on 01/05/2023).

[387] Wahhida Shumi et al. "Environmental Factors That Affect Streptococcus Mutans Biofilm Formation in a Microfluidic Device Mimicking Teeth". In: *BioChip Journal* 4.4 (Dec. 2010), pp. 257–263. ISSN: 2092-7843. DOI: `10.1007/s13206-010-4401-8`. (Visited on 01/08/2023).

[388] J. P. S. Sidhu et al. "Prevalence of Antibiotic Resistance and Virulence Genes in the Biofilms from an Aquifer Recharged with Stormwater". In: *Water Research* 185 (Oct. 2020), p. 116269. ISSN: 0043-1354. DOI: `10.1016/j.watres.2020.116269`. (Visited on 03/15/2023).

[389] Samuel A. Siles et al. "High-Throughput Screening of a Collection of Known Pharmacologically Active Small Compounds for Identification of Candida Albicans Biofilm Inhibitors". In: *Antimicrobial Agents and Chemotherapy* 57.8 (Aug. 2013), pp. 3681–3687. DOI: `10.1128/AAC.00680-13`. (Visited on 04/05/2023).

[390] Manuel Simões, Lúcia C. Simões, and Maria J. Vieira. "A Review of Current and Emergent Biofilm Control Strategies". In: *LWT - Food Science and Technology* 43.4 (May 2010), pp. 573–583. ISSN: 0023-6438. DOI: `10.1016/j.lwt.2009.12.008`. (Visited on 03/25/2023).

[391] Manuel Simões et al. "The Effect of Hydrodynamic Conditions on the Phenotype of Pseudomonas Fluorescens Biofilms". In: *Biofouling* 23.4 (Jan. 2007), pp. 249–258. ISSN: 0892-7014. DOI: `10.1080/08927010701368476`. (Visited on 01/29/2023).

[392] Anirudh Singh et al. "Bacterial Biofilm Infections, Their Resistance to Antibiotics Therapy and Current Treatment Strategies". In: *Biomedical Materials* 17.2 (Feb. 2022), p. 022003. ISSN: 1748-605X. DOI: `10.1088/1748-605X/ac50f6`. (Visited on 04/07/2023).

[393] Mahima Singh and Sriramakamal Jonnalagadda. “Advances in Bioprinting Using Additive Manufacturing”. In: *European Journal of Pharmaceutical Sciences* 143 (Feb. 2020), p. 105167. ISSN: 0928-0987. DOI: `10.1016/j.ejps.2019.105167`. (Visited on 03/14/2023).

[394] Pradeep K. Singh et al. “A Component of Innate Immunity Prevents Bacterial Biofilm Development”. In: *Nature* 417.6888 (May 2002), pp. 552–555. ISSN: 0028-0836. DOI: `10.1038/417552a`.

[395] Rajbir Singh, Debarati Paul, and Rakesh K. Jain. “Biofilms: Implications in Bioremediation”. In: *Trends in Microbiology* 14.9 (Sept. 2006), pp. 389–397. ISSN: 0966-842X. DOI: `10.1016/j.tim.2006.07.001`. (Visited on 04/07/2023).

[396] Albert Siryaporn et al. “Colonization, Competition, and Dispersal of Pathogens in Fluid Flow Networks”. In: *Current biology: CB* 25.9 (May 2015), pp. 1201–1207. ISSN: 1879-0445. DOI: `10.1016/j.cub.2015.02.074`.

[397] Jelmer Sjollema et al. “Detachment and Successive Re-Attachment of Multiple, Reversibly-Binding Tethers Result in Irreversible Bacterial Adhesion to Surfaces”. In: *Scientific Reports* 7.1 (Dec. 2017), pp. 1–13. ISSN: 20452322. DOI: `10.1038/s41598-017-04703-8`.

[398] Stefaan J. Soenen et al. “Cytotoxic Effects of Gold Nanoparticles: A Multiparametric Study”. In: *ACS Nano* 6.7 (July 2012), pp. 5767–5783. ISSN: 1936-0851. DOI: `10.1021/nn301714n`. (Visited on 04/01/2023).

[399] S. M Soini et al. “Effects of Fluid-Flow Velocity and Water Quality on Planktonic and Sessile Microbial Growth in Water Hydraulic System”. In: *Water Research* 36.15 (Sept. 2002), pp. 3812–3820. ISSN: 0043-1354. DOI: `10.1016/S0043-1354(02)00099-4`. (Visited on 01/29/2023).

[400] Cristina Solano, Maite Echeverz, and Iñigo Lasa. *Biofilm Dispersion and Quorum Sensing*. Vol. 18. Elsevier Ltd, Apr. 2014. DOI: `10.1016/j.mib.2014.02.008`.

[401] Mohamed K. Y. Soliman et al. “Biosynthesis of Silver and Gold Nanoparticles and Their Efficacy Towards Antibacterial, Antibiofilm, Cytotoxicity, and Antioxidant Activities”. In: *Applied Biochemistry and Biotechnology* 195.2 (Feb. 2023), pp. 1158–1183. ISSN: 1559-0291. DOI: `10.1007/s12010-022-04199-7`. (Visited on 04/14/2023).

[402] Majken Sønderholm et al. “Tools for Studying Growth Patterns and Chemical Dynamics of Aggregated Pseudomonas Aeruginosa Exposed to Different Electron Acceptors in an Alginate Bead Model”. In: *npj Biofilms and Microbiomes* 4.1 (Feb. 2018), p. 3. ISSN: 2055-5008. DOI: `10.1038/s41522-018-0047-4`. (Visited on 01/08/2023).

[403] Ralph A. Sperling et al. *Biological Applications of Gold Nanoparticles*. Vol. 37. Royal Society of Chemistry, Aug. 2008. DOI: `10.1039/b712170a`.

[404] C. Sprung et al. “Detection and Monitoring of Biofilm Formation in Water Treatment Systems by Quartz Crystal Microbalance Sensors”. In: *Water Science and Technology: A Journal of the International Association on Water Pollution Research* 59.3 (2009), pp. 543–548. ISSN: 0273-1223. DOI: `10.2166/wst.2009.001`.

[405] M. Staal et al. “Ultrabright Planar Optodes for Luminescence Life-Time Based Microscopic Imaging of O2 Dynamics in Biofilms”. In: *Journal of Microbiological Methods* 85.1 (Apr. 2011), pp. 67–74. ISSN: 0167-7012. DOI: `10.1016/j.mimet.2011.01.021`. (Visited on 01/08/2023).

[406] Benjamin J. Staudinger et al. “Conditions Associated with the Cystic Fibrosis Defect Promote Chronic Pseudomonas Aeruginosa Infection”. In: *American Journal of Respiratory and Critical Care Medicine* 189.7 (Apr. 2014), pp. 812–824. ISSN: 1535-4970. DOI: `10.1164/rccm.201312-2142OC`.

[407] Philip S. Stewart. “Diffusion in Biofilms”. In: *Journal of Bacteriology* 185.5 (Mar. 2003), pp. 1485–1491. DOI: `10.1128/JB.185.5.1485-1491.2003`. (Visited on 01/30/2023).

[408] Philip S. Stewart and Michael J. Franklin. “Physiological Heterogeneity in Biofilms”. In: *Nature Reviews Microbiology* 6.3 (Mar. 2008), pp. 199–210. ISSN: 1740-1534. DOI: `10.1038/nrmicro1838`. (Visited on 01/22/2023).

[409] T. L. Stewart and H. S. Fogler. “Biomass Plug Development and Propagation in Porous Media”. In: *Biotechnology and Bioengineering* 72.3 (Feb. 2001), pp. 353–363. ISSN: 0006-3592. DOI: `10.1002/1097-0290(20010205)72:3<353::aid-bit13>3.0.co;2-u`.

[410] Terri L. Stewart and H. Scott Fogler. “Pore-Scale Investigation of Biomass Plug Development and Propagation in Porous Media”. In: *Biotechnology and Bioengineering* 77.5 (Mar. 2002), pp. 577–588. ISSN: 0006-3592. DOI: `10.1002/bit.10044`.

[411] David J. Stickler. “Bacterial Biofilms in Patients with Indwelling Urinary Catheters”. In: *Nature Clinical Practice Urology* 5.11 (Nov. 2008), pp. 598–608. ISSN: 1743-4289. DOI: `10.1038/ncpuro1231`. (Visited on 04/07/2023).

[412] P. Stoodley et al. “Biofilms as Complex Differentiated Communities”. In: *Annual Review of Microbiology* 56.1 (Oct. 2002), pp. 187–209. ISSN: 0066-4227. DOI: `10.1146/annurev.micro.56.012302.160705`.

[413] P. Stoodley et al. “Flowing Biofilms as a Transport Mechanism for Biomass through Porous Media under Laminar and Turbulent Conditions in a Laboratory Reactor System”. In: *Biofouling* 21.3-4 (Jan. 2005), pp. 161–168. ISSN: 0892-7014, 1029-2454. DOI: `10.1080/08927010500375524`. (Visited on 12/27/2022).

[414] P. Stoodley et al. “Influence of Hydrodynamics and Nutrients on Biofilm Structure”. In: *Journal of Applied Microbiology* 85.S1 (1998), 19S–28S. ISSN: 1365-2672. DOI: `10.1111/j.1365-2672.1998.tb05279.x`. (Visited on 01/29/2023).

[415] P. Stoodley et al. “Influence of Hydrodynamics and Nutrients on Biofilm Structure”. In: *Journal of Applied Microbiology Symposium Supplement*. Vol. 85. 1999. DOI: `10.1111/j.1365-2672.1998.tb05279.x`.

[416] P. Stoodley et al. “The Formation of Migratory Ripples in a Mixed Species Bacterial Biofilm Growing in Turbulent Flow”. In: *Environmental Microbiology* 1.5 (Oct. 1999), pp. 447–455. ISSN: 1462-2912. DOI: `10.1046/j.1462-2920.1999.00055.x`.

[417] Paul Stoodley. “Biofilms: Flow Disrupts Communication”. In: *Nature Microbiology* 1.1 (Jan. 2016), pp. 1–2. ISSN: 2058-5276. DOI: `10.1038/nmicrobiol.2015.12`. (Visited on 01/30/2023).

[418] Nikola Strempel et al. “Human Host Defense Peptide LL-37 Stimulates Virulence Factor Production and Adaptive Resistance in Pseudomonas Aeruginosa”. In: *PLOS ONE* 8.12 (Dec. 2013), e82240. ISSN: 1932-6203. DOI: `10.1371/journal.pone.0082240`. (Visited on 01/05/2023).

[419] Jing Su et al. “Periphyton Biofilm Development and Its Role in Nutrient Cycling in Paddy Microcosms”. In: *Journal of Soils and Sediments* 17.3 (Mar. 2017), pp. 810–819. ISSN: 1614-7480. DOI: `10.1007/s11368-016-1575-2`. (Visited on 04/07/2023).

[420] Sowmya Subramanian et al. “Microsystems for Biofilm Characterization and Sensing – A Review”. In: *Biofilm* 2 (Dec. 2020), p. 100015. ISSN: 2590-2075. DOI: `10.1016/j.bioflm.2019.100015`. (Visited on 01/06/2023).

[421] Shamas Tabraiz et al. “Temperature and Immigration Effects on Quorum Sensing in the Biofilms of Anaerobic Membrane Bioreactors”. In: *Journal of Environmental Management* 293 (Sept. 2021), p. 112947. ISSN: 0301-4797. DOI: `10.1016/j.jenvman.2021.112947`. (Visited on 04/12/2023).

[422] Yasmin Tadjdeh. “3D Printing Promises to Revolutionize Defense, Aerospace Industries”. In: *National Defense* 98.724 (2014), pp. 20–23. ISSN: 0092-1491. JSTOR: 27020306. (Visited on 03/14/2023).

[423] Stewart W. Taylor, P. C. D. Milly, and Peter R. Jaffé. “Biofilm Growth and the Related Changes in the Physical Properties of a Porous Medium: 2. Permeability”. In: *Water Resources Research* 26.9 (Sept. 1990), pp. 2161–2169. ISSN: 00431397. DOI: `10.1029/WR026i009p02161`.

[424] Akihiko Terada et al. “Bacterial Adhesion to and Viability on Positively Charged Polymer Surfaces”. In: *Microbiology* 152.12 (Dec. 2006), pp. 3575–3583. ISSN: 13500872. DOI: `10.1099/mic.0.28881-0`.

[425] Jennifer K. Teschler et al. “Living in the Matrix: Assembly and Control of Vibrio Cholerae Biofilms”. In: *Nature reviews. Microbiology* 13.5 (May 2015), pp. 255–268. ISSN: 1740-1526. DOI: `10.1038/nrmicro3433`. (Visited on 09/17/2019).

[426] Nicolas Thewes et al. “Stochastic Binding of Staphylococcus Aureus to Hydrophobic Surfaces”. In: *Soft Matter* 11.46 (Aug. 2015), pp. 8913–8919. ISSN: 17446848. DOI: `10.1039/c5sm00963d`.

[427] Philippe Thomen et al. “Bacterial Biofilm under Flow: First a Physical Struggle to Stay, Then a Matter of Breathing”. In: *PLOS ONE* 12.4 (Apr. 2017). Ed. by Josué Sznitman, e0175197. ISSN: 1932-6203. DOI: `10.1371/journal.pone.0175197`.

[428] Martin Thullner, Josef Zeyer, and Wolfgang Kinzelbach. “Influence of Microbial Growth on Hydraulic Properties of Pore Networks”. In: *Transport in Porous Media* 49.1 (Oct. 2002), pp. 99–122. ISSN: 1573-1634. DOI: `10.1023/A:1016030112089`. (Visited on 11/03/2021).

[429] Alessandro Tocchio et al. “Versatile Fabrication of Vascularizable Scaffolds for Large Tissue Engineering in Bioreactor”. In: *Biomaterials* 45 (Mar. 2015), pp. 124–131. ISSN: 0142-9612. DOI: `10.1016/j.biomaterials.2014.12.031`. (Visited on 03/15/2023).

[430] Tim Tolker-Nielsen. “Biofilm Development”. In: *Microbiology Spectrum* 3.2 (Apr. 2015). ISSN: 2165-0497. DOI: `10.1128/microbiolspec.mb-0001-2014`.

[431] E.W. Tollner et al. “Effect of Soil Total Iron on Magnetic Resonance Image Quality”. In: *Communications in Soil Science and Plant Analysis* 22.19-20 (Dec. 1991), pp. 1941–1948. ISSN: 0010-3624. DOI: `10.1080/00103629109368548`. (Visited on 12/21/2022).

[432] Christopher Torrence and Gilbert P. Compo. “A Practical Guide to Wavelet Analysis”. In: *Bulletin of the American Meteorological Society* 79.1 (Jan. 1998), pp. 61–78. ISSN: 0003-0007, 1520-0477. DOI: `10.1175/1520-0477(1998)079<0061:APGTWA>2.0.CO;2`. (Visited on 04/02/2023).

[433] Boo Shan Tseng et al. “The Extracellular Matrix Protects Pseudomonas Aeruginosa Biofilms by Limiting the Penetration of Tobramycin”. In: *Environmental Microbiology* 15.10 (Oct. 2013), pp. 2865–2878. ISSN: 1462-2920. DOI: `10.1111/1462-2920.12155`.

[434] Yvette C. Udall et al. “The Evolution of Biofilm-Forming Wrinkly Spreaders in Static Microcosms and Drip-Fed Columns Selects for Subtle Differences in Wrinkleality and Fitness”. In: *FEMS Microbiology Ecology* 91.6 (June 2015). ISSN: 1574-6941. DOI: `10.1093/femsec/fiv057`. (Visited on 10/04/2022).

[435] Arturo Urrios et al. “3D-printing of Transparent Bio-Microfluidic Devices in PEG-DA”. In: *Lab on a Chip* 16.12 (June 2016), pp. 2287–2294. ISSN: 1473-0189. DOI: `10.1039/C6LC00153J`. (Visited on 03/14/2023).

[436] Kambiz Vafai, ed. *Porous Media: Applications in Biological Systems and Biotechnology.* Zeroth. CRC Press, Aug. 2010. ISBN: 978-0-429-14162-1. DOI: `10.1201/9781420065428`. (Visited on 09/02/2022).

[437] Sander Van den Driesche et al. “3D Printing Solutions for Microfluidic Chip-To-World Connections”. In: *Micromachines* 9.2 (Feb. 2018), p. 71. ISSN: 2072-666X. DOI: `10.3390/mi9020071`. (Visited on 04/05/2023).

[438] M. C. van Loosdrecht, W. Norde, and A. J. Zehnder. “Physical Chemical Description of Bacterial Adhesion”. In: *Journal of Biomaterials Applications* 5.2 (Oct. 1990), pp. 91–106. ISSN: 0885-3282. DOI: `10.1177/088532829000500202`.

[439] Mark C. M. Van Loosdrecht and Sef J. Heijnen. “Biofilm Bioreactors for Waste-Water Treatment”. In: *Trends in Biotechnology* 11.4 (Apr. 1993), pp. 117–121. ISSN: 0167-7799. DOI: `10.1016/0167-7799(93)90085-N`. (Visited on 04/12/2023).

[440] A.s. Van Wey et al. “Anisotropic Nutrient Transport in Three-Dimensional Single Species Bacterial Biofilms”. In: *Biotechnology and Bioengineering* 109.5 (2012), pp. 1280–1292. ISSN: 1097-0290. DOI: `10.1002/bit.24390`. (Visited on 01/29/2023).

[441] Philippe Vandevivere and Philippe Baveye. “Saturated Hydraulic Conductivity Reduction Caused by Aerobic Bacteria in Sand Columns”. In: *Soil Science Society of America Journal* 56.1 (1992), pp. 1–13. ISSN: 1435-0661. DOI: `10.2136/sssaj1992.03615995005600010001x`. (Visited on 01/31/2023).

[442] Pablo Vasquez Guzman et al. “Near-Field Spray Measurements Using X-Ray Computed Tomography”. In: May 2014.

[443] Suganthan Veerachamy et al. “Bacterial Adherence and Biofilm Formation on Medical Implants: A Review”. In: *Proceedings of the Institution of Mechanical Engineers, Part H: Journal of Engineering in Medicine* 228.10 (Oct. 2014), pp. 1083–1099. ISSN: 0954-4119. DOI: `10.1177/0954411914556137`. (Visited on 04/07/2023).

[444] Bastien Venzac et al. “PDMS Curing Inhibition on 3D-Printed Molds: Why? Also, How to Avoid It?” In: *Analytical Chemistry* 93.19 (May 2021), pp. 7180–7187. ISSN: 0003-2700. DOI: `10.1021/acs.analchem.0c04944`. (Visited on 11/10/2022).

[445] S. Vijayakumar and S. Ganesan. “In Vitro Cytotoxicity Assay on Gold Nanoparticles with Different Stabilizing Agents”. In: *Journal of Nanomaterials* 2012 (Jan. 2012), 14:14. ISSN: 1687-4110. DOI: `10.1155/2012/734398`. (Visited on 04/01/2023).

[446] Vinita Vishwakarma. “Impact of Environmental Biofilms: Industrial Components and Its Remediation”. In: *Journal of Basic Microbiology* 60.3 (2020), pp. 198–206. ISSN: 1521-4028. DOI: `10.1002/jobm.201900569`. (Visited on 01/31/2023).

[447] Jérémy Voisin et al. “Ecological Assessment of Groundwater Ecosystems Disturbed by Recharge Systems Using Organic Matter Quality, Biofilm Characteristics, and Bacterial Diversity”. In: *Environmental Science and Pollution Research* 27.3 (Jan. 2020), pp. 3295–3308. ISSN: 1614-7499. DOI: `10.1007/s11356-019-06971-5`. (Visited on 03/15/2023).

[448] D. A. Graf von der Schulenburg et al. “Three-Dimensional Simulations of Biofilm Growth in Porous Media”. In: *AIChE Journal* 55.2 (2009), pp. 494–504. ISSN: 1547-5905. DOI: `10.1002/aic.11674`. (Visited on 11/01/2021).

[449] Julia A. Vorholt. “Microbial Life in the Phyllosphere”. In: *Nature Reviews Microbiology* 10.12 (Dec. 2012), pp. 828–840. ISSN: 1740-1534. DOI: `10.1038/nrmicro2910`. (Visited on 01/31/2023).

[450] Jurrien M. Vroom et al. “Depth Penetration and Detection of pH Gradients in Biofilms by Two-Photon Excitation Microscopy”. In: *Applied and Environmental Microbiology* 65.8 (Aug. 1999), pp. 3502–3511. ISSN: 0099-2240. (Visited on 12/20/2022).

[451] Michael Wagner and Harald Horn. “Optical Coherence Tomography in Biofilm Research: A Comprehensive Review”. In: *Biotechnology and Bioengineering* 114.7 (2017), pp. 1386–1402. ISSN: 1097-0290. DOI: `10.1002/bit.26283`. (Visited on 11/01/2021).

[452] K. Waszczuk et al. “Evaluation of Pseudomonas Aeruginosa Biofilm Formation Using Piezoelectric Tuning Fork Mass Sensors”. In: *Sensors and Actuators B: Chemical.* Eurosensors XXIV, 2010 170 (July 2012), pp. 7–12. ISSN: 0925-4005. DOI: `10.1016/j.snb.2010.11.019`. (Visited on 01/08/2023).

[453] *Wavelet Analysis for Geophysical Applications - Kumar - 1997 - Reviews of Geophysics - Wiley Online Library.* https://agupubs.onlinelibrary.wiley.com/doi/abs/10.1029/97rg00427. (Visited on 04/02/2023).

[454] L. Weaver et al. “Biofilm Resilience to Desiccation in Groundwater Aquifers: A Laboratory and Field Study”. In: *Science of The Total Environment* 514 (May 2015), pp. 281–289. ISSN: 0048-9697. DOI: `10.1016/j.scitotenv.2014.10.031`. (Visited on 03/13/2023).

[455] Yaoguang Wei et al. "Review of Dissolved Oxygen Detection Technology: From Laboratory Analysis to Online Intelligent Detection". In: *Sensors* 19.18 (Jan. 2019), p. 3995. ISSN: 1424-8220. DOI: `10.3390/s19183995`. (Visited on 01/07/2023).

[456] Jeanette D. Wheeler et al. "Not Just Going with the Flow: The Effects of Fluid Flow on Bacteria and Plankton". In: *Annual Review of Cell and Developmental Biology* 35.1 (Oct. 2019), pp. 213–237. ISSN: 1081-0706. DOI: `10.1146/annurev-cellbio-100818-125119`. (Visited on 10/29/2019).

[457] Laura Allison Wheeler. "Establishment of Ureolytic Biofilms and Their Influence on the Permeability of Pulse-Flow Porous Media Column Systems". Thesis. Montana State University - Bozeman, College of Engineering, 2009. (Visited on 12/29/2022).

[458] Cynthia B. Whitchurch et al. "Extracellular DNA Required for Bacterial Biofilm Formation". In: *Science (New York, N.Y.)* 295.5559 (Feb. 2002), p. 1487. ISSN: 1095-9203. DOI: `10.1126/science.295.5559.1487`.

[459] Marvin Whiteley et al. "Gene Expression in Pseudomonas Aeruginosa Biofilms". In: *Nature* 413.6858 (Oct. 2001), pp. 860–864. ISSN: 1476-4687. DOI: `10.1038/35101627`. (Visited on 04/07/2023).

[460] Tobias Wieland et al. "Inhibition of MDR/MRSA Bacterial Biofilms by the Antimicrobial Peptides Esculaentin 1-A and OH-CATH-30 Monitored by a Thermal Sensor System in Real-Time". In: *2019 20th International Conference on Solid-State Sensors, Actuators and Microsystems & Eurosensors XXXIII (TRANSDUCERS & EUROSENSORS XXXIII)*. June 2019, pp. 1094–1097. DOI: `10.1109/TRANSDUCERS.2019.8808589`.

[461] Dorthe Wildenschild and Adrian P. Sheppard. "X-Ray Imaging and Analysis Techniques for Quantifying Pore-Scale Structure and Processes in Subsurface Porous Medium Systems". In: *Advances in Water Resources* 51 (Jan. 2013), pp. 217–246. ISSN: 03091708. DOI: `10.1016/j.advwatres.2012.07.018`.

[462] Kerry S. Williamson et al. "Heterogeneity in Pseudomonas Aeruginosa Biofilms Includes Expression of Ribosome Hibernation Factors in the Antibiotic-Tolerant Subpopulation and Hypoxia-Induced Stress Response in the Metabolically Active Population". In: *Journal of Bacteriology* 194.8 (Apr. 2012), pp. 2062–2073. ISSN: 0021-9193. DOI: `10.1128/JB.00022-12`. (Visited on 01/22/2023).

[463] M. Wloka et al. "Structure and Rheological Behaviour of the Extracellular Polymeric Substance Network of Mucoid Pseudomonas Aeruginosa Biofilms". In: *Biofilms* 2.4 (Oct. 2005), pp. 275–283. ISSN: 1479-0513, 1479-0505. DOI: `10.1017/S1479050506002031`. (Visited on 01/05/2023).

[464] Otto S. Wolfbeis. "Luminescent Sensing and Imaging of Oxygen: Fierce Competition to the Clark Electrode". In: *BioEssays* 37.8 (2015), pp. 921–928. ISSN: 1521-1878. DOI: `10.1002/bies.201500002`. (Visited on 01/08/2023).

[465] D. W. Wood et al. "N-Acyl-Homoserine Lactone-Mediated Regulation of Phenazine Gene Expression by Pseudomonas Aureofaciens 30-84 in the Wheat Rhizosphere". In: *Journal of Bacteriology* 179.24 (Dec. 1997), pp. 7663–7670. ISSN: 0021-9193. DOI: `10.1128/jb.179.24.7663-7670.1997`.

[466] S. R. Wood et al. "Architecture of Intact Natural Human Plaque Biofilms Studied by Confocal Laser Scanning Microscopy". In: *Journal of Dental Research* 79.1 (Jan. 2000), pp. 21–27. ISSN: 0022-0345. DOI: `10.1177/00220345000790010201`.

[467] S. L. Woodruff et al. "The Effects of Biofilms on Chemical Processes in Surficial Sediments". In: *Freshwater Biology* 41.1 (1999), pp. 73–89. ISSN: 1365-2427. DOI: `10.1046/j.1365-2427.1999.00387.x`. (Visited on 03/13/2023).

[468] Tomas de Wouters et al. "Adhesion Potential of Intestinal Microbes Predicted by Physico-Chemical Characterization Methods". In: *PLOS ONE* 10.8 (Aug. 2015), e0136437. ISSN: 1932-6203. DOI: `10.1371/journal.pone.0136437`. (Visited on 01/08/2023).

[469] Lidong Wu, Xiang Ji, and Jing Kong. "Polymer-Coated Mesoporous Carbon as Enzyme Platform for Oxidation of Bisphenol A in Organic Solvents". In: *ACS Omega* 4.15 (Oct. 2019), pp. 16409–16417. DOI: `10.1021/acsomega.9b01945`. (Visited on 03/15/2023).

[470] Yong Wu et al. "Extracellular Matrix Reorganization during Cryo Preparation for Scanning Electron Microscope Imaging of Staphylococcus Aureus Biofilms". In: *Microscopy and Microanalysis* 20.5 (Oct. 2014), pp. 1348–1355. ISSN: 1431-9276, 1435-8115. DOI: `10.1017/S143192761401277X`. (Visited on 12/19/2022).

[471] Chunguang Xia and Nicholas X. Fang. "3D Microfabricated Bioreactor with Capillaries". In: *Biomedical Microdevices* 11.6 (Dec. 2009), pp. 1309–1315. ISSN: 1572-8781. DOI: `10.1007/s10544-009-9350-4`. (Visited on 03/14/2023).

[472] Yikang Xu et al. "Sensing the Unreachable: Challenges and Opportunities in Biofilm Detection". In: *Current Opinion in Biotechnology.* Analytical Biotechnology 64 (Aug. 2020), pp. 79–84. ISSN: 0958-1669. DOI: `10.1016/j.copbio.2019.10.009`. (Visited on 04/05/2023).

[473] N. Yagi. "8.02 - Synchrotron Radiation". In: *Comprehensive Biomedical Physics.* Ed. by Anders Brahme. Oxford: Elsevier, Jan. 2014, pp. 17–33. ISBN: 978-0-444-53633-4. DOI: `10.1016/B978-0-444-53632-7.00602-X`. (Visited on 12/22/2022).

[474] Qian Yan et al. "A Review of 3D Printing Technology for Medical Applications". In: *Engineering* 4.5 (Oct. 2018), pp. 729–742. ISSN: 2095-8099. DOI: `10.1016/j.eng.2018.07.021`. (Visited on 03/14/2023).

[475] Liang Yang et al. "Distinct Roles of Extracellular Polymeric Substances in Pseudomonas Aeruginosa Biofilm Development". In: *Environmental Microbiology* 13.7 (July 2011), pp. 1705–1717. ISSN: 1462-2920. DOI: `10.1111/j.1462-2920.2011.02503.x`.

[476] Lu Yang et al. "Interdependence of Foreign Exchange Markets: A Wavelet Coherence Analysis". In: *Economic Modelling* 55 (June 2016), pp. 6–14. ISSN: 0264-9993. DOI: `10.1016/j.econmod.2016.01.022`. (Visited on 04/02/2023).

[477] Yutaka Yawata et al. "Microfluidic Studies of Biofilm Formation in Dynamic Environments". In: *Journal of Bacteriology* 198.19 (Sept. 2016), pp. 2589–2595. DOI: `10.1128/JB.00118-16`. (Visited on 11/12/2022).

[478] Yutaka Yawata et al. "Microfluidic Studies of Biofilm Formation in Dynamic Environments". In: *Journal of Bacteriology* 198.19 (), pp. 2589–2595. DOI: `10.1128/JB.00118-16`. (Visited on 11/03/2021).

[479] Yue Yi et al. "Dual Detection of Biochemical Oxygen Demand and Nitrate in Water Based on Bidirectional Shewanella Loihica Electron Transfer". In: *Bioresource Technology* 309 (Aug. 2020), p. 123402. ISSN: 0960-8524. DOI: `10.1016/j.biortech.2020.123402`. (Visited on 01/07/2023).

[480] Seo YoungWoo [Seo and Y. W. Y. "Use of Biofilm Permeable Reactive Barriers for the in Situ Remediation of Mobile Contaminants." In: *Biofilms in bioremediation: current research and emerging technologies* (2016), pp. 201–218. (Visited on 01/31/2023).

[481] Q. Zhao et al. "Effect of Surface Free Energy on the Adhesion of Biofouling and Crystalline Fouling". In: *Chemical Engineering Science* 60.17 (Sept. 2005), pp. 4858–4865. ISSN: 0009-2509. DOI: `10.1016/j.ces.2005.04.006`. (Visited on 12/28/2022).

[482] Shixian Zhao et al. "A Portable and Automatic Dual-Readout Detector Integrated with 3D-printed Microfluidic Nanosensors for Rapid Carbamate Pesticides Detection". In: *Sensors and Actuators B: Chemical* 346 (Nov. 2021), p. 130454. ISSN: 0925-4005. DOI: `10.1016/j.snb.2021.130454`. (Visited on 03/14/2023).

[483] Xiao Zhu et al. “3D Printing Promotes the Development of Drugs”. In: *Biomedicine & Pharmacotherapy* 131 (Nov. 2020), p. 110644. ISSN: 0753-3322. DOI: `10.1016/j.biopha.2020.110644`. (Visited on 03/14/2023).

[484] Ricardo Ziege et al. “Adaptation of Escherichia Coli Biofilm Growth, Morphology, and Mechanical Properties to Substrate Water Content”. In: *ACS Biomaterials Science & Engineering* 7.11 (Nov. 2021), pp. 5315–5325. DOI: `10.1021/acsbiomaterials.1c00927`. (Visited on 12/28/2022).

[485] Susan E. Ziegler and David R. Lyon. “Factors Regulating Epilithic Biofilm Carbon Cycling and Release with Nutrient Enrichment in Headwater Streams”. In: *Global Change and River Ecosystems—Implications for Structure, Function and EcosystemServices.* Ed. by R. Jan Stevenson and Sergi Sabater. Developments in Hydrobiology 215. Dordrecht: Springer Netherlands, 2010, pp. 71–88. ISBN: 978-94-007-0608-8. DOI: `10.1007/978-94-007-0608-8_6`. (Visited on 03/15/2023).